NASA CR-174664
84SRD006

EFFECTS OF VANE/BLADE RATIO AND SPACING ON FAN NOISE

Volume I

by
P.R. Gliebe
and
R.A. Kantola

Prepared for

NATIONAL AERONAUTICS AND SPACE ADMINISTRATION

NASA-Lewis Research Center
Contract NAS3-22062

1 Report No. NASA CR-174664	2 Government Accession No.	3. Recipient's Catalog No
4 Title and Subtitle Effects of Vane/Blade Ratio and Spacing on Fan Noise Vol. I - Final Technical Report		5 Report Date December 1983 6 Performing Organization Code
7 Author(s) P.R. Gliebe, General Electric Company, Aircraft Engine Group, Cincinnati, OH; R.A. Kantola, formerly, General Electric Company, Corporate Research & Development, Schenectady, NY		8. Performing Organization Report No. 84SRD006 10. Work Unit No.
9. Performing Organization Name and Address General Electric Company Corporate Research and Development Schenectady, NY 12301		11. Contract or Grant No. NAS3-22062 13. Type of Report and Period Covered
12. Sponsoring Agency Name and Address National Aeronautics and Space Administration Washington, DC		14. Sponsoring Agency Code

15 Supplementary Notes

Project Manager: John F. Groeneweg, Fluid Mechanics and Instrumentation Divison
NASA-Lewis Research Center
21000 Brookpark Road, Cleveland, OH 44135

16. Abstract

The effects of vane/blade ratio and spacing on the noise characteristics of a high-speed fan were investigated experimentally and analytically. The experimental investigation was carried out on a 50.8 cm (20 in.) diameter scale model fan stage in an anechoic chamber with an inflow turbulence control screen installed. The forty-four blade rotor was tested with forty-eight vane and eighty-six vane stator rows, over a range of axial rotor-stator spacings from 0.5 to 2.3 rotor tip chords. A two-dimensional strip theory model of rotor-stator interaction noise was employed to predict the measured tone power level trends, and good overall agreement with measured trends was obtained.

The Final Technical Report documenting the program results is contained in Volume I herein. Complete tabulations of 1/3-octave band acoustic measurements are given in Volume II

17. Key Words (Suggested by Author(s))	18. Distribution Statement Unclassified Unlimited		
19. Security Classif. (of this report) Unclassified	20. Security Classif. (of this page) Unclassified	21. No. of Pages 162	22. Price*

* For sale by the National Technical Information Service, Springfield, Virginia 22161

TABLE OF CONTENTS

LIST OF FIGURES

LIST OF FIGURES (Cont'd)

LIST OF FIGURES (Cont'd)

LIST OF FIGURES (Cont'd)

LIST OF FIGURES (Cont'd)

LIST OF TABLES

FOREWORD

The bulk of the experimental testing and hardware/instrumentation buildup and assembly was carried out under the direction of Mr. R.E. Warren. The processing of narrowband spectra from the analog data was carried out under the supervision and careful scrutiny of Mr. R.H. Wells. The success of this program is due in great measure to the tireless efforts of these two gentlemen. Mr. R.S. Coffin assisted in the preparation of many of the figures and tables of the final report and his help is gratefully acknowledged. The initial NASA Program Monitors, Ms. L.M. Shaw and Mr. John F. Groeneweg, provided excellent guidance and assistance in ironing out the administrative and technical difficulties encountered during the course of the program and their patience, understanding, and helpfulness are greatly appreciated.

ABSTRACT

The effects of vane/blade ratio and spacing on the noise characteristics of a high-speed fan were investigated experimentally and analytically. The experimental investigation was carried out on a 50.8 cm- (20 in.-)diameter scale model fan stage in an anechoic chamber with an inflow turbulence control screen installed. The forty-four blade rotor was tested with forty-eight vane and eighty-six vane stator rows, over a range of axial rotor-stator spacings from 0.5 to 2.3 rotor tip chords. A two-dimensional strip theory model of rotor-stator interaction noise was employed to predict the measured tone power level trends, and good overall agreement with measured trends was obtained.

SUMMARY

An experimental and analytical investigation of the effects of vane/blade number ratio and axial spacing on the noise characteristics of a high-speed fan stage was carried out. The experimental measurements were conducted on a 50.8 cm- (20 in.-) diameter fan stage having a design tip speed of 427 m/s (1400 ft/sec). The tests were carried out in the General Electric Corporate Research and Development anechoic chamber fan noise facility. The objective of these experiments was to quantify the effects of rotor-to-stator axial spacing for a typical "cut-off" fan design and a typical "cut-on" fan design. The cut-off fan design is typical of current technology fan designs used in modern high bypass ratio engines, where the vane number is approximately twice the blade number so that the fundamental blade passing frequency tone produced by rotor-stator interaction is nonpropagating for subsonic tip speeds. The cut-on fan design has approximately the same number of vanes as blades, producing a propagating blade passing frequency tone due to rotor-stator interaction at subsonic tip speed. By employing fewer vanes but maintaining approximately the same stator cascade solidity, the vane performance may be improved due to the lower resulting aspect ratio. Further, there may be a potential weight and manufacturing cost benefit.

A forty-four blade rotor designed by NASA (designated "Rotor 11"), with a forty-eight vane stator and an eighty-six vane stator set was tested. Rotor-to-stator axial spacings of 0.5, 1.27 and 2.3 rotor tip chords were tested for the forty-eight vane stator configuration, and axial spacings of 0.5, 0.9,, 1.27 and 2.3 chords were tested for the eighty-six vane configuration. Forward radiated noise measurements were made with microphones placed on a 5.18 m- (17 ft-) radius arc every 10° from 0° (fan centerline) to 110°. Inlet duct wall-mounted pressure transducers, an aft duct traversing sound probe, and a blade-mounted transducer were employed to provide diagnostic and corroborative information to support and supplement the far field measurements.

An inflow turbulence control screen, essentially a hemispherical honeycomb dome assembly, was installed over the fan inlet, along with a specially contoured "reverse cone" inlet bellmouth, to remove and/or attenuate ingested inflow disturbances due to atmospheric and chamber generated turbulence, vortices, and distortions. The objective of this screen-bellmouth device was to reduce the inflow disturbance-rotor interaction noise sources to a level well below the rotor-stator interaction levels, so that changes in spacing and vane number could be detected and evaluated. The fan was tested over a range of speeds from 54% to 100% of design and at two throttle settings corresponding to a medium and a high loading level.

Theoretical predictions of rotor-stator interaction tone noise were carried out for all the configurations tested experimentally. An existing General Electric Aircraft Engine Group computer program was used for this purpose, this program having been previously developed under Independent Research and Development Program funds. This computer program predicts the forward and aft radiated tone sound power level spectrum resulting from rotor-stator potential field interaction and rotor-wake-stator interaction. The computer program model employs a streamline-by-streamline analysis of the fan stage annulus from hub-to-tip accounting for spanwise variations in flow and geometric parameters on the unsteady blade and vane forces and acoustic source strengths.

The experimental results obtained from this program showed that the fan inlet blade passing tones, when they are cut on, exhibit a definite decrease in level with increasing rotor-stator spacing. The rate of decrease was found to be small for the fundamental tone ($n = 1$), and became larger with increasing harmonic number ($n = 2, 3$, etc.). Beyond a spacing of approximately 1.5 chords, the tone levels did not change appreciably, probably due to contamination from residual inflow distortion turbulence-rotor interaction noise and/or the proximity of the broadband noise floor. No perceptible difference between forty-eight vane and eighty-six vane harmonic falloff rates was observed in the far field tone levels.

Aft duct probe sound level measurements were analyzed to obtain relative estimates of the effects of rotor-stator spacing on aft radiated tone levels. The results were in substantial agreement with the trends observed for the forward radiated far field tones. One interesting trend observed is that the tone fall off rate with increasing spacing is somewhat greater than that of the forward radiated tones, especially at the higher speeds and higher fan operating line.

Comparisons were made between the theoretical model predictions of tone PWL versus spacing trends and measured trends. On the whole, agreement between experiment and prediction was quite good, with the exception that the leveling off of tone PWL beyond a spacing of approximately 1.5 chords was not predicted by the model. This deficiency in the predicted trends was attributed to an inadequate modeling of the wake merging process at large axial spacings and to the neglect of the residual inflow turbulence and distortion-rotor interaction noise generation in the predictions.

Conclusions from this study indicated that the fan tone directivity patterns are highly lobular, with lobe widths that are rather narrow, such that microphones placed at 10° intervals are insufficient to accurately define the field shapes. A traversing microphone arrangement that provides a continuous polar trace is recommended in any future experimental evaluations.

The vane/blade ratio has a significant effect on the shape of the fan rotor-stator noise harmonic spectrum. High vane/blade ratios (approximately two) tend to produce harmonic peaks at the second or third harmonic of blade passage frequency, whereas low vane/blade ratios (approximately one) tend to produce peaks at the first or second harmonic. Rotor-stator axial spacing also affects the harmonic spectrum shape. As spacing is increased, the tone levels fall off at a rate that increases with increasing harmonic number.

As speed is increased from typical low-speed approach power settings to high speeds such that the fan tip Mach number goes from subsonic to supersonic values, the effect of spacing and vane/blade ratio diminishes such that very little effect is noticeable in the forward arc at supersonic tip speeds. The aft duct noise, however, still exhibits the previously described dependency on vane/blade ratio and spacing at supersonic tip speeds. Conclusions from this effort showed that the forward radiated fan tone noise becomes dominated by the rotor-alone field at supersonic tip speeds, whereas the aft radiated noise is still controlled by rotor-stator interaction.

Section 1

INTRODUCTION

Current high bypass fans used in commercial jet engines have, in the recent past, been designed with rotor blades and stator vane numbers such that they do not produce acoustic energy in propagating spinning modes at the fundamental blade passing frequency for subsonic tip speeds. As a second precaution, rather wide separations of the rotor and stator are used to reduce the level of the harmonics of the blade passing frequency, which in the usual case do propagate to the far field. With the ever-increasing cost of fuel, engine manufacturers are being forced to reduce the rotor-stator spacing to raise fan efficiency and to reduce engine weight. The acoustic penalties, particularly the possibility of increased levels of the higher harmonic of blade passing frequency, must then be carefully evaluated. An accurate, theoretically based fan noise prediction scheme that has been calibrated against a set of high-quality experimental data is required to make these evaluations. Such a combination of data and theory has not appeared in the literature, apparently due to the lack of fan noise data that parametrically varies rotor-stator spacing and is free of the excess noise generated by inlet turbulence and distortion interaction with the fan rotor. One such data set from an anechoic wind tunnel along with rotor wake data has appeared in References 14-16 but a comparison with analysis was not included. The objective of this program was to provide uncontaminated data set and an analytical prediction. Preliminary results appeared in Reference 18.

The experiments were conducted at the General Electric Corporate Research and Development anechoic chamber in Schenectady, New York. This anechoic chamber facility has demonstrated the capability to produce fan noise data substantially free from excess noise caused by rotor-turbulence interaction. Both inlet flow contouring and a turbulence reduction structure are used to achieve this end. The test vehicle used in this investigation was a 0.504 m- (20 in.-) diameter fan model. A test matrix with a large range of tip speeds (from subsonic to supersonic) was investigated. Two stator sets were investigated in combination with a forty-four blade rotor; a cut-off set with eighty-six vanes and a cut-on set with forty-eight vanes. For the eighty-six vane set, four rotor-stator spacings were tested and for the forty-eight vane set, three spacings were tested. With both stator sets, the range of spacing was from 0.5 to 2.3 rotor chords. Twelve microphones were used to measure the far field sound radiation from 0° to 110° to the inlet centerline. The in-duct aft radiated fan noise sound level was measured with a traversing sound probe.

A computational procedure for carrying out a streamline-by-streamline analysis of rotor-stator interaction noise has been developed at GE AEBG under Independent Research and Development Program funds. This procedure is designed to utilize the fan stage axisymmetric flow field streamline aerodynamic design analysis results as input. The model includes not only viscous wake interaction noise, but also the potential field (blade pressure field due to loading) interactions of both the rotor and stator upon each other. Compressibility effects are included in both viscous wake and potential field interaction sources, although the potential field interaction source model is only valid for subsonic relative Mach numbers. This analysis procedure was used to predict the rotor-stator interaction tone sound power levels for all of the rotor-stator configurations tested in this program, and comparisons of predicted versus measured trends were carried out.

Section 2

DESCRIPTION OF FACILITY AND INSTRUMENTATION

A schematic diagram of the facility is shown in Figure 1. The anechoic chamber was designed to simulate a free field acoustic arena and provide adequate aerodynamic operation. It is approximately 10.7 m (35 ft) wide by 7.6 m (25 ft) long by 3.1 m (10 ft) high as measured from the tips of the foam wedges. A free field acoustic environment was achieved by covering walls, ceiling, and floor with an array of 0.7 m (28 in.) long polyurethane foam wedges, which provide less than ± 1 dB standing wave ratio at 200 Hz.

To achieve the lowest possible amount of inlet distortion and turbulence, the sidewalls, ceiling and floor of the anechoic chamber are porous. This porous box arrangement is achieved by a manifolding system whereby air flow is distributed from a filter house through 15.2 cm (6 in.) deep U-shaped channels surrounding the chamber. The array of foam wedges is secured to the channels so that the air flow enters the chamber by passing through small openings between the wedges. It has been demonstrated in a prior program [1] that such an aspirating chamber arrangement reduces in-flow distortion to the fan.

To further reduce inlet distortion, a flared reverse cone inlet, as shown in Figure 2, is used. The reverse cone inlet acts as a shroud covering all of the "upstream" hardware associated with the inlet and other test instrumentation. This hardware has, in the past, been identified as a major source of inlet distortion [1]. Along with the addition of the reverse cone inlet, great care was taken to aerodynamically clean up the chamber and remove all objects that protrude into the inlet flow field and, therefore, possibly generate flow distortions and turbulence. To further eliminate flow distortions and turbulence that reside in the boundary layer, the reverse cone inlet is equipped with an internal suction surface, as shown in Figure 3.

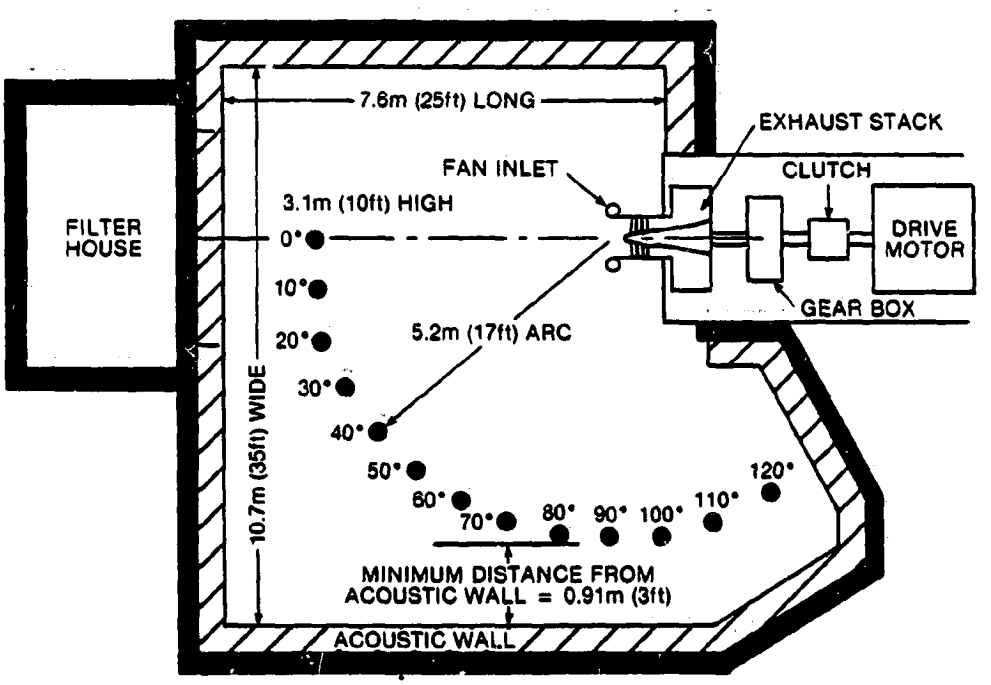

Figure 1. Schematic of General Electric Schenectady Anechoic Chamber Facility.

Figure 2. Fan Reverse Cone Inlet Installed.

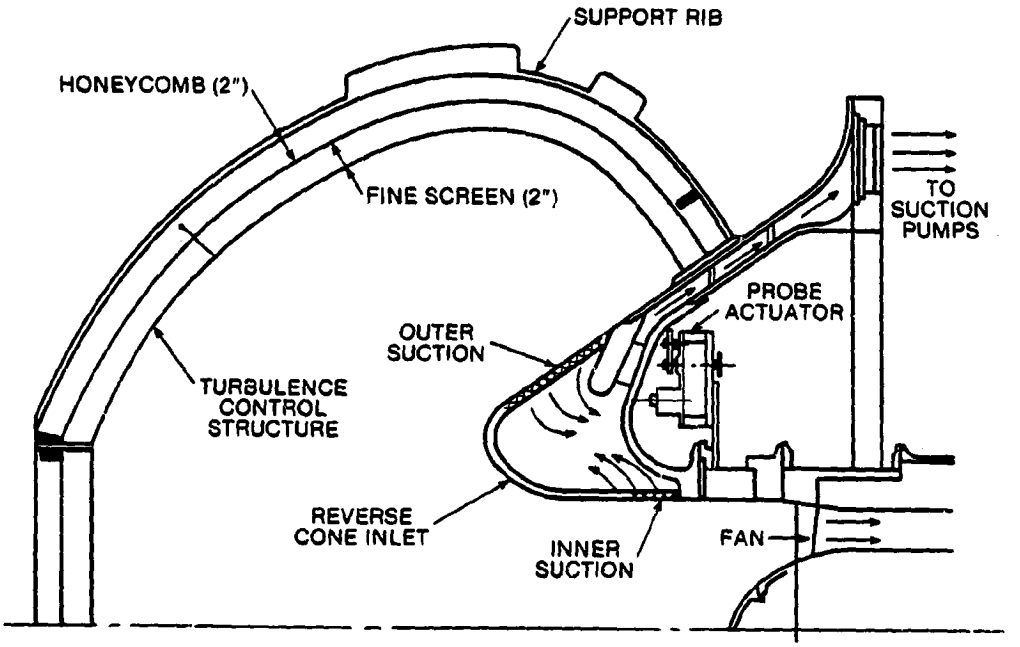

Figure 3. Assembly Sketch of Reverse Cone Inlet and Turbulence Control Structure (TCS).

The test configuration also employs a turbulence control structure (TCS) to condition the inlet flow and is shown in Figures 3, 4 and 5. The TCS used for this program is very similar in size and shape to that used in the earlier work of Shaw et al. [2] and Woodward et al. [3]. The major difference is that in this current design, the inner fine screen is displaced 5.08 cm (2 in.) downstream of the trailing edge of the honeycomb. This screen placement was based on the work of Morel [4] who found that in contracting flows, the separation between the honeycomb and the screen was very beneficial in reducing the axial turbulence intensity. This TCS was designed and fabricated by General Electric's Aircraft Engine Business Group as part of a General Electric-sponsored program. The TCS is nearly hemispherical in shape – 2.10 m (82.5 in.) at its largest diameter, 1.31 m (51.38 in.) long, and is of a two-layer construction. The first or outermost layer consists of aluminum honeycomb plus a support screen under the honeycomb, as shown in Figure 4. The honeycomb is 5.08 cm (2 in.) thick with irregular shaped cells measuring approximately 0.95 cm (3/8 in.) in width with a wall thickness of 0.063 mm (0.0025 in.). The second inner layer is a fine mesh (20 by 20) of 0.356 mm- (0.014 in.-) diameter wire. As can be seen in Figure 5, the TCS is divided into twelve sectors with 10.8 cm (4.25 in.) deep ribbing. The ribs are 0.318 cm (0.125 in.) thick and the screens are welded to the ribs. The complete structure was built and installed in such a way, see Figure 5, as to minimize the wakes from the support structure and, therefore, offer minimal flow distortion and self-generated turbulence.

The acoustic measurements were made in the anechoic chamber using an array of twelve 0.635 cm (0.25 in.) microphones. The microphones were located every 10°, from 0° (fan centerline) to 110° at an arc radius of 5.2 m (17 ft), as measured from the center of the inlet, one rotor diameter upstream from the rotor face (see Figure 1). The microphones were calibrated by a piston-phone prior to each run. Atmospheric absorption is accounted for via the Society of Automotive Engineers Specification Number ARP866. No other acoustic corrections were applied to this data.

Data acquisition is controlled by a series minicomputer that obtains the acoustic signals from a real-time, one-third octave band analyzer and samples the temperatures and pressure signals. By the use of a scanning multichannel amplifier, each microphone signal is sequentially analyzed and the signal level

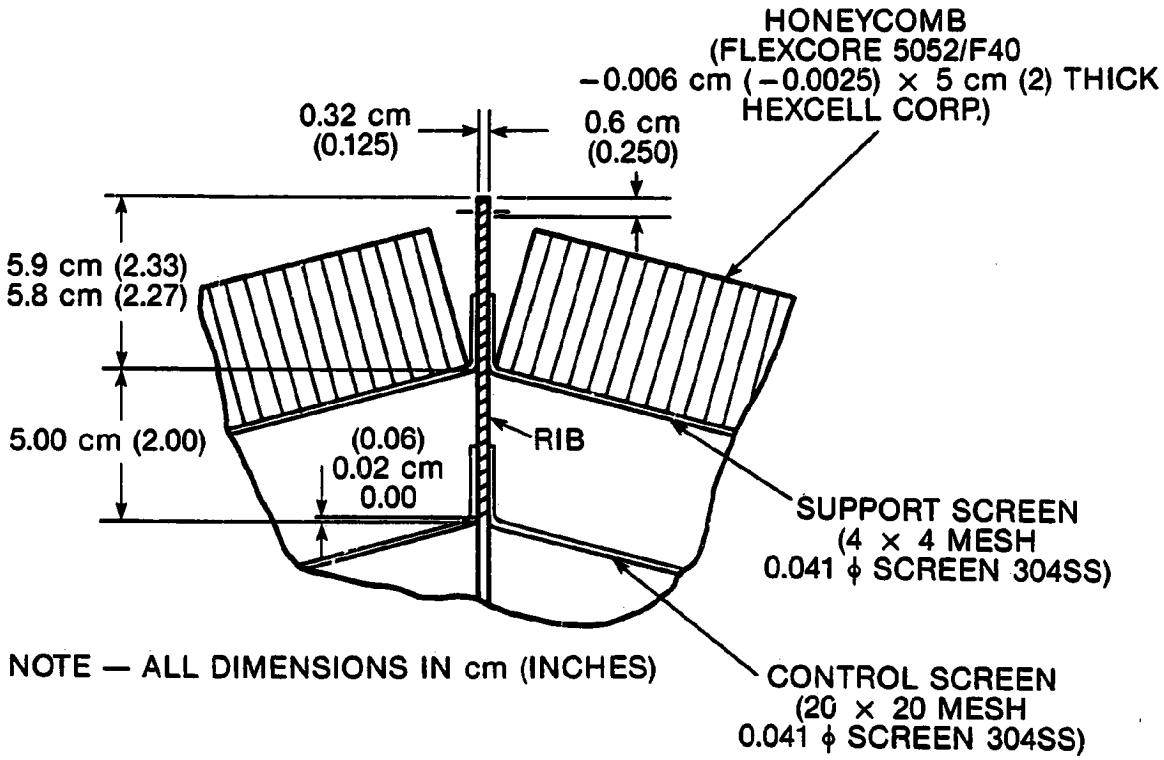

Figure 4. Fabrication Detail of Turbulence Control Structure.

of each one-third octave band (100 Hz to 80 kHz) stored on magnetic tape. For operational monitoring, a three-dimensional plot of the one-third octave band analysis of the SPL of each microphone is displayed on an oscilloscope as the microphone array is sampled. For backup, and when longer averaging times are necessary, the acoustic signals are recorded simultaneously on a tape recorder. After all the signals have been accumulated, the computer corrects the data for nonuniform response of the microphones and can correct for any known nonfree field effects of the arena. Using these corrected values of the sound pressure level, the computer then calculates the overall average sound pressure levels for each microphone, the one-third octave band acoustic power levels, and the overall acoustic power level. The raw and calculated data are then stored on magnetic tape.

While the computer is processing the acoustic data, simultaneous measurement and calculation of all pertinent parameters for determination of the fan flow conditions and ambient conditions are also carried out and recorded on magnetic tape. As all the pertinent data exists on one magnetic tape, the acoustic information is readily normalized by the computer immediately following the test.

In addition to the far field microphone array for measuring forward radiated noise, a probe was installed in the duct downstream of the fan stators to measure aft radiated sound levels. The probe was originally designed to separate hydrodynamic turbulent fluctuations from random sound pressure fluctuations when the source is broadband in nature, as described in [5]. The probe is illustrated in Figure 6 and contains two miniature pressure transducers as shown. For the present tests, sound-flow separation techniques were not employed, since the tone levels were of primary interest and the acoustic signal dominates at the fan tone frequencies. The probe is traversable in the radial direction and probe sound level measurements from both sensors (designated K2 and K4) were recorded at two radial immersion depths for all speeds and throttle settings of all seven fan configurations tested.

Two inlet duct wall-mounted miniature pressure sensors were also installed in front of the fan rotor. One was located at the juncture of the inlet lip and the duct wall (K5), and the other was located just upstream of the fan rotor (K6). Figure 6 shows the relative locations of these sensors.

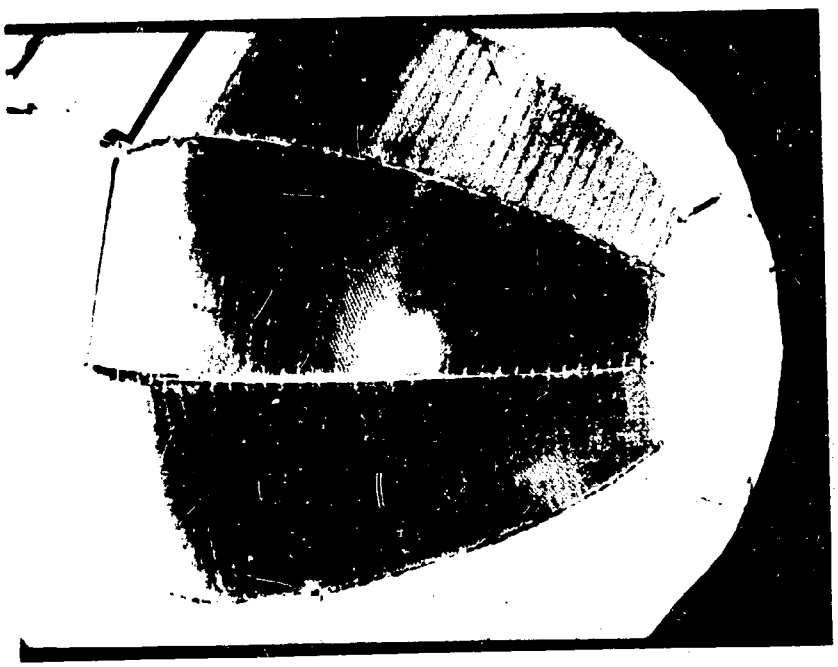

Figure 5. Reverse Cone Inlet with Turbulence Control Structure Installed.

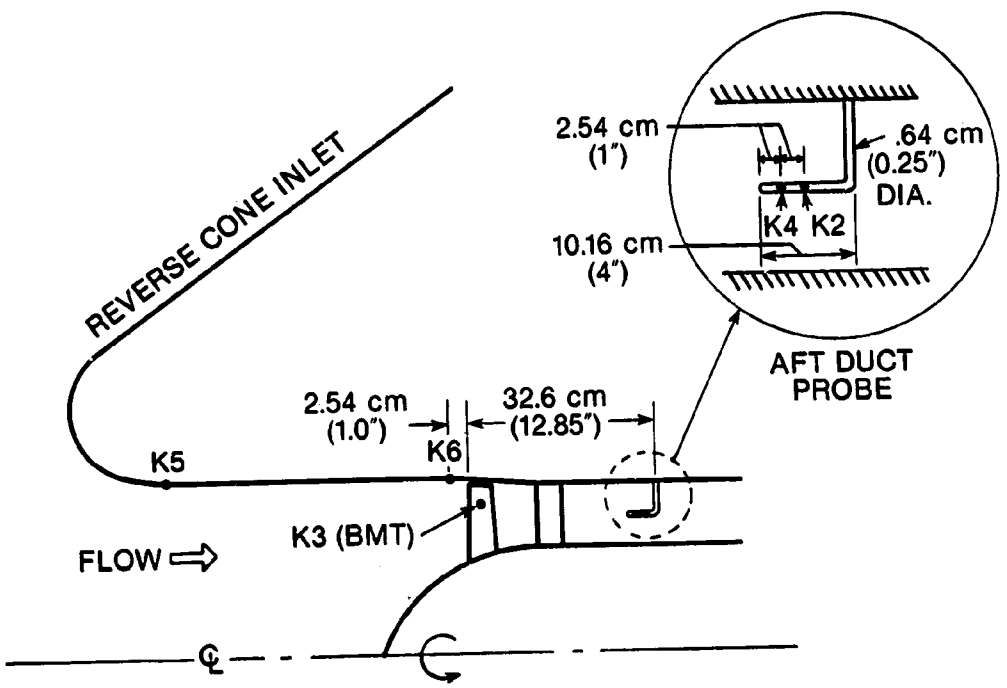

Figure 6. Schematic of Internal Acoustic Sensor Instrumentation Locations.

Section 3

DESCRIPTION OF FAN CONFIGURATIONS

The fan stage used in this investigation utilizes a forty-four blade transonic rotor with a 0.504 m-(20 in.-) tip diameter, designated as NASA Rotor 11. The rotor flow path and blade design is given in [6] and some of the important fan design parameters are given in Table 1.

Table 1

TEST FAN STAGE DESIGN CHARACTERISTICS

Rotor Inlet Tip Diameter	0.504 m (19.84 in.)
Pressure Ratio	1.574
Rotor Blade Number	44
Stator Vane Number	86
Vane/Blade Ratio	1.95
Inlet Guide Vanes	None
Rotor Inlet Hub/Tip Radius Ratio	0.50
Rotor-Stator Tip Spacing	1.27 Rotor Chords
Rotor Rotative Speed	16100 rpm
Rotor Tip Speed	424.9 m/sec. (1394 ft./sec.)
Rotor Tip Inlet Relative Mach Number	1.394
Rotor Chord (Midspan)	4.62 cm (1.817 in.)
Stator Chord (Midspan)	2.55 cm (1.005 in.)
Rotor Aspect Ratio	2.5
Stator Aspect Ratio	2.3
Rotor Tip Solidity	1.298
Stator Tip Solidity	1.433
Corrected Inlet Weight Flow	29.5 Kg/sec. (65 lbs./sec.)
Adiabatic Efficiency	85.5% (80.9% Measured)

Two sets of stators or outlet guide vanes (OGV's) were tested with Rotor 11 at various axial spacings downstream of the rotor trailing edge. An eighty-six vane stator row, previously tested in [1] at a nominal rotor-stator axial spacing of 1.27 tip rotor chord lengths, was tested in the present investigation at 0.5, 0.9, 1.27, and 2.3 chord spacings. The 0.9 chord spacing configuration, although not part of the original contract effort, was built and tested as part of a GE Aircraft Engine Group internal research and development program and the results from that investigation are included herein for completeness. A forty-eight vane stator row, originally designed for the Rotor 11 stage at 0.5 chord axial spacing in [6], was tested in the present investigation at rotor-stator spacing-to-chord ratios of 0.5, 1.27, and 2.3.

The vane/blade ratio combination eighty-six/forty-four represents a typical high bypass ratio cut-off fan design configuration where the rotor-stator interaction tone noise at blade passing frequency is designed to be nonpropagating (according to classical spinning mode duct theory) at subsonic tip speeds. The vane/blade ratio combination forty-eight/forty-four represents a cut-on design currently being studied for advanced energy efficient engine designs. Cross-sectional sketches of the various fan rotor-stator combinations tested are shown in Figures 7 and 8. Pitchline (50% span) solidities for the forty-eight vane and eighty-six vane stator assemblies were 1.57 and 1.78, respectively.

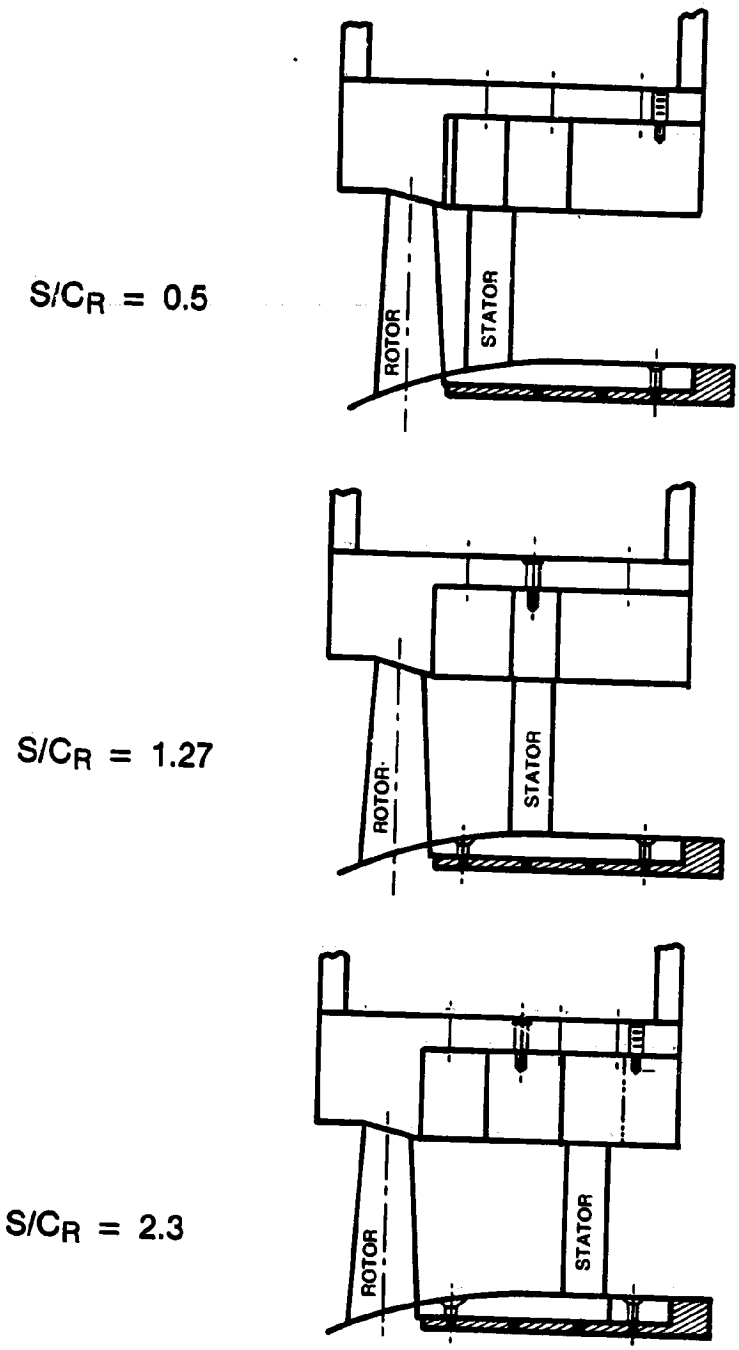

Figure 7. Cross-Section Sketches of 86-Vane Fan Stage Configuration.

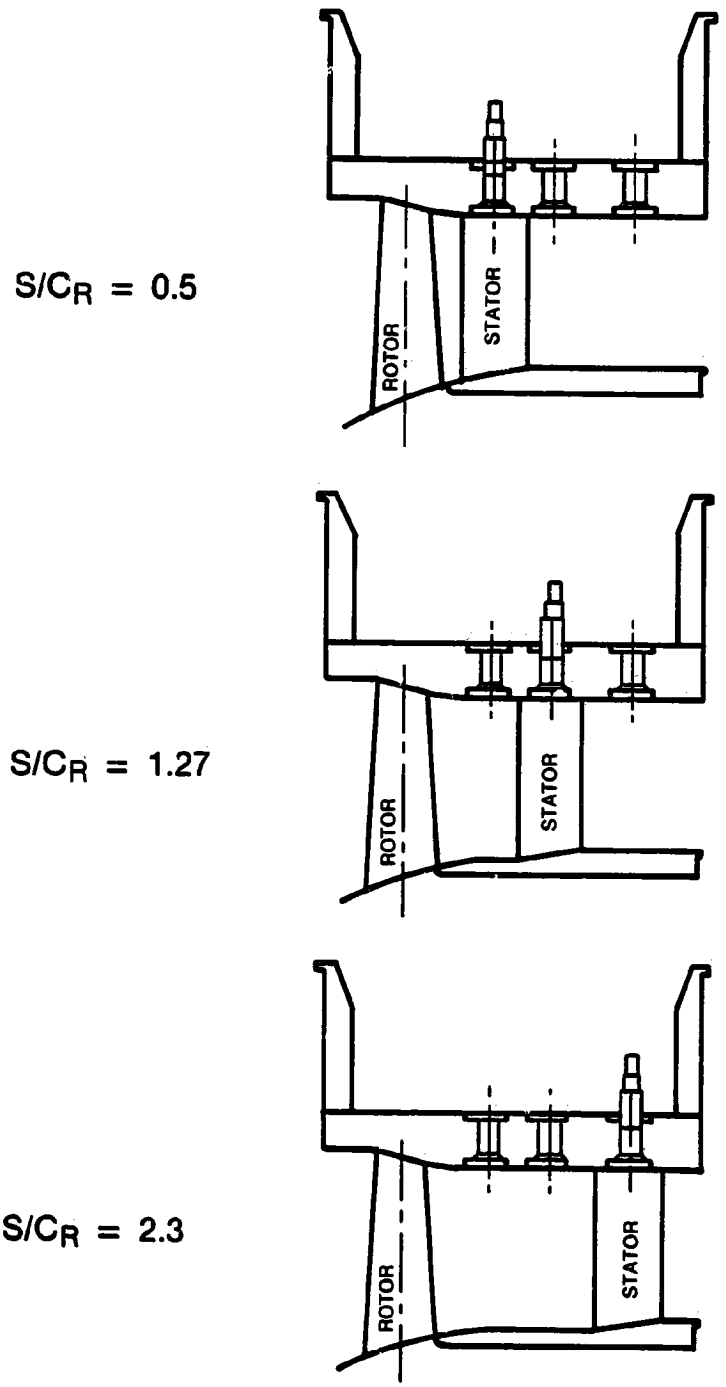

Figure 8. Cross-Section Sketches of 48-Vane Fan-Stage Configuration.

Section 4

AERODYNAMIC PERFORMANCE

Aerodynamic measurements were taken to determine the effects of the various stator configurations on the fan stage performance. The instrumentation included four total pressure, total temperature rakes with five radial stations each, located downstream of the rotor and a 0.56 m- (22 in.-) diameter orifice located in the fan discharge piping for flow measurements. With this information, plus the chamber static pressure (the inlet was assumed to be loss-free), the fan performance map was established for various configurations (see Figure 9). Very little change in aerodynamic performance was seen in going from the smallest to largest spacing for the eighty-six vane set, as shown in Figure 9.

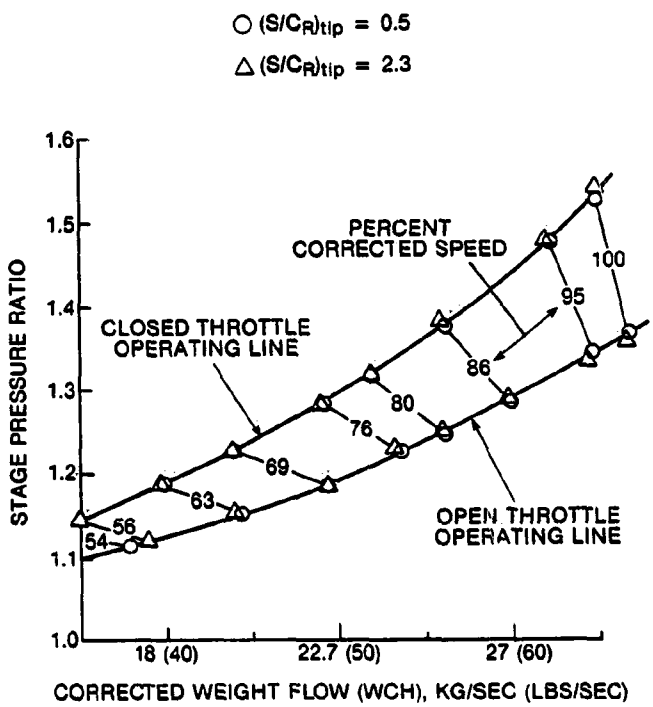

Figure 9. Fan Stage Performance Map for 86-Vane/Rotor 11 Configuration.

Section 5

INFLOW CONTROL CONFIGURATION SELECTION

Selection of the proper combination of inlet "cleanup" elements was the first task at hand. The primary question to resolve was determining if the inlet duct should be a smooth, rigid wall, or if it should contain a feltmetal surface to provide boundary layer suction as shown in Figure 3. To determine this, the eighty-six vane (cut-off) stator design was investigated at the 1.27 spacing-to-chord ratio. As this is a cut-off rotor-stator design below 74% speed, its blade passing frequency noise characteristic is a good indicator of the amount of inlet turbulence and distortion being ingested by the fan. Figure 10 illustrates the comparison between the hardwall (smooth, rigid duct) case and the feltmetal suction surface bleed duct (see [1]) at a suction flow rate of 5% of the fan flow. There are several items to note here. First, the hardwall case exhibits a clear cut-on of the blade passing frequency (BPF) noise; secondly, the presence of suction causes reduction of BPF level that is substantial for the cut-on speed conditions. This reduction of BPF at cut-on fan speeds could be caused by the feltmetal liner acting as a short section of acoustic treatment. To better understand this observation, the SPL spectra at various far field angles were examined as shown in Figure 11. Here the reductions are seen to be wide band in nature, indicating a treatment-like effect. It also should be noted that the hardwall data shows only slight evidence of any BPF tone content. In view of the adequate performance of the hardwall inlet and the complication of the effects of the feltmetal liner with suction, the hardwall inlet was used as the inlet configuration for the rest of the test program.

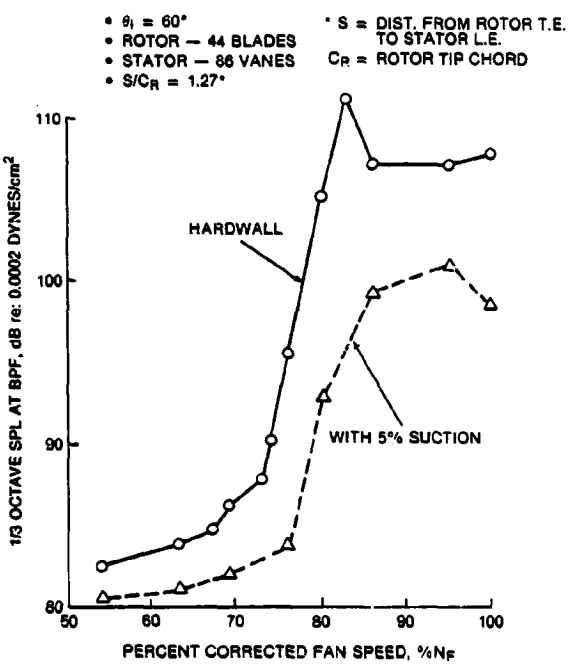

Figure 10. Cut-On of Blade Passing Frequency Noise with and without Inlet Duct Boundary Layer Suction, Open Throttle Operating Line.

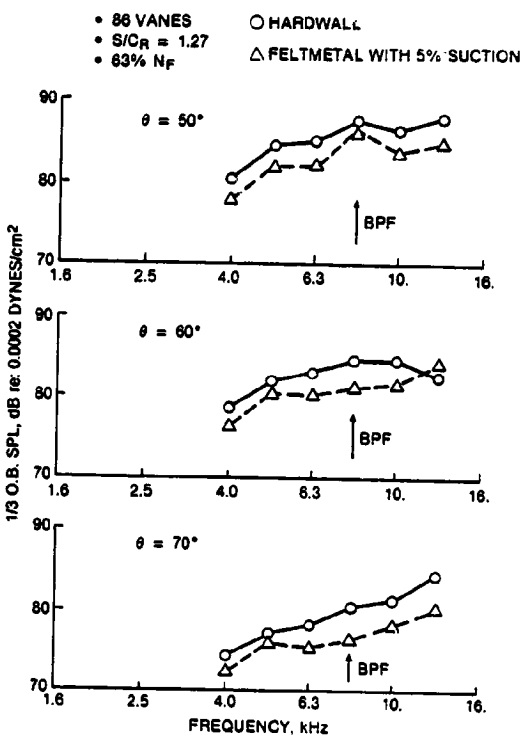

Figure 11. **Effect of Inlet Duct Boundary Layer Suction on 1/3-Octave SPL Spectrum in Vicinity of Blade Passing Frequency, Open Throttle Operating Line.**

Section 6

FAR FIELD ACOUSTIC TEST RESULTS

6.1 One-Third Octave Measurements

The various fan configurations were run over a range of fan speeds from 54% to 100% of design speed, at two throttle settings corresponding to the open throttle and closed throttle operating lines shown in Figure 9. The closed throttle operating line is representative of a typical high bypass ratio turbofan operating line at sea level static (test stand) operation. The open throttle operating line is typical of an in-flight operating line of a turbofan engine (at low fan speeds) simulating landing approach conditions.

The measured trends of the inlet arc one-third octave sound power level (PWL) versus fan speed for the band containing the blade passing frequency (BPF) tone are presented in Figures 12 and 13.

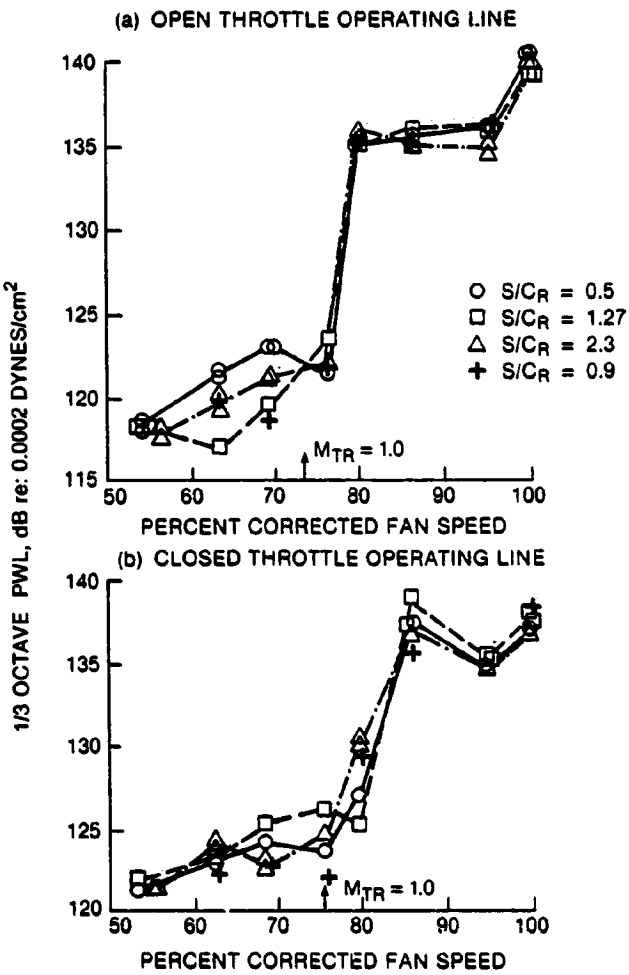

Figure 12. Effect of Rotor/Stator Spacing on BPF Tone 1/3-Octave PWL vs. Speed Characteristics for the 86-Vane Configuration.

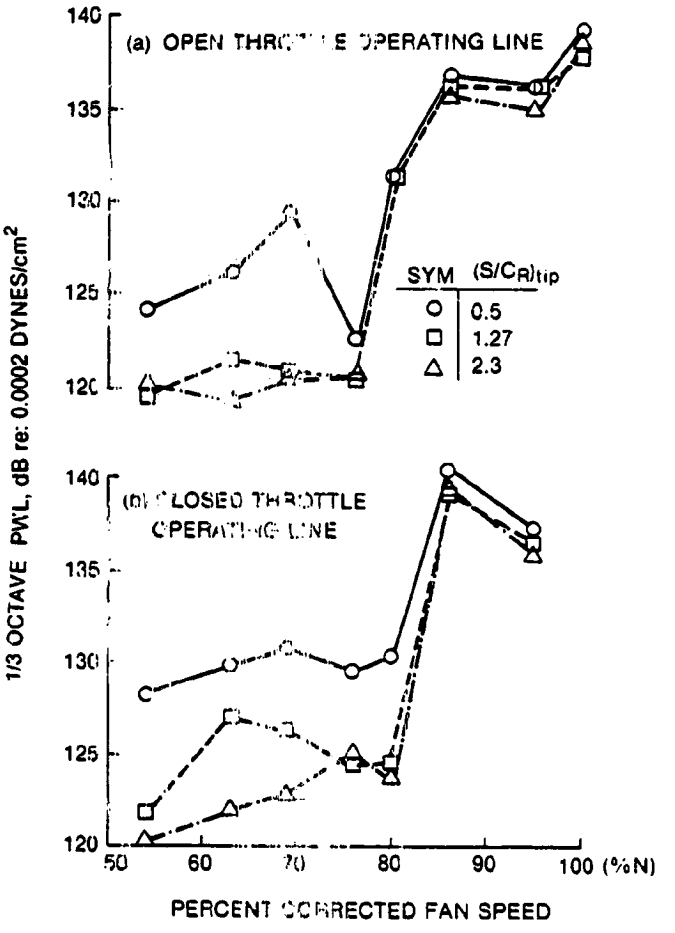

Figure 13. Effect of Rotor/Stator Spacing on BPF Tone 1/3-Octave PWL vs. Speed Characteristics for the 48-Vane Configurations.

Figures 12a and 12b show the BPF PWL versus speed trends for the eighty-six vane configuration for open and closed throttle operating lines, respectively. The corresponding forty-eight vane configuration trends are shown in Figures 13a and 13b.

As mentioned earlier, the eighty-six vane stator data exhibits cut on above 76% corrected speed. For this rotor-stator set, cut on occurs very near the rotor tip relative sonic velocity point, as can be seen in Figure 12.

At the supersonic speeds, the rotor-alone noise dominates, and the BPF noise emission is practically independent of rotor-stator spacing. At the subsonic rotor speeds, there is some variation of the BPF tone. This could be due to three sources: (1) ingested turbulence or inflow distortion, (2) slight misalignment of the inlet hardware causing a protrusion into the flow, or (3) a nonuniformity of either the rotor or the stator blades. If this BPF tone were controlled by inlet turbulence or distortion ingested from the anechoic chamber, then the tone level would be independent of the effects of stator configuration or test buildup. If it were due to a slight rotor-stator nonuniformity that causes a once per rev perturbation that can cause a cut-on spinning mode pattern, then the BPF level should reduce as spacing is increased. The effects of misalignment during inlet buildup would be random and as such should cause a BPF tone level that is random with respect to spacing. From the nature of the subsonic BPF tone levels, it appears that the rotor-stator nonuniformity and inlet buildup variances are the principal contributors to the residual BPF tones.

For the cut-on stator set (forty-eight vanes), the effect of reducing the rotor-stator spacing is to cause an increase in the BPF tone level (as seen in Figures 13a, 13b). Again as in the eighty-six vane results, at supersonic tip speeds, the noise is controlled by rotor-alone noise and is independent of spacing. It should be noted here that the individual microphone results should not be compared directly, and the power level (PWL) results are more appropriate for comparisons of the eighty-six and forty-eight vane results. This is due to the large differences in the vane numbers resulting in differences in spinning mode lobe numbers and their radiation patterns. For the forty-eight vane set, these subsonic BPF tones are expected, whereas for the eighty-six vane set, the subsonic BPF tones are anomalies.

The inlet arc power level versus spacing trends for the first three harmonics of BPF are shown in Figures 14 and 15. At 54% speed, Figure 14, the second harmonic of the eighty-six vane configuration decreases gradually from a spacing-to-chord ratio of 0.5 to 2.3. The third harmonic, on the other hand, drops very rapidly from $s/c_R = 0.5$ to $s/c_R = 1.27$ and then levels out as s/c_R goes to 2.3. Thus, the third harmonic tone level is much higher than the second harmonic tone level at the closest spacing, $s/c_R = 0.5$. At 69% speed, Figure 15, the second and third harmonics are nearly the same level, except for the open throttle data at s/c_R of 1.27 and larger. At 69% speed, the third harmonic trend has changed as now the level increases slightly in going from $s/c_R = 0.5$ to $s/c_R = 0.9$.

The behavior of the forty-eight vane stator noise data is somewhat simpler, as seen in Figures 14 and 15. The second harmonic of BPF is always the strongest (for $s/c_R = 0.5$ and 1.27), with the BPF level only slightly lower, and the third harmonic the weakest. Increasing the pressure ratio (closing the throttle) generally causes an increase in the tone levels.

The effect of rotor-stator spacing on the entire one-third octave PWL spectrum is shown in Figure 16 for 54% fan speed. For the eighty-six vane configurations, spacing appears to have negligible effect on the spectrum for frequencies below the second harmonic of BPF. A small effect is observed at the 1/3-octave band between 2X BPF and 3X BPF, which does not contain a tone, and the spectrum is observed to drop dramatically as spacing is increased for 1/3-octave bands at 3X BPF and higher, which may contain a tone harmonic. For the forty-eight vane cases, the BPF levels drop appreciably from 0.5 to 1.27 chord spacing. The second harmonic band level is much more sensitive to spacing than the third harmonic band level, and just the opposite trend is observed for the eighty-six vane configurations. Also, the forty-eight vane levels do not appear to be appreciably affected by spacing at higher than 3X BPF frequencies, as opposed to the rather large sensitivity to spacing observed for the eighty-six vane configurations at high frequencies. The effect of spacing does not appear to be materially altered by the change in operating line at this speed. At the closest spacing, there is a marked difference in spectral rolloff rate between the forty-eight and eighty-six vane configurations above 2X BPF.

Although substantial changes in one-third octave band levels containing BPF harmonic tones can be observed in going from $(s/c_R)_{tip} = 0.5$ to $(s/c_R)_{tip} = 0.9$ or 1.27, the trends between $(s/c_R)_{tip} = 0.9$ and 2.3 are not very consistent or large. It is apparent that a clear understanding of the actual behavior of the noise characteristics as a function of spacing cannot be deduced from examination of one-third octave band results alone. For most of the spectrum of interest, the frequencies are higher than 10 kHz, and the true distinction between tone and broadband level contributions is not easily extracted unless the tone dominates the 1/3-octave band. It can be speculated, for example, that the flattening out of the PWL versus spacing trends shown in Figures 14 through 16 between $(s/c_R)_{tip} = 1.0$ and 2.3 is due to the bands containing the tones becoming more controlled by the broadband noise, which is not materially affected by rotor-stator spacing. The remainder of the data presentation and analysis is, therefore, focused on narrowband spectral characteristics. All of the one-third octave data for all configurations is tabulated in the Comprehensive Data Report, Volume 2.

6.2 Narrowband Spectra

Far field microphone 20 Hz bandwidth narrowband spectra were generated and plotted for the experimental points taken. Spectra were generated at microphone angles of 30°, 40°, 50°, and 60° for eight (8) speeds at both operating lines and for each of the seven (7) configurations. This resulted in approximately 450 narrowband spectral plots. In addition, the spectra at microphone angles of 0° to 20°

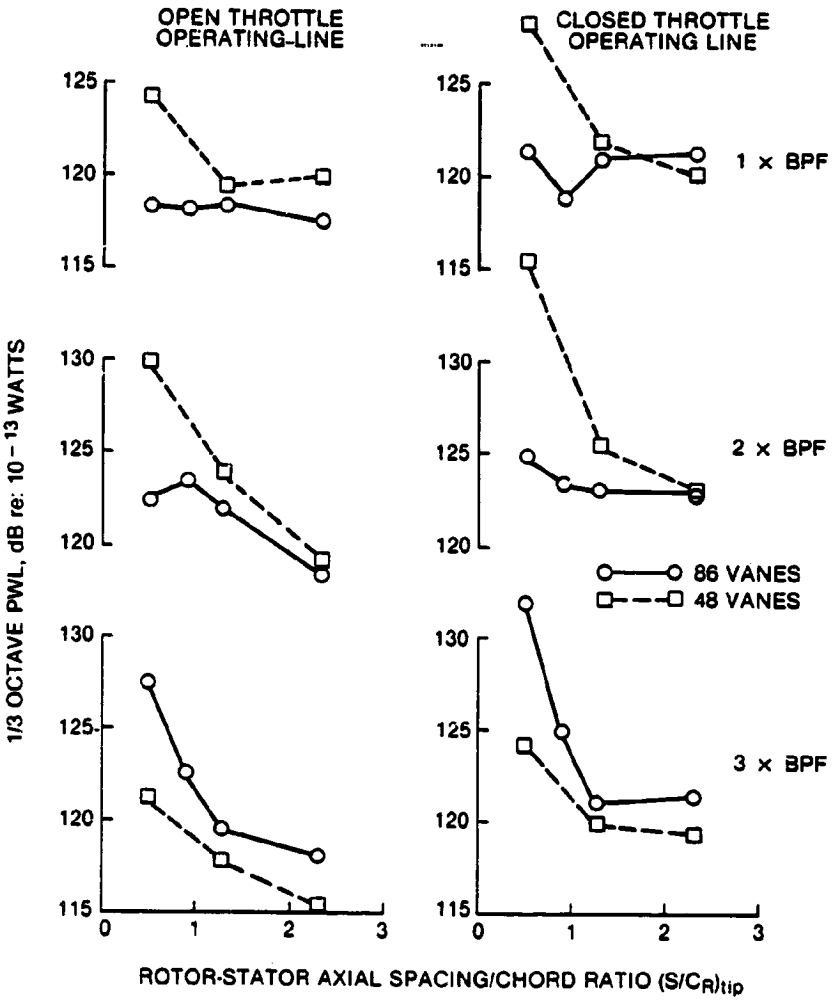

Figure 14. 1/3-Octave Tone PWL vs. Spacing Experimental Trends – 54% N_F.

and 70° to 110° were also generated for each configuration, but only at 54% speed and open throttle operating line. It would have been desirable to analyze the narrowband spectra at all angles for all speeds and for both operating lines, but the time and budget allowed did not permit so extensive an analysis (approximately 1350 spectra). In retrospect, as will be seen later, it probably would have been more fruitful to forego some of the high-speed narrowband spectral analysis in exchange for more complete (i.e., at all angles) spectral information at the lower speeds.

Some typical examples of narrowband spectra are discussed in the following paragraphs. All of the spectra-generated cannot be presented in this report because of the large amount of space required to do so, but sufficient samples will be presented to show trends. The blade passage frequency harmonic tone levels have been scaled down from the narrowband spectrum plots and have been tabulated for all configurations, speeds, and angles. These tabulations, along with internal probe and wall sensor tone levels (to be discussed later), are presented in Appendix B.

Narrowband (far field) spectrum comparison plots are presented in Figures 17 through 38. Each figure shows the measured spectrum at a given far field angle θ, for a given combination of speed (% N_F) and throttle setting (open or closed), at the closest ($s/c_R = 0.5$) and widest ($s/c_R = 2.3$) axial

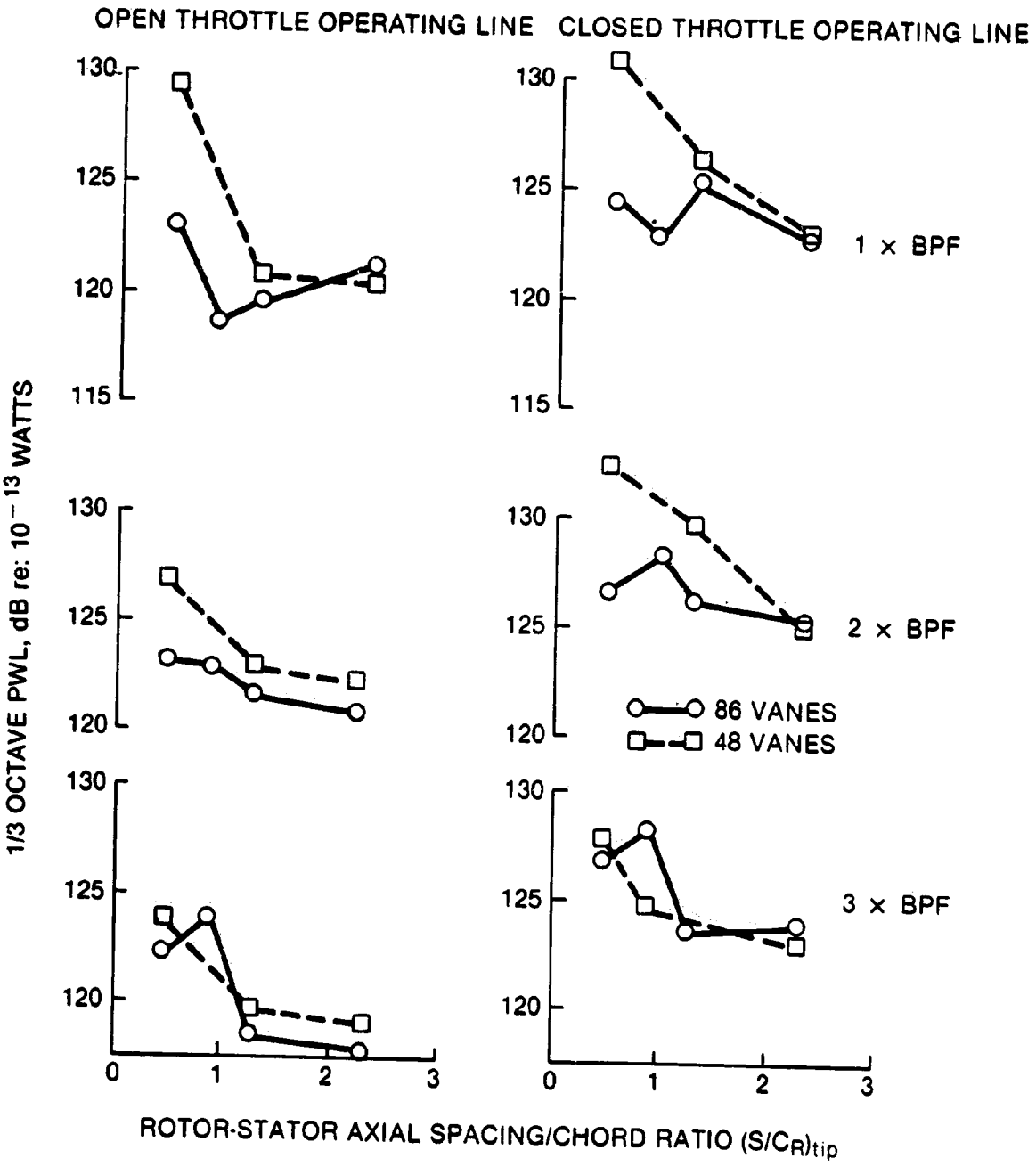

Figure 15. 1/3-Octave Tone PWL vs. Spacing Experimental Trends – 69% N_F.

spacings. Table 2 lists the different parameters which were varied from figure to figure and the associated figure numbers, for all of the narrowband spectra presented in this section. It should be noted again that these are only a small fraction of the total number of spectra-generated and that they represent examples selected to illustrate certain observed features and trends.

The narrow band spectra for the eighty-six vane configurations at $s/c_R = 0.5$ and 2.3 are shown in Figures 17, 18, 19, and 20 for far field angles of $\theta = 0°$, 30°, 60° and 90°, respectively. This set of spectra is shown to illustrate how the effects of axial spacing are observed to vary around the arc from 0° to 90°. It can be seen that there is a large drop in tone levels from the closest to the widest spacing, especially for the higher harmonic tones and that this reduction is observable at all angles shown.

Another interesting observation from examining these figures (17-20) is that the spectra at the closest spacing show substantial "skirting" at the tone frequencies, i.e., the tone is not a sharp spike, but exhibits a broad base, as if there exists modulation of the tone. Coincident with the "skirting," there is observed to be shaft-multiple harmonic tones of relatively low level protruding above the

Table 2

LIST OF FAR FIELD NARROWBAND SPECTRUM COMPARISONS FOR CLOSEST ($S/C_R = 0.5$ AND WIDEST (S/CR = 2.3) AXIAL SPACINGS

N_V	θ	$\%N_F$	O/L	Figure
86	0	54	OP	17
86	30	54	OP	18
86	60	54	OP	19
86	90	54	OP	20
48	0	54	OP	21
48	30	54	OP	22
48	60	54	OP	23
48	90	54	OP	24
86	30	69	OP	25
86	60	69	OP	26
86	30	80	OP	27
86	60	80	OP	28
86	30	95	OP	29
86	30	54	CL	30
86	60	54	CL	31
86	30	69	CL	32
86	60	69	CL	33
86	30	80	CL	34
48	30	69	OP	35
48	60	69	OP	36
48	30	69	CL	37
48	60	69	CL	38

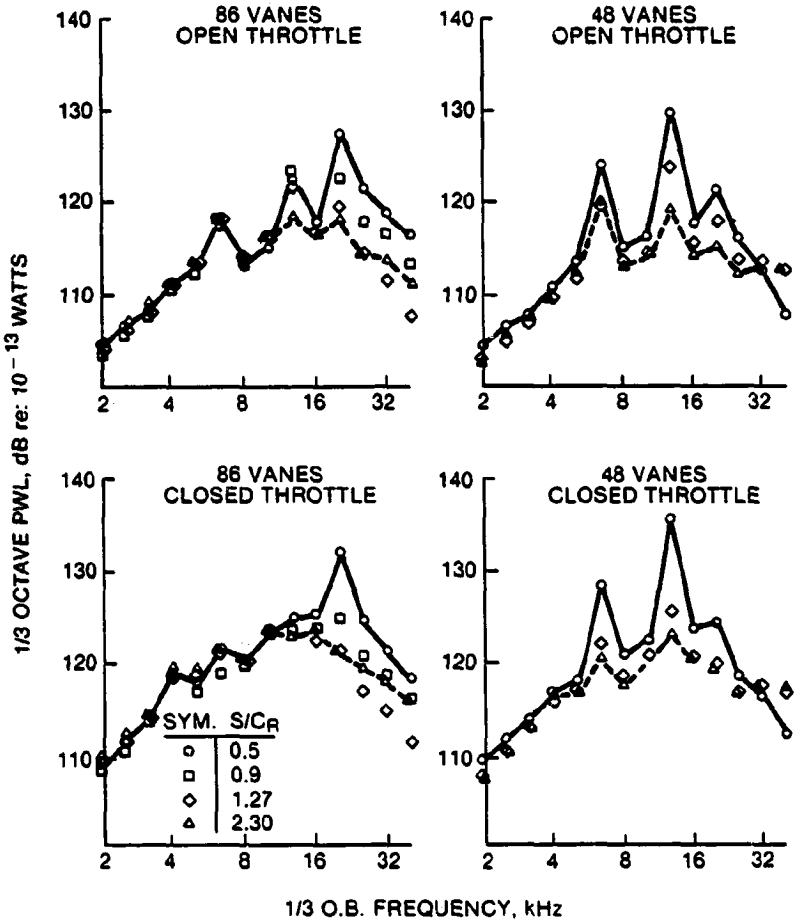

Figure 16. Effect of Rotor/Stator Spacing on 1/3 – Octave-Band PWL Spectrum – 54% N_F.

broadband level between the BPF harmonic tones. It is speculated that these shaft-harmonic tones are caused by irregularities in the rotor blading due to manufacturing differences from blade to blade and/or slight (but randomly distributed) differences in rotor wake profile from blade to blade. It is thought that the closest spacing is close enough for these irregularities to provide a modulation of the rotor potential field-stator interaction tone generation process, thus producing the multiple-shaft harmonic tones. Also, the blade-to-blade variations in rotor wake profiles probably decay rapidly with downstream distance and, therefore, do not contribute at larger spacings. Although not shown here, the spectra for the 0.9 spacing configuration also exhibit the multiple-shaft harmonic phenomenon. A final observation is that little change in the base broadband levels is observed in going from 0.5 to 2.3 chord spacing.

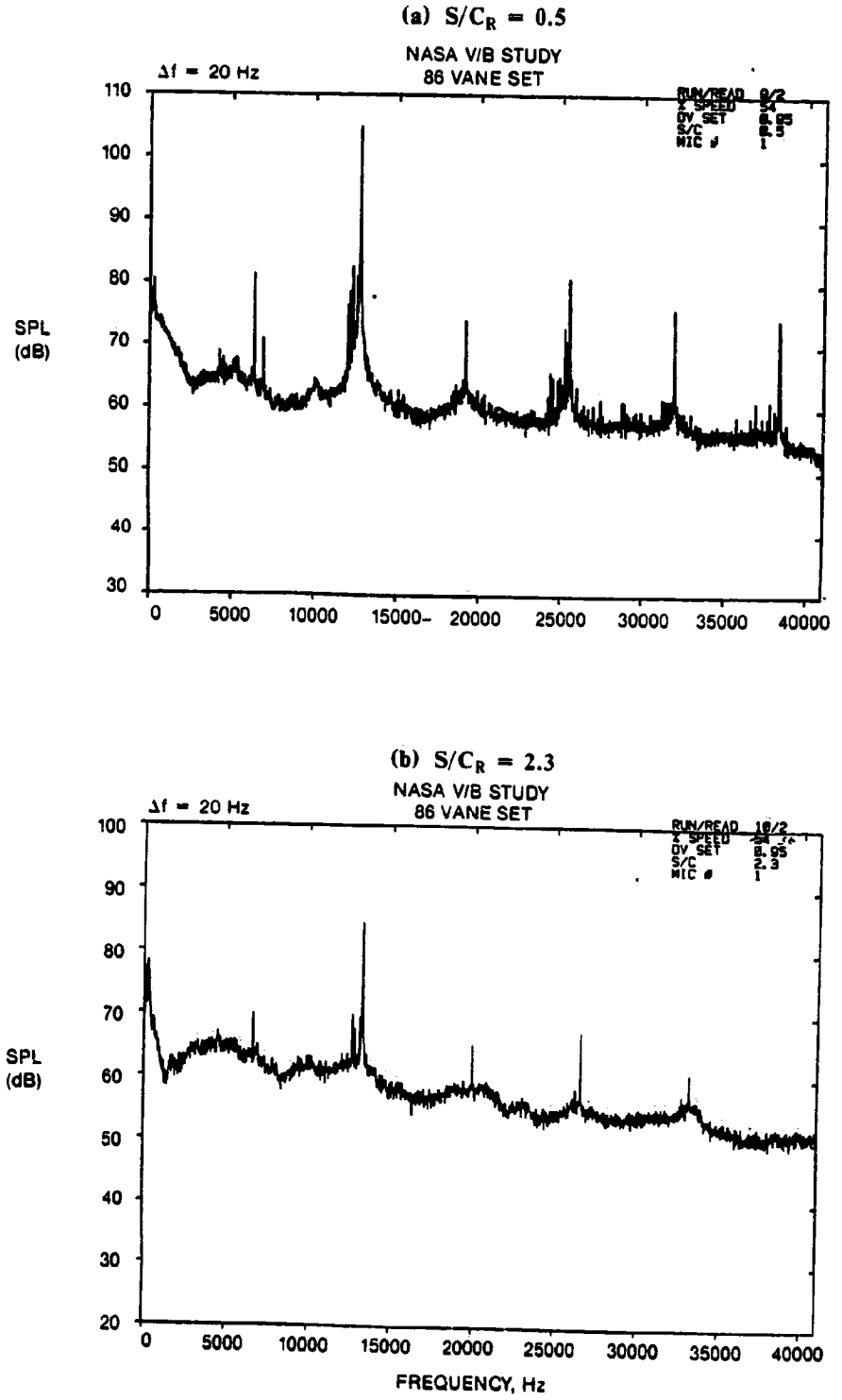

Figure 17. Narrowband Spectra for 86-Vane Configurations at $\theta = 0°$; 54% N_F and Open Throttle O/L.

(a) S/C_R = 0.5

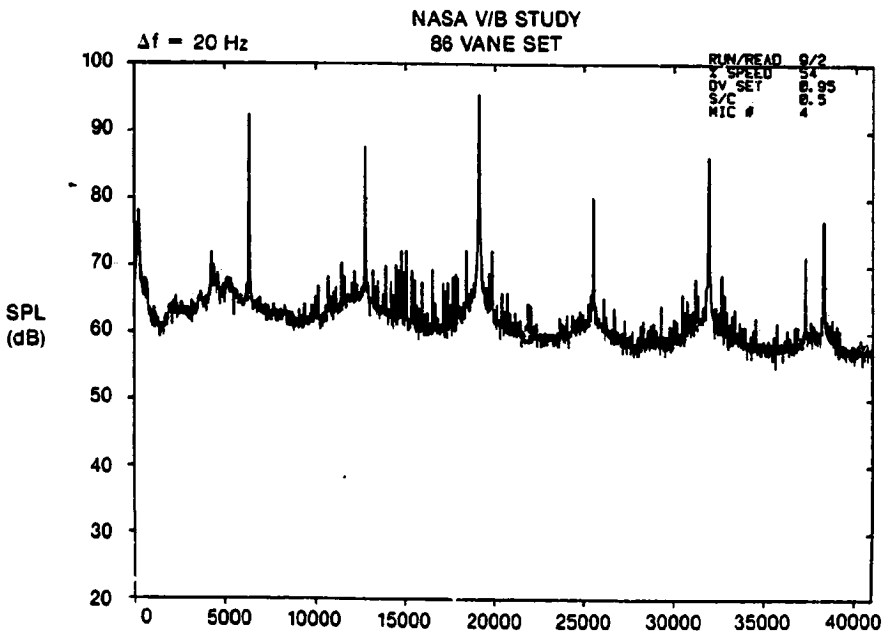

(b) S/C_R = 2.3

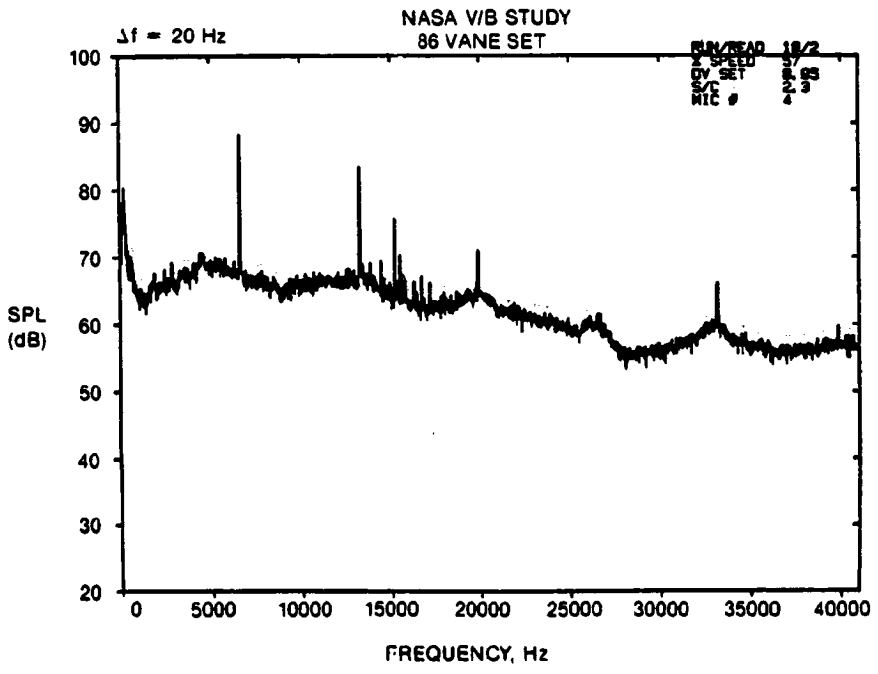

Figure 18. Narrowband Spectra for 86-Vane Configurations at θ = 30°; 54% N_F and Open Throttle O/L.

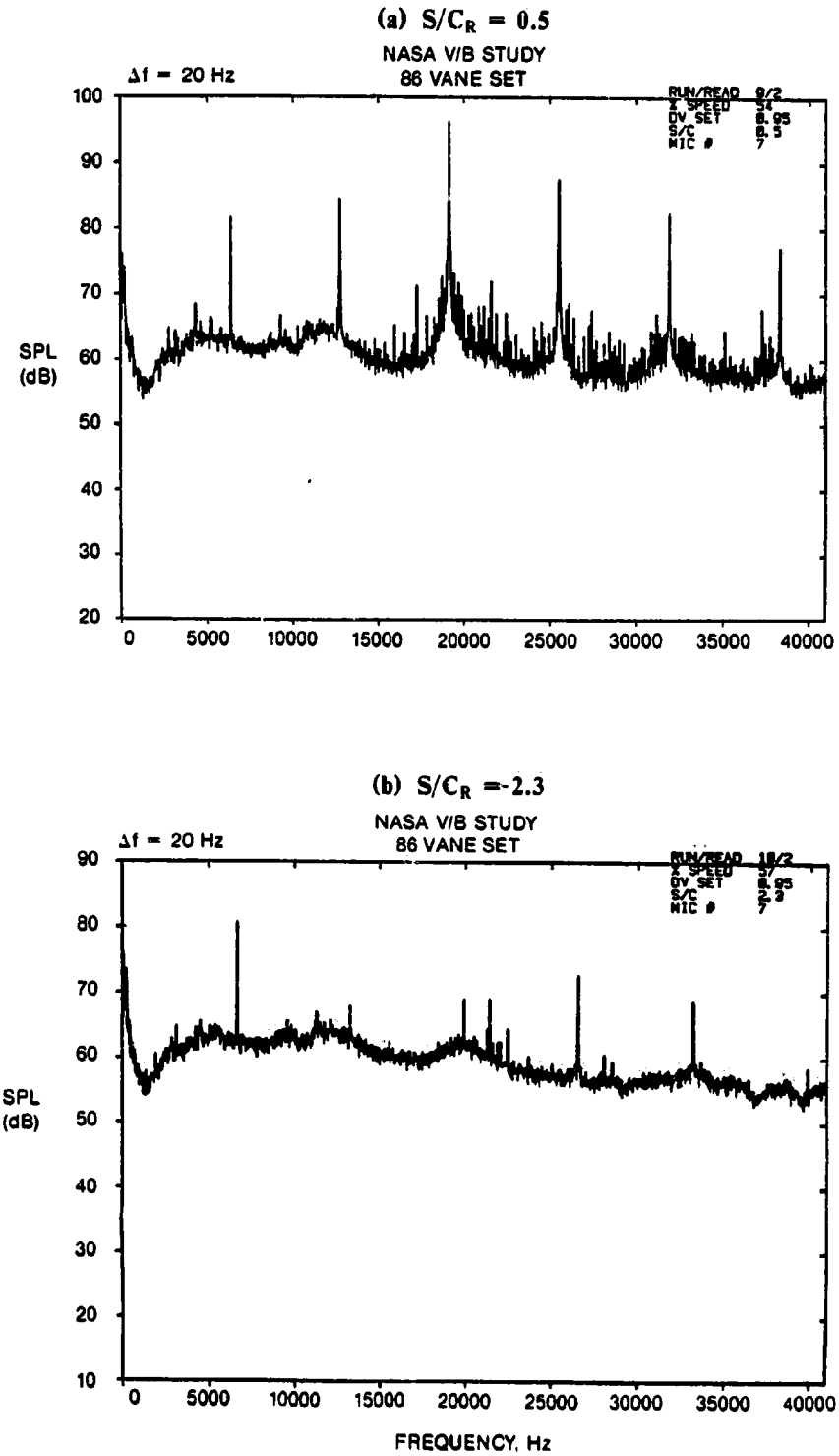

Figure 19. Narrowband Spectra for 86-Vane Configurations at θ = 60°; 54% N_F and Open Throttle O/L.

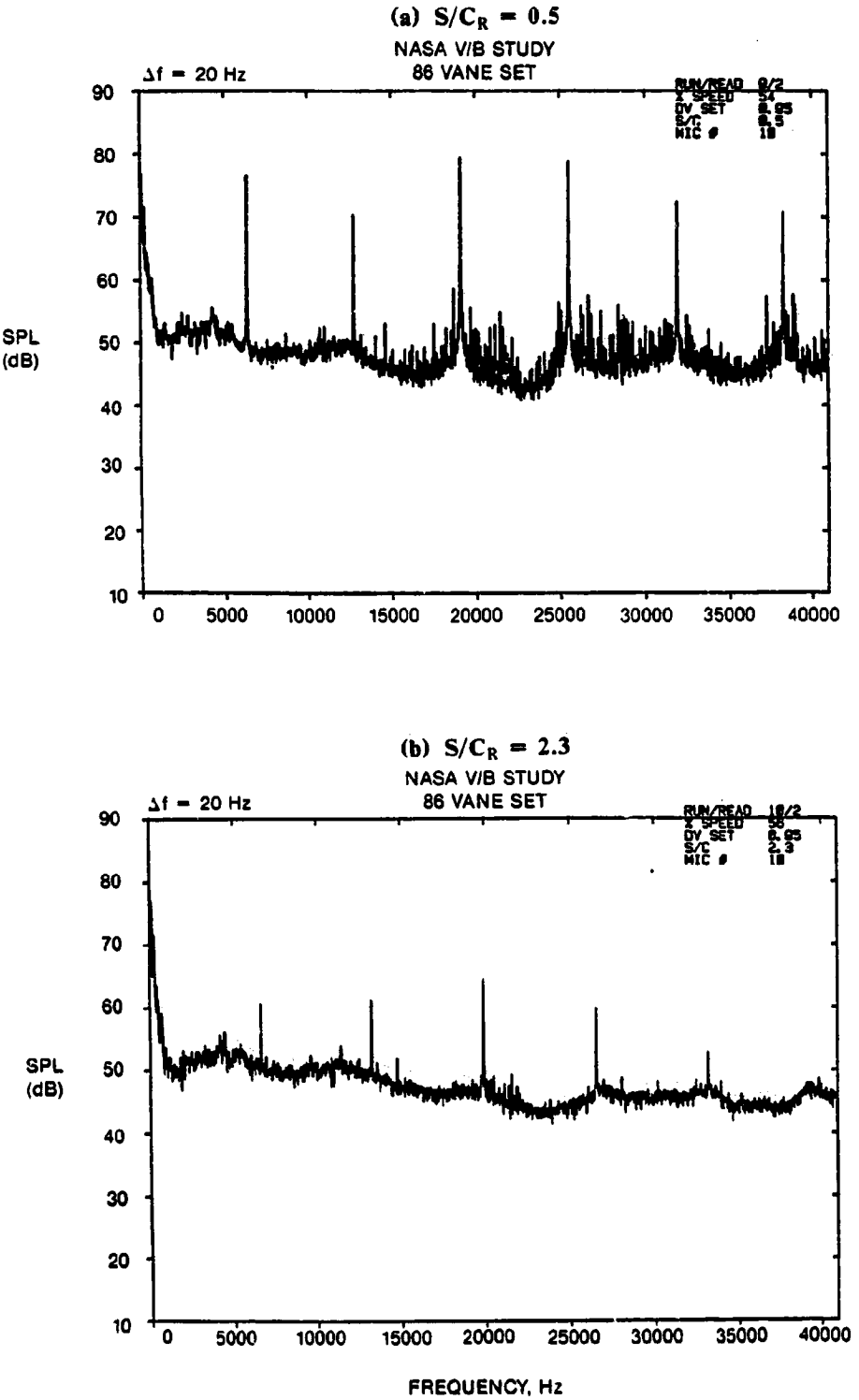

Figure 20. **Narrowband Spectra for 86-Vane Configurations at θ = 90°; 54% N_F and Open Throttle O/L.**

The corresponding spectra for the forty-eight vane configurations are shown in Figures 21, 22, 23, and 24 for $\theta = 0°$, 30°, 60° and 90°, respectively. In general, the tone levels for second harmonic (n = 2) of BPF, and higher, are observed to drop considerably with increased spacing at all angles, whereas the reductions in the fundamental tone (n = 1) are significant at $\theta = 60°$ and 90°, with little change observed at $\theta = 0°$ and 30°. The multiple-shaft harmonic tones are again observed for the closest spacing $s/c_R = 0.5$. There appears to be a slight reduction in broadband noise due to increased spacing for the forty-eight vane configurations, and this reduction varies from 0 dB at frequencies below BPF to about 3-5 dB at 5.5X BPF, although not consistently from angle to angle.

Narrowband spectra for the higher speeds of 69%, 80%, and 95% are shown in Figures 25 through 29 for the eighty-six vane configurations on the open throttle operating line. Spectra at 30° and 60° are shown for 69% and 80% speed. At 69% speed (Figures 25 and 26), increasing spacing reduces the 3 and 4X BPF harmonics, but has only a small effect on 1 and 2X BPF (1X BPF actually increases in Figure 25). A similar effect is observed at 80% speed for $\theta = 30°$, but the effect of spacing is almost negligible at $\theta = 60°$. In fact, at $\theta = 60°$, the rotor-alone and multiple pure tone or "buzz saw" noise appear to dominate the spectrum. At 95% speed, Figure 29, the rotor-alone and multiple pure tones dominate the spectrum even at $\theta = 30°$, as the rotor inlet relative Mach number is greater than unity over a significant portion of the fan rotor span. Thus, based on these results, rotor-stator spacing effects are not very strong at speeds where the rotor inlet relative Mach number exceeds unity for forward radiated noise. This is consistent with the one-third octave results presented in the previous section.

The above narrowband results have all been for the open throttle operating line. Some examples of narrowband spectra for the closed throttle operating line are shown in Figures 30 through 34 for the eighty-six vane configurations. In general, the tone reductions due to increased spacing from $s/c_R = 0.5$ to 2.3 tend to be larger than those observed for the open throttle operating line cases and some appreciable reduction in BPF tone levels is observed (Figures 32 and 33). The change in broadband level with spacing appears to be negligible at 54% speed (Figures 30 and 31), while the broadband noise actually increases by about 5 dB at 69% speed.

Most of the narrowband spectra presented above have been for the eighty-six vane configurations, with the exception of the 54% speed, open throttle forty-eight vane spectra shown in Figures 21 through 24. Figures 35 and 36 show narrowband spectra for the forty-eight vane set at 69% speed and open throttle setting. Appreciable reductions in all harmonics of BPF with increased spacing are observed for this speed, including the fundamental BPF tone. A sizable reduction in broadband noise is also observed on the order of 5-7 dB on the average. The corresponding closed throttle setting spectra are shown in Figures 37 and 38. Again, both tone and broadband noise are reduced as spacing is increased with the exception of the second harmonic (2X BPF) tone at $\theta = 30°$ (Figure 37).

6.3 Narrowband Tone Level Trends

As discussed in the previous section, the SPL values of the blade passage frequency tones, and second and third harmonics, have been scaled from the narrowband spectra for all configurations at all speeds tested, and these tone levels have been tabulated in Appendix B. For the 54% and 63% speed points, the first five harmonics have been included. The tone SPL values are given for $\theta = 30°$, 40°, 50°, and 60° at all speeds, and for 54% speed, the values at all twelve microphones ($\theta = 0°$ to 110°) have been tabulated.

The 54% speed, open throttle points are the only conditions for which complete narrowband tone directivities have been obtained.

Figure 39 shows narrowband directivity patterns for the eighty-six vane stage as a function of axial spacing ratio s/c_R. Only second and third harmonic levels are shown, as the eighty-six vane/forty-four blade combination should give a cut-off blade passing tone (BPF) at subsonic tip speeds. Although there is qualitatively a general trend that the tone levels decrease with axial spacing, the trend at any one observer angle is significantly different from that at any other angle.

(a) $S/C_R = 0.5$

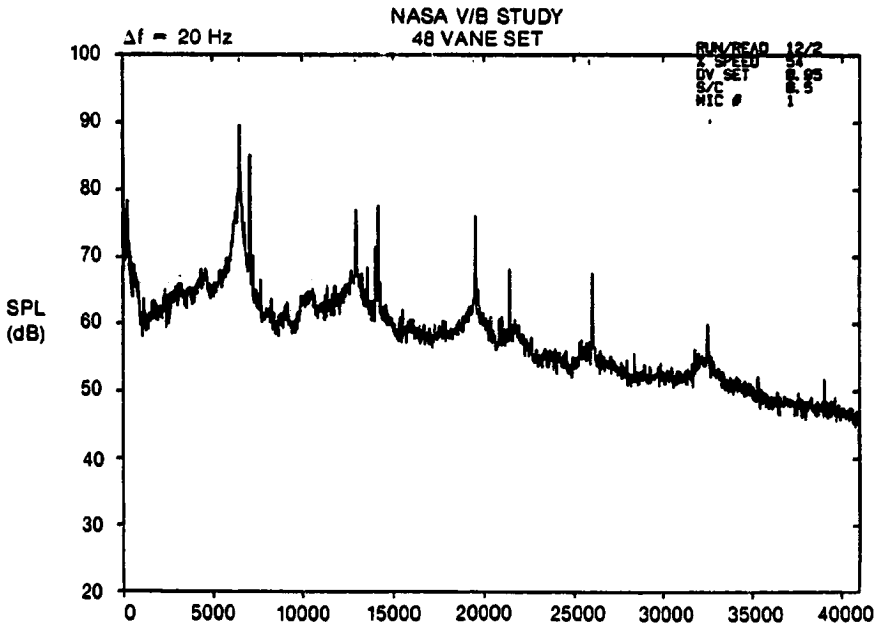

(b) $S/C_R = 2.3$

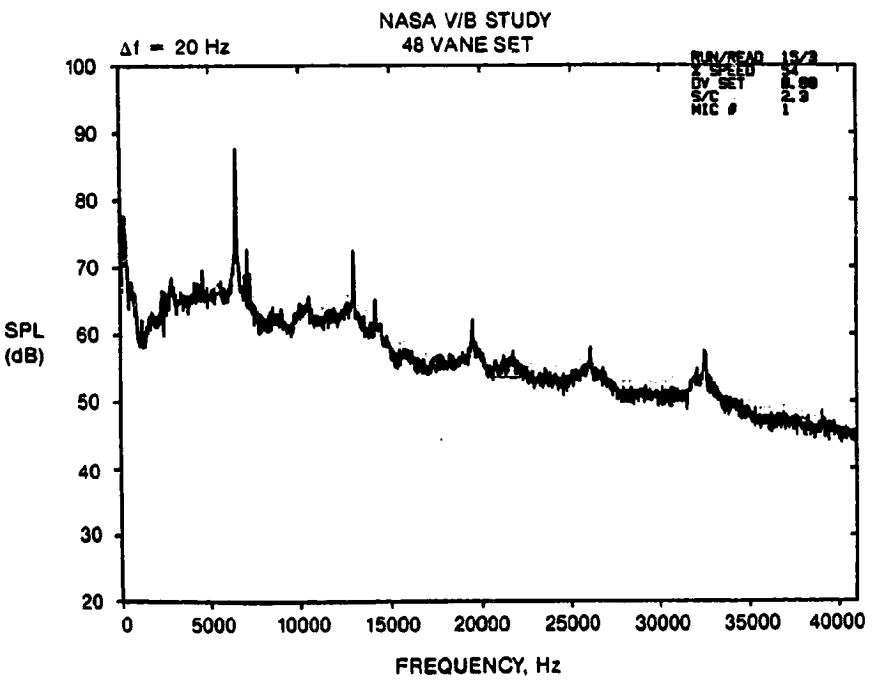

Figure 21. **Narrowband Spectra for 48-Vane Configurations at $\theta = 0°$; 54% N_F and Open Throttle O/L.**

(a) $S/C_R = 0.5$

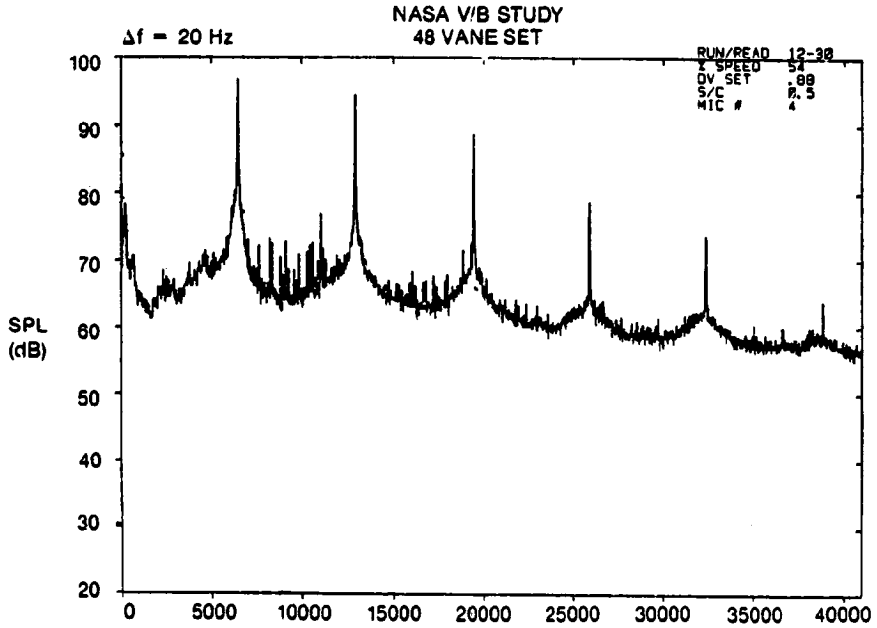

(b) $S/C_R = 2.3$

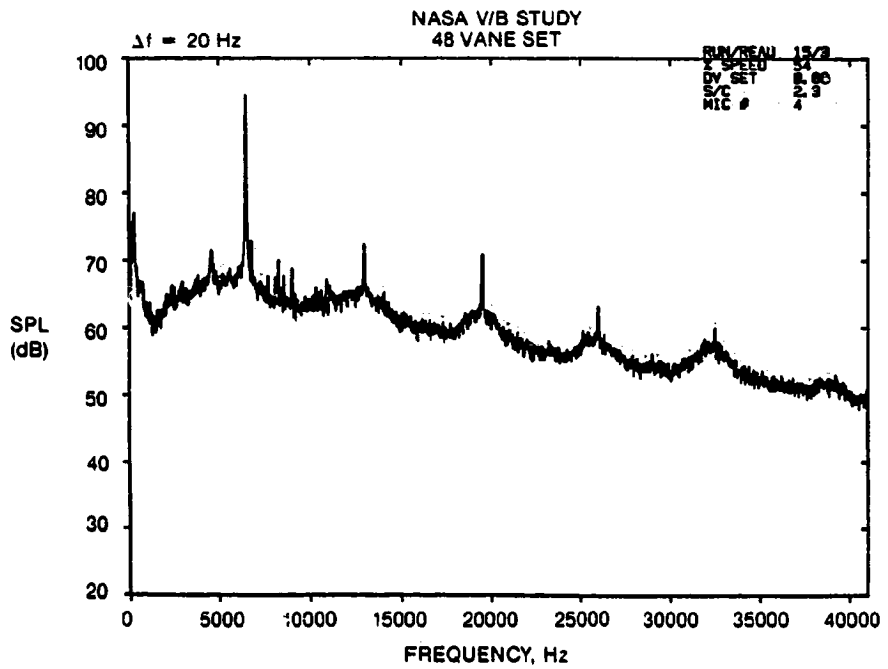

Figure 22. Narrowband Spectra for 48-Vane Configurations at $\theta = 30°$; 54% N_F and Open Throttle O/L.

(a) $S/C_R = 0.5$

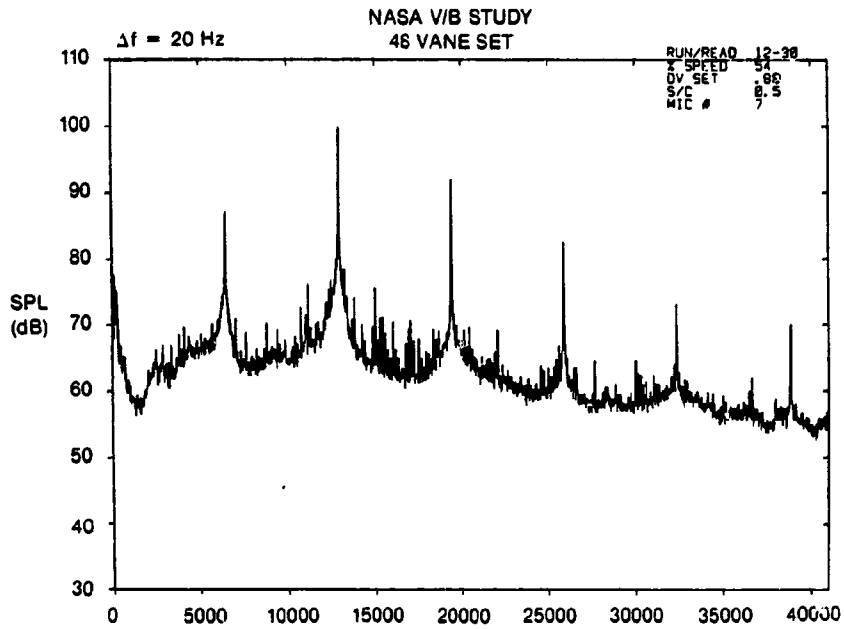

(b) $S/C_R = 2.3$

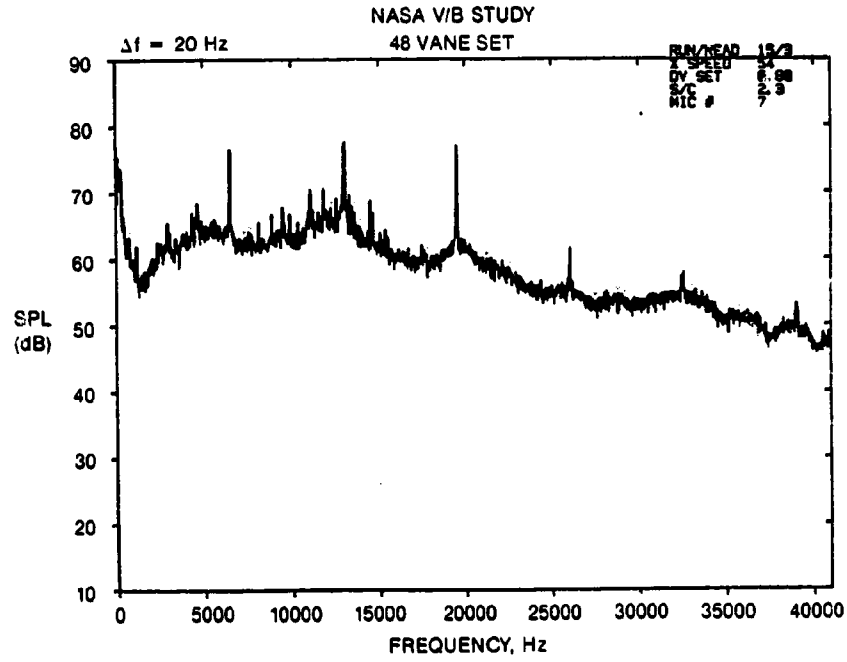

Figure 23. **Narrowband Spectra for 48-Vane Configurations at $\theta = 60°$; 54% N_F and Open Throttle O/L.**

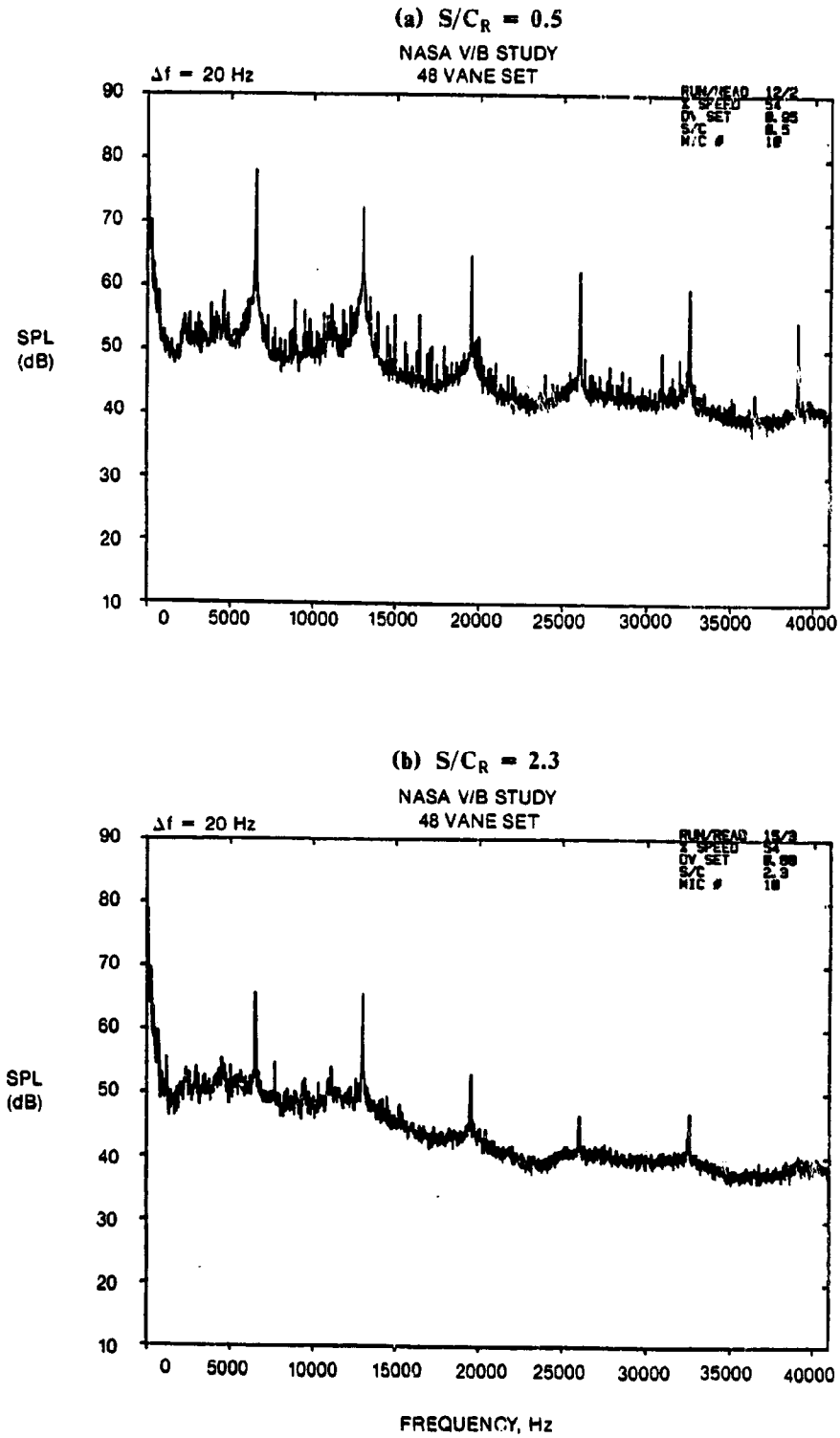

Figure 24. **Narrowband Spectra for 48-Vane Configurations at θ = 90°; 54% N_F and Open Throttle O/L.**

(a) $S/C_R = 0.5$

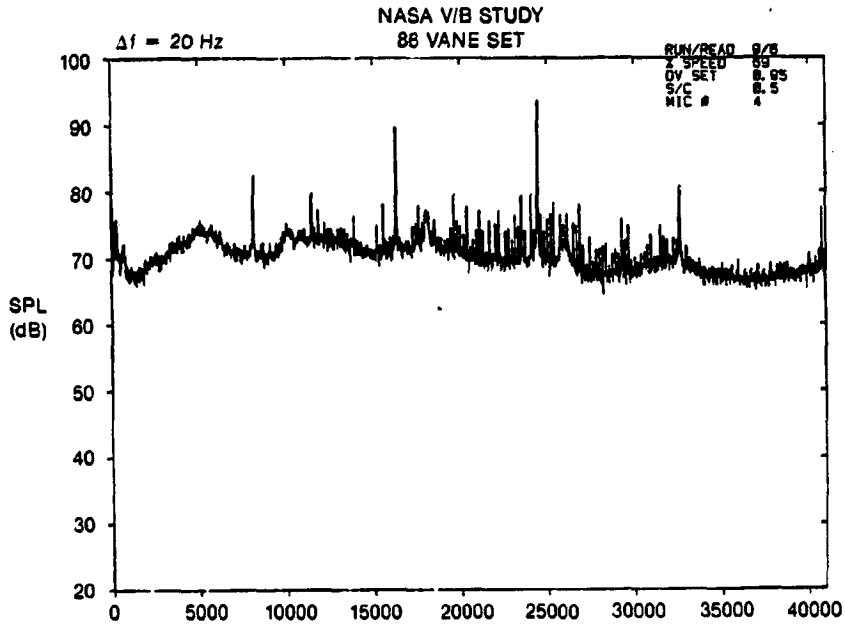

(b) $S/C_R = 2.3$

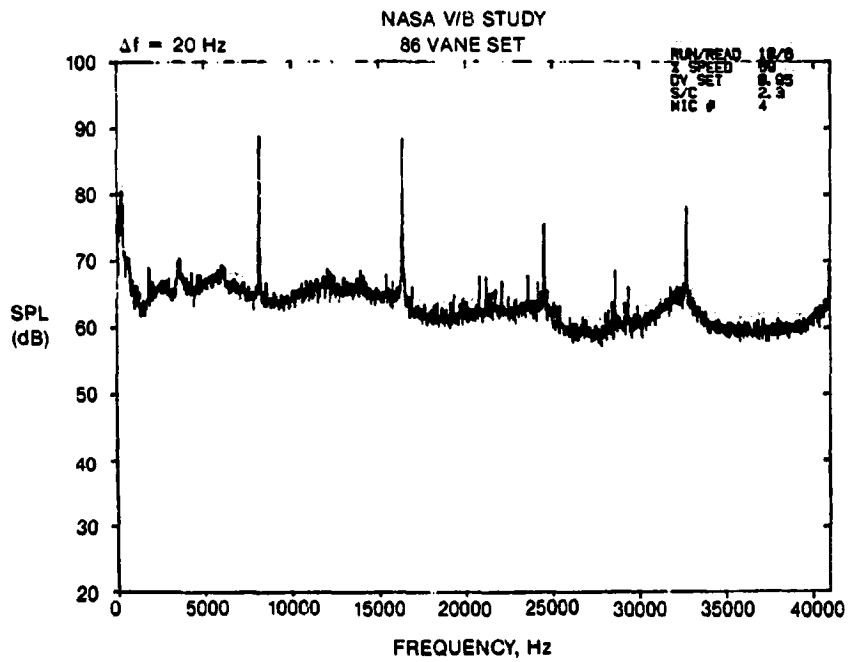

Figure 25. Narrowband Spectra for 86-Vane Configurations at $\theta = 30°$; 69% N_F and Open Throttle O/L.

(a) $S/C_R = 0.5$

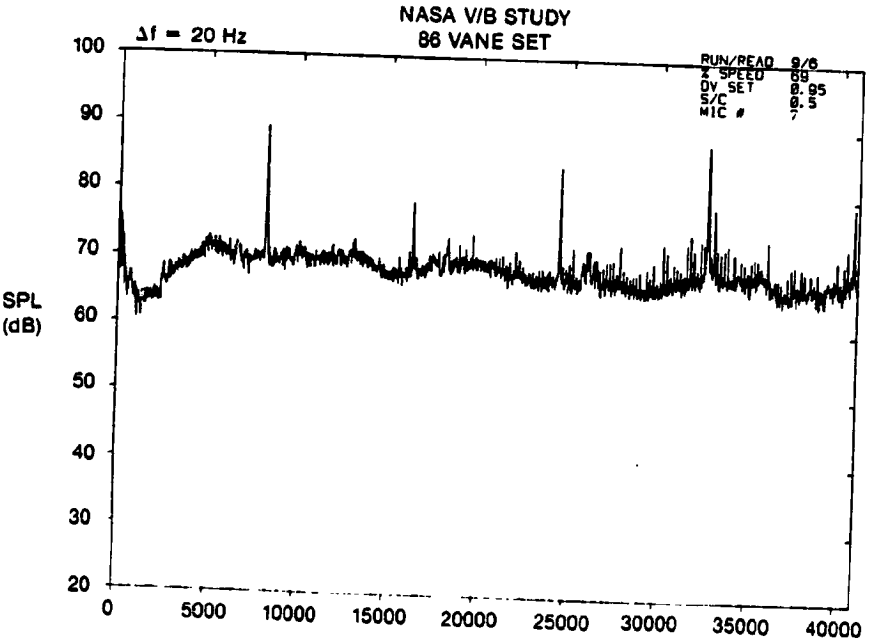

(b) $S/C_R = 2.3$

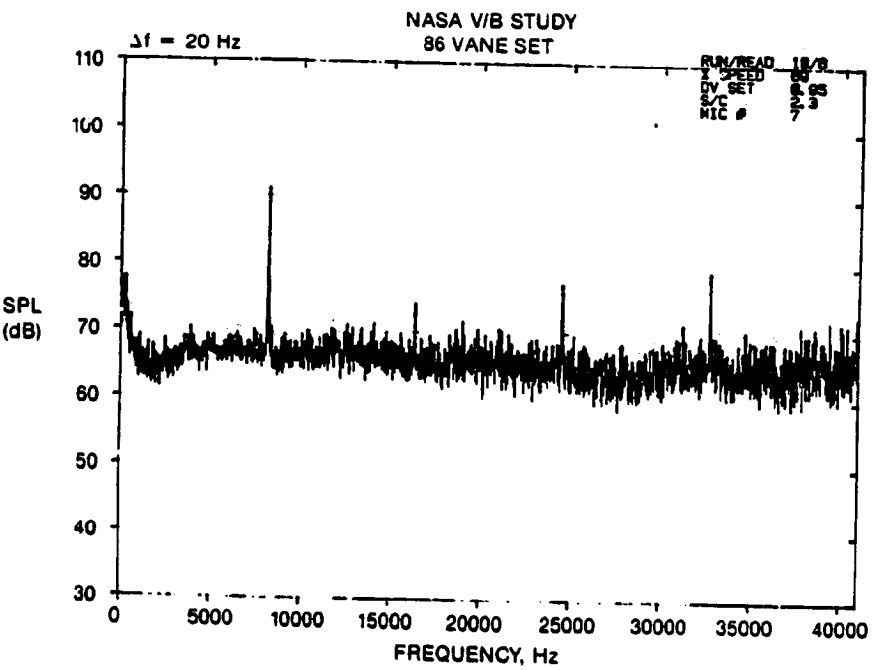

Figure 26. Narrowband Spectra for 86-Vane Configurations at $\theta = 60°$; 69% N_F and Open Throttle O/L.

(a) $S/C_R = 0.5$

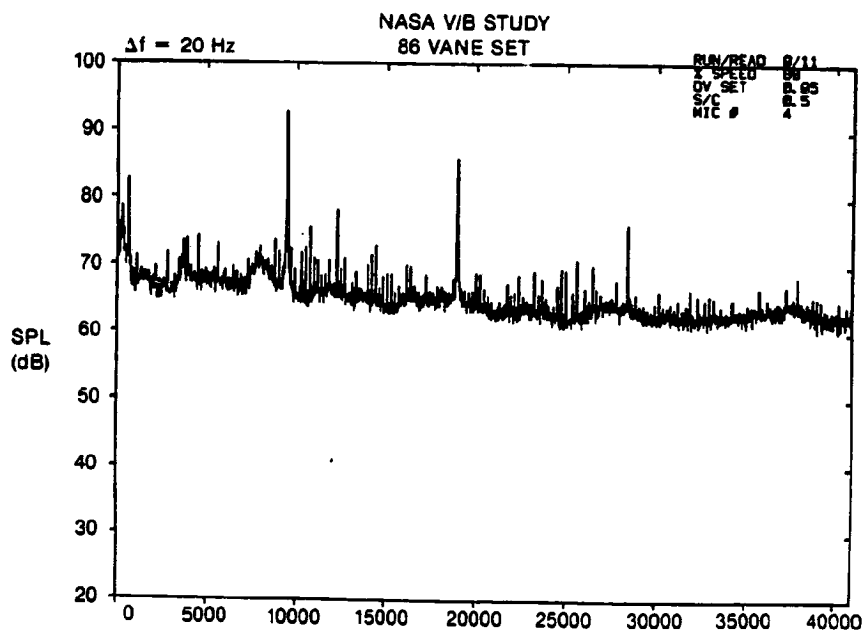

(b) $S/C_R = 2.3$

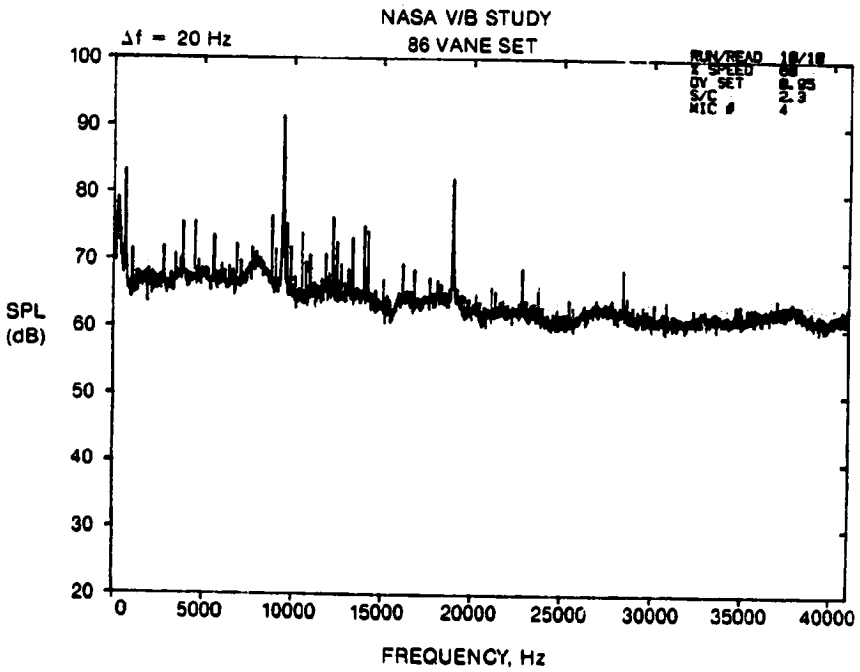

Figure 27. Narrowband Spectra for 86-Vane Configurations at $\theta = 30°$; 80% N_F and Open Throttle O/L.

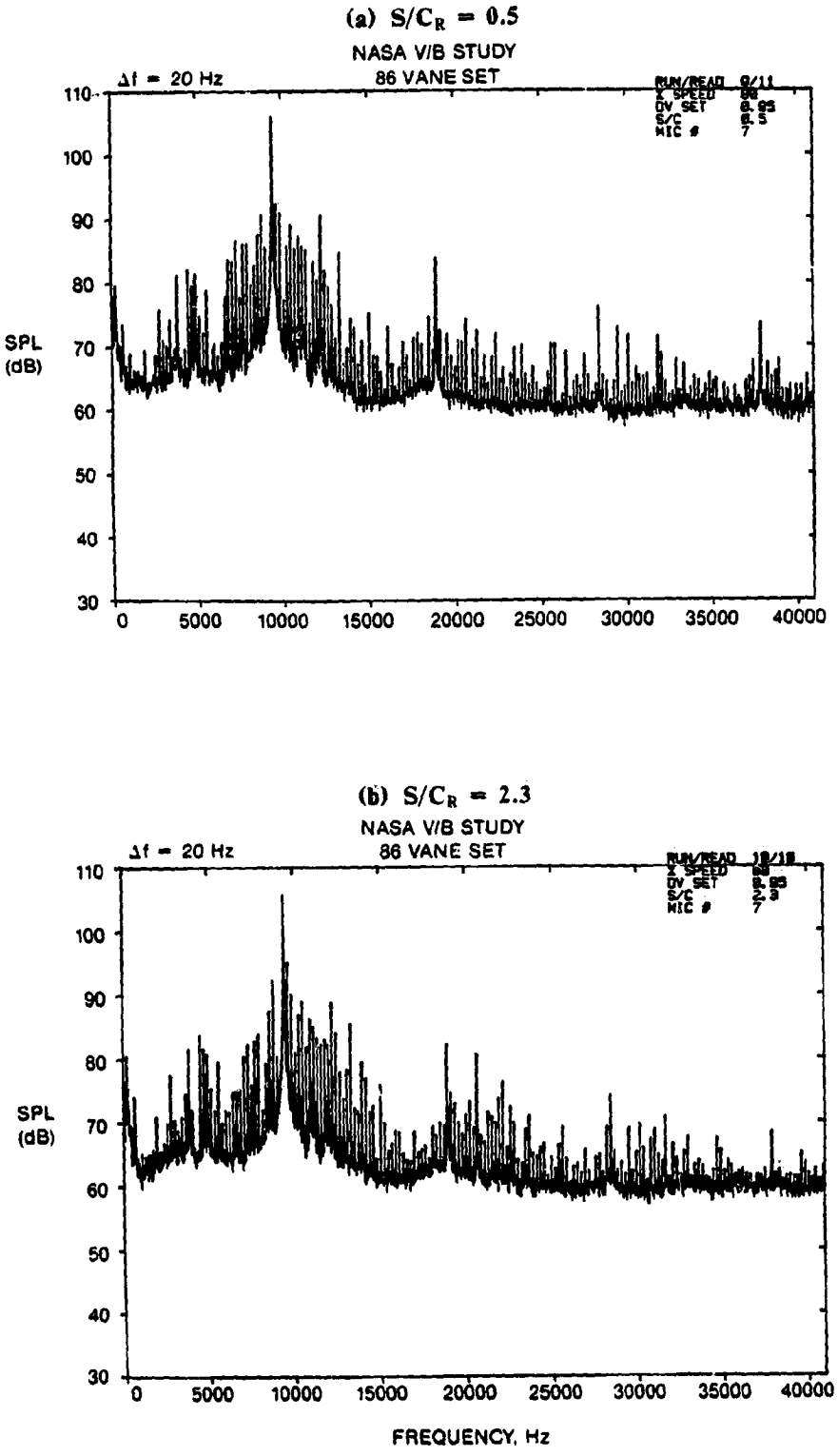

Figure 28. **Narrowband Spectra for 86-Vane Configurations at θ = 60°; 80% N_F and Open Throttle O/L.**

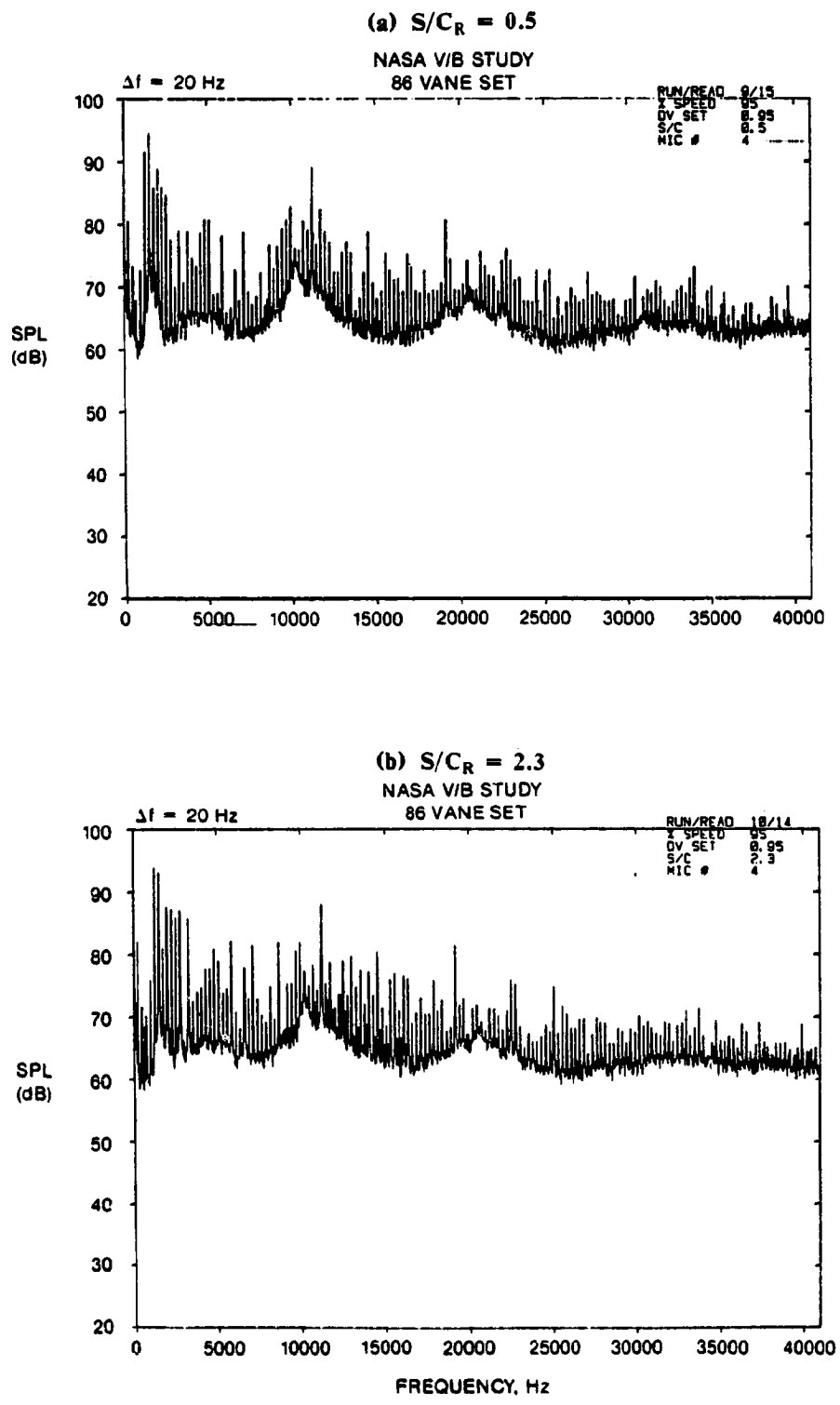

Figure 29. Narrowband Spectra for 86-Vane Configurations at θ = 30°; 95% N_E and Open Throttle O/L.

(a) $S/C_R = 0.5$

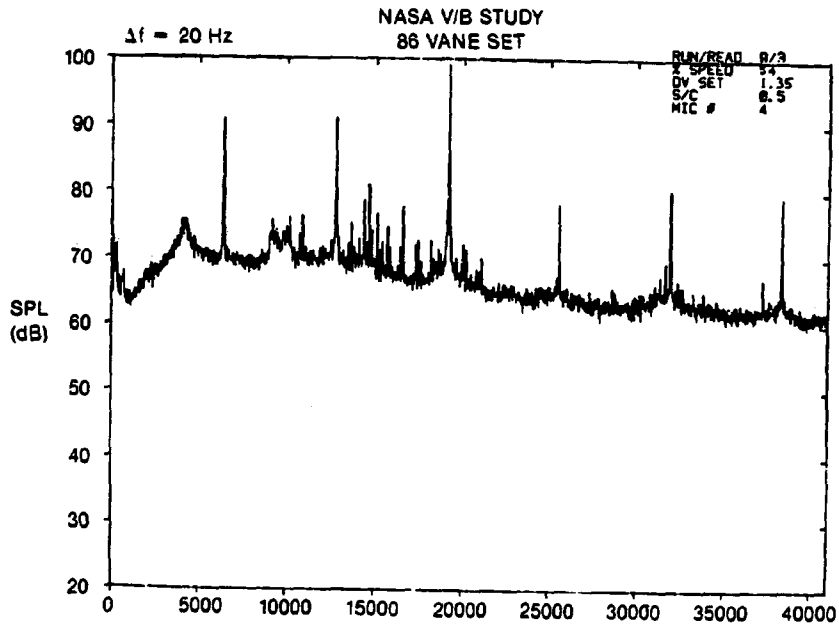

(b) $S/C_R = 2.3$

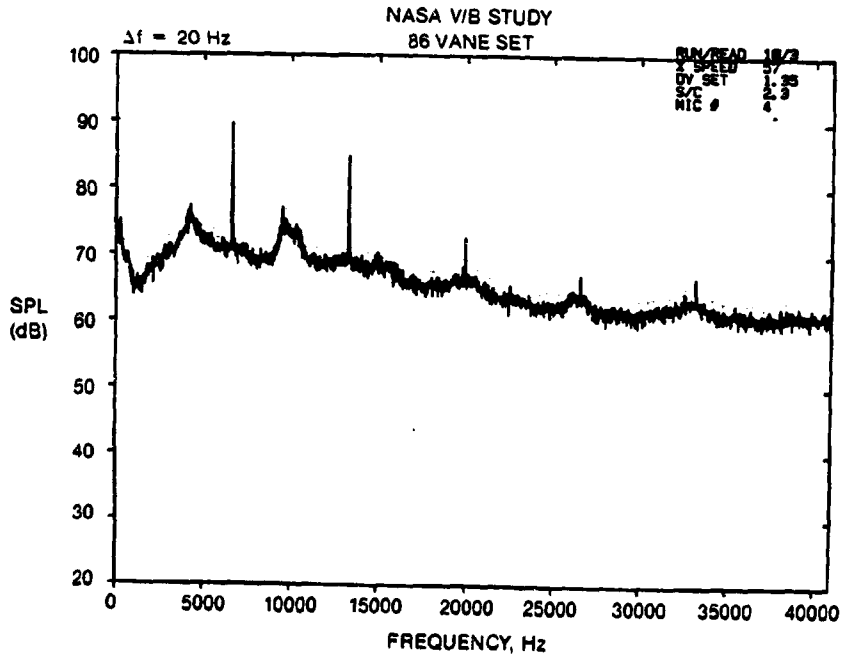

Figure 30. **Narrowband Spectra for 86-Vane Configurations at $\theta = 30°$; 54% N_F and Closed Throttle O/L.**

(a) $S/C_R = 0.5$

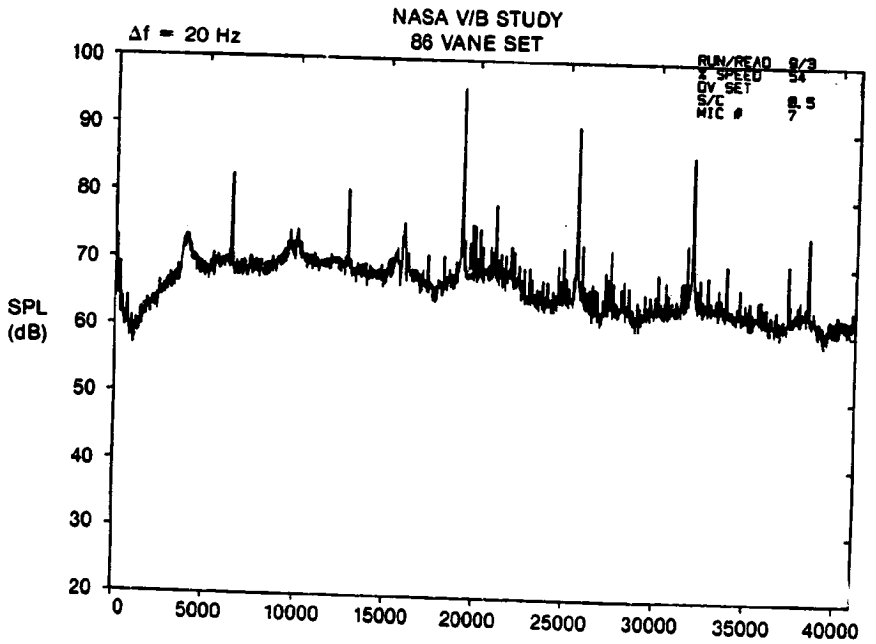

(b) $S/C_R = 2.3$

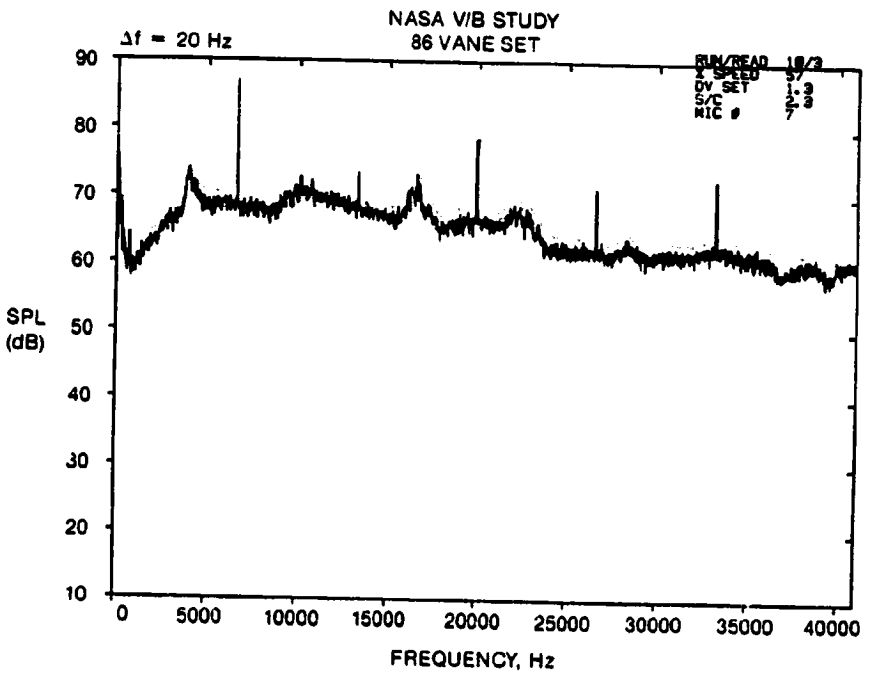

Figure 31. Narrowband Spectra for 86-Vane Configurations at $\theta = 60°$; 54% N_F and Closed Throttle O/L.

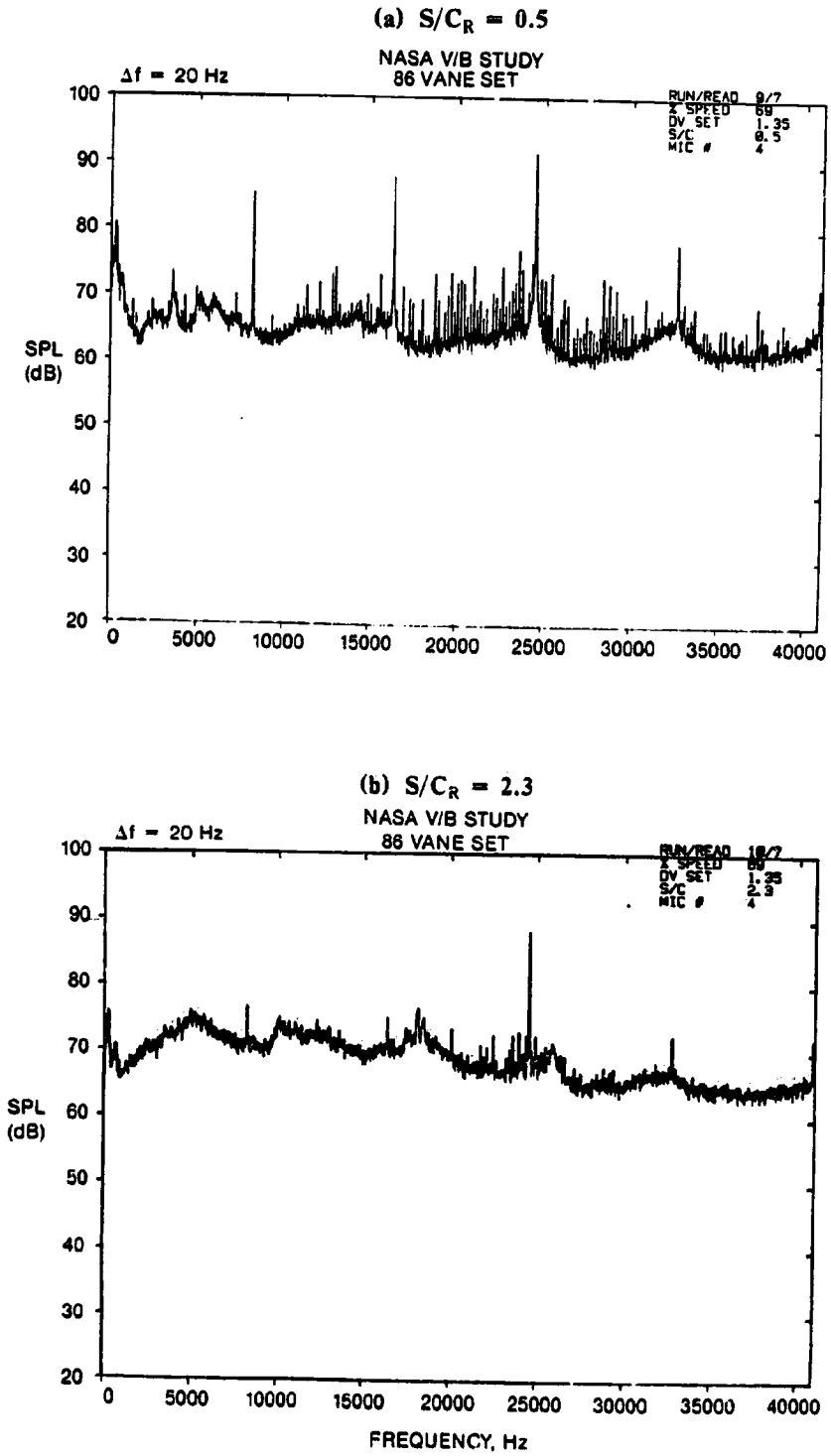

Figure 32. Narrowband Spectra for 86-Vane Configurations at θ = 30°; 69% N_F and Closed Throttle O/L.

(a) $S/C_R = 0.5$

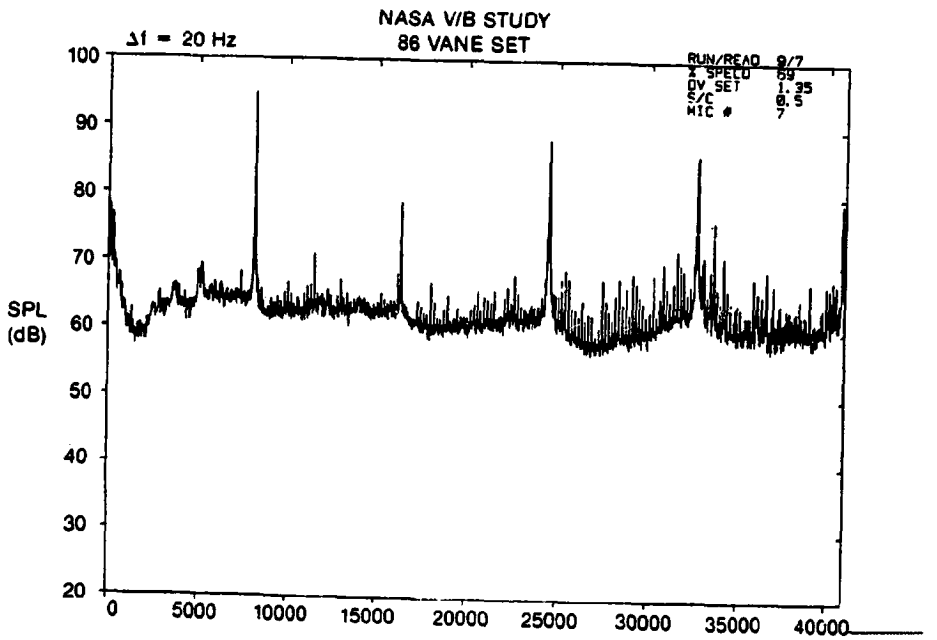

(b) $S/C_R = 2.3$

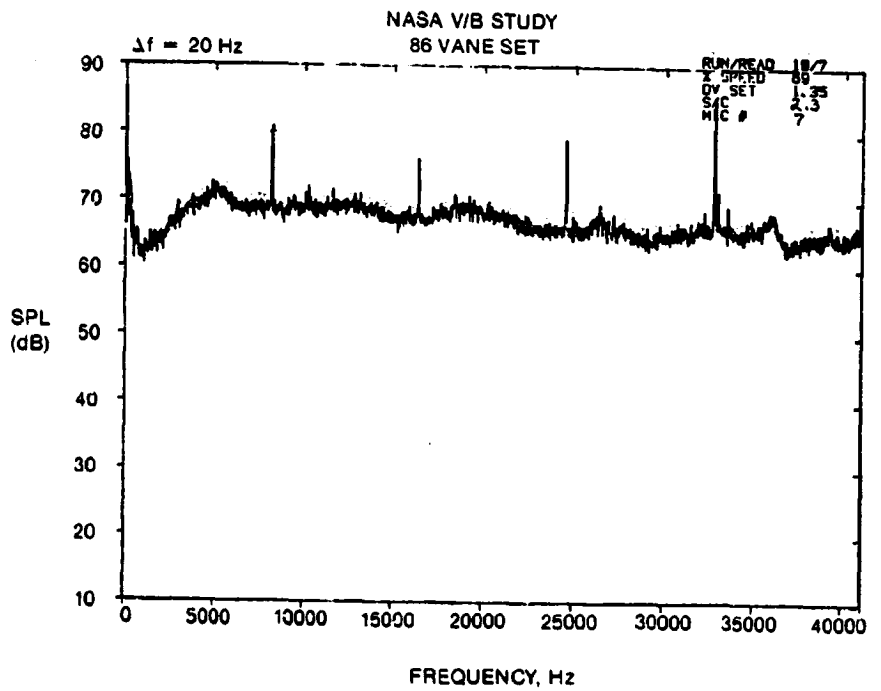

Figure 33. **Narrowband Spectra for 86-Vane Configurations at $\theta = 60°$; 69% N_F and Closed Throttle O/L.**

(a) $S/C_R = 0.5$

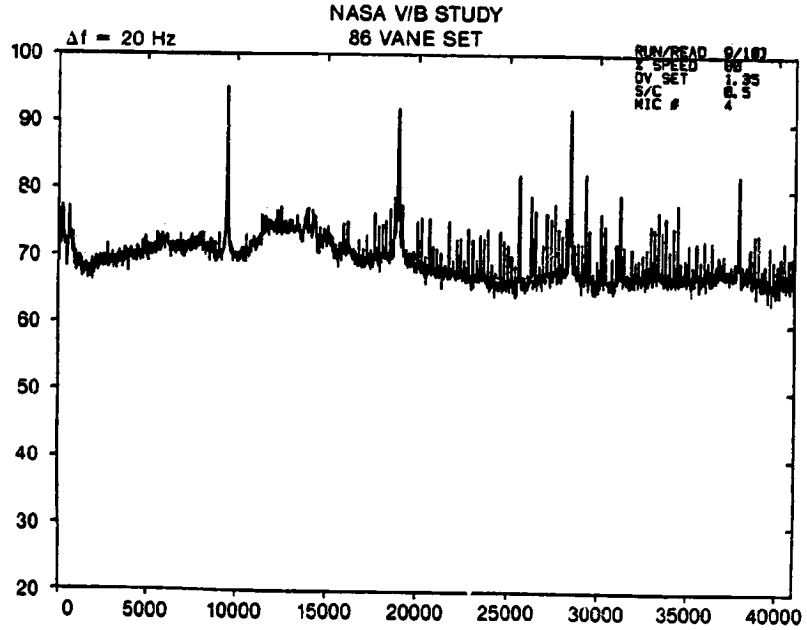

(b) $S/C_R = 2.3$

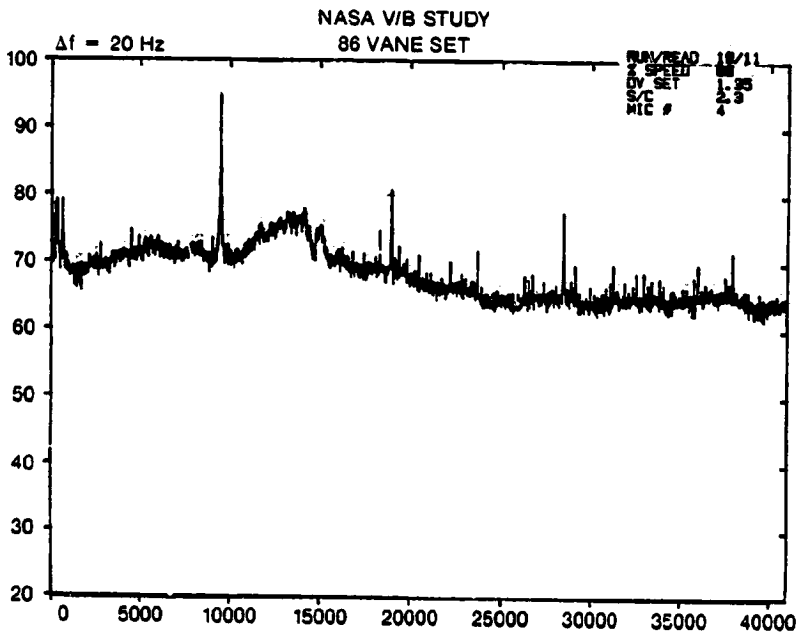

Figure 34. **Narrowband Spectra for 86-Vane Configurations at $\theta = 30°$; 80% N_F and Closed Throttle O/L.**

(a) $S/C_R = 0.5$

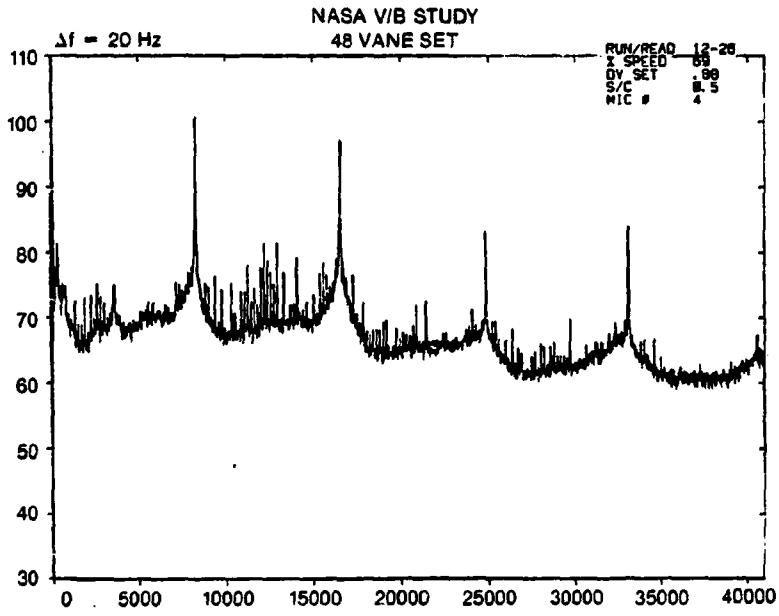

(b) $S/C_R = 2.3$

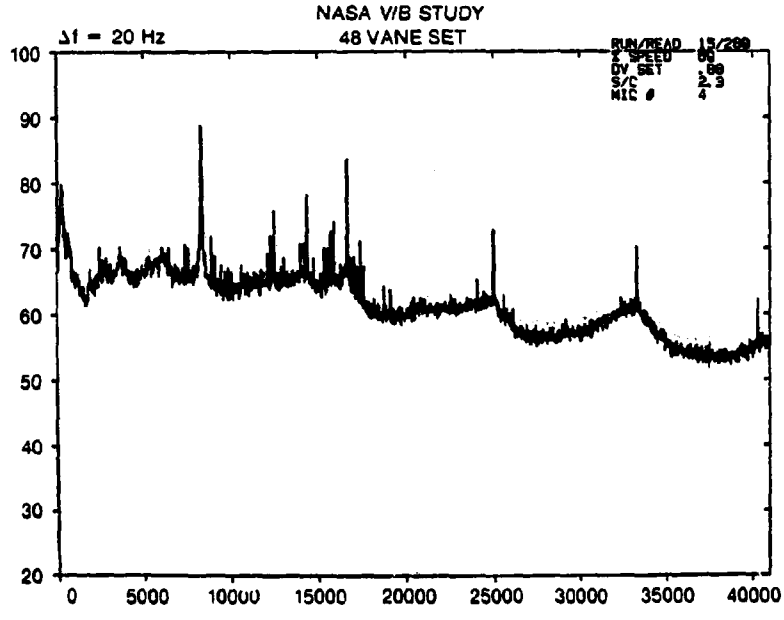

Figure 35. **Narrowband Spectra for 48-Vane Configurations at $\theta = 30°$; 69% N_F and Open Throttle O/L.**

(a) S/C_R = 0.5——

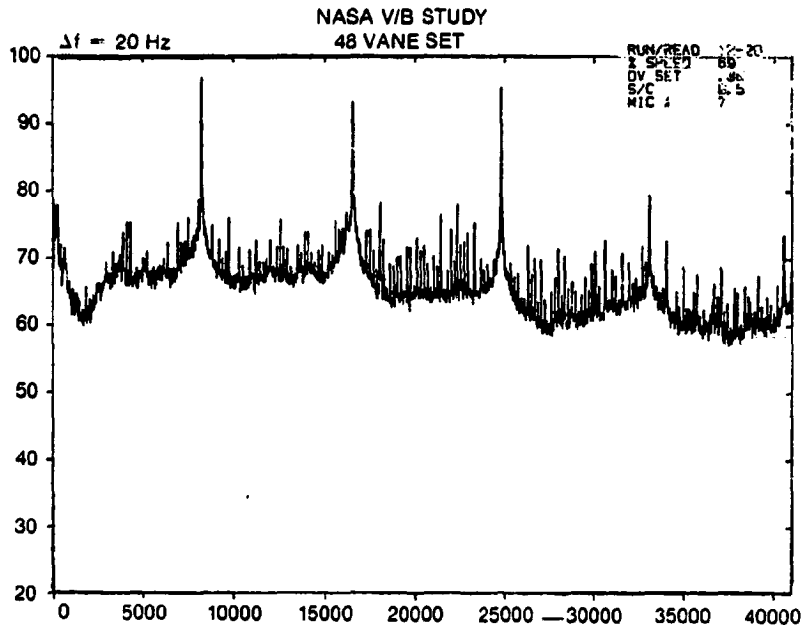

(b) S/C_R = 2.3

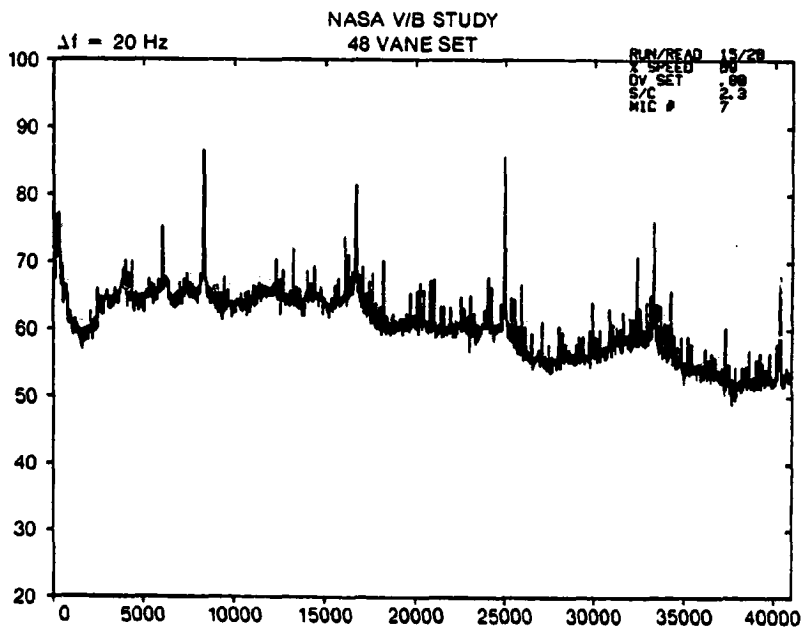

Figure 36. **Narrowband Spectra for 48-Vane Configurations at θ = 60°; 69% N_F and Open Throttle O/L.**

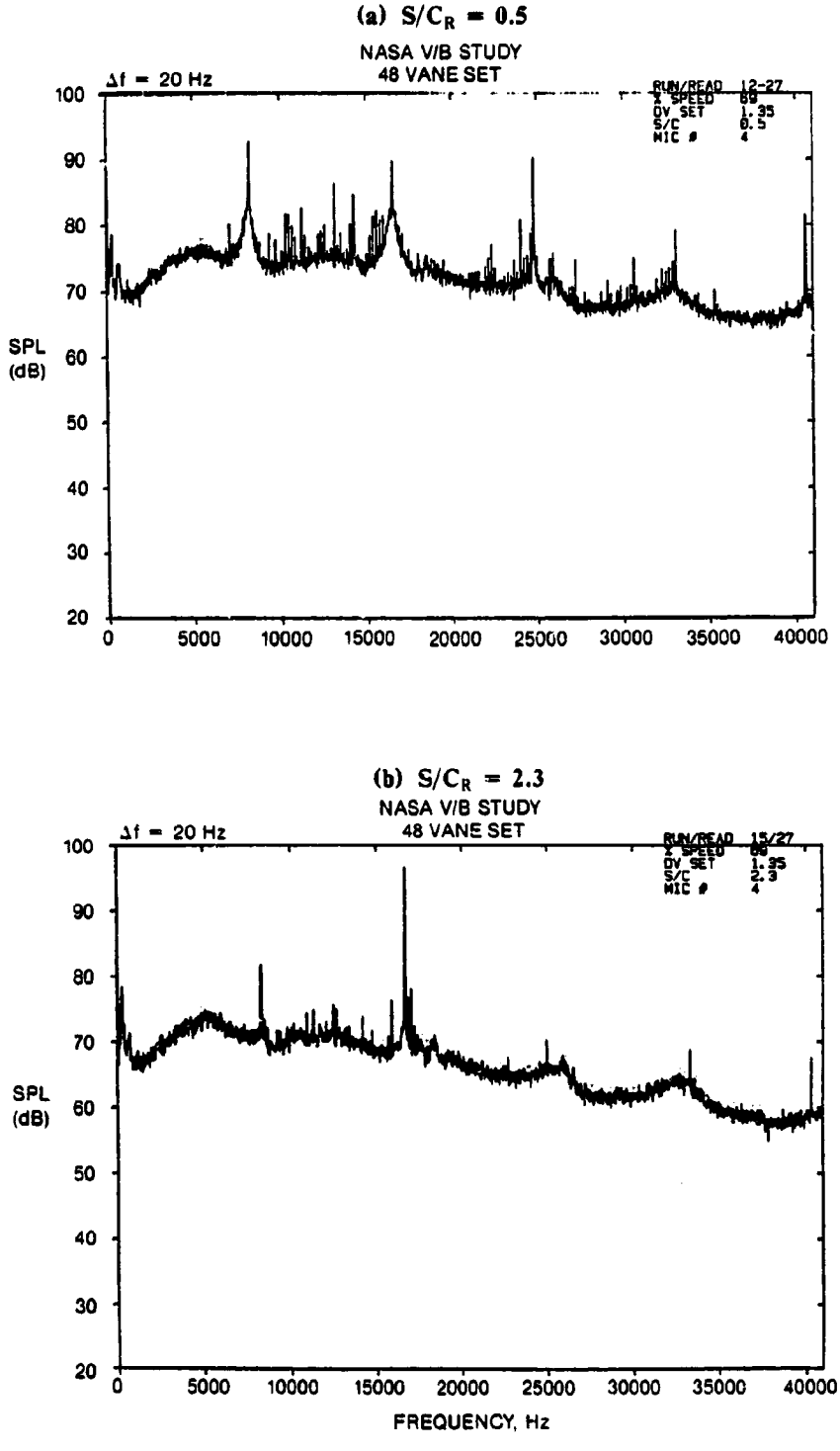

Figure 37. Narrowband Spectra for 48-Vane Configurations at $\theta = 30°$; 69% N_F and Closed Throttle O/L.

(a) $S/C_R = 0.5$

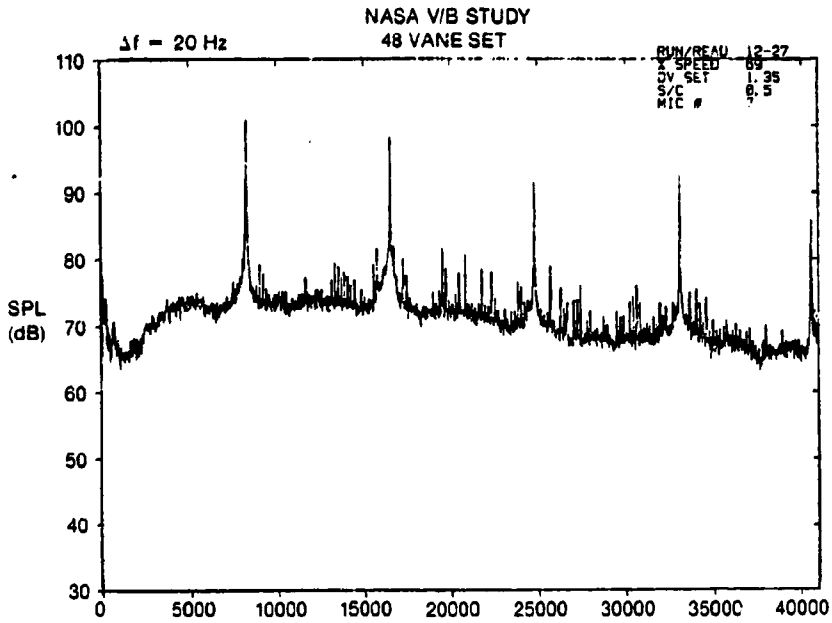

(b) $S/C_R = 2.3$

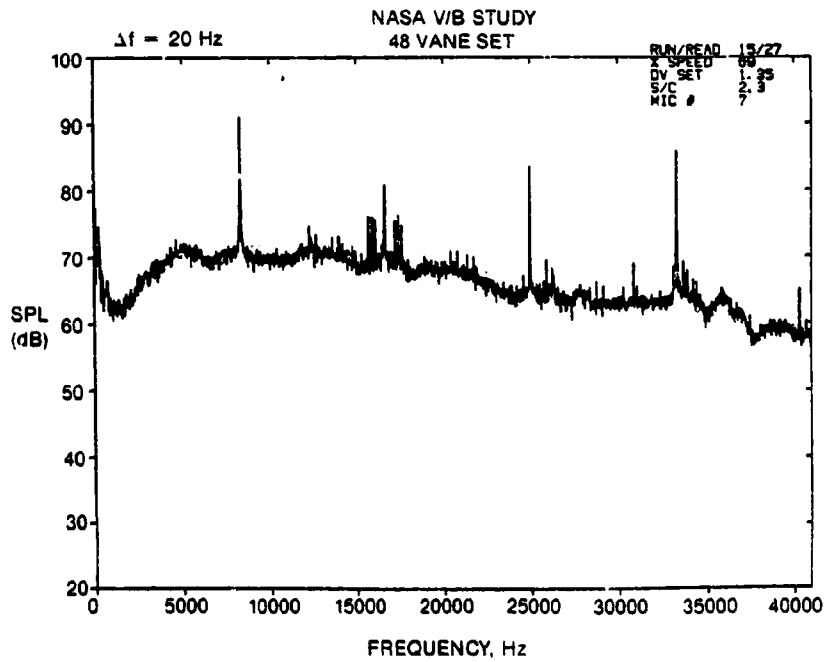

Figure 38. Narrowband Spectra for 48-Vane Configurations at $\theta = 60°$; 69% N_F and Closed Throttle O/L.

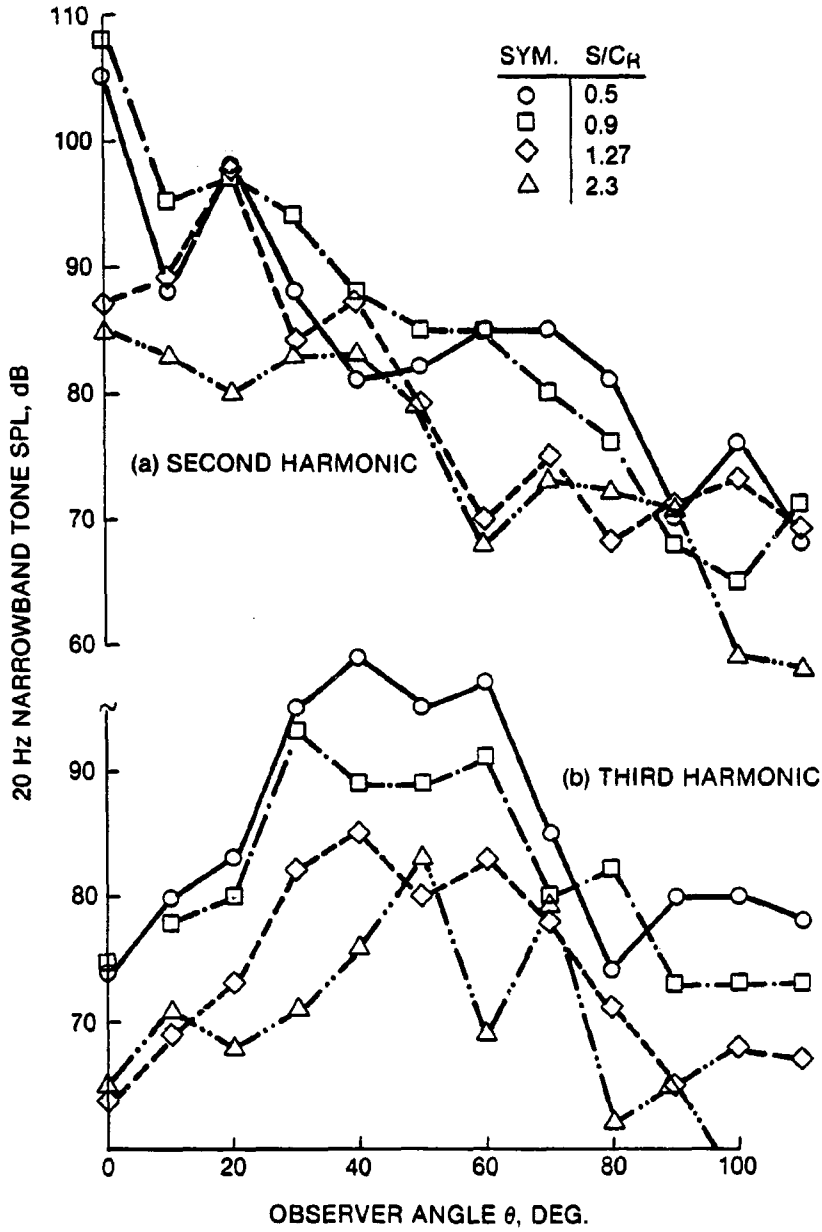

Figure 39. Narrowband Tone Directivity Patterns for 86-Vane Configurations; 54% N_F and Open Throttle O/L.

Figure 40 shows the measured narrowband directivity patterns for the forty-eight vane fan stage as a function of axial spacing ratio. The fundamental BPF tone is included since this is a cut-on fan design. Again, it is observed that although the general trend is for the tone levels to drop with spacing, the trend is inconsistent from angle to angle.

It is believed that the scrambled picture given by Figures 39 and 40 is due in great measure to the highly lobular structure of the interaction tone directivity patterns and the difficulty associated with getting the peaks and valleys in precisely the same angular location relative to the microphones from run to run. The shifting of the directivity lobes is believed to be very sensitive to changes in speed and small differences in fan speed from point to point could conceivably produce significant changes in observed tone levels at a given microphone location. Cursory comparisons of narrowband spectra from this test with narrowband spectra taken on the E^3 scale model test program (forty-eight vanes, $s/c_R = 2.3$) showed remarkably good agreement on broadband levels but tone levels differed by as much as 10 dB, although the general trends of harmonic spectra shape were similar. Also, the "sawtooth" shapes of the directivity patterns are indicative of a lobular pattern with an insufficient number of microphones to define them.

The partial directivity patterns ($30° \leqslant \theta \leqslant 60°$) for 54% speed and closed throttle setting are shown in Figure 41. The partial directivity patterns for 69% speed at open and closed throttle settings are given in Figures 42 and 43, respectively. In general, the results for the eighty-six vane BPF tones shown in Figures 41 through 43 indicate no really consistent effect of stator spacing, implying that the source of the BPF tone for the eighty-six vane, cut-off design is probably not due to rotor-stator interaction. For the 54% speed, closed throttle condition (Figure 41), even the second harmonic (2X BPF) tone does not appear to be materially affected by rotor-stator spacing. With only a few exceptions, the previous observations made regarding the inconsistent variation in tone level versus spacing from angle to angle appear to persist at the higher closed throttle operating line and at the higher speed of 69% N_F, probably for the same reasons speculated earlier.

Tone power level calculations were carried out for the 54% speed, open throttle cases where narrowband spectra had been reduced at all microphone locations from 0° to 110°. In addition, a "partial power level" was defined, using only the 30° through 60° microphone levels, and this "partial power level," designated as PPWL (dB re: 10^{-13} watts), was also computed for all speeds and both operating lines. Trends of PWL and/or PPWL versus spacing ratio were compiled and are displayed in Figures 44 through 48, corresponding to 54% through 80% speed, respectively.

Figure 44 shows the tone PWL versus spacing trends for 54% speed. Both the total tone PWL ($\theta = 0°$ to 110°) and the partial tone PPWL ($\theta = 30°$ to 60°) are displayed for the open throttle operating line. The two representations illustrate the degree to which the partial power (PPWL) approximates the total power (PWL). For the eighty-six vane configurations, Figure 44a, it is observed that the two measures of power versus spacing agree closely for the first and third harmonics. The agreement is not as good for the second harmonic, however, because the sound pressure levels at angles less than 30° exceed the 30° to 60° levels by an appreciable amount, as shown in Figure 39. The discrepancy varies erratically with spacing, however, because the directivity pattern itself changes erratically with spacing.

For the forty-eight vane configurations, Figure 44b, the PPWL versus spacing trends agree with the PWL versus spacing trends very well, and the trends appear to be more regular and monotonic than those for the eighty-six vane configurations. The apparent irregular trends of the eighty-six vane data (Figure 44a) may, however, be due in part to the extra spacing data points at s/c_R=0.9 which are not present in the forty-eight vane curves.

It can be seen from all of the data shown in Figures 44 through 48 that the BPF tone for the eighty-six vane cases does not vary appreciably with rotor-stator spacing, at any of the speeds and throttle settings shown. Moreover, the forty-eight vane BPF tones appear to be appreciably higher than the eighty-six vane tones at the closest spacing and then approach the eighty-six vane levels asymptotically as spacing is increased. From these results it was again concluded that the source of the BPF tone is not rotor-stator related for the eighty-six vane configurations. This BPF tone source is, therefore, probably rotor/inflow distortion or turbulence related and is present in both eighty-six vane and forty-eight

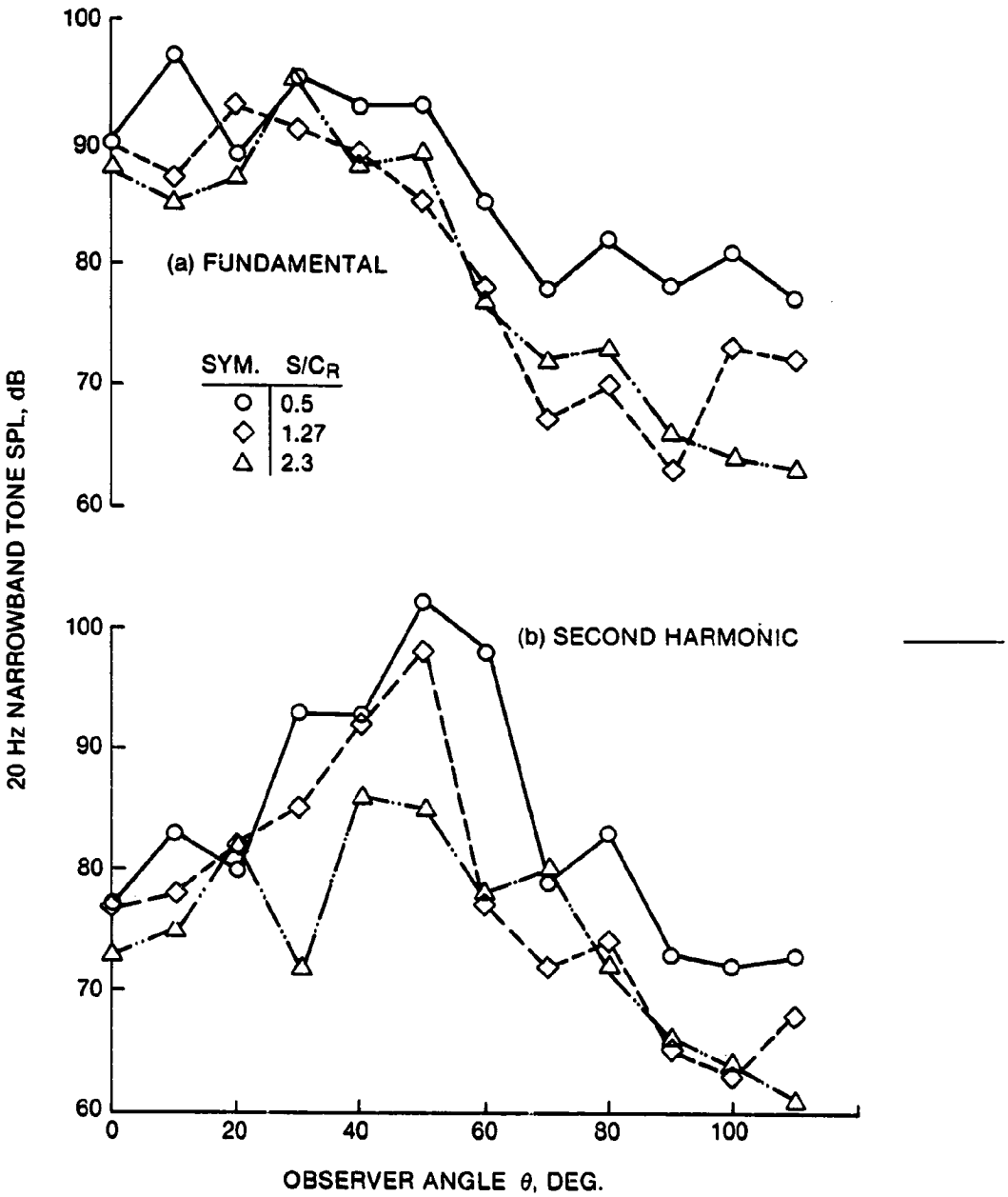

Figure 40. **Narrowband Tone Directivity Patterns for 48-Vane Configurations; 54% N_F and Open Throttle O/L.**

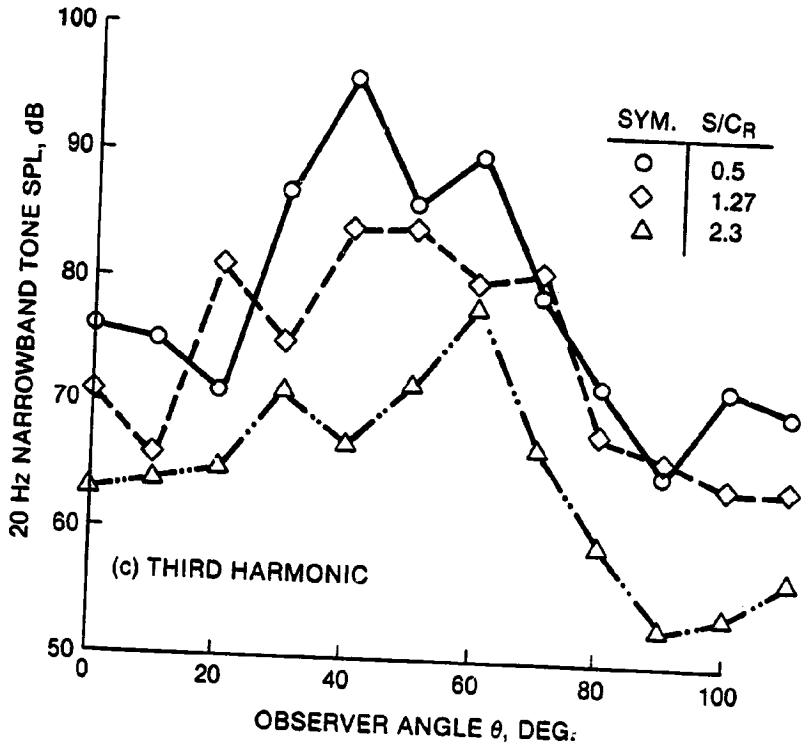

Figure 40. (Cont'd)

vane configurations. It exhibits levels comparable to the rotor-stator interaction levels (forty-eight vane configuration) for axial spacings greater than about one rotor chord.

The PPWL versus spacing trends for the second harmonic (2X BPF) tones shown in Figures 44 through 48 are similar for the forty-eight and eighty-six vane configurations, except at the tightest spacing on the open throttle operating line. On the closed throttle operating line, the forty-eight vane cases show higher levels, by as much as 5 to 10 dB. In general, the third harmonic (3X BPF) tone levels are comparable for the forty-eight vane and eighty-six vane configurations at both throttle settings. It also appears that the sensitivity of the tone PPWL to spacing decreases as speed increases, especially on the open throttle operating line. At 80% speed, Figure 48, the tone levels change very little with spacing at open throttle.

6.4 Tone Accel/Decel Characteristics

Tracking filter analysis of the BPF tone and the second and third harmonics of BPF was carried out for each configuration. The fan speed was slowly varied from 54% speed to 100% speed and back to 54% speed again, and the far field data was recorded during the transient slow accel and/or decel. The data was subsequently analyzed using a 1500 Hz bandwidth tracking filter centered at BPF, 2X BPF, and 3X BPF.

The results of the tracking filter analysis of the BPF tone versus % speed characteristics are displayed in Appendix C for all those points which were analyzed in this fashion. Only the open throttle operating line accel-decel runs were analyzed and only at the 60° microphone location. A total of thirty-two accels and decels are given in Appendix C for the various combinations of vane number and axial spacing.

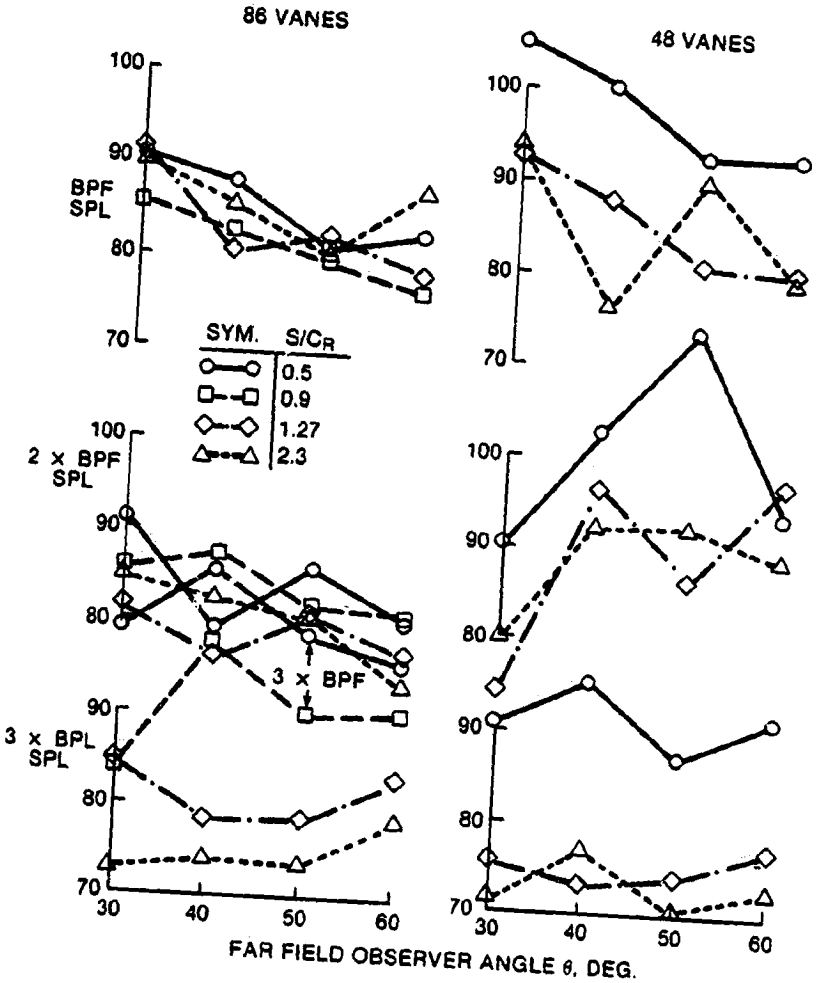

Figure 41. Partial 20 Hz Narrowband Directivity Patterns for 54% N_F and Closed Throttle.

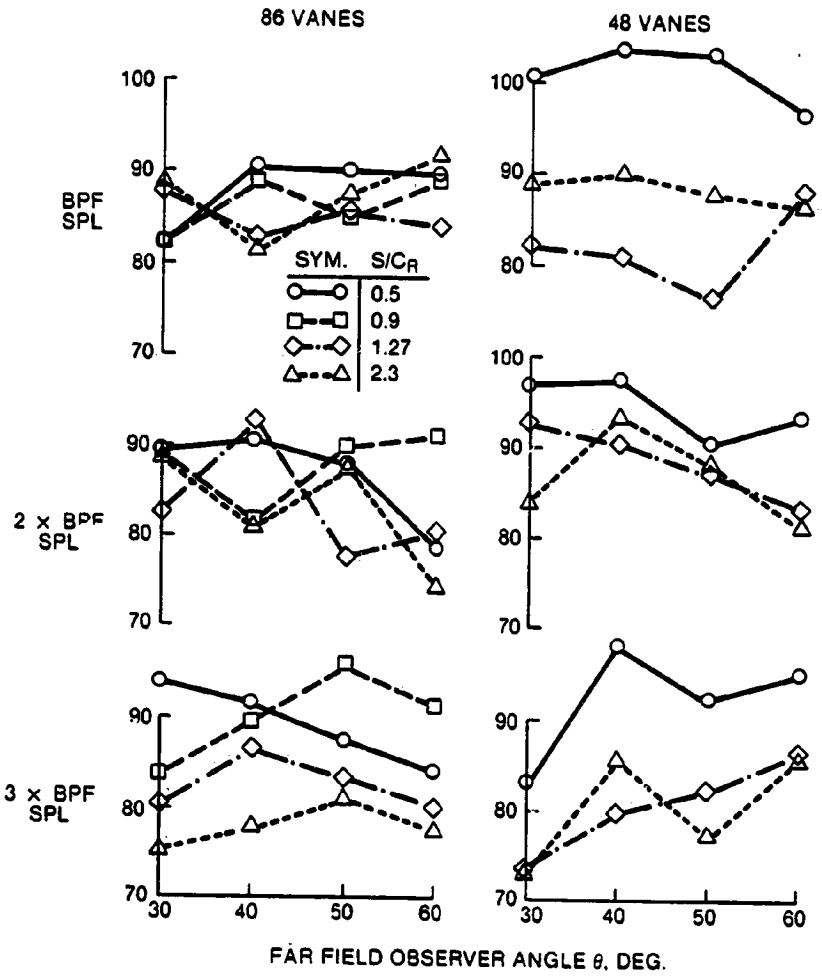

Figure 42. Partial 20 Hz Narrowband Directivity Patterns for 69% N_F and Open Throttle.

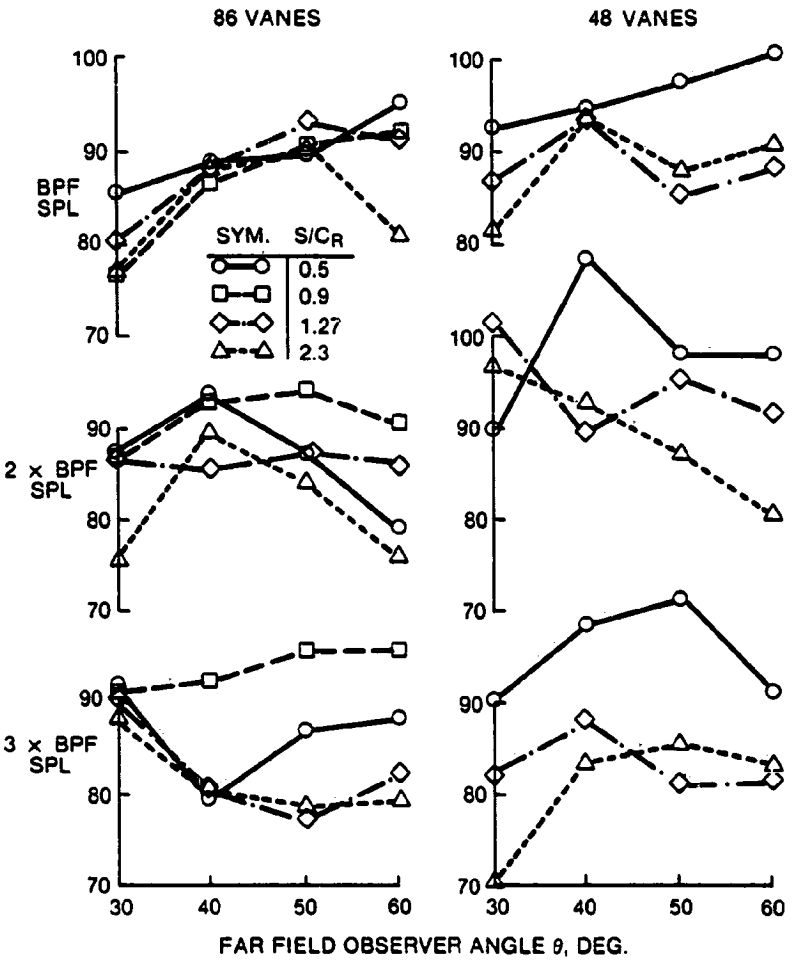

Figure 43. Partial 20 Hz Narrowband Directivity Patterns for 69% N_F and Closed Throttle.

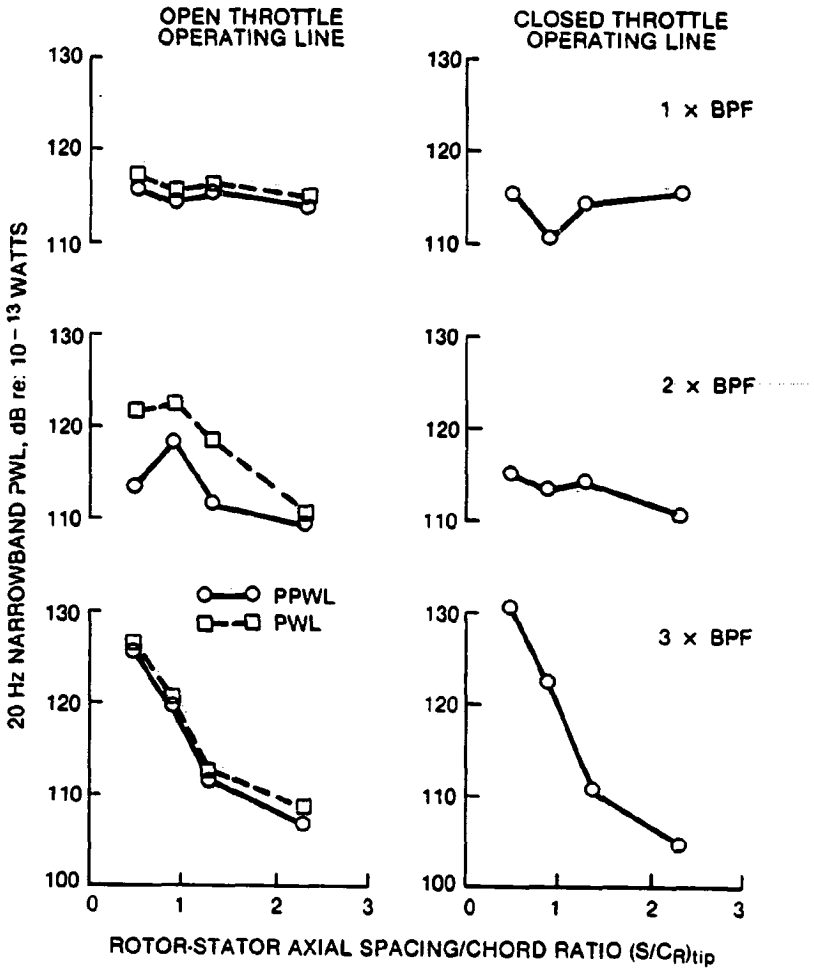

Figure 44(a). Tone PWL vs. Spacing Trends at 54% N_F; 86-Vane Configurations.

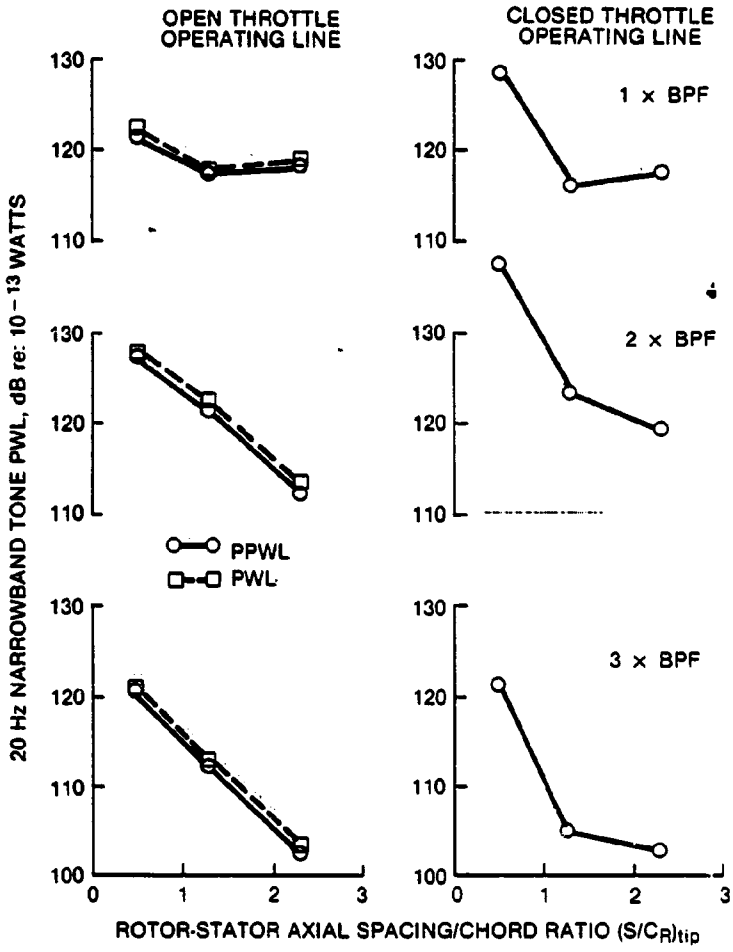

Figure 44(b). **Tone PWL vs. Spacing Trends at 54% Speed; 48-Vane Configurations.**

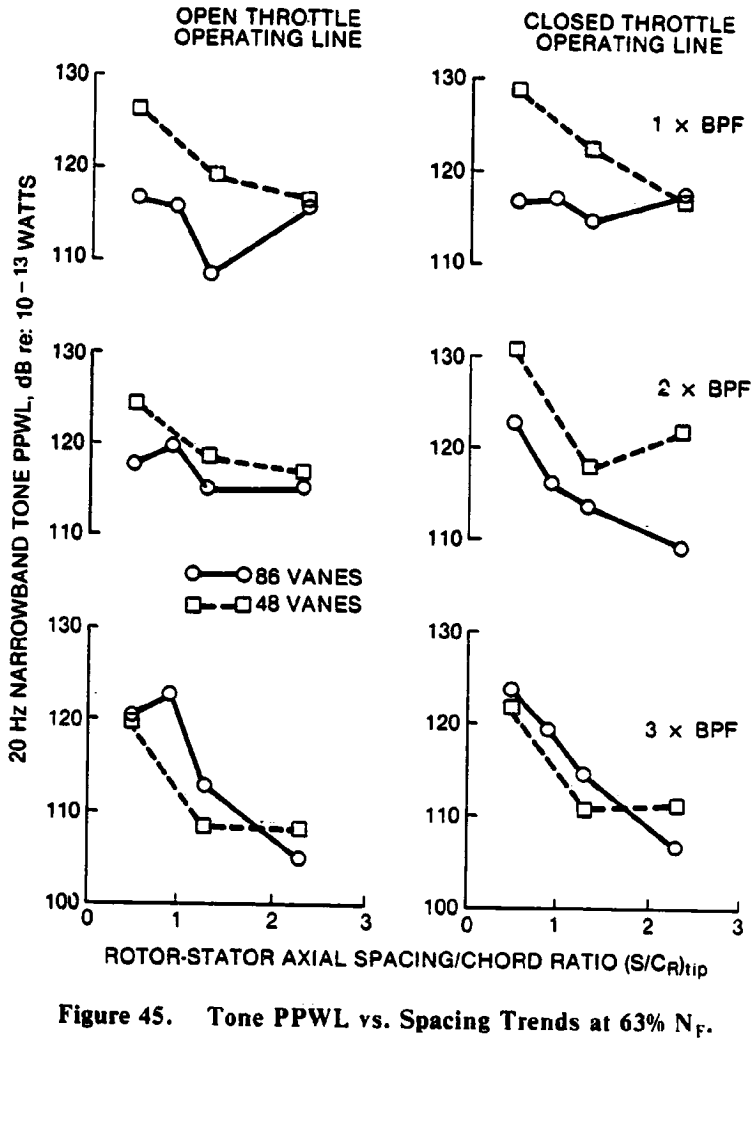

Figure 45. Tone PPWL vs. Spacing Trends at 63% N_F.

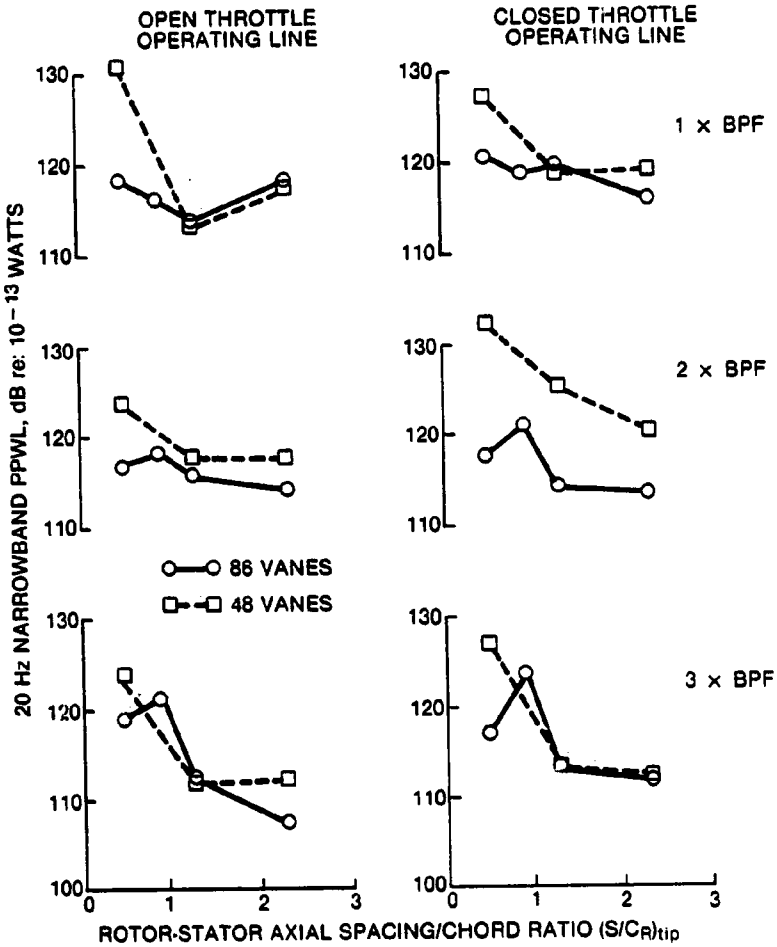

Figure 46. Tone PPWL vs. Spacing Trends at 69% N_F.

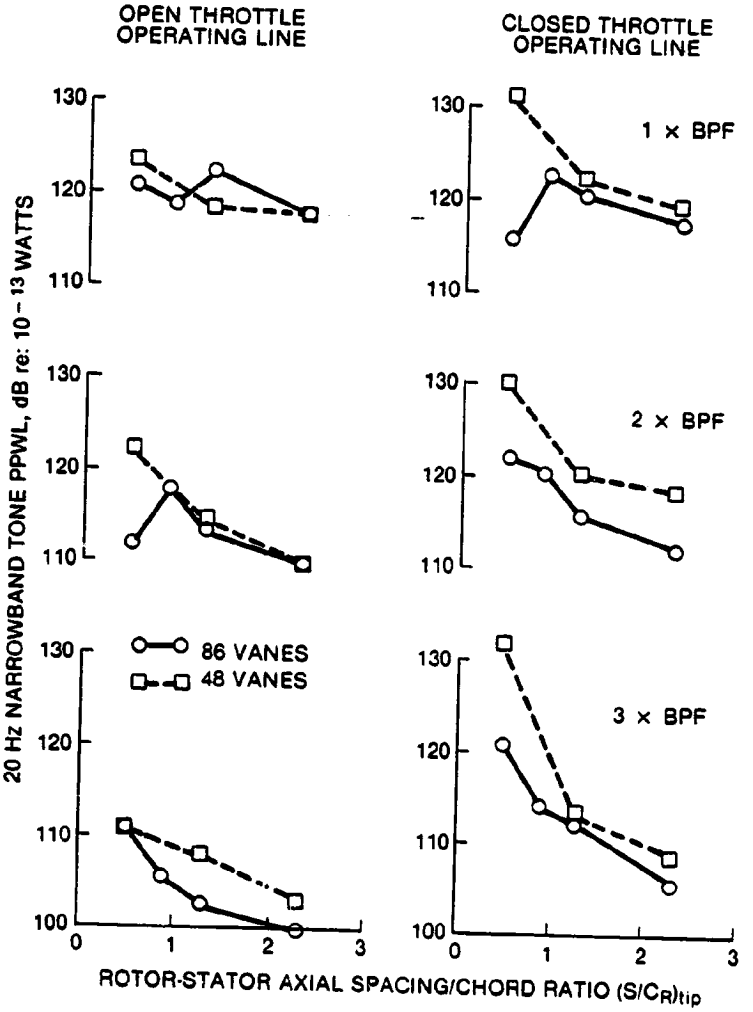

Figure 47. Tone PPWL vs. Spacing Trends at 76% N_F.

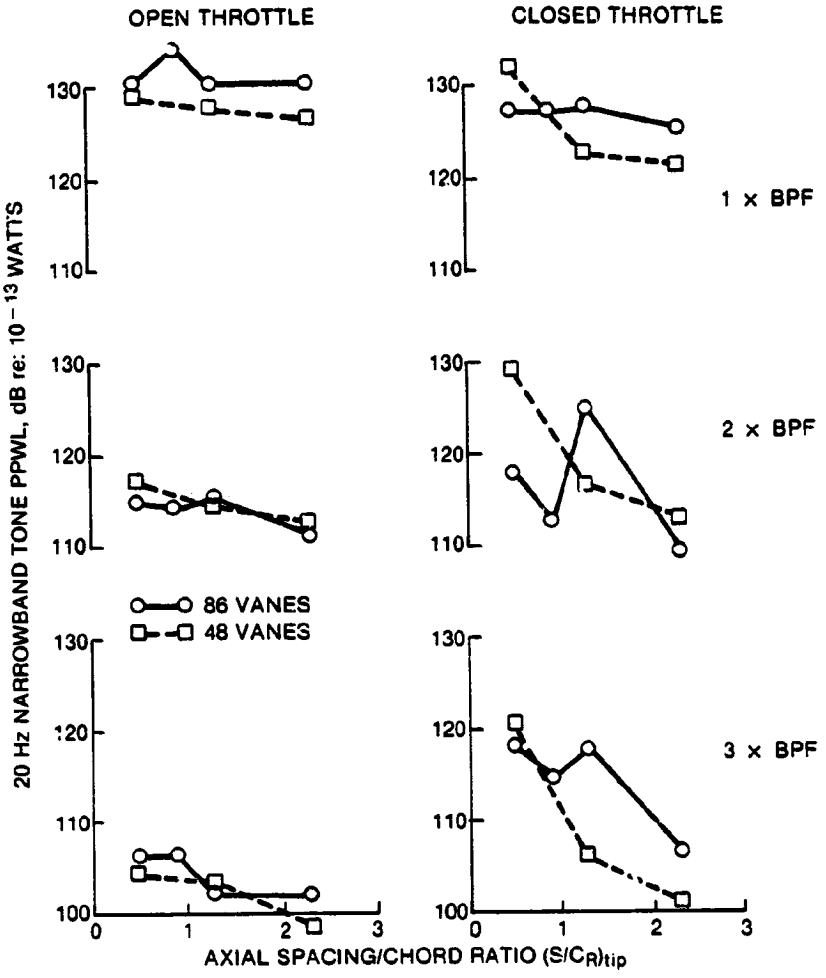

Figure 48. Tone PPWL vs. Spacing Trends at 80% N_F.

A typical BPF tone accel characteristic is shown in Figure 49. The tip speed Mach number is unity at approximately 80% speed while the rotor inlet relative Mach number is unity at about 73% speed. It can be seen from Figure 49 that the BPF tone level rises rapidly at about 79% speed, indicating the onset of the rotor-alone pressure field propagation. The characteristic of the tone level versus % speed trace does not change appreciably between accels and decels except that the cut off of the rotor-alone pressure field during a decel occurs about 2% higher in speed than the cut on of the rotor-alone field during an accel.

The second and third harmonic tone level versus speed characteristics do not exhibit as sudden a rise in level at the apparent rotor-alone cut-on speed (approximately 78-79% N_F) nor is the change in level as large from subsonic to supersonic conditions. Typical second and third harmonic noise level accel characteristics are shown in Figures 50 and 51, respectively. It is observed that the tone levels (Figures 49 through 51) do not climb steadily with increasing speed, but rather oscillate about a constant mean value in the subsonic range. Once the speed exceeds the transition between subsonic and supersonic operation, the higher supersonic level again remains fairly flat as speed is increased. The fundamental tone does exhibit rather large swings in level, however, in the supersonic range. These swings in the level are probably due to the lobe shifts in the radiation pattern and the number of lobes excited with change in the speed.

The above described characteristics appear to hold for all the configurations tested. One distinguishing feature of the forty-eight vane results versus the eighty-six vane results is that the fine scale oscillations in tone levels with increasing speed are much lower in amplitude. There also appears to be more "lobular" or medium scale oscillation behavior in the tones for the subsonic speed range.

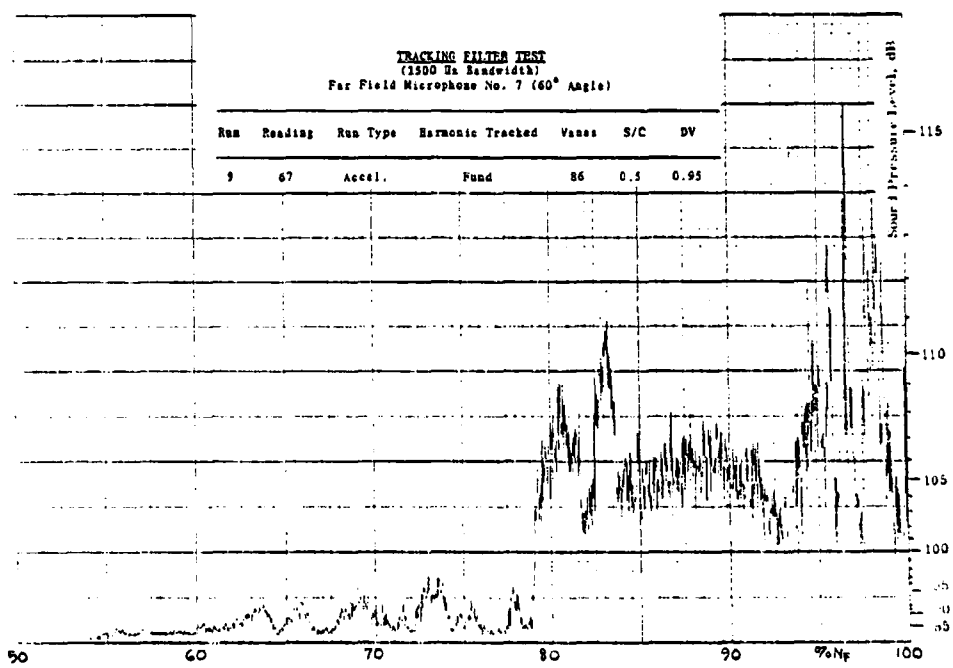

Figure 49. Tracking Filter Test (1500 Hz Bandwidth) Far Field Microphone No. 7 (60° Angle).

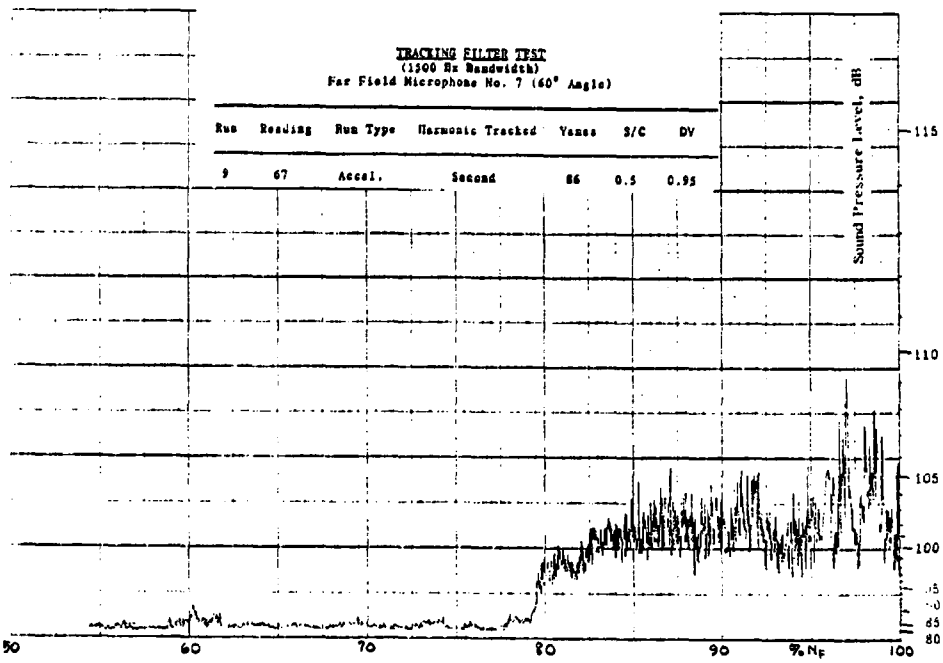

Figure 50. Tracking Filter Test (1500 Hz Bandwidth) Far Field Microphone No. 7 (60° Angle).

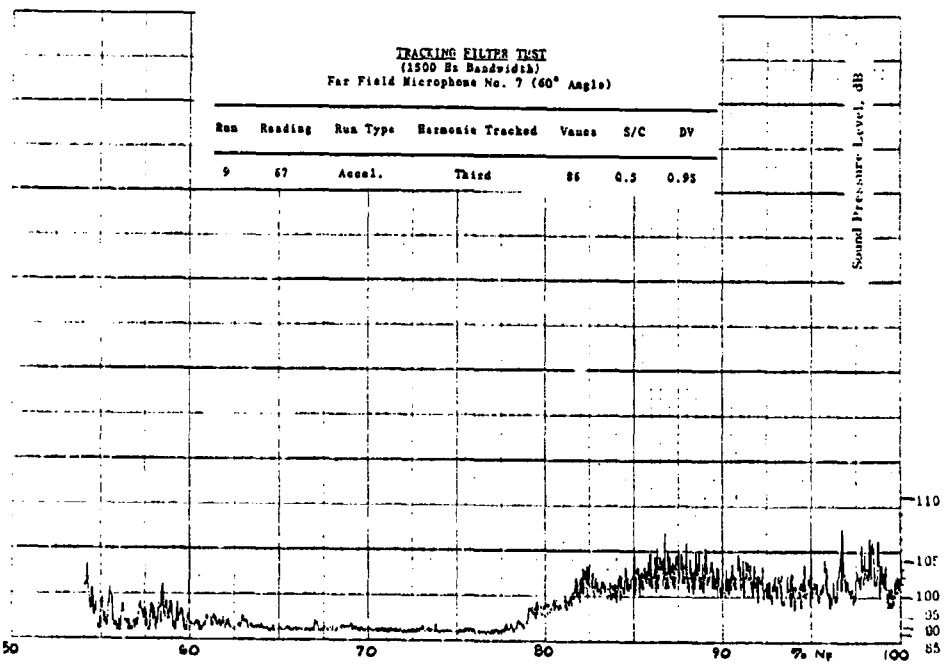

Figure 51. Tracking Filter Test (1500 Hz Bandwidth) Far Field Microphone No. 7 (60° Angle).

Section 7

NEAR FIELD ACOUSTIC TEST RESULTS

7.1 Aft Duct Probe Spectra

As described in Section 2 and illustrated in Figure 6, sound level measurements were made in the exhaust duct downstream of the stator vanes with a traversing probe. The probe sting aligned with the flow contains two miniature sensors designated K4 (forward position) and K2 (aft position). The measurements were taken at two immersions, and outer immersion readings are designated by subscript "o" (e.g., $K2_o$ or $K4_o$), while inner immersion readings are designated by subscript "i" ($K2_i$ or $K4_i$). The immersion locations were 17.3 and 69.3% the duct height from the outer wall for the "outer" and "inner" immersions, respectively, for the eighty-six vane configurations.

Because of some confusion arising from changes in personnel during the test program, the data for the forty-eight vane configurations was inadvertently taken at 2.5 and 30.5% of span from the outer wall for the "outer" and "inner" immersions, respectively. This inconsistency with the eighty-six vane data with respect to immersion locations makes a direct comparison between eighty-six vane and forty-eight vane results somewhat questionable in terms of absolute levels, but the trends with spacing, speed, throttle settings and harmonic number should be reasonable. This difficulty is further compounded by the lack of in situ calibration of the aft duct probe.

Typical examples of aft duct probe sound pressure level spectra are shown in Figures 52 through 60. The format is similar to that for the far field SPL spectra shown in Figures 17 through 38. Figures 52 and 53 show the aft duct SPL spectra for the eighty-six vane configurations at 54% speed and open throttle at the "outer" immersion for sensors K2 and K4, respectively. Figures 54 and 55 show the corresponding results for the "inner" immersion. A large reduction in tone levels from the $s/c_R = 0.5$ spectrum to the $s/c_R = 2.3$ spectrum is evident. A hump of broadband noise occurs in Figures 53 and 55. It was speculated that this hump in the broadband noise spectrum could be caused by probe vortex shedding and/or vibration, to which the K4 sensor is particularly susceptible. The former appears unlikely since, for a probe stem diameter of 0.635 cm (0.25 in.) and a flow velocity of 122 m/s (400 ft/sec), the Strouhal number fd/V for 26,000 Hz is 1.35. This is an order of magnitude higher than the classical Strouhal number of 0.15 to 0.25 usually associated with vortex shedding. Although the source of this peculiar hump of noise is not known, it does not affect the tone levels and does not appear to be sensitive to stator configuration.

Some examples of aft duct spectra at the closed throttle condition are shown in Figures 56 and 57 at 69.3% immersion. The large tone reductions as axial spacing is increased are again evident, as is the peculiar broadband noise hump for the K4 sensor spectra. There does not appear to be any dramatic change in the character of the aft duct spectrum in going from open to closed throttle.

The aft duct probe spectra at 69% speed and closed throttle setting are shown in Figure 58 for the K2 sensor at 69.3% immersion. The trend with spacing is seen to be the same as that observed for 54% N_F, Figure 56. The tone protrusions are somewhat higher at the higher speed, however. At a very high speed where the tip speed Mach number is supersonic, the effect of spacing on tone level is still quite large, as seen in Figure 59. This figure shows the aft duct K2 sensor probe spectra at 69.3% immersion for the eighty-six vane configurations at 95% speed and closed throttle. It can be seen that there is a significant reduction in aft duct tone levels with increased spacing in contrast to the trends observed for the forward radiation far field spectra. Also, there is little or no contribution of multiple pure tone (MPT) or "buzz saw" noise to the spectra, again in contrast to the forward radiated far field spectra which were dominated by MPT noise at this speed (see Figure 29). A typical set of forty-eight vane configuration spectra are shown in Figure 60, and they exhibit the same characteristics as the eighty-six vane spectra, except for the dominant BPF tone.

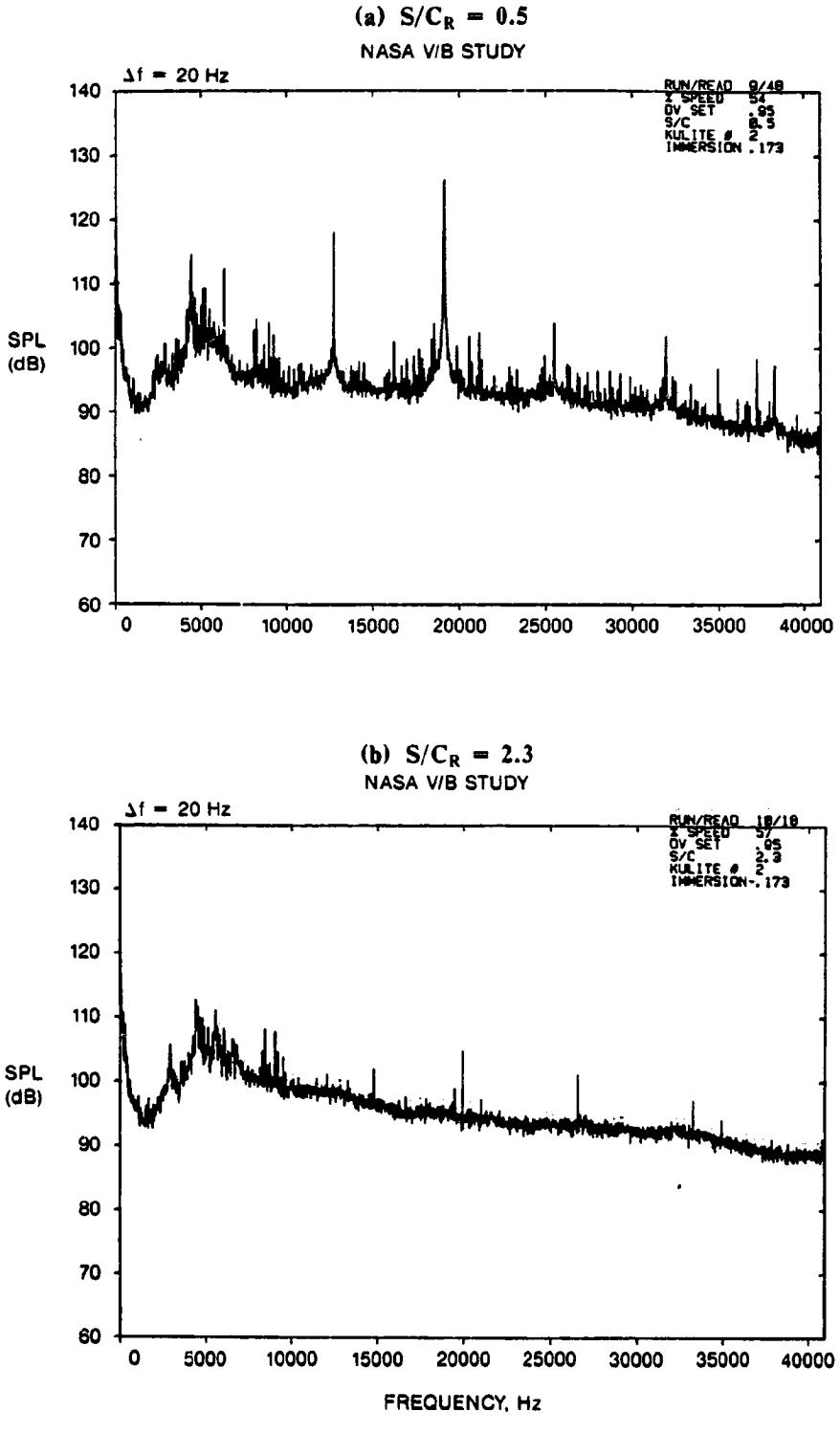

Figure 52. Aft Duct Probe Spectra for 86-Vane Configuration at 54% N_F and Open Throttle, 17.3% Immersion K2 Sensor.

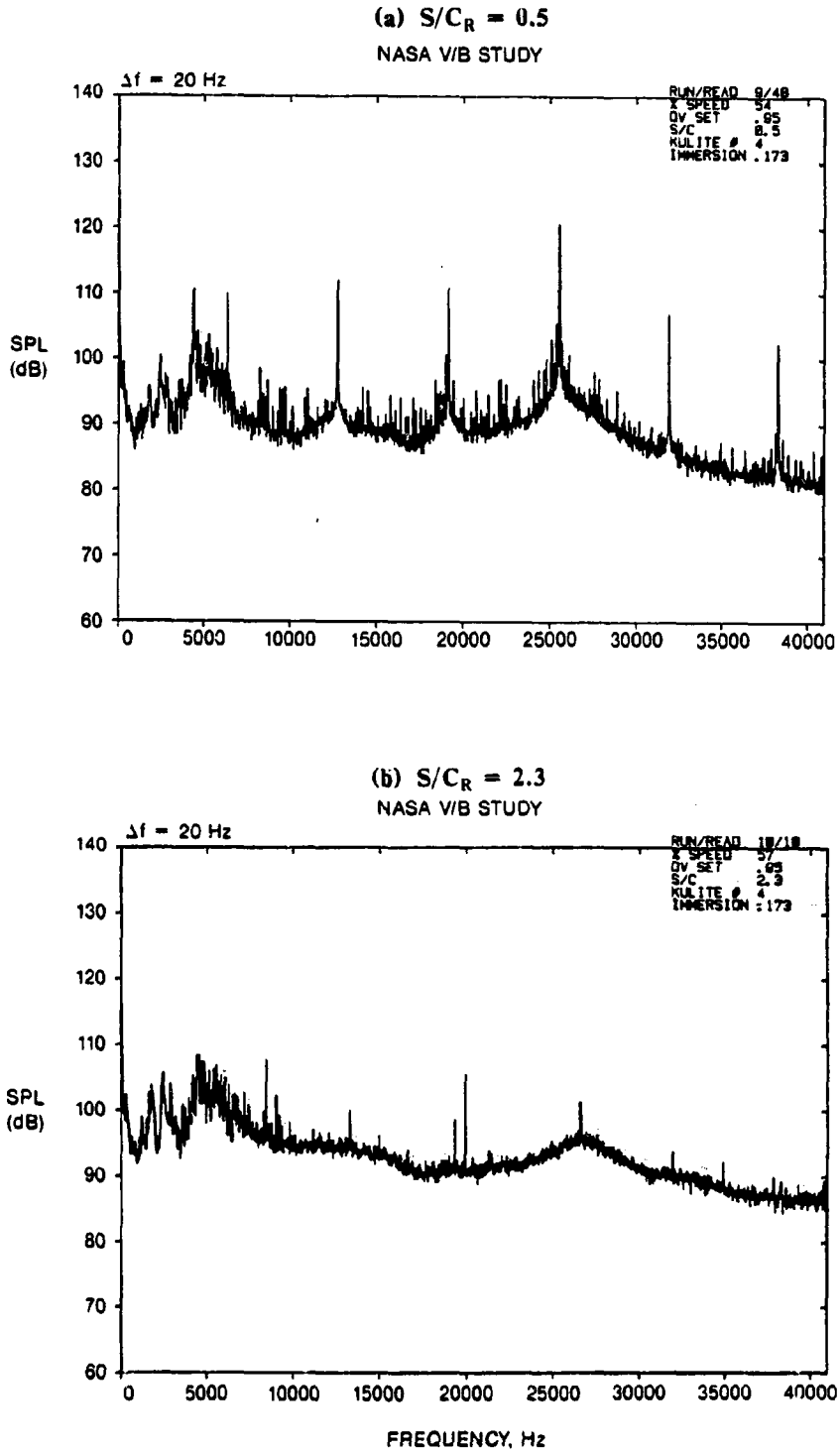

Figure 53. Aft Duct Probe Spectra for 86-Vane Configuration at 54% N_F and Open Throttle, 17.3% Immersion K4 Sensor.

(a) $S/C_R = 0.5$

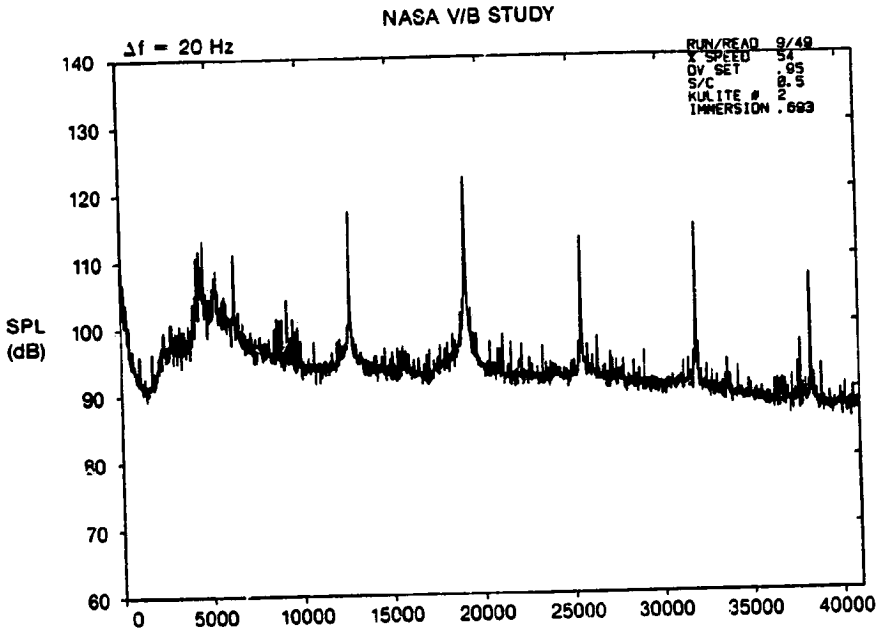

(b) $S/C_R = 2.3$

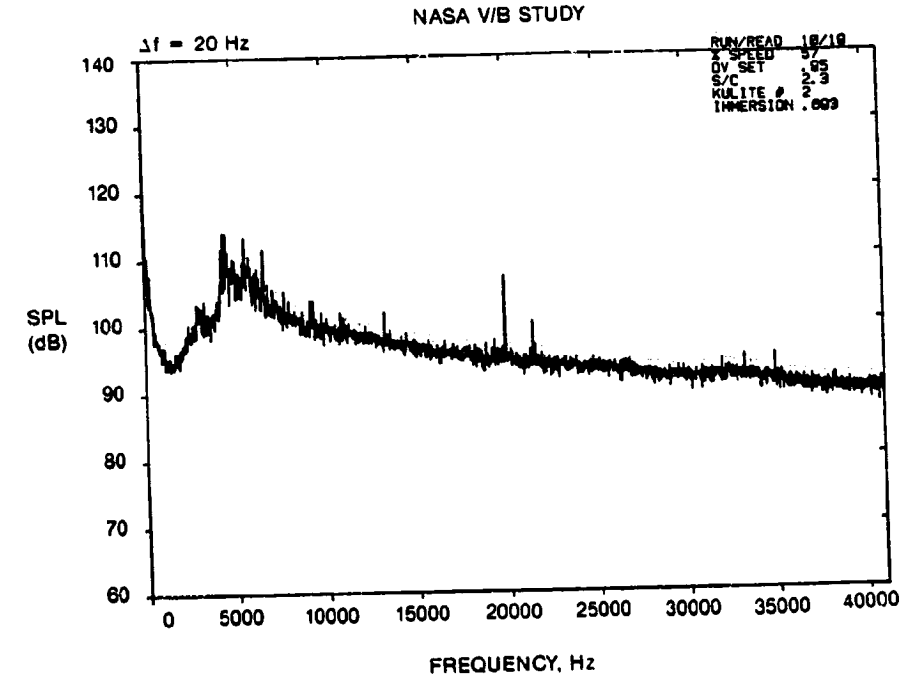

Figure 54. Aft Duct Probe Spectra for 86-Vane Configuration at 54% N_F and Open Throttle, 69.3% Immersion K2 Sensor.

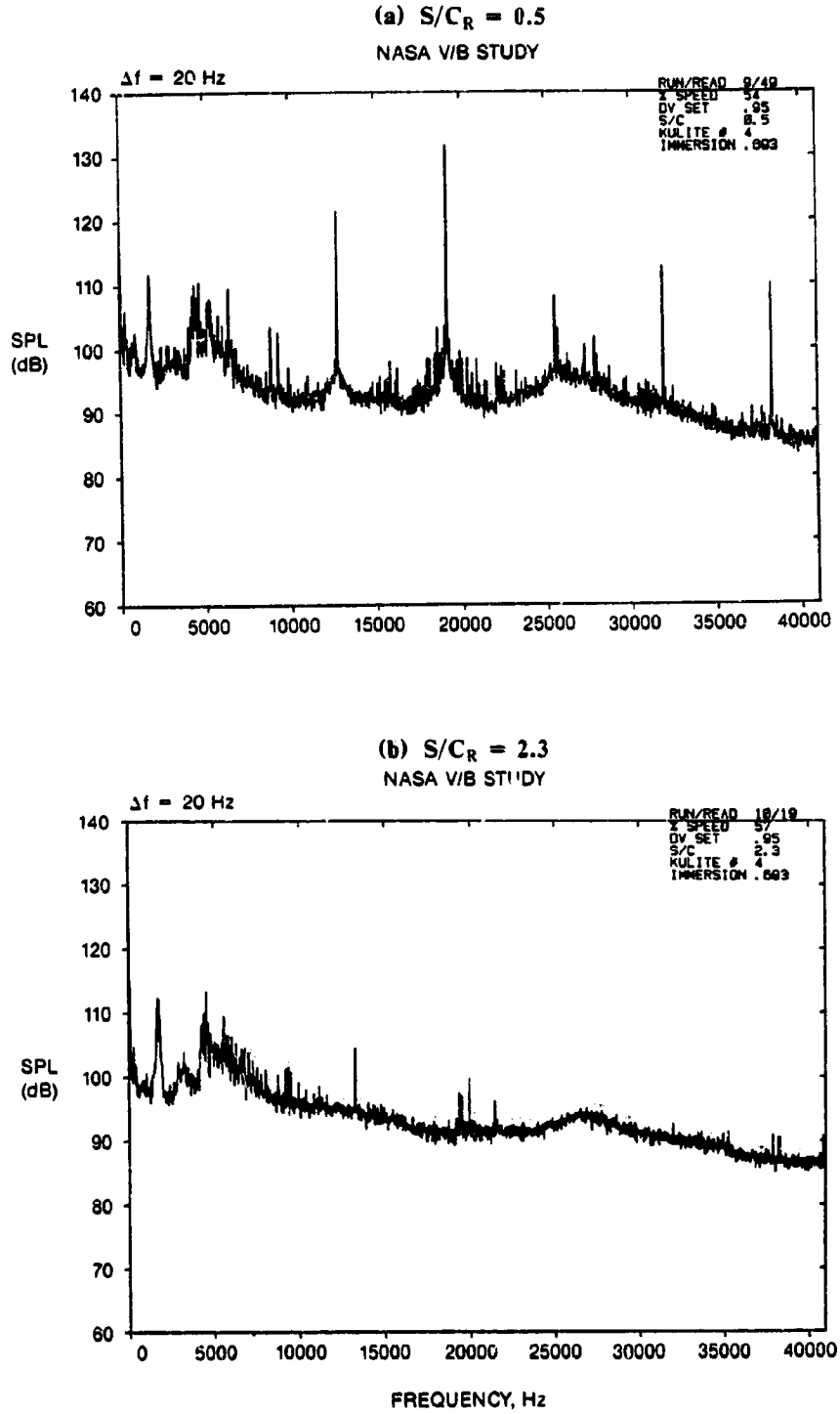

Figure 55. Aft Duct Probe Spectra for 86-Vane Configuration at 54% N_F and Open Throttle, 69.3% Immersion K4 Sensor.

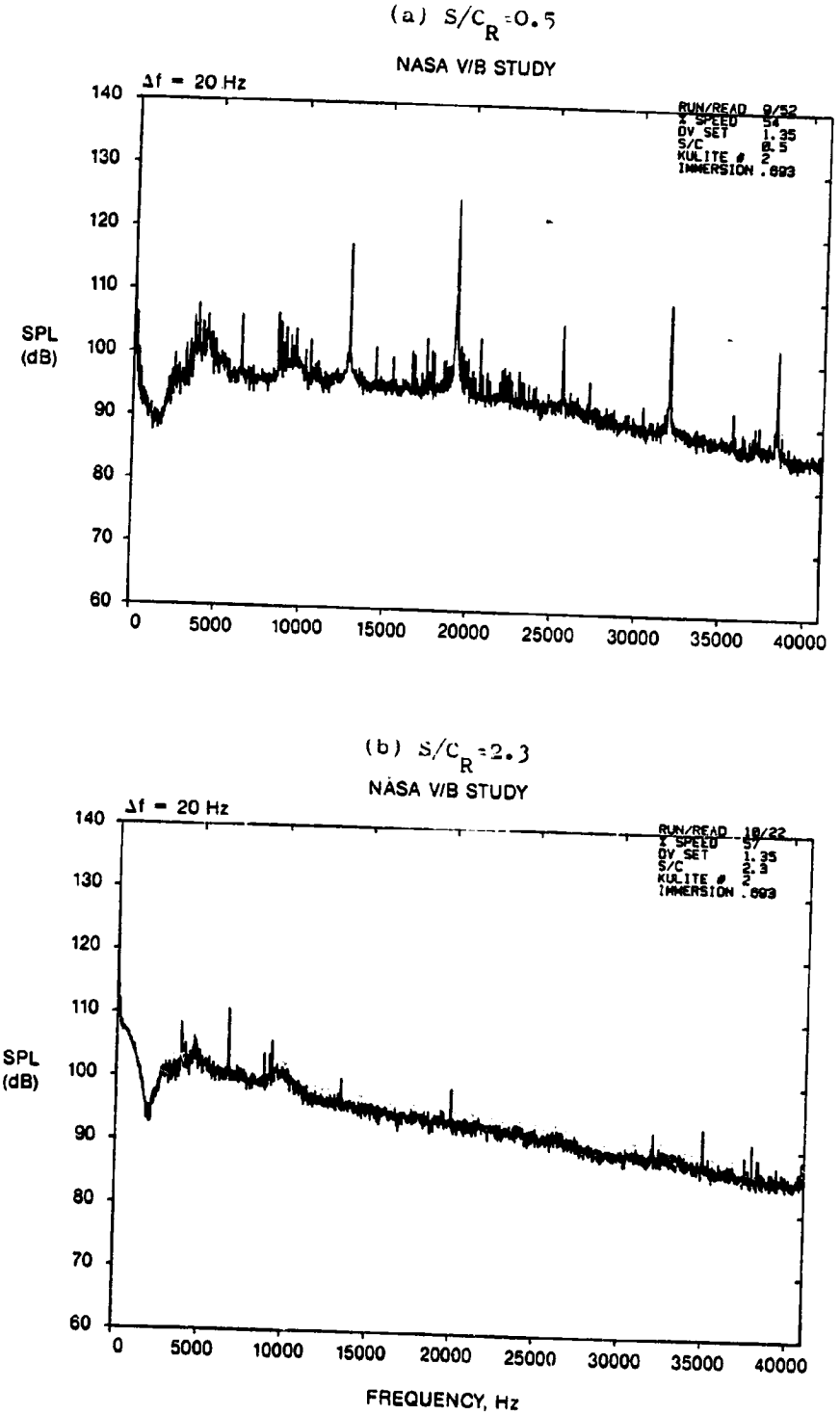

Figure 56. **Aft Duct Probe Spectra for 86-Vane Configuration at 54% N_F and Closed Throttle, 69.3% Immersion K2 Sensor.**

(a) $S/C_R = 0.5$

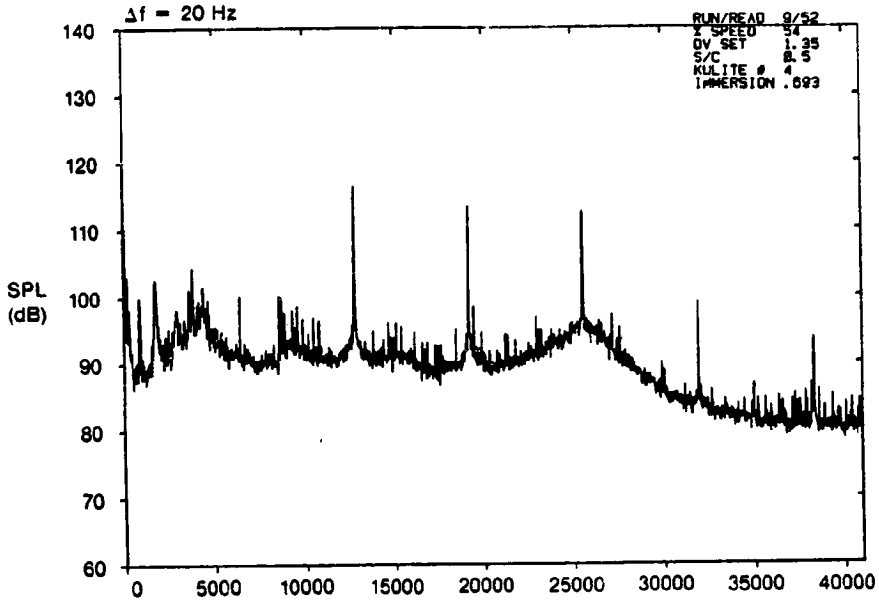

(b) $S/C_R = 2.3$

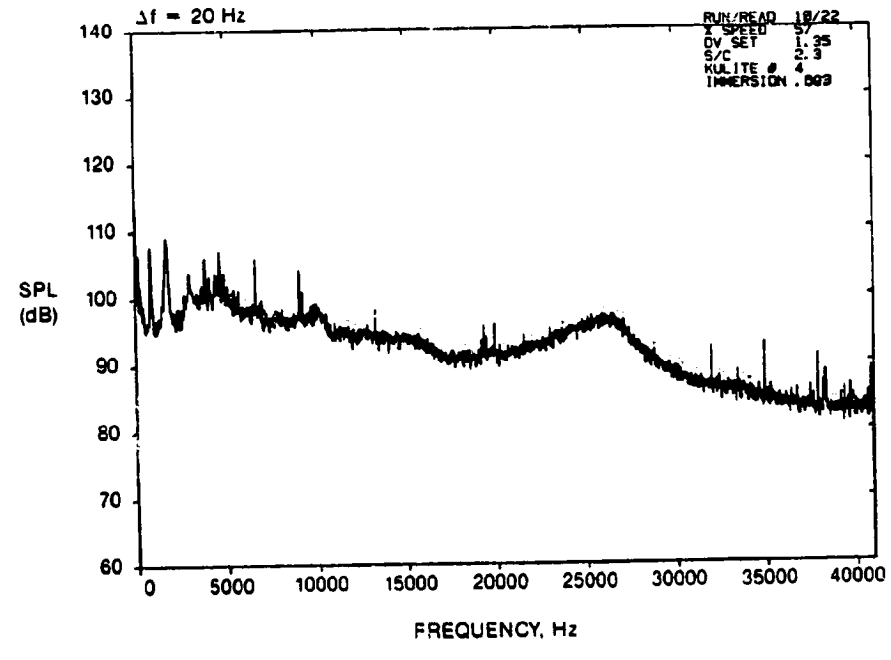

Figure 57. Aft Duct Probe Spectra for 86-Vane Configuration at 54% N_F and Open Throttle, 69.3% Immersion K4 Sensor.

(a) $S/C_R = 0.5$

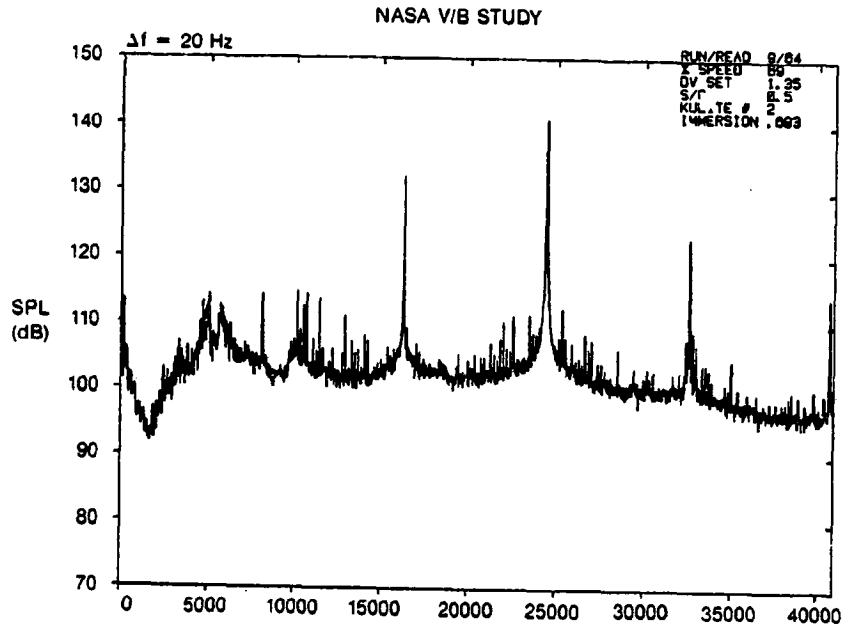

(b) $S/C_R = 2.3$

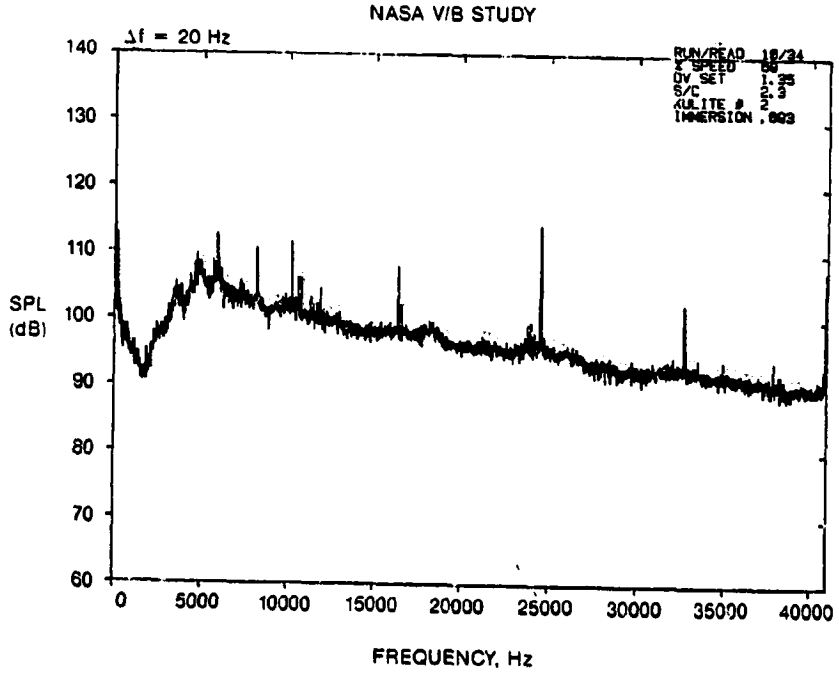

Figure 58. Aft Duct Probe Spectra for 86-Vane Configuration at 69% N_F and Closed Throttle, 69.3% Immersion K2 Sensor.

(a) $S/C_R = 0.5$

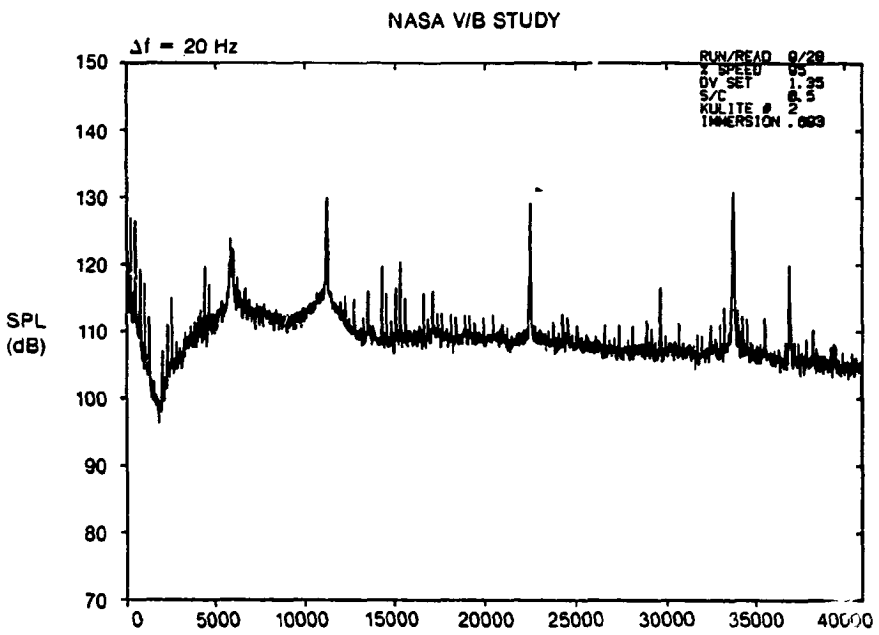

(b) $S/C_R = 2.3$

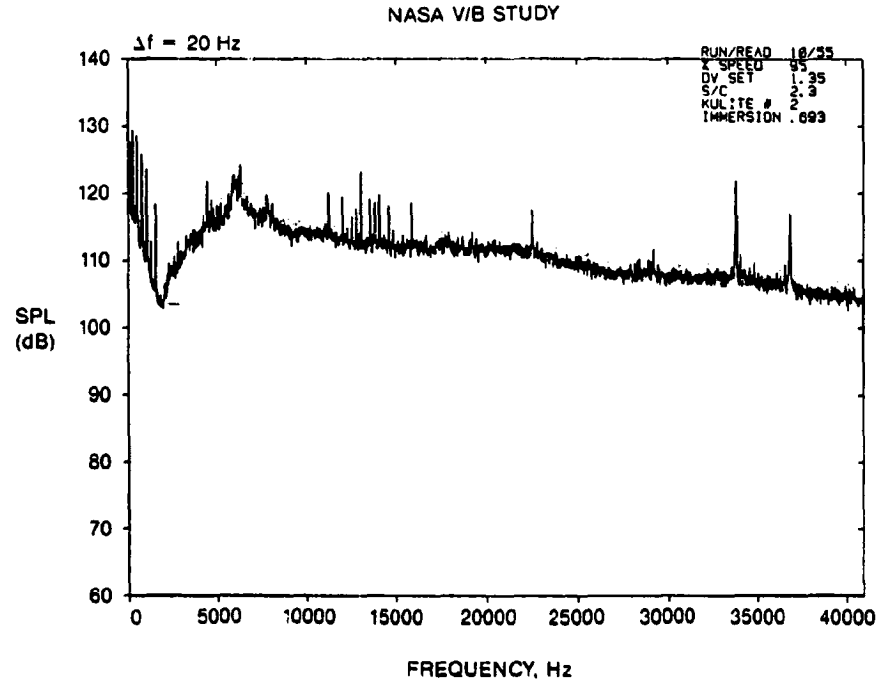

Figure 59. Aft Duct Probe Spectra for 86-Vane Configuration at 95% N_F and Closed Throttle, 69.3% Immersion K2 Sensor.

(a) $S/C_R = 0.5$

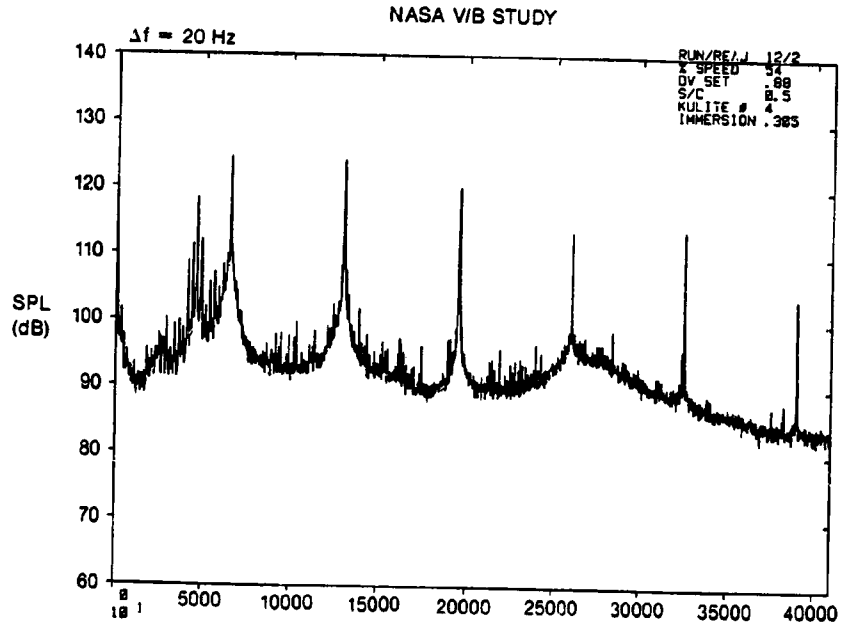

(b) $S/C_R = 2.3$

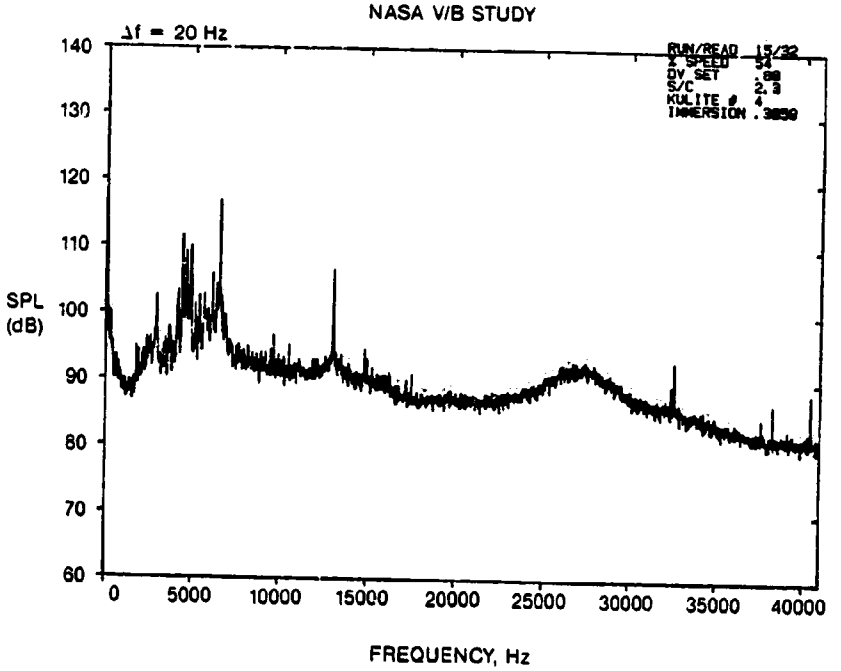

Figure 60. **Aft Duct Probe Spectra for 48-Vane Configuration at 54% N_F and Open Throttle, 30.5% Immersion K4 Sensor.**

It should be remarked that the trends described in the preceding paragraphs and illustrated in Figures 52 through 60 are general observations that exhibit considerable variability from point to point, immersion to immersion, and sensor to sensor. It was, therefore, desirable to perform some sort of data averaging in order to better quantify the trends. The tone levels were, therefore, scaled from the spectra and have been tabulated in Appendix B, along with the far field microphone tone levels. The tone levels from each sensor-immersion combination were then averaged to obtain a representative duct average SPL value. These average levels were then examined in terms of trends with spacing and vane number.

The tone level spectra (SPL versus harmonic number n) have been plotted for each of the vane number/spacing combinations tested, at 54 and 63% speed, for both open and closed throttle settings. The values from all four sensor-immersion combinations are shown and these results are displayed in Figures 61 through 67. These results indicate that although there is considerable spread or scatter in the levels, there does not appear to be any one sensor-immersion combination which is consistently in disagreement with the others.

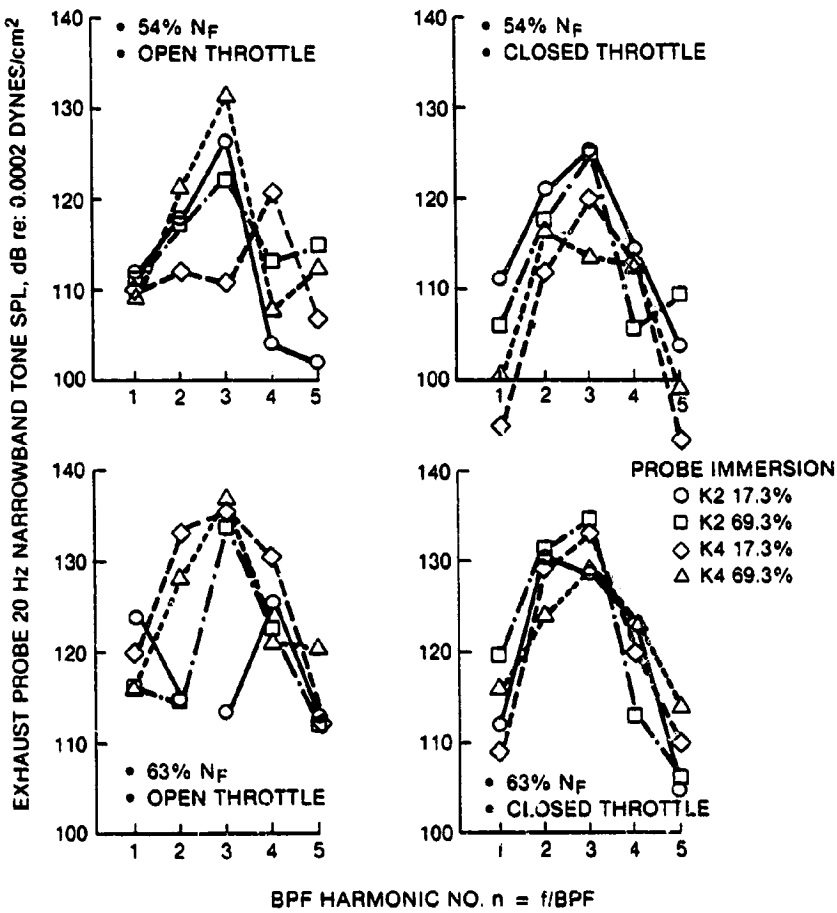

Figure 61. Aft Duct Probe Harmonic Spectra 86-Vanes and $S/C_R = 0.5$.

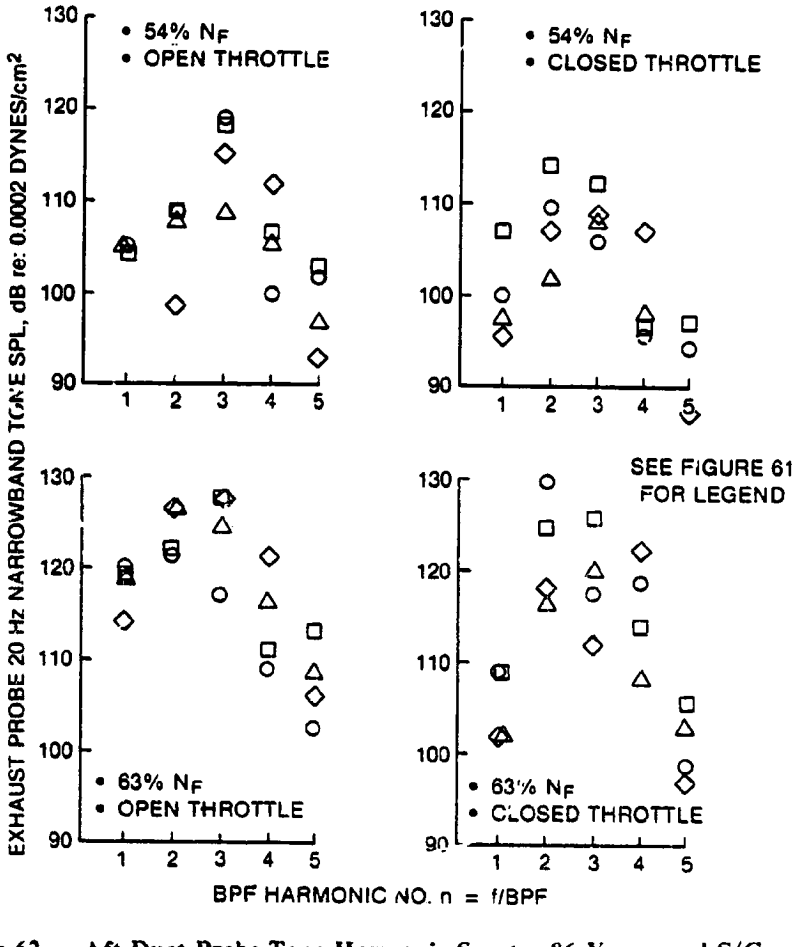

Figure 62. Aft Duct Probe Tone Harmonic Spectra 86-Vanes and S/C_R = 0.9.

The average SPL spectra derived from Figures 61 through 67 are shown in Figures 68 through 71, where the tone harmonic average SPL spectra at different spacings are compared. Examination of these comparisons shows several interesting features. The eighty-six vane configurations show a peak in the spectrum at the third harmonic (n = 3), as was observed for the far field spectra, for the closer spacings. The forty-eight vane configurations show a peak at the fundamental (n = 1) harmonic, and the falloff with harmonic number is much more rapid than for the eighty-six vane spectra. The eighty-six vane configurations show a more or less progressive drop in the spectrum with increasing spacing until s/c_R = 2.3, where the spectrum generally is as high as (or higher than) the spectrum at s/c_R of 1.27. For the forty-eight vane configurations, the drop with spacing is progressive for the 54% speed cases (Figures 68 and 69), but very little change is observed between the two largest spacing levels at 63% speed (Figures 70 and 71).

The aft duct average tone SPL values, derived from an arithmetic average of the four levels obtained from the four sensor-immersion combinations recorded, have been plotted versus rotor-stator axial spacing-chord ratio. These aft duct probe average SPL versus spacing trends are shown in Figures 72 through 76 for 54% through 80% corrected speed, respectively. These trends can be compared with the corresponding trends obtained from the inlet radiated far field data shown in Figures 44 through 48, and the data presentation format is similar. It is noted in passing that, if flow convection

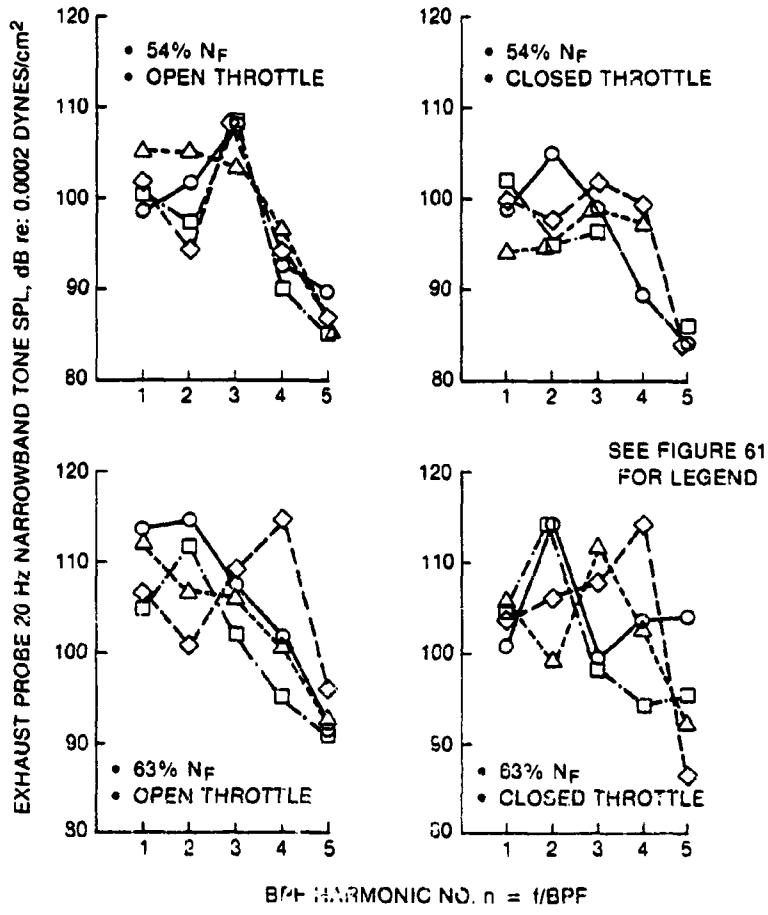

Figure 63. Aft Duct Probe Tone Harmonic Spectra 86-Vanes and S/C_R = 1.27.

effects are ignored and standard day values of air density and speed of sound are assumed, the conversion from average SPL to acoustic power PWL in the aft duct yields a correction of less than 1.0 dB, so that the average SPL levels shown in Figures 72 through 76 (and 68 through 71 as well) are roughly equivalent to PWL within the above-stated assumptions and approximations. It can be seen that the levels shown in Figures 72 through 76 are in reasonable agreement with the inlet PWL levels shown in Figures 44 through 48.

The aft duct SPL versus spacing trends are similar to the inlet PPWL versus spacing trends with a couple of exceptions. First, the dropoff rate with spacing increase is somewhat larger for the aft duct, especially for the higher speeds. Secondly, the peculiar noise (inlet PWL) increase in going from s/c_R = 0.5 to 0.9 for the eighty-six vane second harmonic tone in most cases (eight out of ten) does not occur in the aft duct SPL. Thirdly, the aft duct BPF tone is much higher for the forty-eight vane configurations than for the eighty-six vane configurations for most of the cases shown in Figures 72 through 76. In contrast, the inlet arc PWL BPF tones are comparatively close for forty-eight and eighty-six vane configurations. It should be remembered, however, that the immersion locations for the forty-eight vane configurations were different than those of the eighty-six vane configurations so that a direct comparison of levels in the aft duct may be misleading.

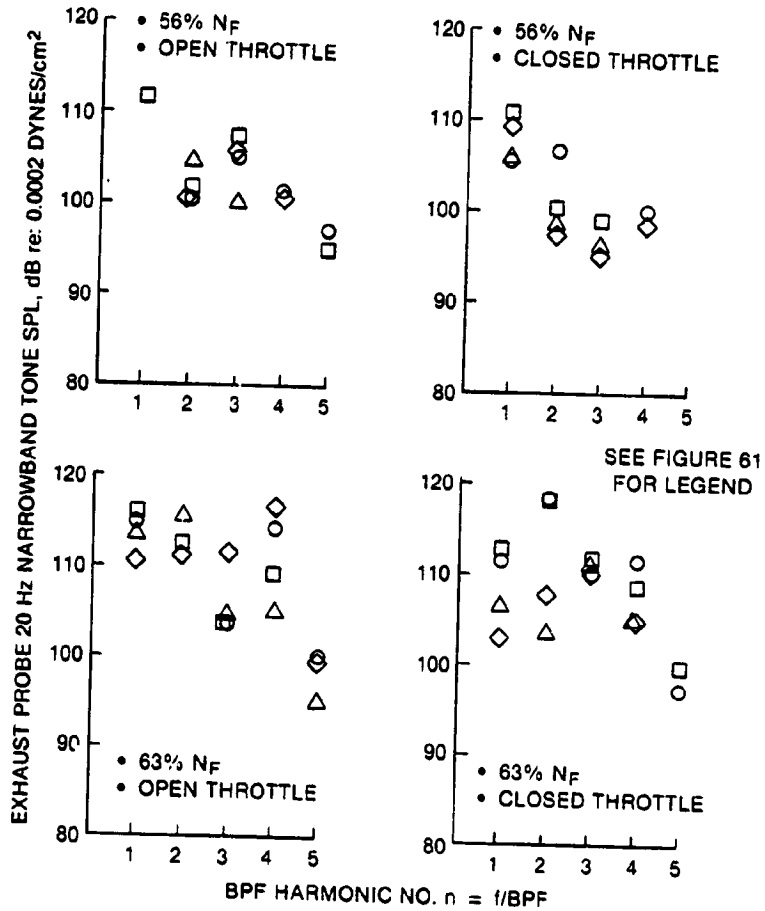

Figure 64. Aft Duct Probe Tone Harmonic Spectra 86-Vanes and S/C_R = 2.3.

7.2 Inlet Duct Transducer Spectra

Pressure transducers were mounted on the inlet casing annulus wall, shown in Figure 6 as sensors K5 and K6. Narrowband spectra were reduced from the signals of these sensors at 54%, 63%, 80% and 95% speed. The blade passage harmonic tone levels have been scaled from the spectra and are tabulated in Appendix B. Examples of typical inlet duct wall spectra are shown in Figures 77 through 80.

The K6 sensor is very close to the rotor tip leading edge and, therefore, its response is undoubtedly heavily influenced by the rotor steady flow pressure field which rotates with the rotor. Detailed analysis of this data was, therefore, not carried out, although the tone levels are tabulated in Appendix B for future reference. Examination of the tone levels (Appendix B) for the K5 sensor spectra revealed no consistent or sensible trend with spacing, so further analysis of this inlet duct data was abandoned.

7.3 Blade-Mounted Transducer Spectra

A blade-mounted rotating pressure transducer, designated as sensor K3 in Figure 6, was used in the tests performed in this program. However, reliable data was only obtained for the eighty-six vane, 0.5 spacing configuration. Blade-mounted transducer (BMT) signal data was processed for 54%, 63%, 69%, 76% and 80% speed for this configuration.

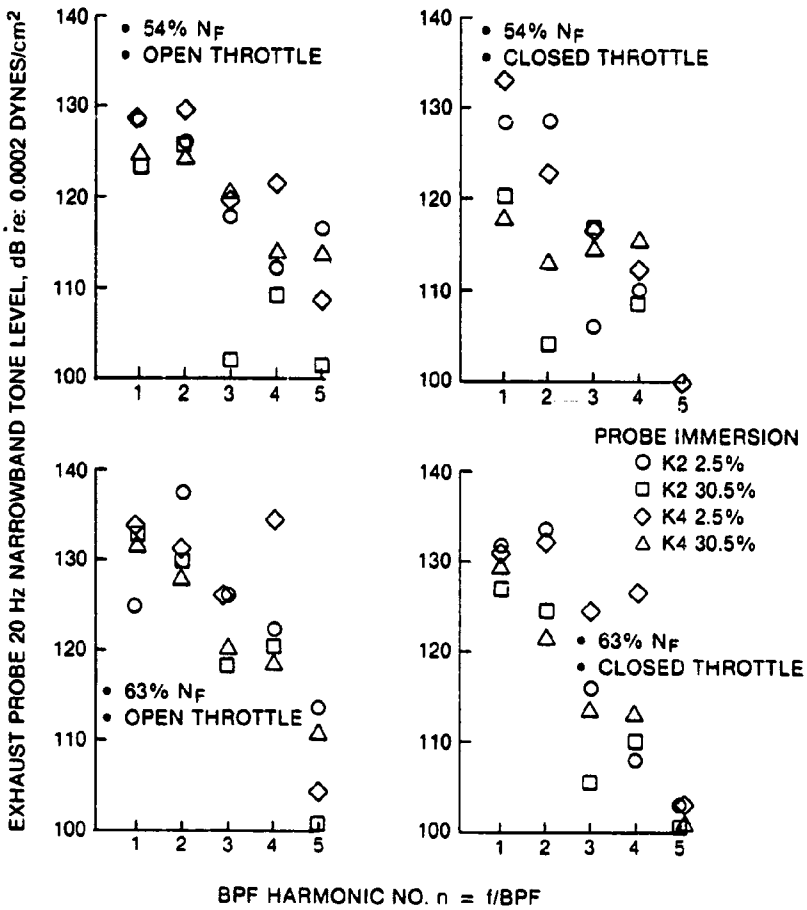

Figure 65. Aft Duct Probe Tone Harmonic Spectra 48-Vanes and $S/C_R = 0.5$.

The character of the blade-mounted transducer (BMT) harmonic spectra at 54% and 80% fan speed is displayed in Figure 81. A general observation is that the lower harmonics are much more prevalent at the higher speed condition. Also a distinct eighty-sixth harmonic occurs at both speeds, which is attributable to the potential field loading of the closely spaced eighty-six vane assembly on the rotor blade. The progression of lower frequency harmonic activity with fan speed is illustrated further in Figure 82, where BMT harmonic spectra at 63%, 69% and 76% fan speeds are shown. Note that Figure 81 is for the closed throttle setting of 1.35, whereas Figure 82 is for the open throttle setting of 0.95. Since both throttle settings suggest similar lower order harmonic behavior, this trend is believed to be relatively independent of throttle setting. The cause of this increase in lower order harmonic strength is not directly known; however, since it occurs over a range of harmonics, it may be due to inflow turbulence/distortion components. At low fan speeds, which characterize lower flow rates through the turbulence control structure, very little low frequency harmonic activity is observed. However, at higher fan speeds and higher flow rates, more low frequency activity is observed. The waveform from which the harmonic spectra were generated is obtained in the conventional manner of averaging the local signal until a representative steady circumferential pattern is attained. An example of the BMT waveform is displayed in Figure 83. The waveform again displays the information of the harmonic spectra as it shows slowly undulating lower frequency components with a strong eighty-sixth order component superimposed.

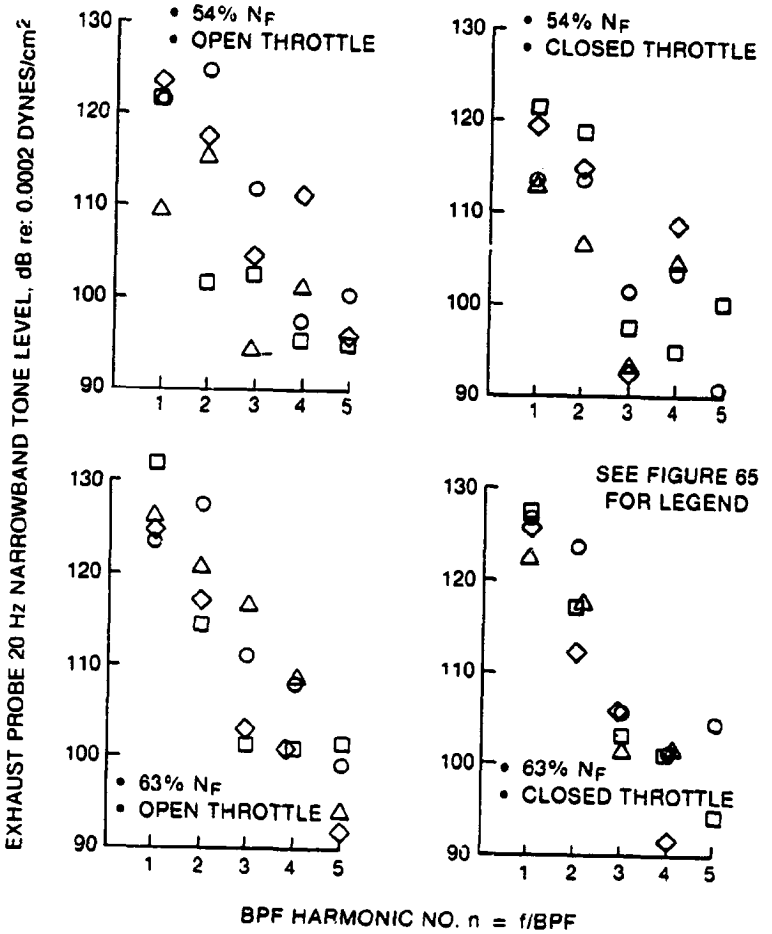

Figure 66. Aft Duct Probe Tone Harmonic Spectra 48-Vanes and $S/C_R = 1.27$.

The eighty-sixth order component is viewed as a potential noise generation mechanism for the second harmonic of the blade passage frequency (BPF) tone. The amplitude of eighty-sixth BMT harmonic component as a function of fan speed for open and closed throttle setting is shown in Figure 84. The amplitude scale of Figure 84 is in volts to magnify the differences observed; however, on a dB scale, the 63% speed eighty-sixth BMT harmonic was 9.5 dB lower for the closed throttle case compared to the open throttle operating condition.

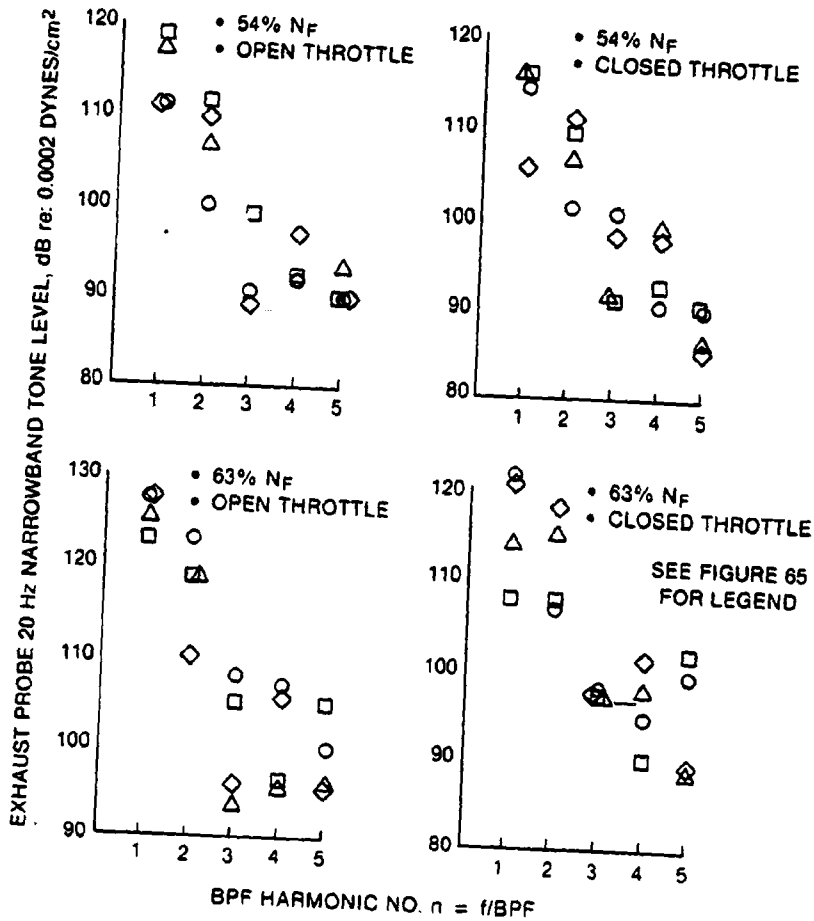

Figure 67. Aft Duct Probe Tone Harmonic Spectra 48-Vanes and $S/C_R = 2.3$.

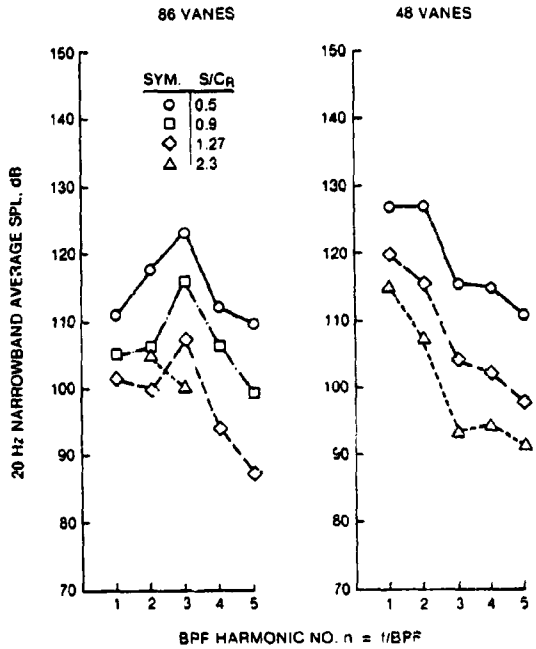

Figure 68. Effect of Axial Spacing on Aft Duct Tone Harmonic Spectrum, 54% N_F and Open Throttle.

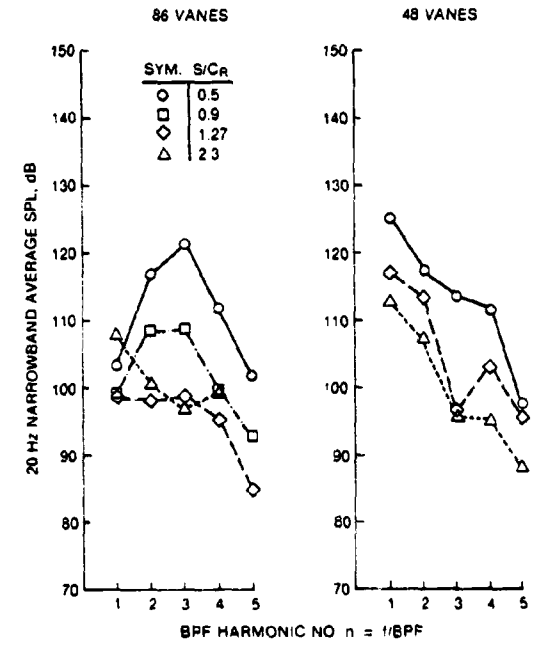

Figure 69. Effect of Axial Spacing on Aft Duct Tone Harmonic Spectrum, 54% N_F and Closed Throttle.

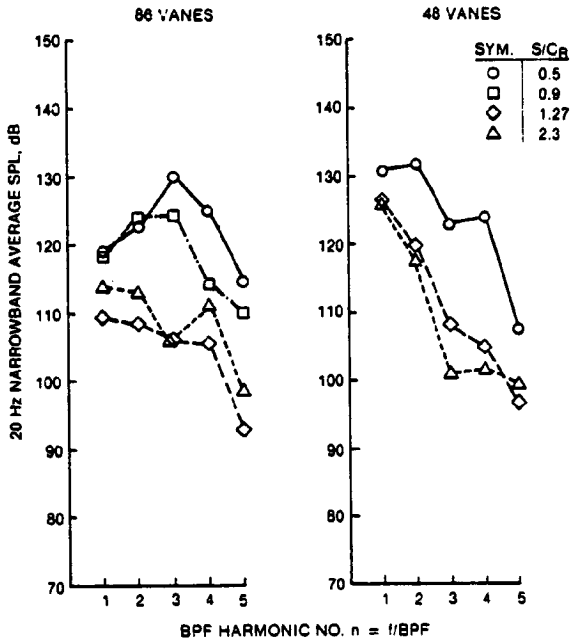

Figure 70. **Effect of Axial Spacing on Aft Duct-Tone Harmonic Spectrum, 63% N_F and Open Throttle.**

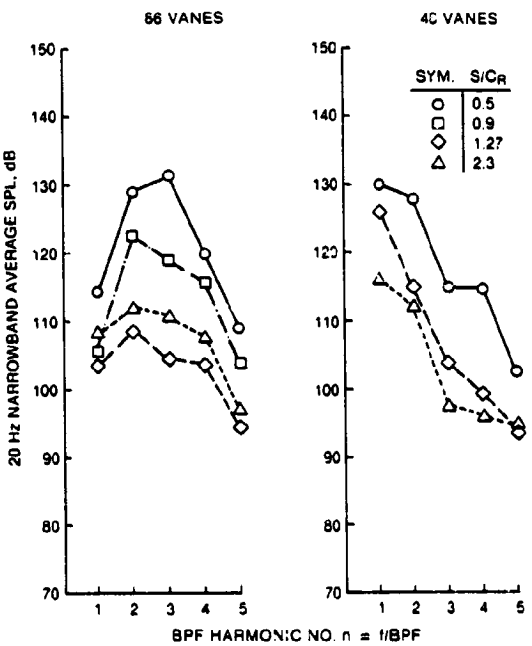

Figure 71. **Effect of Axial Spacing on Aft Duct Tone Harmonic Spectrum, 63% N_F and Closed Throttle.**

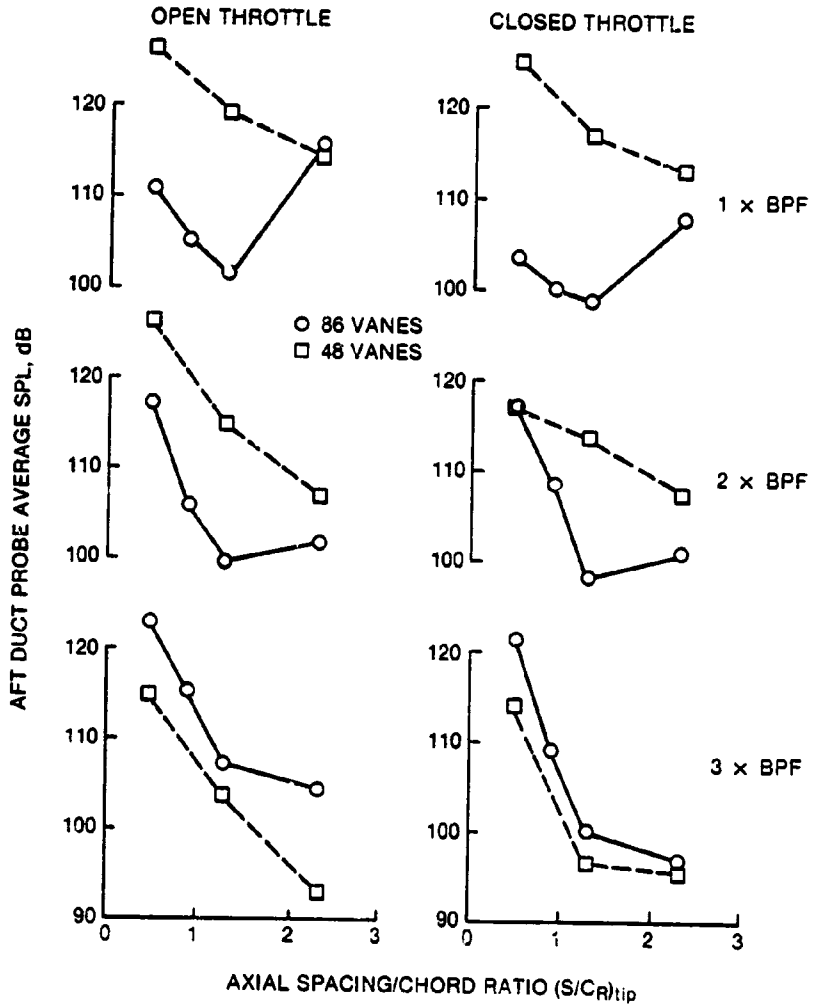

Figure 72. Aft Duct Probe Average SPL vs. Spacing Trends at 54% Speed.

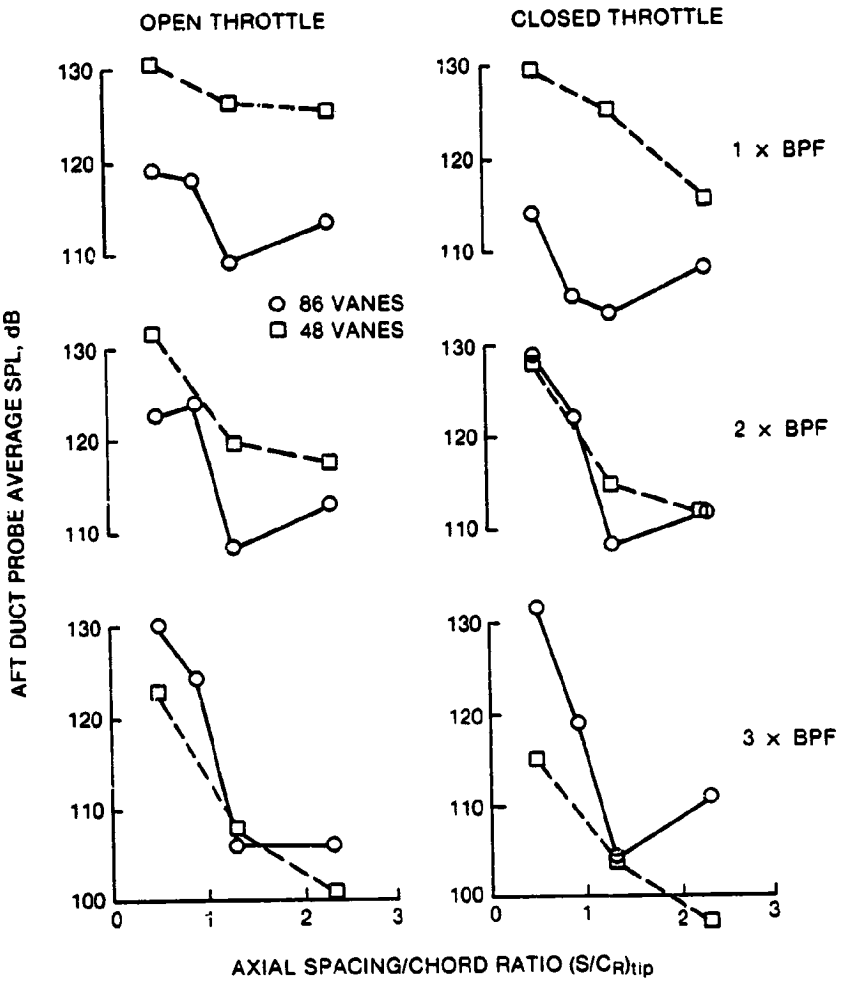

Figure 73. Aft Duct Probe Average SPL vs. Axial Spacing Trends at 63% Speed.

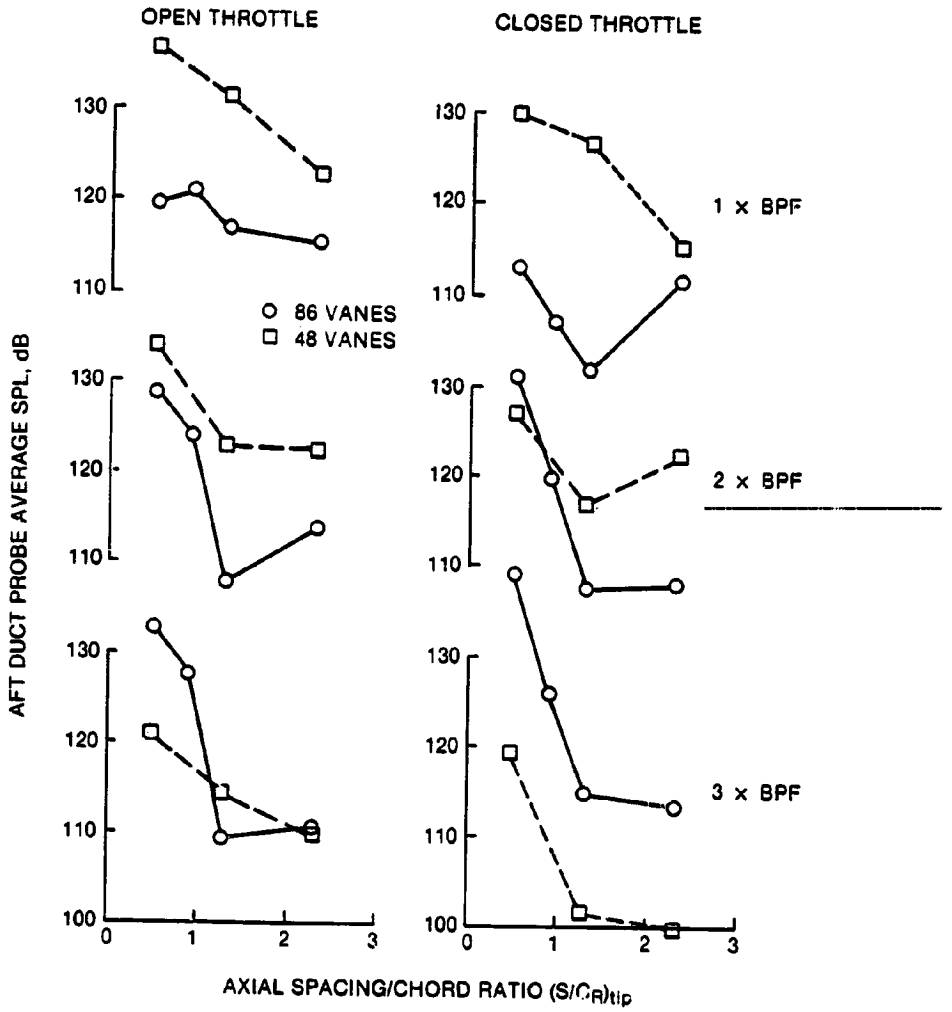

Figure 74. **Aft Duct Probe Average SPL vs. Axial Spacing Trends at 69% Speed.**

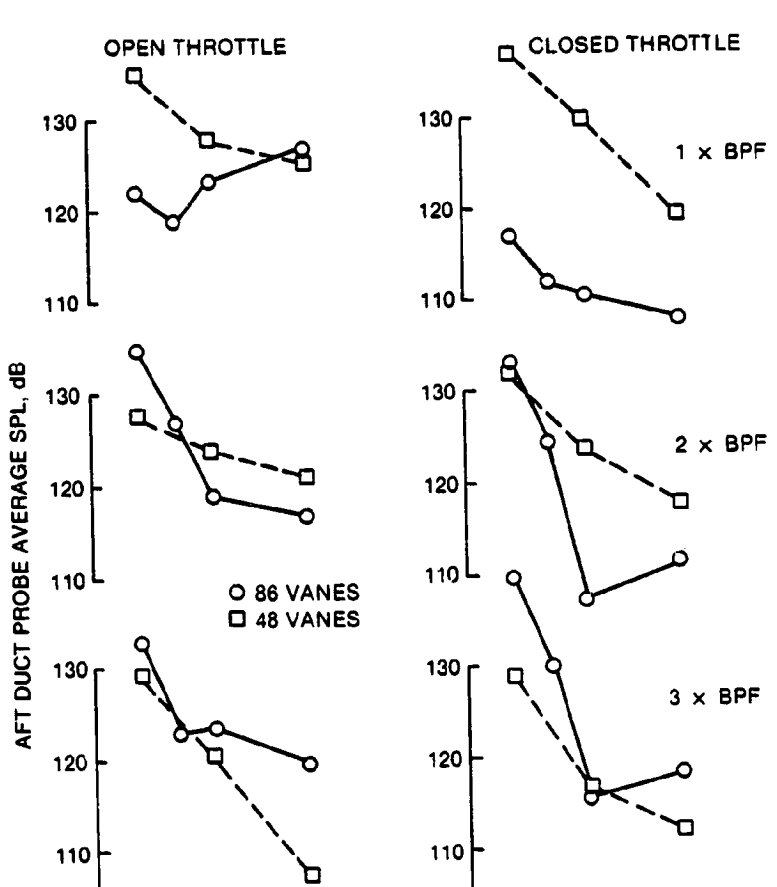

Figure 75. Aft Duct Probe Average SPL vs. Axial Spacing Trends at 76% Speed.

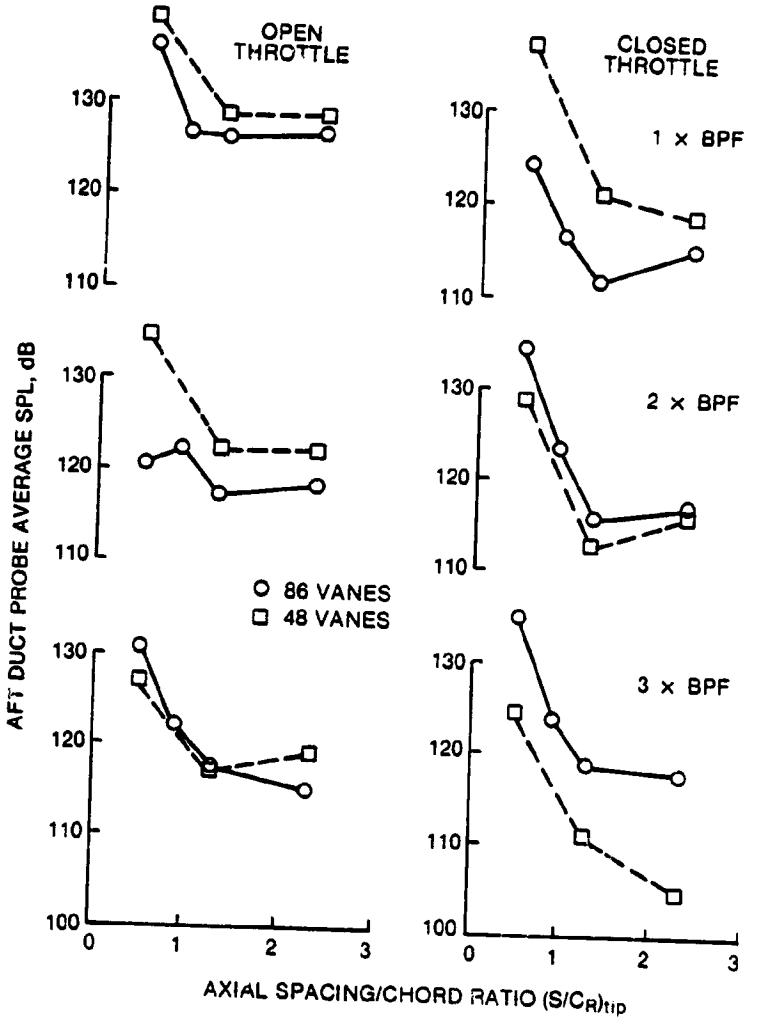

Figure 76. **Aft Duct Probe Average SPL vs. Axial Spacing Trends at 80% Speed.**

(a) S (a) $S/C_R = 0.5$

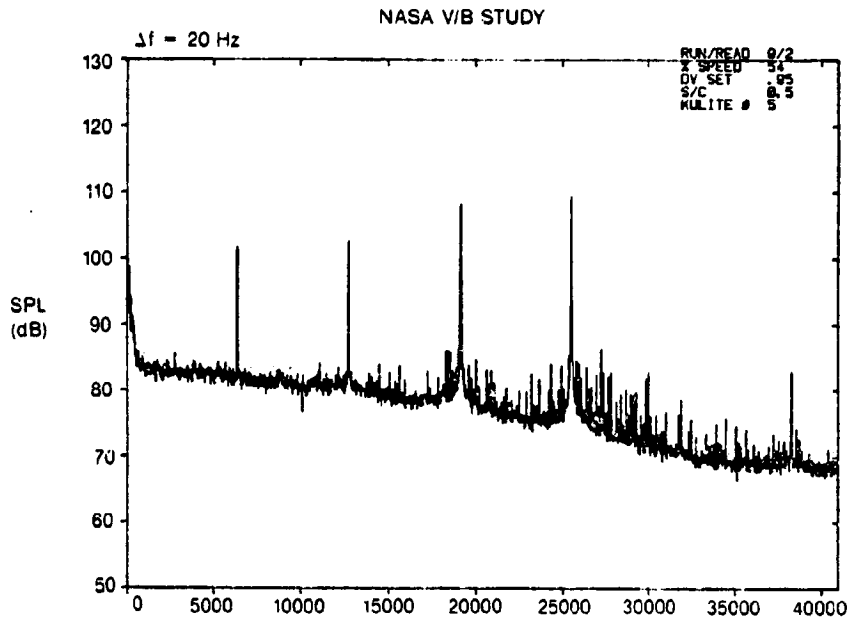

(b) $S/C_R = 2.3$

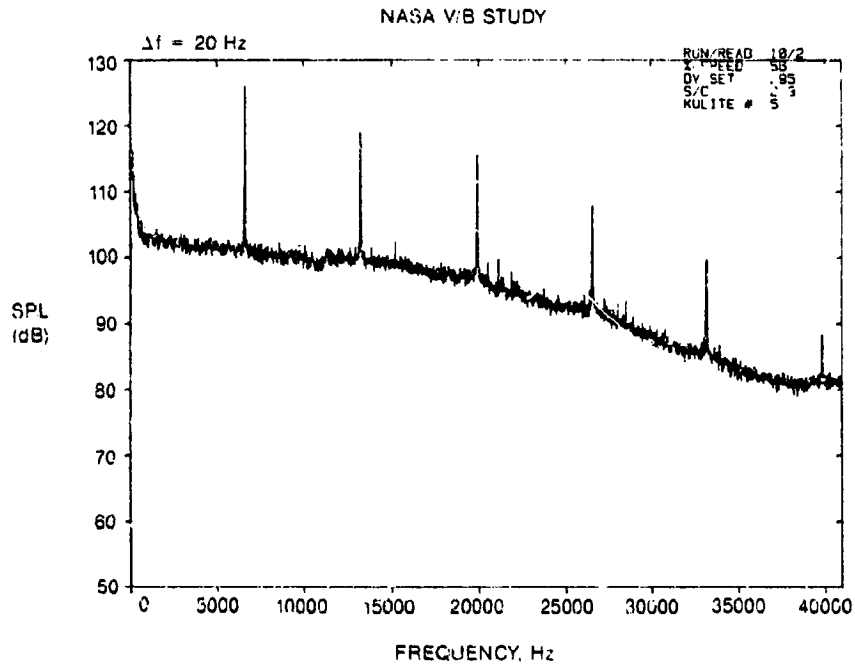

Figure 77. Inlet Duct Wall SPL Spectra for Sensor K5, 86-Vane Configuration at 54% N_F and Open Throttle O/L.

(a) $S/C_R = 0.5$

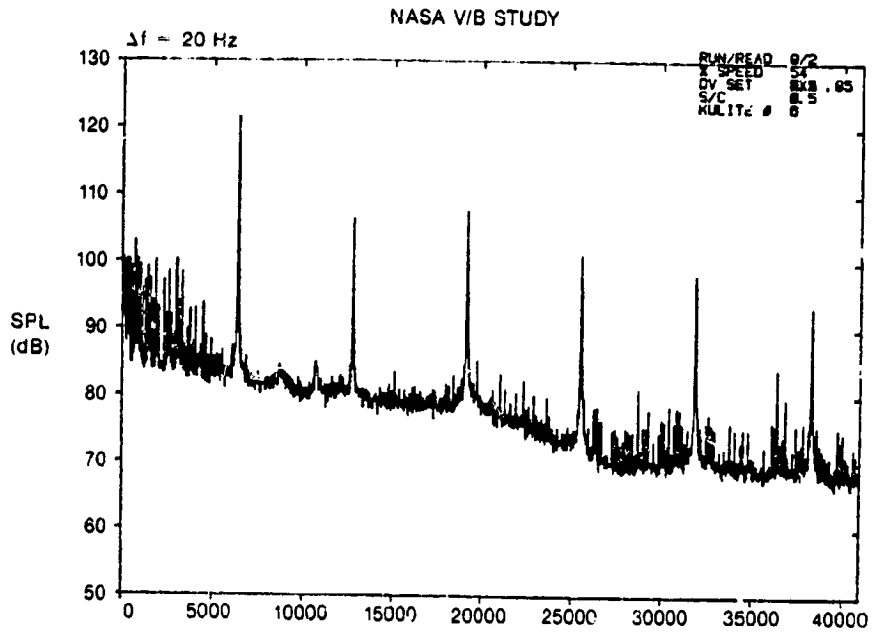

(b) $S/C_R = 2.3$

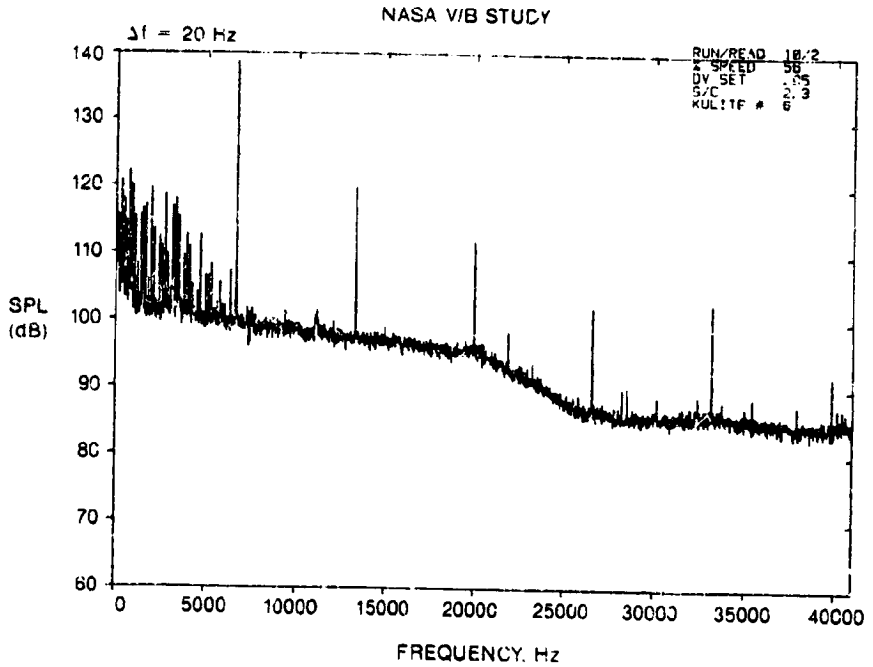

Figure 78. Inlet Duct Wall SPL Spectra for K6 Sensor, 86-Vane Configuration at 54% N_F and Open Throttle C/L.

(a) $S/C_R = 0.5$

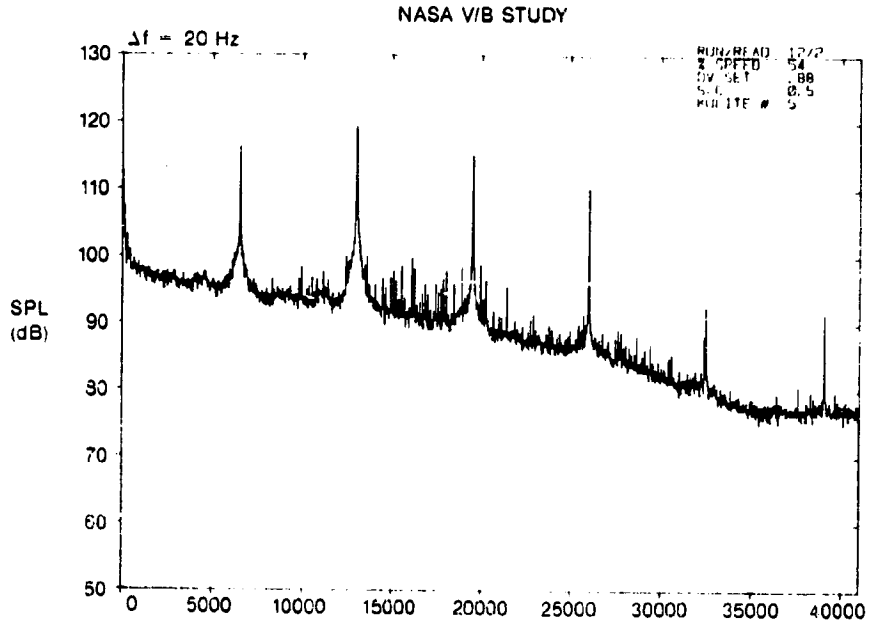

(b) $S/C_R = 2.3$

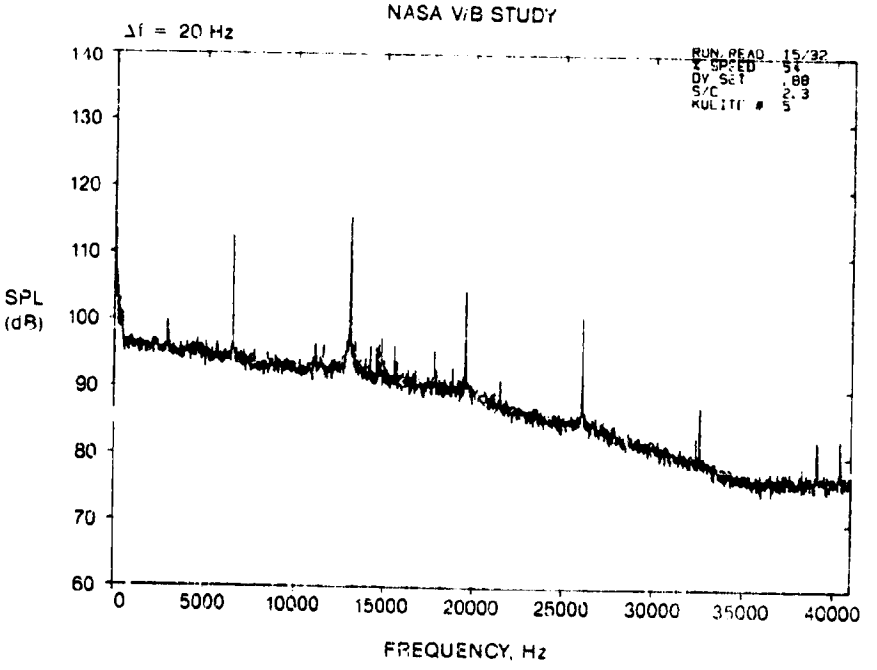

Figure 79. Inlet Duct Wall SPL Spectra for K5 Sensor, 48-Vane Configuration at 54% N_F and Open Throttle O/L.

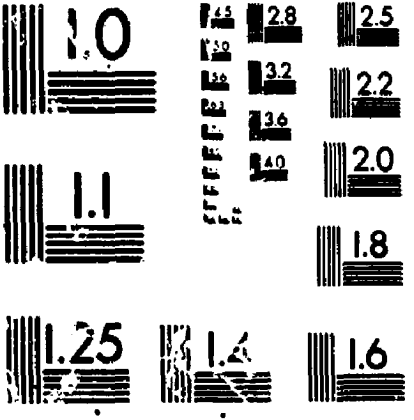

MICROCOPY RESOLUTION TEST CHART
NATIONAL BUREAU OF STANDARDS
STANDARD REFERENCE MATERIAL 1010a
(ANSI and ISO TEST CHART No. 2)

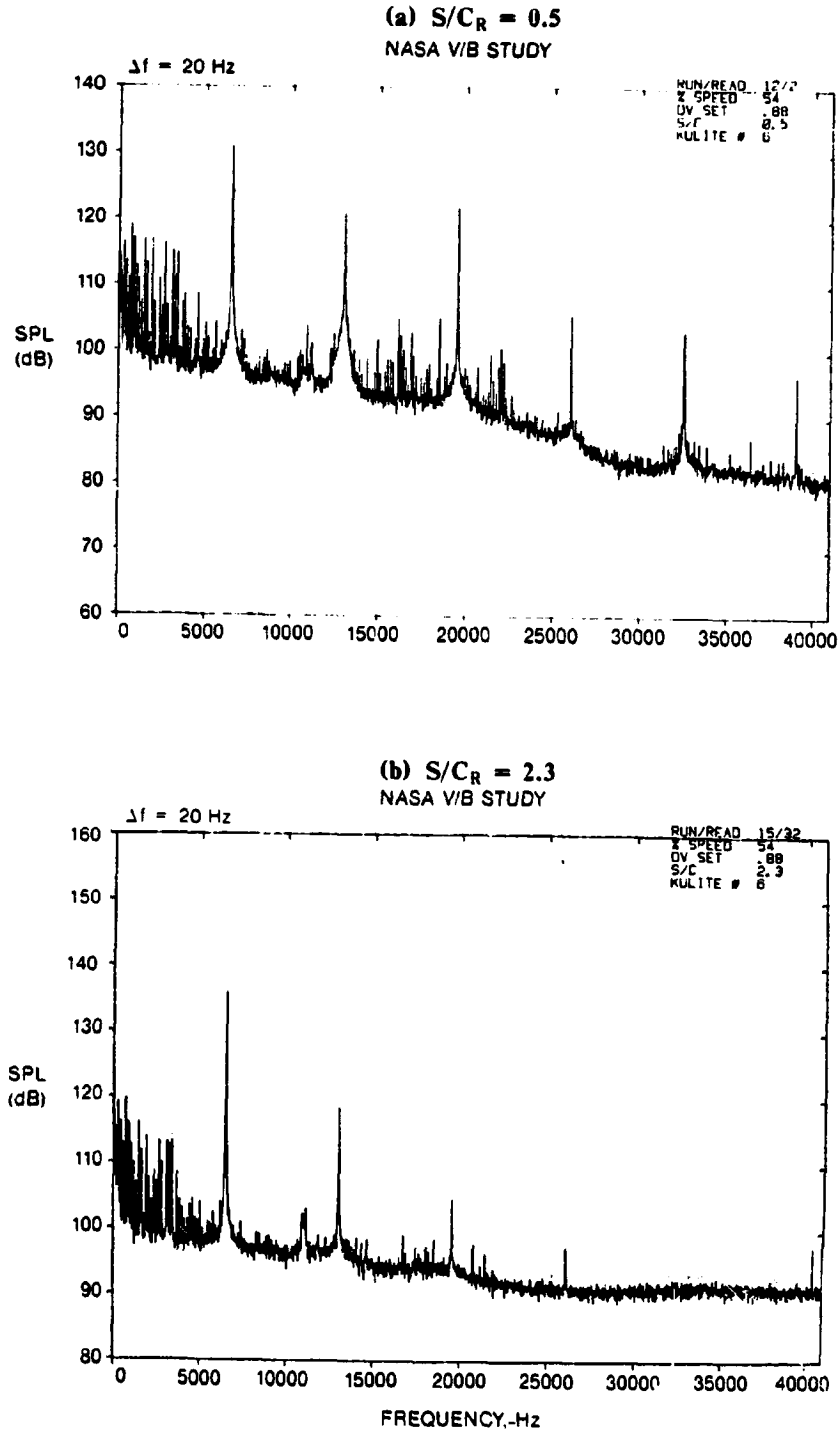

Figure 80. **Inlet Duct Wall SPL Spectra for K6 Sensor, 48-Vane Configuration at 54% N_F and Open Throttle O/L.**

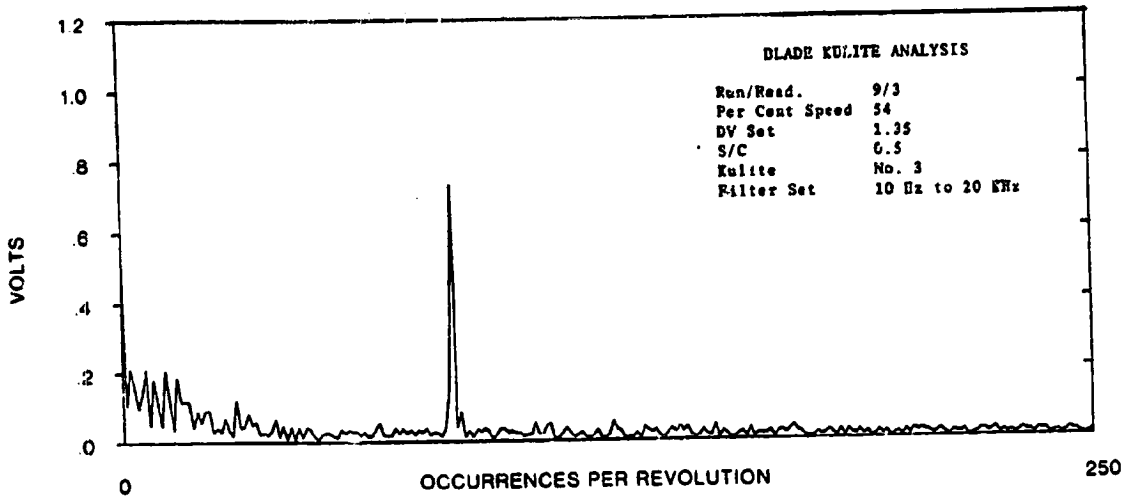

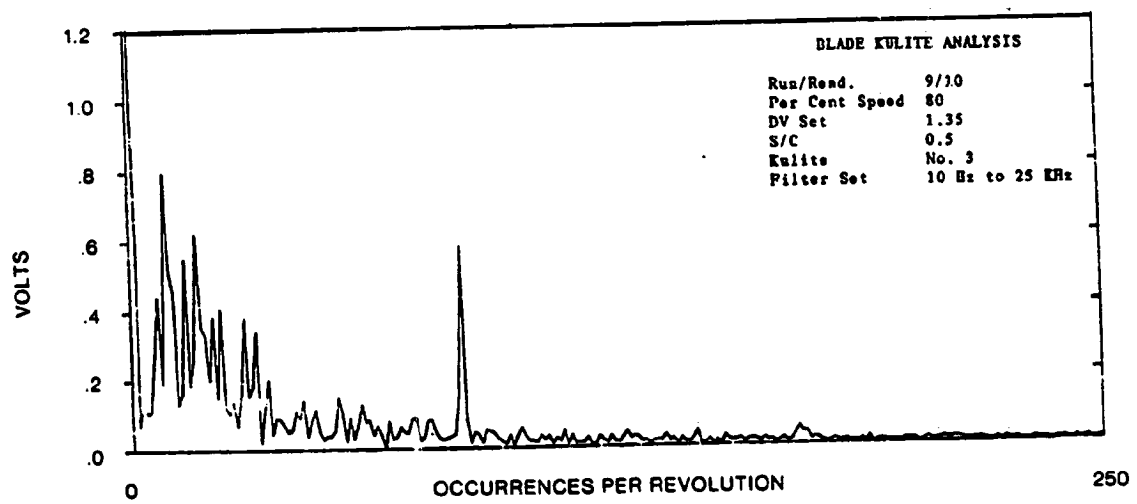

Figure 81. Blade Mounted Transducer Harmonic Spectra for 54 and 80% Speed.

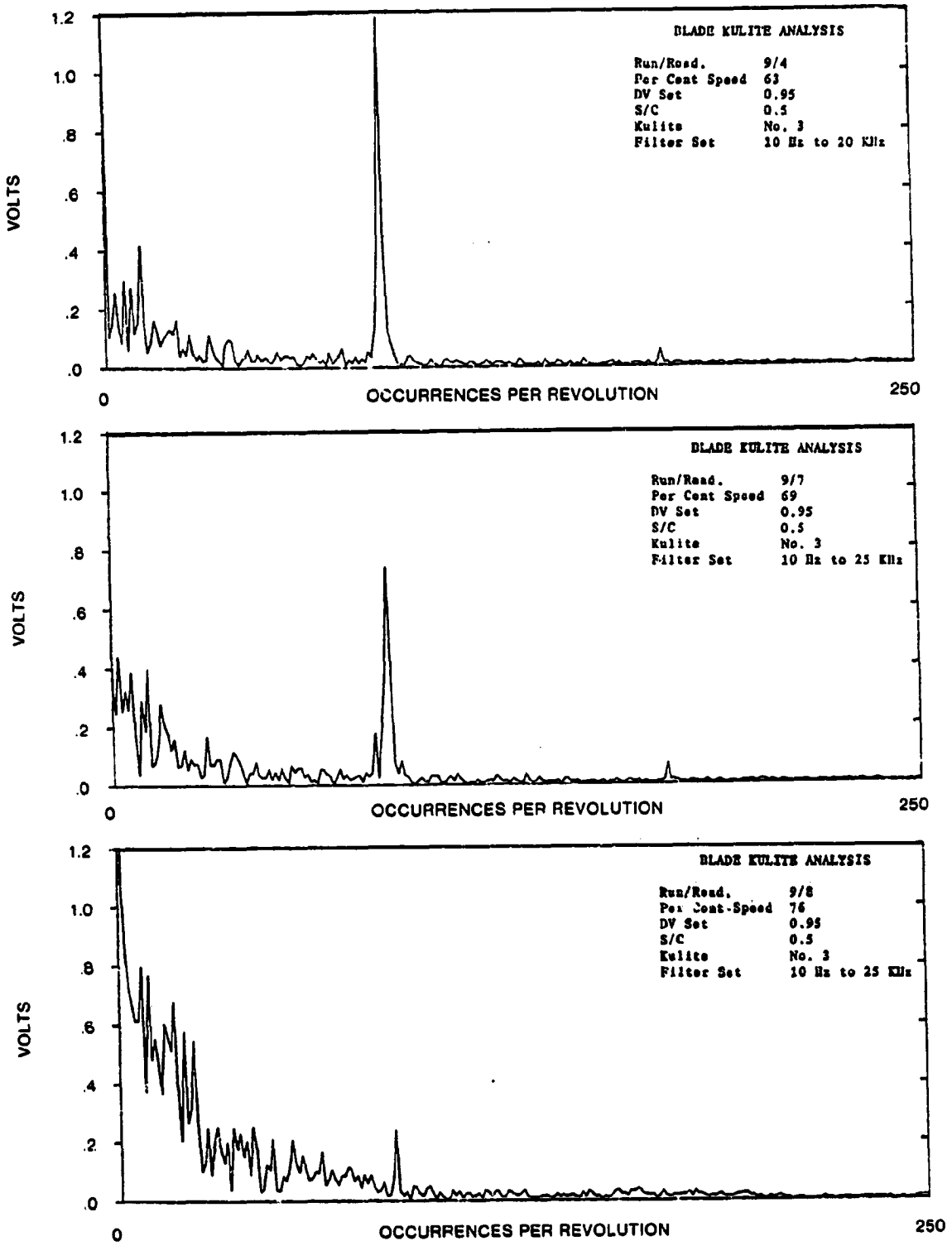

Figure 82. Blade Mounted Transducer Harmonic Spectra for 63, 69, and 76% Speed.

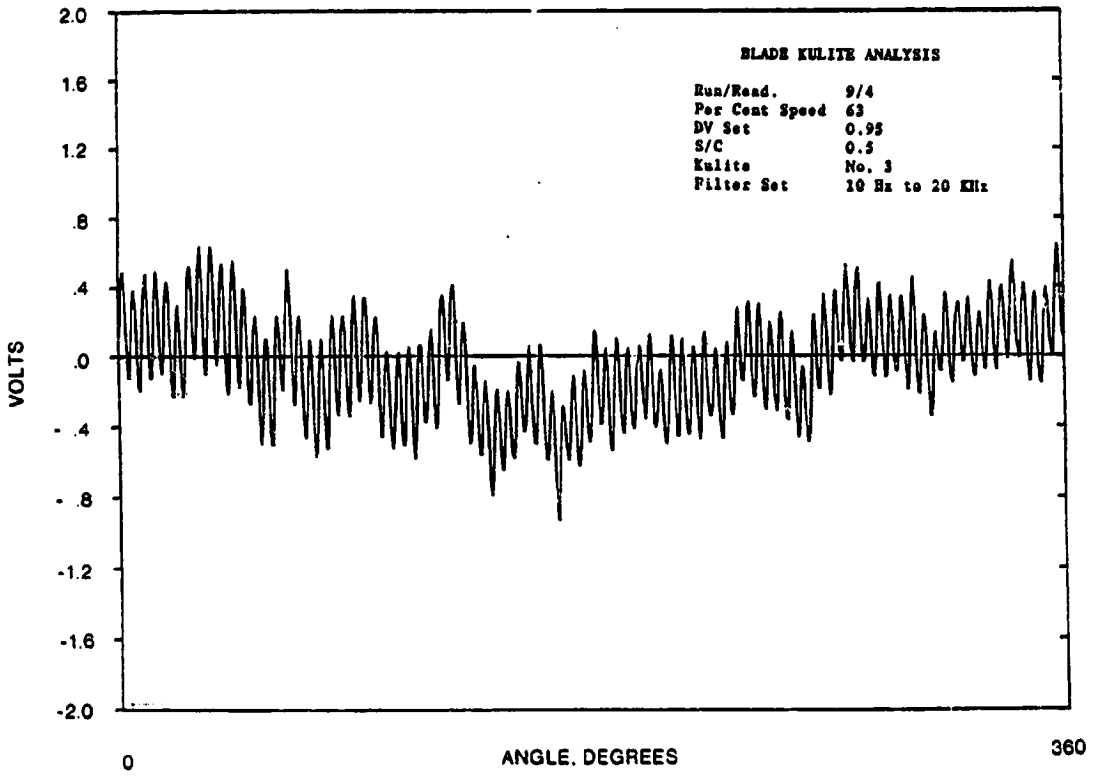

Figure 83. Representative Blade Mounted Transducer Circumferentially Averaged Waveform.

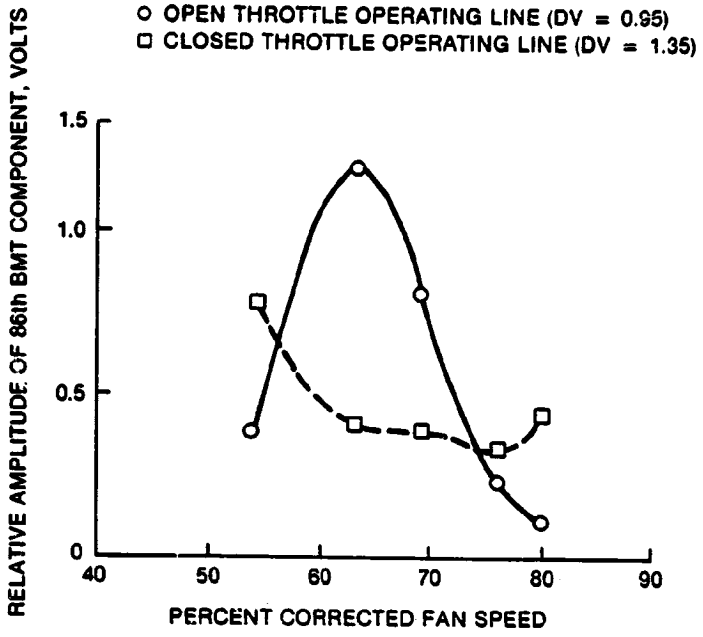

Figure 84. Blade Mounted Transducer 86th Harmonic Amplitude Results.

Section 8

ROTOR-STATOR NOISE ANALYTICAL MODEL DESCRIPTION

8.1 Noise Source Mechanisms

The rotor-stator tone interaction noise model utilized for predictions to compare with measurements is based on a simplified, two-dimensional analysis of the blade row interaction mechanisms, coupled to a compatible two-dimensional acoustic radiation model. The model can predict the in duct acoustic power level radiated upstream and downstream of a rotor-stator stage at blade passing frequency and its harmonics. Four interaction mechanisms are considered in this model as follows:

1. *Stator Potential Field-Rotor Interaction* — Interaction noise produced by the steady pressure field around the stator vanes, due to vane loading, interacts with the upstream rotor. Unsteady blade forces are produced on the rotor and the rotor becomes the noise producing source.
2. *Rotor Potential Field-Stator Interaction* — Interaction noise produced by the steady pressure field (in a rotating reference frame) around the rotor blades due to blade loading, interacts with the downstream stator. Unsteady vane forces are produced on the stator and the stator becomes the noise producing source.
3. *Rotor Vortex-Stator Interaction* — The unsteady forces produced on the rotor by the stator potential field (first mechanism) results in regular, periodic vortices being shed from the rotor blade trailing edges and these shed vortices interact with the downstream stator to produce unsteady vane forces. The stator vanes become the noise source.
4. *Rotor Wake-Stator Interaction* — The viscous wakes shed by the rotor blades appear as a periodic gust to the stator vanes producing unsteady vane forces and hence, tone noise. The stator is the noise source.

The first two mechanisms are thought to be small for rotor-stator axial spacings greater than half of a rotor chord. The third mechanism is a second order effect of the first and hence is probably negligible. The fourth mechanism is thought to be the dominant one for most fan stage applications. All four mechanisms are retained in the prediction model, however, so that a quantitative assessment of their relative contributions to the total interaction generated tone levels can be made for the fan stages for which measurements have been made.

In order to simplify the computations, it has been assumed that each of the four mechanisms produces tone levels independent of the others, i.e., the relative phasing between any two mechanisms is ignored; and the contributions from each mechanism are summed on a mean square pressure or acoustic power basis. This assumption was felt reasonable in view of the approximations made in modeling the individual mechanisms themselves. Figure 85 illustrates the above described four mechanisms of rotor-stator interaction.

A theoretical model of the above mechanisms was originally formulated by Kemp and Sears [7, 8] for two-dimensional, incompressible cascades. The Kemp-Sears theory was later extended to compressible, subsonic flows by Osborne [9]. These models provided theoretical estimates of the unsteady lift forces produced on the excited blade row due to the interaction mechanisms described above for a stator-rotor stage. The tone noise radiated from a blade row due to periodic unsteady forces on the blades was analyzed by Mani [10] for a two-dimensional flat plate cascade.

The present rotor-stator interaction tone noise prediction model is based on the theories of References 7 through 10 with several modifications. The expressions given in [9] for the interaction-induced unsteady lift forces were first revised to apply to rotor-stator (rather than stator-rotor) stages. Also, in

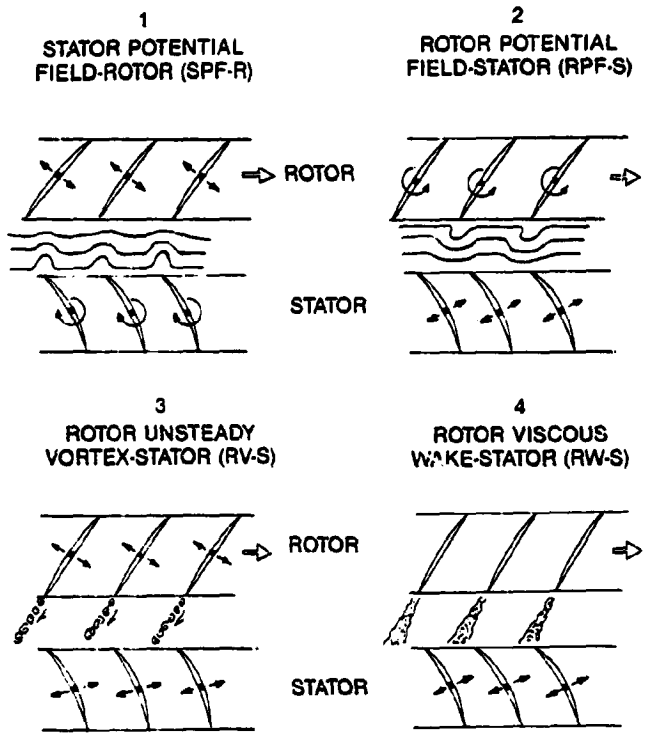

Figure 85. Illustration of Rotor/Stator Interaction Tone Noise Generation Mechanisms.

order to reduce the computational complexity and execution time, simplified approximations to the expressions given in [9] were derived by making use of the limiting forms of Bessel functions in the limits of small and large arguments. These approximations resulted in a considerable savings in computer program size and execution time with only a few percent change in unsteady lift amplitude prediction relative to the "exact" expressions given in [9]. Since the expressions given in [9], particularly for the potential field interactions, were based on an idealized point source model of the potential field, more precise estimates were not really warranted in view of the effort involved to do so.

The unsteady lift response function utilized in the viscous wake interaction mechanism of [9] is a so-called "low frequency" response function in that it was derived from a compressible theory which assumes that a certain reduced frequency parameter Ω is appreciably less than unity, where Ω is defined as $\Omega = \omega/\beta^2$, and where $\omega = \nu c/2V$. In the above, ω is the reduced frequency; ν is the dimensional radian frequency of the disturbance incident upon the blade or airfoil of interest; c is the blade chord; V is the average or mean velocity of the flow incident upon the blade; β is a compressibility parameter $\beta = \sqrt{1 - M^2}$; and M is the incident Mach number V/c_0, where c_0 is the freestream speed of sound. For a typical fan stage with N_B rotor blade wakes impinging upon a stator row, Ω is on the order of 10 for the fundamental blade passing frequency excitation. The "low frequency" response function is, therefore, not really applicable and a so-called "high frequency" unsteady lift response function developed by Amiet [11] was substituted in the unsteady blade force calculation for cases where $\Omega >$ 1.

As described in [10] for a two-dimensional cascade of N_B blades interacting with a cascade of N_V vanes, acoustic spinning modes are generated at frequencies which are multiples of blade passing frequency ν_B. The n^{th} harmonic of ν_B will have a spinning mode lobe number m given by

$$m = nN_B - kN_V \tag{1}$$

where k is any integer. In order for a given mode of frequency $n\nu_B$ and lobe number m to propagate upstream and downstream of the duct unattenuated, it must satisfy the duct mode cut-on criterion

$$(nN_B - m\theta)\ M_t > m\sqrt{1 - M_a^2} \tag{2}$$

Thus for given values of n, N_B, and flow parameters M_a, M_t (the centerline value of the strip being used) , and θ (the normalized swirl Mach number), only certain modes can propagate, corresponding to permissible values of k. The range of permissible values of k that produce propagating modes in can be shown to obey the inequality

$$\left[\frac{nN_B}{N_V}\right]\left[1 - \frac{M_e}{1 + \theta M_e}\right] < k < \left[\frac{nN_B}{N_V}\right]\left[1 + \frac{M_e}{1 - \theta M_e}\right] \tag{3}$$

where

$$M_e = \frac{M_t}{\sqrt{1 - M_a^2}}$$

For each of the mechanisms previously described, the resulting unsteady blade or vane lift force of amplitude F_m will then produce a spinning acoustic mode of intensity I_m^+ (upstream) and I_m^- (downstream) of the form

$$I_m^{\pm} = \frac{F_m^2}{2\rho_0 c_0}\,\eta^{\pm} \tag{4}$$

where $\eta^{\pm}$ is the acoustic duct radiation efficiency in the upstream (+) and downstream (−) directions for the acoustic mode generated and depends upon the frequency and lobe number of the acoustic mode as well as the flow parameters M_a, M_t, and θ in the duct as discussed in [10], and given by Equations (22-28) of Reference [10].

It may be noted that for $\theta > 0$, i.e., when there is mean swirl upstream of the stator and downstream of the rotor, it is possible for a given mode to be propagating upstream of a blade row and be cut-off or decaying exponentially with axial distance downstream of the blade row or vice versa. It has been observed in certain predictions, for example, that stator-generated modes sometimes decay in the downstream direction but propagate in the upstream direction where high levels of swirl are present, only to be cut-off or reflected in the process of being transmitted through the upstream rotor.

The expected cut-on circumferential modes for the configurations tested in this program have been calculated using Equations (1-3). The modes that propagate upstream of the rotor ($\theta = 0$) have been calculated for 1X BPF, 2X BPF and 3X BPF at each of the speeds tested. These expected modes are listed in Tables 3 (48-vane) and 4 (86-vane). At the bottom of these tables, the value of k which corresponds to each of the modes, is also listed. Note that k = 0 corresponds also to rotor-alone pressure field radiation. It is also observed that the 48-vane configuration (Table 3), in addition to having a cut-on 1X BPF tone at subsonic tip speeds, also has more cut-on modes contributing to 2X BPF and 3X PF than does the 86-vane configuration (Table 4).

To account for transmission loss of acoustic energy through the rotor cascade for upstream propagating modes generated by the stator cascade, a transmission loss model for upstream propagating waves through a rotating cascade was developed using an actuator disk approximation model of the rotor similar to the semiactuator disk model of Kaji and Okazaki [12]. The actuator disk approach was selected because it can be applied to blade rows with turning, which can be substantial in the hub sections of a fan rotor. The actuator disk approximation does not exhibit any explicit dependence on sound frequency (wave number), but as shown in [12], this effect is relatively small on transmission loss, while the effect of blade row turning or loading is substantial.

One additional modification to the formulations for rotor-wake-stator interaction of [8-10] was made, consisting of incorporating a different rotor wake velocity deficit and wake width versus distance

Table 3

PREDICTED CUT-ON CIRCUMFERENTIAL MODE NUMBERS (m) FOR 48-VANE CONFIGURATION

%N_F	M_t	1 × BPF				2 × BPF				
54	0.682		−4				+40,	−8,	−56	
63	0.796		−4				+40,	−8,	−56	
69	0.876		−4				+40,	−8,	−56	
76	0.969	+44,	−4			+88,	+40,	−8,	−56	
80	1.022	+44,	−4			+88,	+40,	−8,	−56	
86	1.102	+44,	−4,	−52		+88,	+40,	−8,	−56,	−104
95	1.223	+44,	−4,	−52		+88,	+40,	−8,	−56,	−104
100	1.291	+44,	−4,	−52	+136*,	+88,	+40,	−8,	−56,	−104
	k =	0	1	2	−1	0	1	2	3	4

* These Modes are Cut Off for Closed-Throttle Operating Line

3 − BPF								
		+84,	+36,	−12,	−60			
		+84,	+36,	−12,	−60,	−108		
		+84,	+36,	−12,	−60,	−108		
	+132,	+84,	+36,	−12,	−60,	−108		
	+132,	+84,	+36,	−12,	−60,	−108		
	+132,	+84,	+36,	−12,	−60,	−108,	−156	
+180,	+132,	+84,	+36,	−12,	−60,	−108,	−156	
+180,	+132,	+84,	+36,	−12,	−60,	−108,	−156,	−204*
−1	0	1	2	3	4	5	6	7

Table 4

PREDICTED CUT-ON CIRCUMFERENTIAL MODE NUMBERS (m) FOR 86-VANE CONFIGURATION

%N_F	M_t	1 × BPF		2 × BPF			3 × BPF			
54	0.682	None			+2			+46,	−40	
63	0.796	None			+2			+46,	−40	
69	0.876	None			+2			+46,	−40	
76	0.969	+44,	−42	+88,	+2,	−84	+132,	+46,	−40,	−126
80	1.022	+44,	−42	+88,	+2,	−84	+132,	+46,	−40,	−126
86	1.102	+44,	−42	+88,	+2,	−84	+132,	+46,	−40,	−126
95	1.233	+44,	−42	+88,	+2,	−84	+132,	+46,	−40,	−126
100	1.291	+44,	−42	+88,	+2,	−84	+132,	+46,	−40,	−126
	k=	0	1	0	1	2	0	1	2	3

correlation. The new velocity deficit and wake width correlations were taken from the results of a study by Mugridge and Morfey [13] which was based on data for a wider range of airfoil types as well as cascade data. It was found from parametric study computation results that this wake model gave a much better prediction of harmonic spectrum shape than the Kemp-Sears model of [8] does. Details of the prediction model formulation used are given in Appendix A.

8.2 Computational Model Description

The computational procedure developed for predicting rotor-stator interaction tone noise utilizes a streamline-by-streamline evaluation sequence whereby the noise levels are calculated at several radial or spanwise locations along the blades, corresponding to axisymmetric streamlines in the fan flow path. Incremental annulus areas are assigned to each streamline and the tone acoustic power levels computed from each streamline are then summed to give the total acoustic power generated and radiated upstream and downstream of the fan stage. Figure 86 illustrates the streamline-by-streamline subdivision and evaluation procedure. On each streamline, the flow is characterized by an equivalent two-dimensional cascade rotor-stator stage model with an equivalent average axial Mach number M_a, tip speed Mach number, M_t, and rotor-stator gap swirl Mach number θM_t, as shown in Figure 86. The rotor wake development is characterized by the rotor drag coefficient C_{DR}, as discussed in [8] and [9]. The geometric parameters required are rotor and stator stagger angles γ_R and γ_S, rotor and stator solidities σ_R and σ_S, and rotor and stator blade and vane numbers N_B and N_V.

The basic rotor-stator computation scheme developed for the prediction of interaction tones is illustrated in Figure 87. A given fan stage flow path is subdivided into stream tube annuli as shown in Figure 86. The steady state aerodynamic parameters and blading geometry parameters are determined from prior calculations and/or experimental measurements. For each streamline, the unsteady blade and/or vane forces are evaluated using the previously described modifications of the Osborne theory [9]. This evaluation is done for each frequency or blade passing harmonic of interest for each of the four interaction sources at all cut-on modes which abide by the criterion of Equation 3. For each

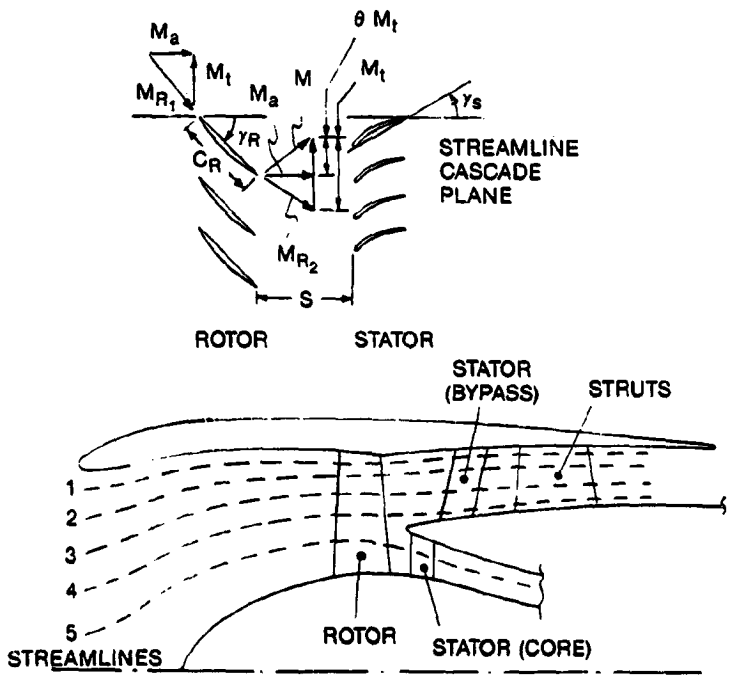

Figure 86. Illustration of Streamline-by-Streamline Analysis of Rotor/Stator Interaction Noise.

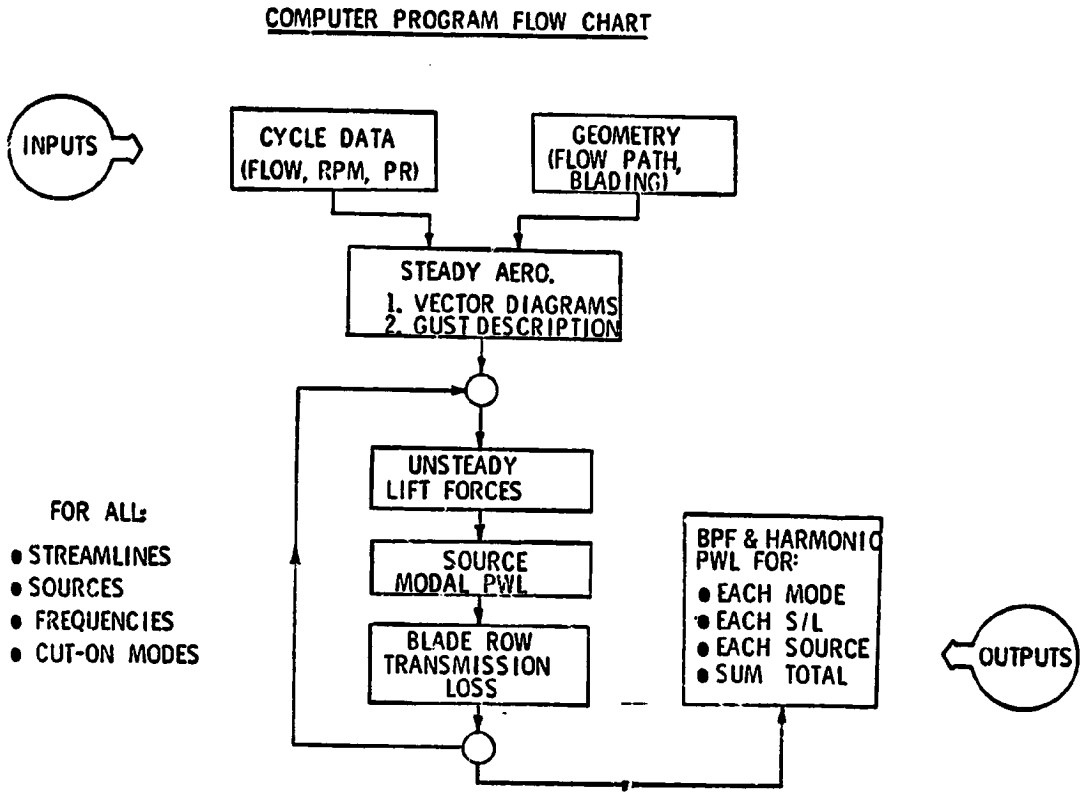

Figure 87. Rotor/Stator Tone Noise Prediction Computer Program Flow Chart.

stator-generated upstream propagating mode, a transmission loss factor is applied as described above. The contributions from all sources are then summed (on a sound power basis) to give the total power in a given mode, and the acoustic power in all propagating modes are then summed to give the total power at a given harmonic produced by a given stream tube or annular increment. Finally, a summation is made over all stream tubes to yield the total tone power in each mode and summed over all modes.

The above analytical model approach is one step higher in sophistication compared to a straightforward two-dimensional calculation carried out at some effective radius in the fan annulus. It does provide some accounting for the radial or spanwise variations in acoustic source strengths, which may result from the existing radial variations in blade geometry, mean flow vector diagram parameters, loadings, and wake properties. As such, it should provide useful evaluations of the spanwise variation in the source noise. It cannot, however, provide a truly three-dimensional sound field prediction in the fan duct since phase relationships along the span are ignored in the present model. Nevertheless, it is expected to provide reasonable estimates of total tone acoustic power and should predict the correct trends for variations in rotor-stator axial spacing and vane number.

8.3 Rotor-Stator Interaction Tone Predictions

Predictions were made of the rotor-stator interaction tones for the Rotor 11 fan stage vane/blade ratio and axial spacings tested utilizing the analytical model described in the previous section. The aerodynamic parameters required as input to the prediction model were derived from the aerodynamic performance measurement data reported in [6]. The aerodynamic performance measurements reported in

[6] were made on a configuration consisting of Rotor 11 (forty-four blades) and a forty-eight vane stator row at approximately 0.5 rotor chord axial spacing. It was assumed, since no additional data was available, that the rotor aerodynamic performance remained unchanged for the other vane number/spacing configurations tested in the present program.

The fan flow path was subdivided into five annuli, with midradius locations at 10%, 30%, 50%, 70%, and 90% of immersion from the casing. Input values of M_a, M_t, θ and C_{DR} (rotor drag coefficient) were derived from interpolation of the aerodynamic traverse data as a function of corrected fan speed and rotor inlet flow coefficient. C_{DR} was calculated from measured total pressure loss coefficients. It was found that the radial variation in axial Mach number M_a was very small at the part-speed conditions of interest (54% to 80% N_F), and it was also found that M_a did not vary appreciably in the axial direction either. Values of M_t, θ and C_{DR} evaluated at the rotor exit were used for prediction model input. The rotor loading coefficient θ was found to vary considerably from hub to tip but was relatively invariant with fan speed for a given throttle (DV) setting. In going from open throttle to closed throttle, the axial Mach number M_a decreases, while both swirl coefficient θ and rotor drag coefficient C_{DR} increase.

Calculations of rotor-stator interaction tone levels were carried out for the Rotor 11 twenty-inch-diameter fan stage (forty-four blades) for 54%, 63%, 69%, 76%, and 80% corrected speed. Results for forty-eight vanes are given in Tables 5 and 6, while results for eighty-six vanes are given in Tables 7 and 8. Results for both open throttle (DV = 0.95) and closed throttle (DV = 1.35) are given. For each vane number and throttle setting, results have been computed at nominal rotor-to-stator spacings of 0.5, 0.9, 1.27, and 2.3 rotor chords.

It was found that the rotor viscous wake-stator interaction was by far the dominant mechanism for all of the cases computed. The stator potential field/rotor interaction mechanism ranked second, but was on the order of 50 dB lower in resultant noise level than that of the viscous wake interaction. A comparison of predicted source contributions to tone harmonic levels for the closest rotor-stator spacings tested ($s/c_R = 0.5$) are given in Table 9 for the streamline closest to the hub, 90% immersion. For this configuration, the noise sources are predicted to be strongest at the hub and typical variations of tone PWL versus spanwise position are shown in Figure 88.

The noise source distributions shown in Figure 88 indicate a strong hub dominance in both forward and aft-radiated noise. This is due to the higher unsteady lift forces created near the hub because of higher rotor drag coefficient, shorter spacing-to-chord ratio and higher relative velocity into the stator (because of larger swirl at the hub).

8.4 Rotor Transmission Loss Analytical Study

The Fan Source Noise Acoustics Prediction Computer Program was used to study the effect of rotor transmission loss on the predicted rotor-stator interaction forward radiated noise levels for the Rotor 11 stage configurations tested in this program.

Calculations of rotor-stator interaction noise tone power levels for the first five harmonics were carried out with the rotor transmission loss and without the rotor transmission loss. The difference in upstream radiated tone power levels with, and without, transmission loss effects represents the influence of rotor transmission loss itself. The effective rotor transmission loss was computed as a function of rotor tip speed Mach number, and is plotted in Figures 89 through 92. Note that the net transmission loss cannot be obtained by merely computing a transmission loss from the transmission loss model or subroutine, because the tones are comprised of several spinning modes, each having a particular amplitude relative to the total level, and each having its own transmission loss (and spanwise distributions of same).

Figure 89 shows the net transmission loss versus tip speed Mach number characteristics for the 48-vane stator on the open throttle operating line. These results show that the transmission loss is relatively constant, approximately 5-7 dB, for the higher harmonics $\eta \geq 2$ for subsonic tip speeds. For $M_t \geq 1.0$, a gradual rise in tone transmission loss is predicted, reaching 10 dB at $M_t = 1.3$. The fundamental tone (n = 1) has a relatively small transmission loss of about 2-3 dB for $M_t < 0.9$, and then

Table 5

PREDICTED ROTOR/STATOR TONE PWL 48 VANES
$(S/C)_{nom.}$ = 0.5 and 0.9

				Upstream			Downstream		
V	S/C	DV	%N	n = 1	2	3	1	2	3
48	0.5	0.95	54	125.7	128.4	117.6	136.9	136.0	121.9
		(OP)	63	127.2	131.9	119.0	137.4	140.0	127.8
			69	127.7	132.2	122.0	137.5	141.5	131.1
			76	128.0	134.6	124.6	142.4	141.4	134.7
			80	128.3	134.4	124.7	145.2	142.0	136.4
		1.35	54	131.1	124.6	113.4	139.6	134.5	113.9
		(CL)	63	132.1	129.6	116.1	139.9	139.4	121.8
			69	132.6	132.3	118.0	140.2	140.2	125.7
			76	132.7	132.7	122.1	140.1	141.4	130.2
			80	132.6	134.4	124.2	145.9	141.4	133.5
	0.9	0.95	54	124.5	124.9	110.6	135.8	132.5	114.4
		(OP)	63	126.0	128.7	112.1	136.3	136.8	121.6
			69	126.6	129.2	116.1	136.5	138.4	124.7
			76	127.0	131.7	118.7	141.5	138.5	128.8
			80	127.2	131.6	118.9	144.3	139.1	130.6
		1.35	54	129.3	118.7	105.7	137.8	129.0	105.3
		(CL)	63	130.4	124.4	108.2	138.3	135.1	112.5
			69	130.9	127.7	110.2	138.6	135.9	116.3
			76	131.2	128.7	114.6	138.7	137.7	121.9
			80	131.2	130.9	117.2	144.5	137.7	126.5

exhibits a rapid rise, as M_t exceeds 0.9, reaching a maximum value of 17 dB at M_t = 1.1. Figure 90 shows the transmission loss versus tip speed Mach number characteristics for the 48-vane stator configuration along the closed-throttle operating line. The qualitative trends are similar to those in Figure 89, but the levels are somewhat lower by 1-3 dB.

Corresponding transmission loss versus tip speed characteristics for the 86-vane stator configuration are shown in Figures 91 and 92 for the open-throttle and closed-throttle operating lines, respectively. For this configuration, both the first and second harmonic trends differ from those of the higher harmonics. First, the first harmonic has no value until $M_t > 0.93$, since this is the so-called cut-off stator design. Secondly, once the fundamental tone cuts-on, the transmission loss is much higher, peaking at 27 dB, than for the 48-vane stator configuration. Finally, the second-harmonic characteristic shows a rapid rise in transmission loss when M_t exceeds 0.76, peaking at 14 dB at M_t = 1.0. The trends for the closed-throttle operating line (Figure 92) are similar to the trends for the open-throttle operating line (Figure 91), but again the absolute levels are somewhat lower.

To gain additional insight into the effects (predicted by the present analytical model) of rotor transmission loss on forward-radiated tone power levels, the spanwise or radial distributions for the tone power levels with, and without, transmission loss were compared. Two speeds were selected for comparison:

(a) N_F = 69%, corresponding to M_t = 0.88, and
(b) N_F = 74%, corresponding to M_t = 0.94.

Table 6

PREDICTED ROTOR/STATOR TONE PWL 48 VANES
$(S/C)_{nom.}$ = 1.27 and 2.3

V	S/C	DV	%N	Upstream n = 1	2	3	Downstream 1	2	3
48	1.27	0.95	54	123.7	121.9	103.9	135.0	129.3	107.6
		(OP)	36	125.3	125.9	105.7	135.5	133.9	116.1
			69	125.8	126.6	110.8	135.7	135.6	118.9
			76	126.3	129.2	113.4	140.7	135.9	123.5
			80	126.6	129.1	113.5	143.6	136.5	125.3
		.135	54	128.1	113.5	97.6	136.4	123.7	96.9
		(CL)	63	129.3	119.7	100.4	137.1	131.1	103.8
			69	129.9	123.3	102.5	137.4	132.2	107.5
			76	130.3	124.9	107.4	137.7	134.3	113.9
			80	130.3	127.8	110.6	143.3	134.4	119.7
	2.3	0.95	54	121.5	113.6	85.0	132.6	120.5	89.5
		(OP)	63	123.2	117.9	88.1	133.4	125.8	101.7
			69	123.9	119.1	96.9	133.7	127.9	104.1
			76	124.5	122.0	99.7	138.6	128.6	190.6
			80	124.8	121.9	99.5	141.5	129.3	111.1
		1.35	54	124.7	99.4	74.1	132.8	109.9	73.7
		(CL)	63	126.3	106.8	77.9	133.8	119.9	80.4
			69	127.0	110.8	80.3	134.3	121.7	83.7
			76	127.8	114.3	86.7	135.0	124.9	91.7
			80	128.1	118.9	91.6	139.9	125.4	100.7

These speeds bracket the region where the fundamental n = 1 tone exhibits a rapid rise (see Figures 89 through 92).

The spanwise distributions of upstream radiated tone PWL with, and without, rotor transmission loss are shown in Figure 93 for the 48-vane stator configuration on the open-throttle operating line. The first three harmonic tones are shown. Similar comparisons for the closed-throttle operating line are shown in Figure 94. One dramatic effect of rotor transmission loss depicted by the trends shown in Figures 93 and 94 is that the transmission loss changes the tip-dominated "source" distribution to a hub-dominated distribution upstream of the rotor.

The 86-vane configuration spanwise distributions for open-throttle and closed-throttle operating lines are shown in Figures 95 and 96, respectively. These trends show even more dramatically the reversal from a tip-dominated spanwise distribution to a hub-dominated distribution produced by the rotor transmission loss. It is also interesting to note that, at 69% speed (M_t = 0.88), the fundamental tone is cut-on at all but the hub streamlines before being transmitted through the rotor, and then is completely cut off by the rotor. This is due to the change in cut-off ratio or propagation wave number in the downstream-of-rotor to the upstream-of-rotor regions due to swirl velocity change.

A study of the relative transmission loss contributions to the various spinning modes contributing to each tone harmonic level was also carried out for the tip streamline (10% immersion). The tip streamline was selected because it usually exhibited the largest transmission loss, according to the results shown in Figures 93 through 96. The 74% speed (M_t = 0.94) cases were examined. The modal tone

Table 7

PREDICTED ROTOR/STATOR TONE PWL 86 VANES
$(S/C)_{nom.}$ = 0.5 and 0.9

				Upstream			Downstream		
V	S/C	DV	%N	n = 1	2	3	1	2	3
86	0.5	0.95	54		124.8	124.8		124.1	130.6
		(OP)	63		125.3	128.0		125.3	131.7
			69		125.9	128.9		126.5	132.9
			76	126.8	127.1	129.4	151.5	138.2	135.5
			80	127.2	127.9	129.4	154.7	142.0	137.3
		1.35	54		125.8	115.8		125.2	126.8
		(CL)	63		126.9	124.6		127.0	127.5
			69		127.9	126.0		128.4	128.4
			76	131.2	129.7	128.2	147.9	133.6	130.8
			80	131.8	130.7	129.1	155.4	140.3	133.0
	0.9	0.95	54		121.4	117.9		120.6	123.9
		(OP)	63		122.0	121.6		122.0	125.3
			69		122.8	122.7		123.3	126.7
			76	126.0	124.1	123.7	150.7	134.8	129.3
			80	126.7	125.0	123.8	153.9	138.9	131.2
		1.35	54		121.5	105.2		120.7	119.8
		(CL)	63		122.8	117.2		122.6	120.2
			69		123.9	118.9		124.1	121.0
			76	129.5	125.9	121.4	146.3	128.7	123.6
			80	130.7	127.3	122.7	153.9	135.2	125.8

PWL values, in bar chart form, are shown for the 48-vane stator configuration, on the open-throttle operating line in Figure 97. The open bars denote levels without rotor transmission loss, while the shaded bars denote levels with rotor transmission loss included. Each circumferential mode (m) contributing to the tone is shown, as well as the summed levels. For example, the fundamental tone (n = 1 harmonic) in Figure 97 shows two circumferential modes contributing: m = −4 and M = −52. Without transmission loss, the m = −52 mode dominates, giving a level of 139 dB. In contrast, with transmission loss included, the m = −52 mode becomes cut-off and only the m = −4 mode contributes. The m = −4 mode suffers about 12 dB in transmission loss, resulting in a net upstream radiated level of 110 dB (for this streamline), compared to the source level of 138 dB.

Similar results for the closed-throttle operating line, 48-vane configuration are shown in Figure 98. It can be observed that, for each harmonic shown in Figures 97 and 98, the largest negative cut-on spinning mode dominates the tone level if rotor transmission loss is ignored, while the lowest negative or highest positive mode dominates the tone when rotor transmission loss is accounted for. Analogous results for the 86-vane stator configuration are shown in Figures 99 and 100 for the open-throttle and closed-throttle operating lines, respectively. Because of the higher vane number, there are fewer contributing modes, and so a clear trend with mode numbers is not evident, although the transmission loss itself does increase as mode number goes from positive to negative values.

As fan speed is increased, however, additional modes become "cut on," at the tip region first, producing higher noise levels out at the tip relative to the hub (see Figures 95 and 96). But, these modes

Table 8

PREDICTED ROTOR/STATOR TONE PWL 86 VANES
$(S/C)_{nom.}$ = 1.27 and 2.3

				Upstream			Downstream		
V	S/C	DV	%N	n = 1	2	3	1	2	3
86	1.27	0.95	54		118.3	111.2		117.5	117.2
		(OP)	63		119.1	115.3		119.1	119.1
			69		120.0	116.7		120.6	120.9
			76	125.2	121.6	118.1	149.9	131.7	123.6
			80	126.2	122.6	118.3	153.2	136.2	125.8
		1.35	54		117.4	93.9		116.4	111.9
		(CL)	63		119.0	190.4		118.6	112.4
			69		120.1	111.2		120.2	113.3
			76	128.1	122.6	114.3	144.8	124.5	116.4
			80	129.8	124.2	116.0	152.6	130.8	119.0
	2.3	0.95	54		190.6	92.8		108.9	98.5
		(OP)	63		111.9	97.8		111.0	102.2
			69		112.2	100.0		113.0	105.0
			76	123.0	114.3	102.5	147.5	123.1	108.7
			80	124.7	115.6	103.0	151.1	128.6	112.1
		1.35	54		106.1	62.5		104.8	88.7
		(CL)	63		108.3	86.8		107.6	89.9
			69		109.6	89.0		109.2	91.0
			76	124.0	112.9	93.6	140.7	113.6	95.6
			80	127.2	115.3	96.6	149.0	119.8	99.7

become "cut off" in the forward propagation through the rotor, and hence the noise is still hub-dominated in the forward direction. The aft-radiated noise would still contain the additional mode contributions out at the tip at these higher fan speeds (69 to 74%).

From the above results, it can be concluded that accounting for rotor transmission loss in predicting upstream-radiated rotor-stator interaction tone levels is very important in predicting the correct levels as well as the correct trends with tip speed and throttling or loading. In addition, the correct evaluation of rotor transmission loss effects on the detailed modal composition is important in selecting the proper inlet duct liner/treatment design, since the rotor transmission characteristics can change the dominant mode contributing to the tone to be suppressed.

Table 9

PREDICTED CONTRIBUTIONS OF ROTOR/STATOR INTERACTION MECHANISMS TO TOTAL TONE INTERACTION NOISE LEVELS

- Upstream-Radiated PWL
- 86 Vanes
- Axial Spacing S/C_R = 0.5
- Open Throttle, DV = 0.95
- Hub Streamline

$\%N_F$	n	SPF/R	RPF/S	RV/S	RW/S	TOTAL
54	2	65.8	49.5	19.5	122.0	122.0
	3	62.9	0	19.3	118.6	118.6
63	2	66.4	50.0	16.1	122.6	122.6
	3	50.8	0	20.9	124.7	124.7
69	2	66.3	49.9	13.1	123.4	123.4
	3	57.2	0	17.9	126.0	126.0
76	2	65.7	49.1	12.8	124.6	124.6
	3	59.5	0	0	126.9	126.9

SPF/R — Stator Potential Field/Rotor Interaction
RPF/S — Rotor Potential Field/Stator Interaction
RV/S — Rotor Unsteady Vortex/Stator Interaction
RW/S — Rotor Viscous Wake/Stator Interaction

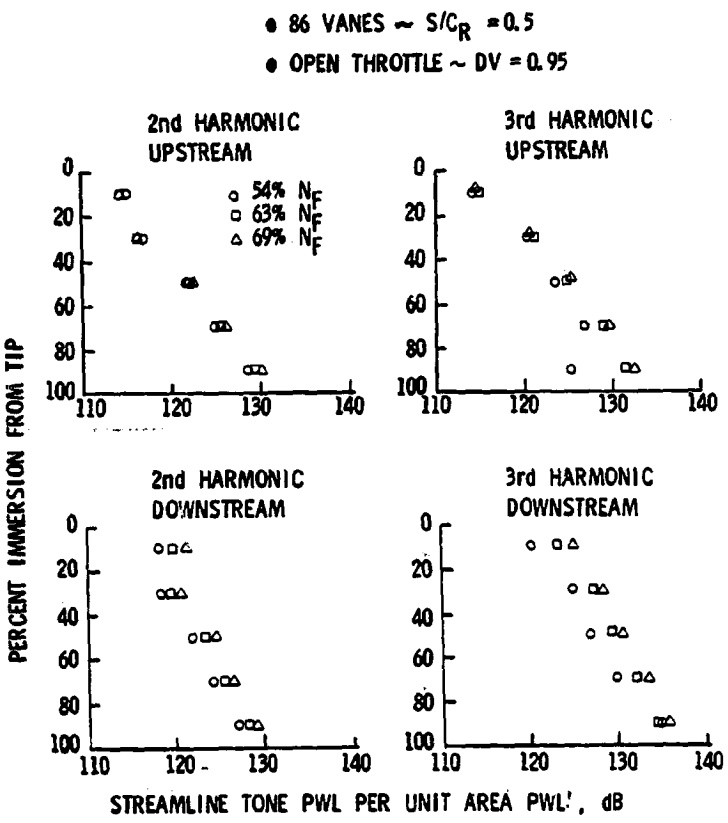

Figure 88. **Predicted Radial Distributions of Tone Noise per Unit Annulus Area ($PWL_{SL} - 10_{\log} A_{SL}$).**

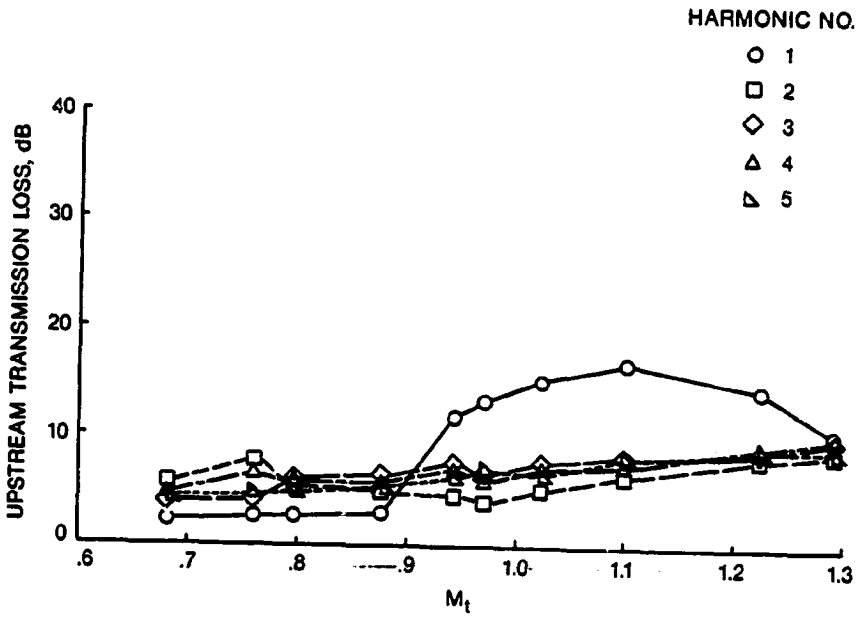

Figure 89. **Calculated Rotor Transmission Loss of Tone PWL vs. Tip Speed Mach Number M_t for 48-vane Configuration on Open-throttle Operating Line.**

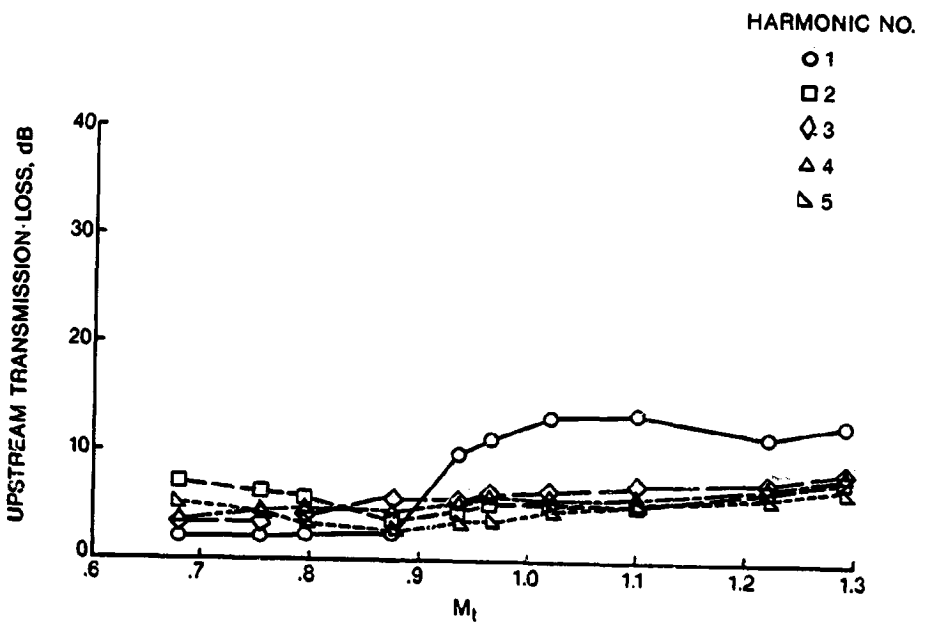

Figure 90. **Calculated Rotor Transmission Loss of Tone PWL vs. Tip Speed Mach Number M_t for 48-vane Configuration on Open-throttle Operating Line.**

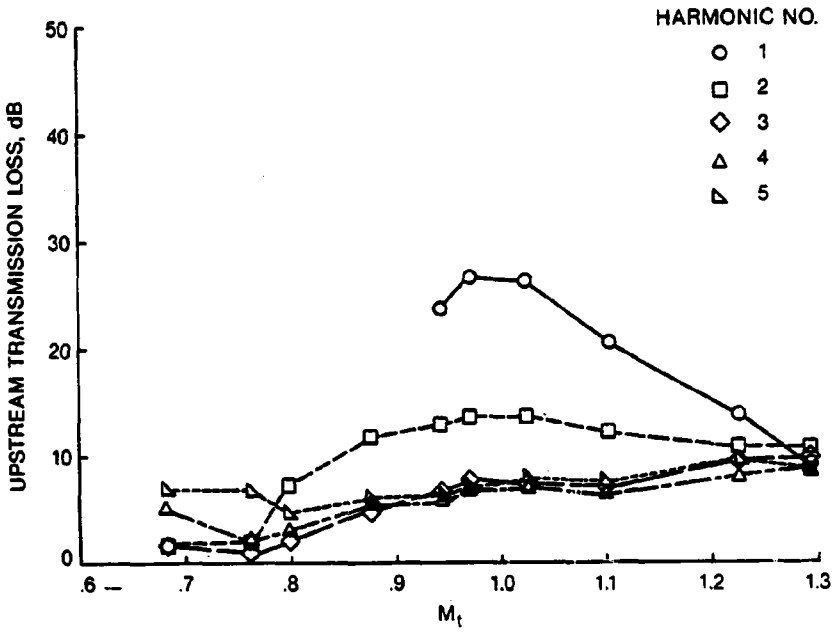

Figure 91. Calculated Rotor Transmission Loss of Tone PWL vs. Tip Speed Mach Number M_t for 86-vane Configuration on Open-throttle Operating Line.

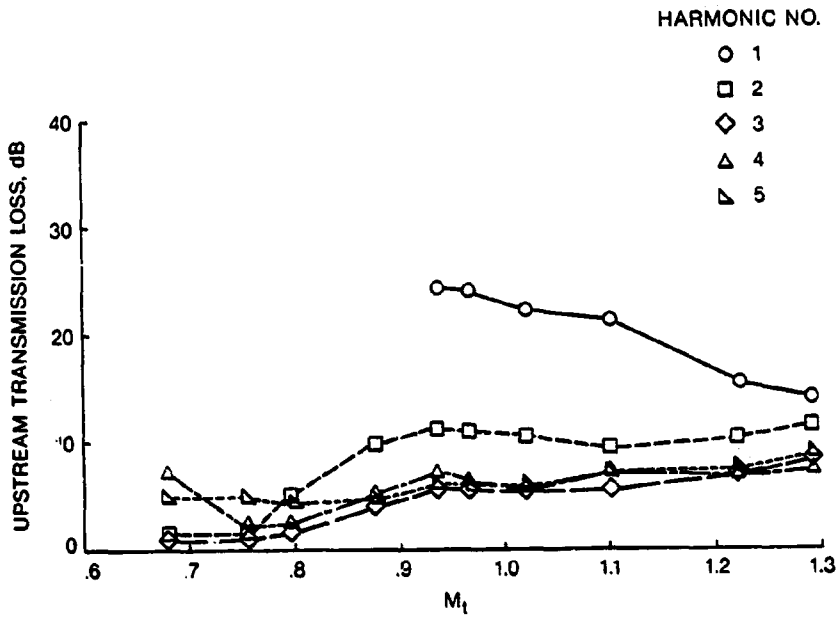

Figure 92. Calculated Rotor Transmission Loss of Tone PWL vs. Tip Speed Mach Number M_t for 48-vane Configuration on Closed-throttle Operating Line.

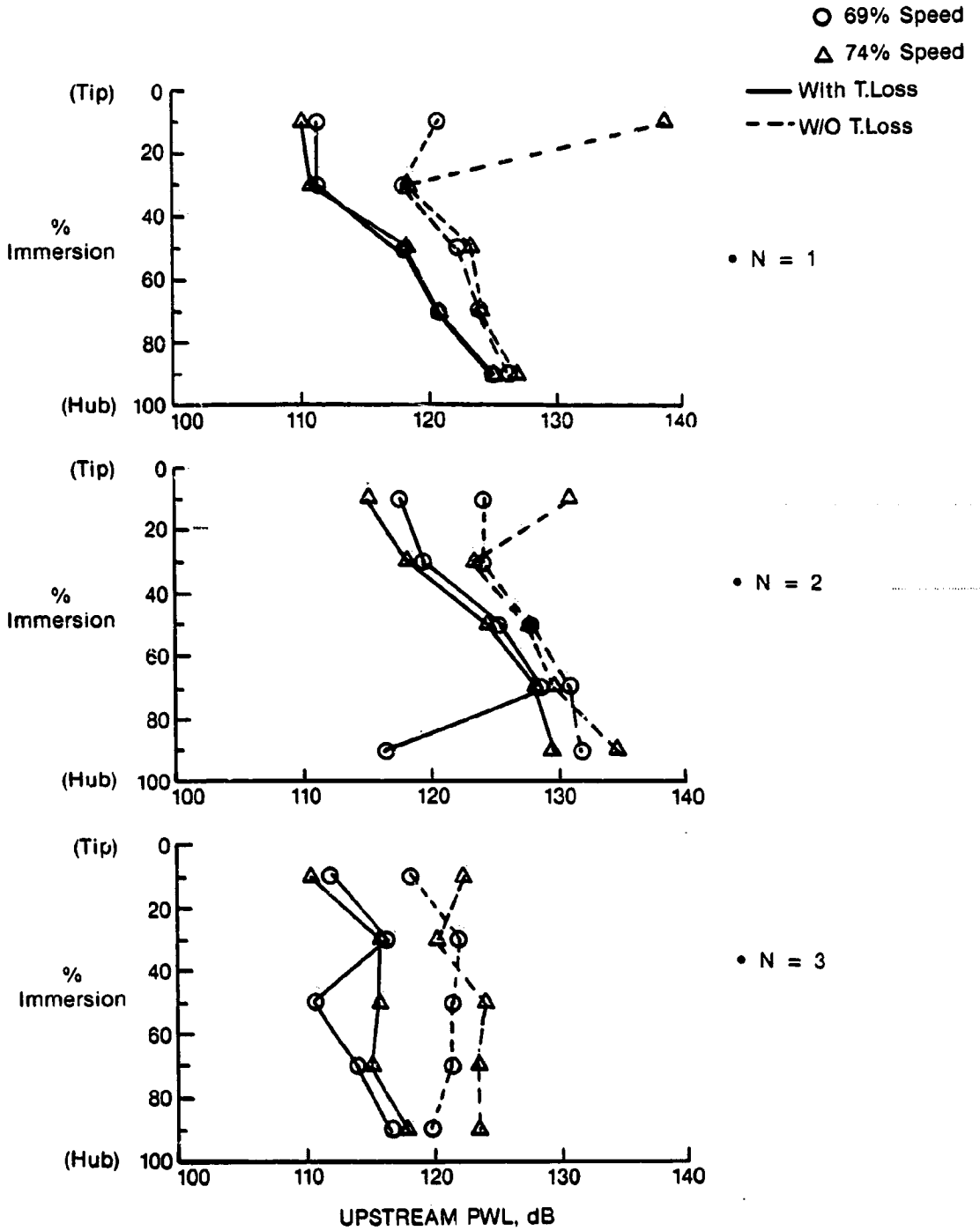

Figure 93. Calculated Upstream-radiated Spanwise Tone PWL Distribution for 48-vane Configuration on Open-throttle Operating Line, With and Without Rotor Transmission Loss.

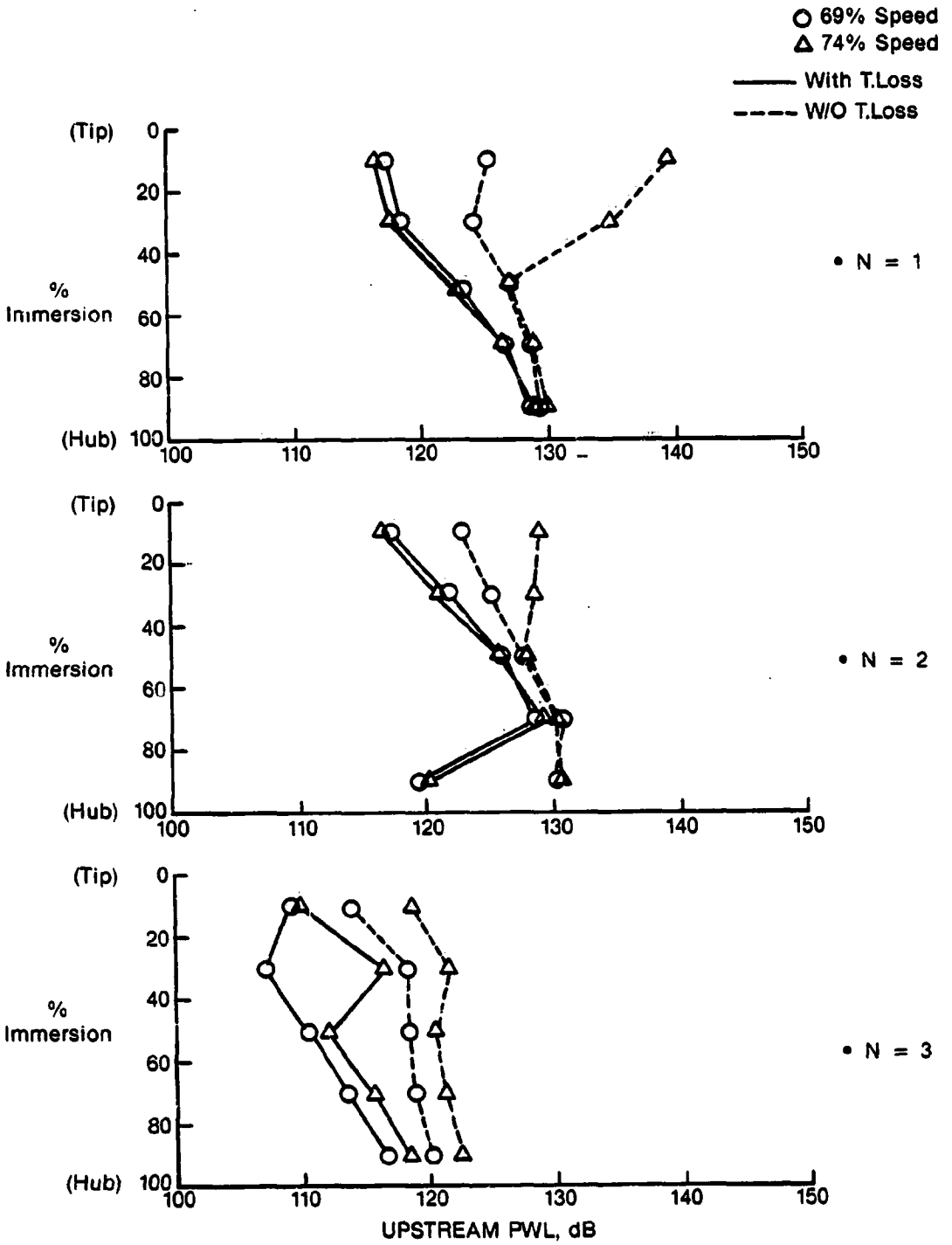

Figure 94. **Calculated Upstream-radiated Spanwise Tone PWL Distribution for 48-vane Configuration on Closed-throttle Operating Line, With and Without Rotor Transmission Loss.**

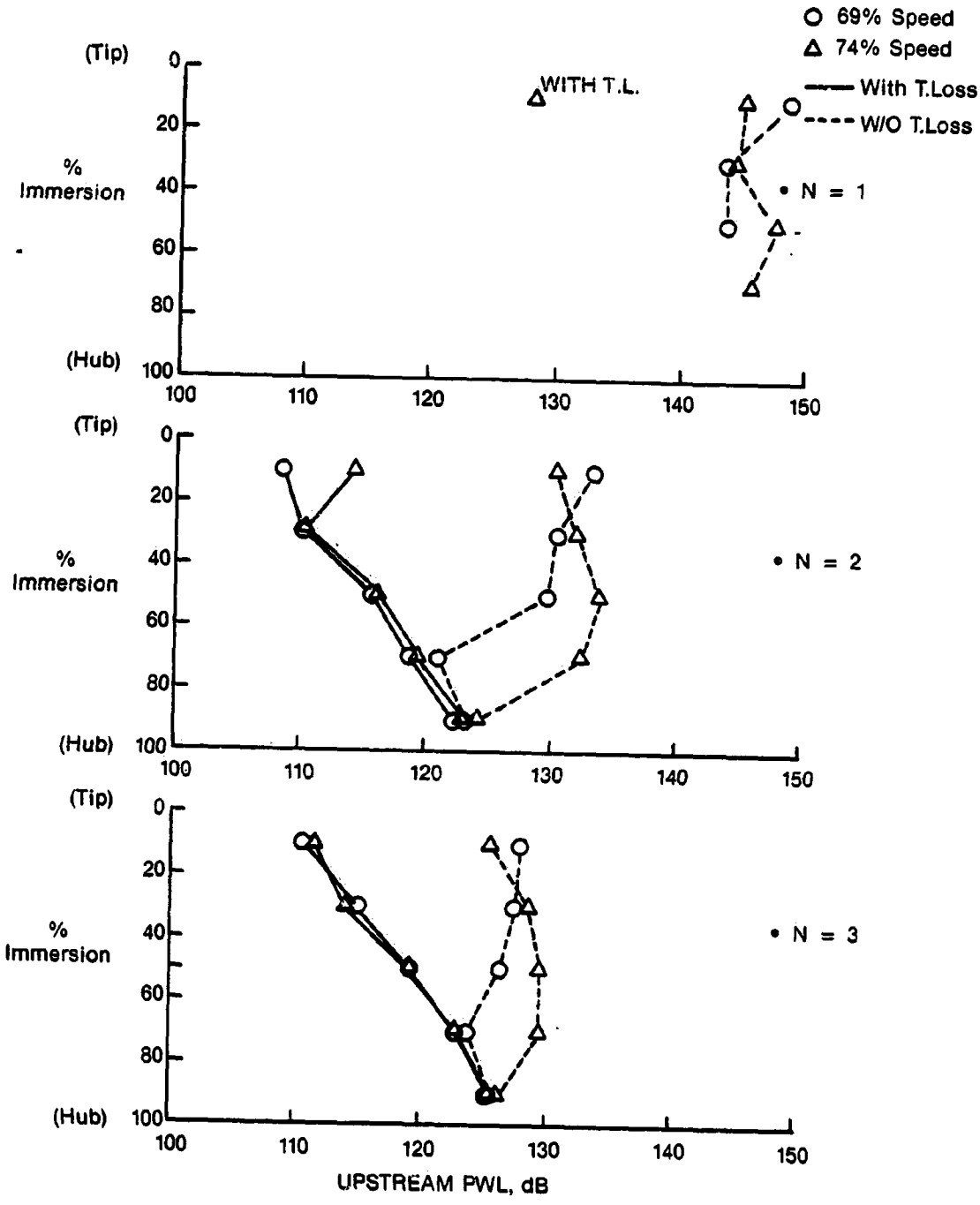

Figure 95. Calculated Upstream-radiated Spanwise Tone PWL Distribution for 86-vane Configuration on Open-throttle Operating Line, With and Without Rotor Transmission Loss.

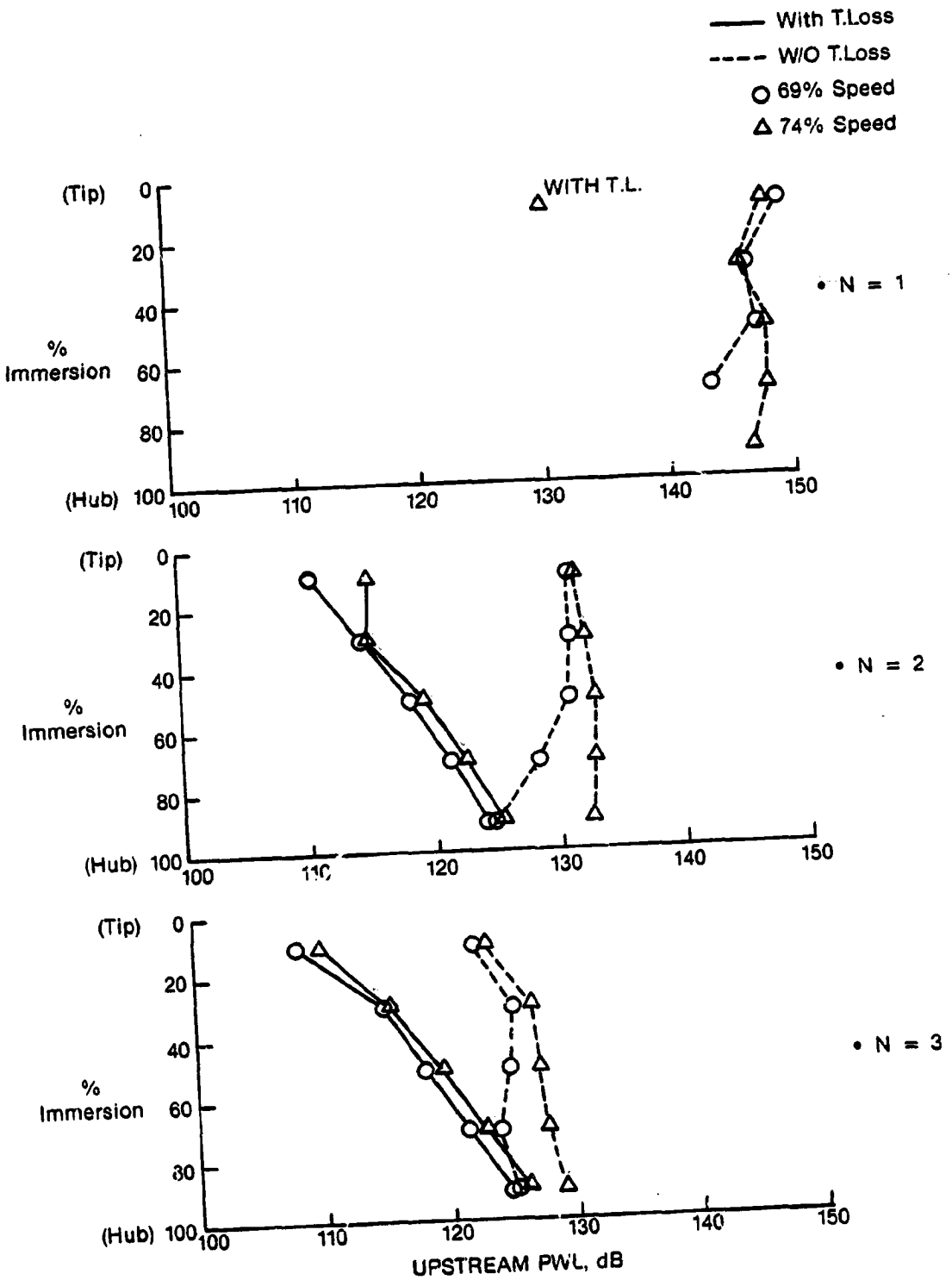

Figure 96. **Calculated Upstream-radiated Spanwise Tone PWL Distribution for 86-vane Configuration on Closed-throttle Operating Line, With and Without Rotor Transmission Loss.**

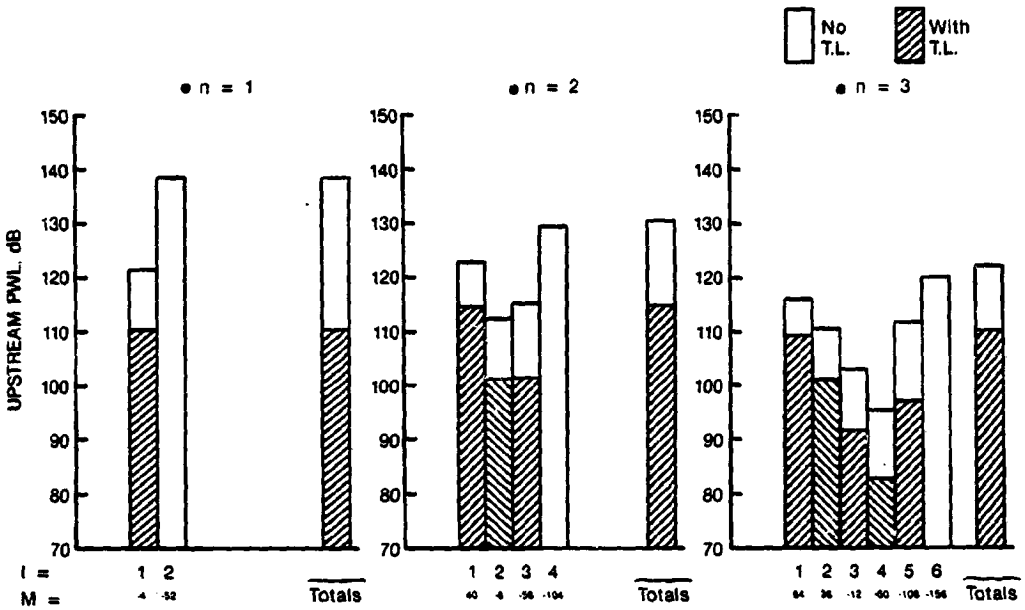

Figure 97. Modal Decomposition of Upstream-radiated Tone PWL for Tip Streamline, With and Without Rotor Transmission Loss; 48-vane Configuration on Open-throttle Operating Line at 74% Speed.

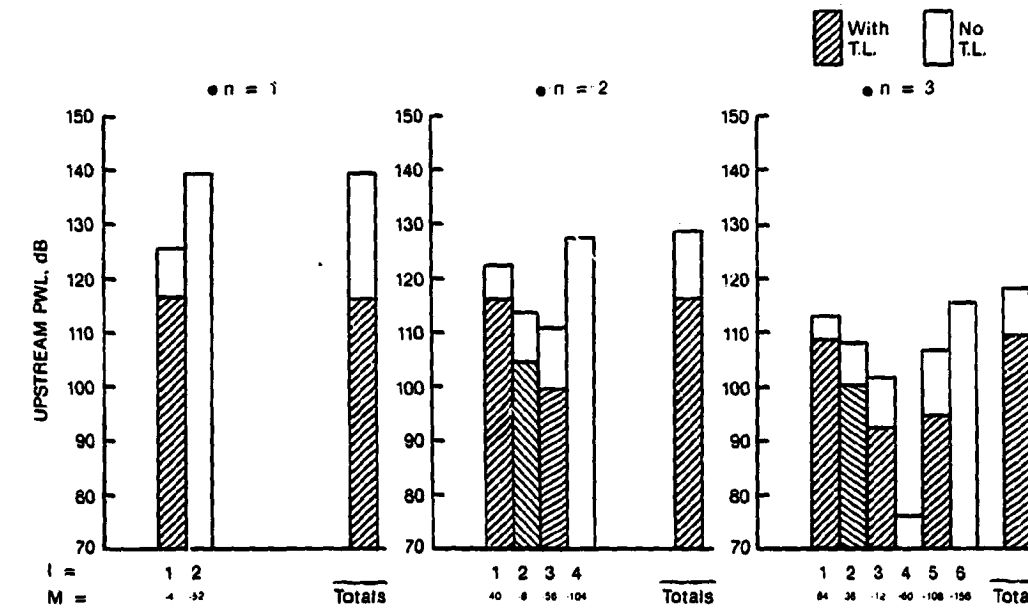

Figure 98. Modal Decomposition of Upstream-radiated Tone PWL for Tip Streamline, With and Without Rotor Transmission Loss; 48-vane Configuration on Closed-throttle Operating Line at 74% Speed.

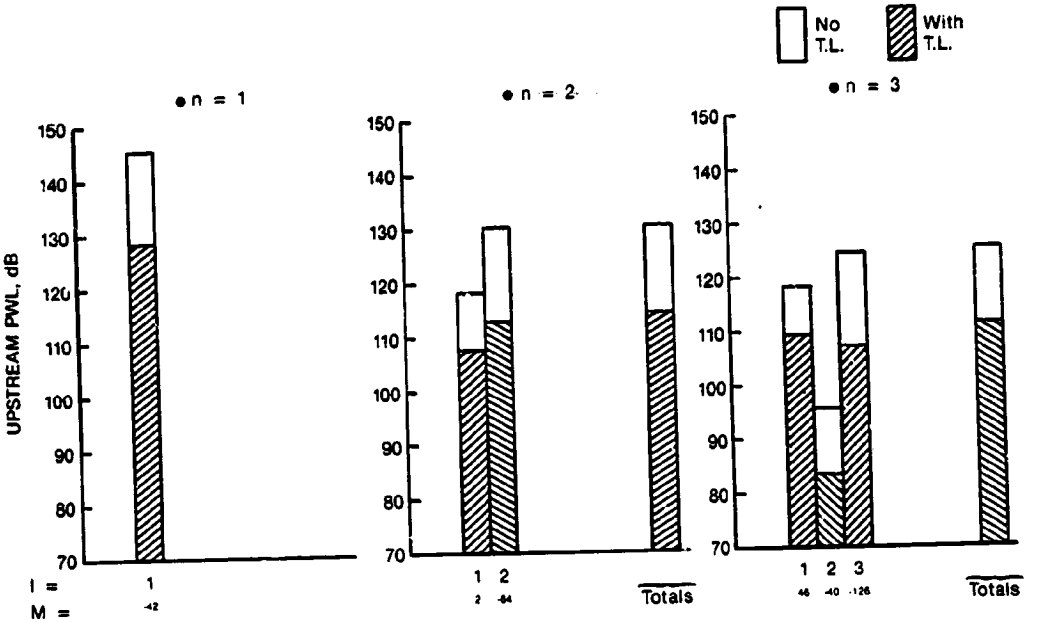

Figure 99. **Modal Decomposition of Upstream-radiated Tone PWL for Tip Streamline, With and Without Rotor Transmission Loss; 86-vane Configuration on Open-throttle Operating Line at 74% Speed.**

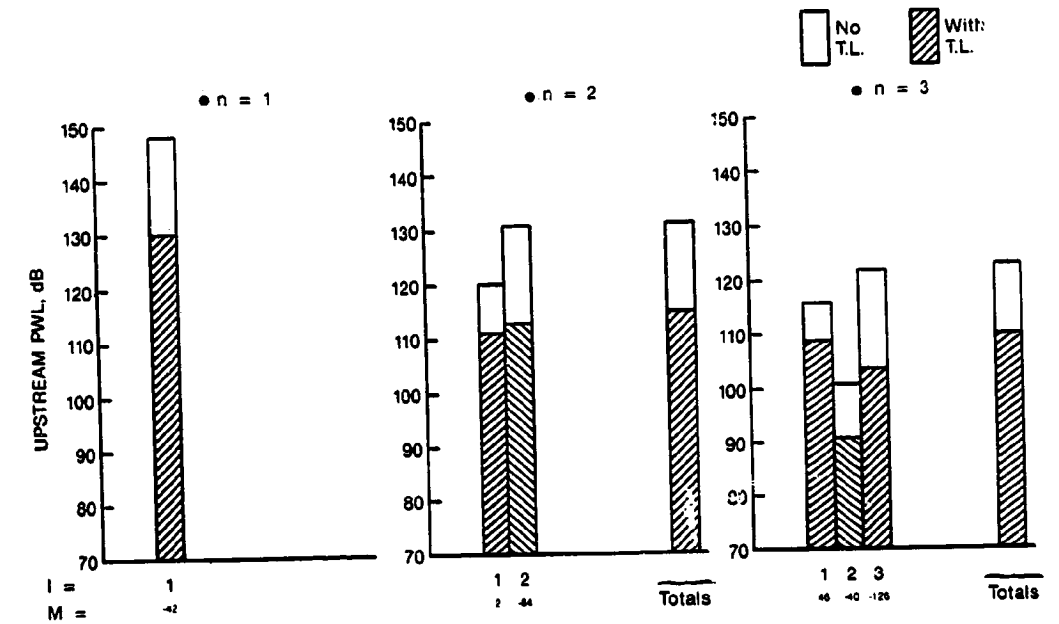

Figure 100. **Modal Decomposition of Upstream-radiated Tone PWL for Tip Streamline, With and Without Rotor Transmission Loss; 86-vane Configuration on Closed-throttle Operating Line at 74% Speed.**

Section 9

PREDICTION VERSUS MEASUREMENT COMPARISONS

The forward radiated tone PWL versus spacing trends are shown in Figure 101 with both measured (from far field microphones) and predicted traces compared. The results in Figure 101 are for 54% speed, the only speed for which narrowbands all around the arc (0° "to" 110°) were reduced. Looking first at Figure 101a, the eighty-six vane configurations, the agreement between measured and predicted PWL at open throttle is seen to be excellent except for the 3X BPF level at the widest ($s/c_R = 2.3$) spacing. The closed throttle cases do not show as good agreement — the predicted levels underestimating the measured levels by 10-15 dB for the 3X BPF tone. The agreement between prediction and measurement is again reasonably good for the forty-eight vane configurations at open throttle (Figure 101b), but again the 2X BPF and 3X BPF tone levels are underpredicted at the closed throttle condition. It also appears that the falloff with spacing is correctly predicted at close spacings ($0.5 \leq s/c_R \leq 1.27$), but is overpredicted at larger spacings. The change in falloff rate with harmonic number is predicted reasonably well.

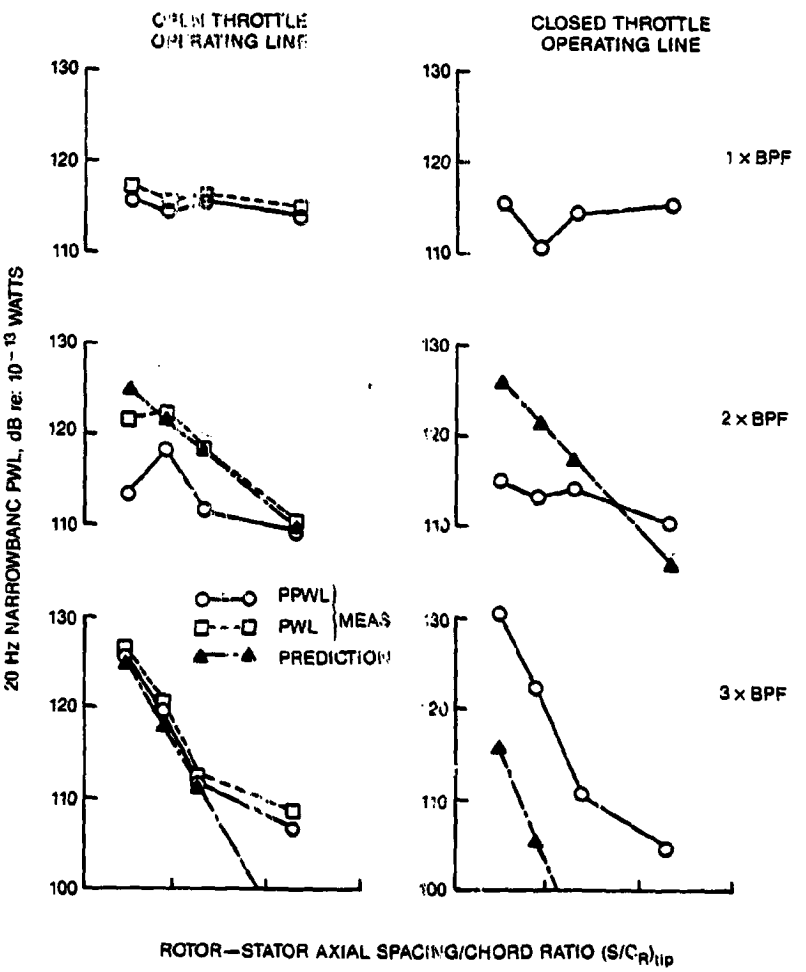

Figure 101(a). Predicted vs. Measured Tone PWL vs. Spacing Trends at 54% N_T; 86-Vane Configurations.

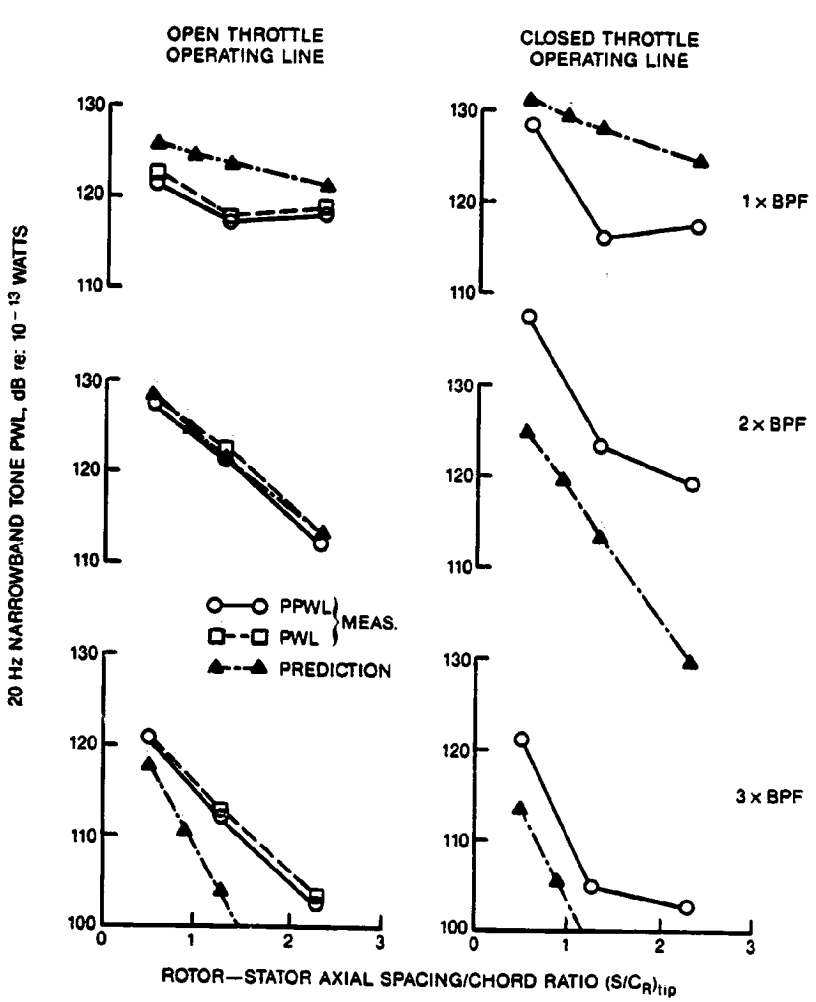

Figure 101(b). Predicted vs. Measured Tone PWL vs. Spacing Trends at 54% Speed; 48-Vane Configurations.

Measurement versus prediction comparisons are shown in Figures 102 through 105 for 63% through 80% corrected speed, respectively. The solid symbols denote the predicted levels, while the open symbols denote the measured levels. The measured levels are partial PWL values, i.e., the PWL computed from integrating from $\theta = 30°$ "to" 60°, whereas the predictions are total forward radiated PWL values. The predictions are lossless, i.e., no air attenuation is included, whereas the measured values include atmospheric attenuation losses which vary from ~0.2 dB to ~2.0 dB over the frequency range of 6.3 to 20 kHz. At the lower speeds, N_F = 54% and 63%, the agreement between measured and predicted trends is better at open throttle than at closed throttle, whereas at the higher speeds, the closed throttle cases give better agreement.

For the cut-on stator design (forty-eight vanes), the BPF tone is overpredicted by 5-10 dB except at the highest speeds (76% and 80%) where agreement between prediction and measurement is quite good. Note that the eighty-six vane configuration is predicted to have a cut-on BPF tone (from both rotor-stator interaction and rotor-alone noise) at 76% speed and above, and this is reflected in the measured trends.

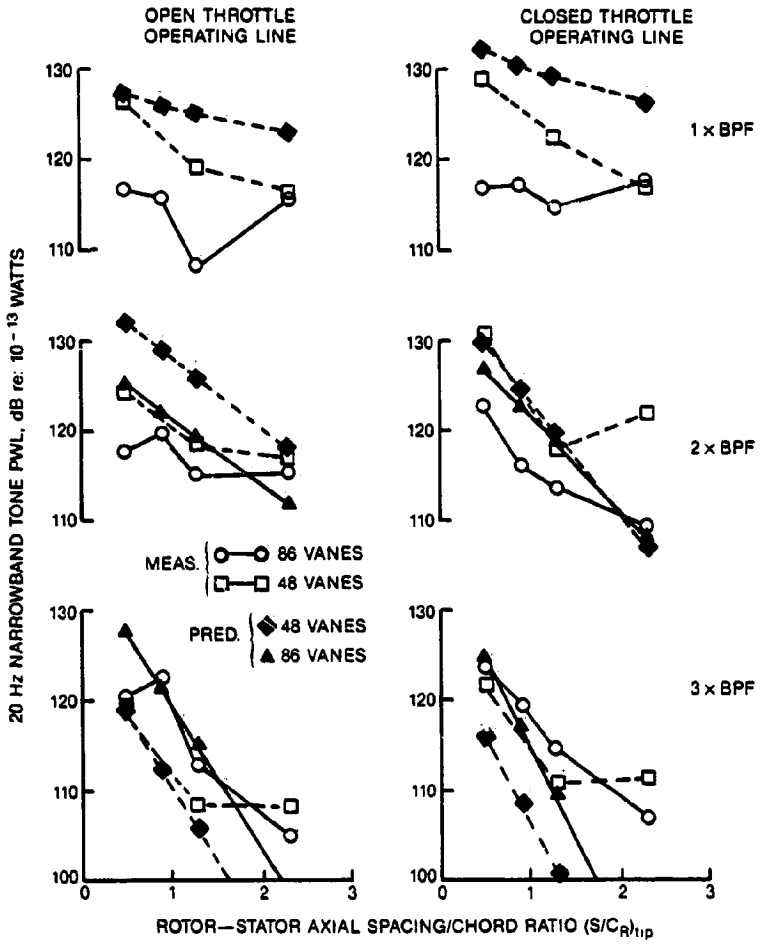

Figure 102. Predicted vs. Measured Tone PPWL vs. Spacing Trends at 63% N_F.

It was mentioned previously in Section 7 that the aft duct average SPL was a close approximation to the PWL because of the annulus area and conversion factor magnitudes involved, provided convective terms in the estimation of PWL from SPL were neglected. It, therefore, seems reasonable to attempt to compare measured duct average SPL versus spacing trends obtained from the aft duct probe with predicted aft radiation tone PWL versus spacing trends. Figure 106 shows the predicted (PWL) and measured (average SPL) tone levels versus spacing trends for the aft duct at 54% speed. The predicted BPF tones (forty-eight vane configurations) were so much higher (approximately 135 to 140 dB, see Tables 3 through 6) than the measured ones that they had to be omitted from the figure. Also, some of the predicted 2X BPF tone levels at the closer spacings had to be omitted from the figure for the same reason. The agreement between predicted and measured 3X BPF tone levels is relatively good, both in magnitude and trend with spacing and vane number.

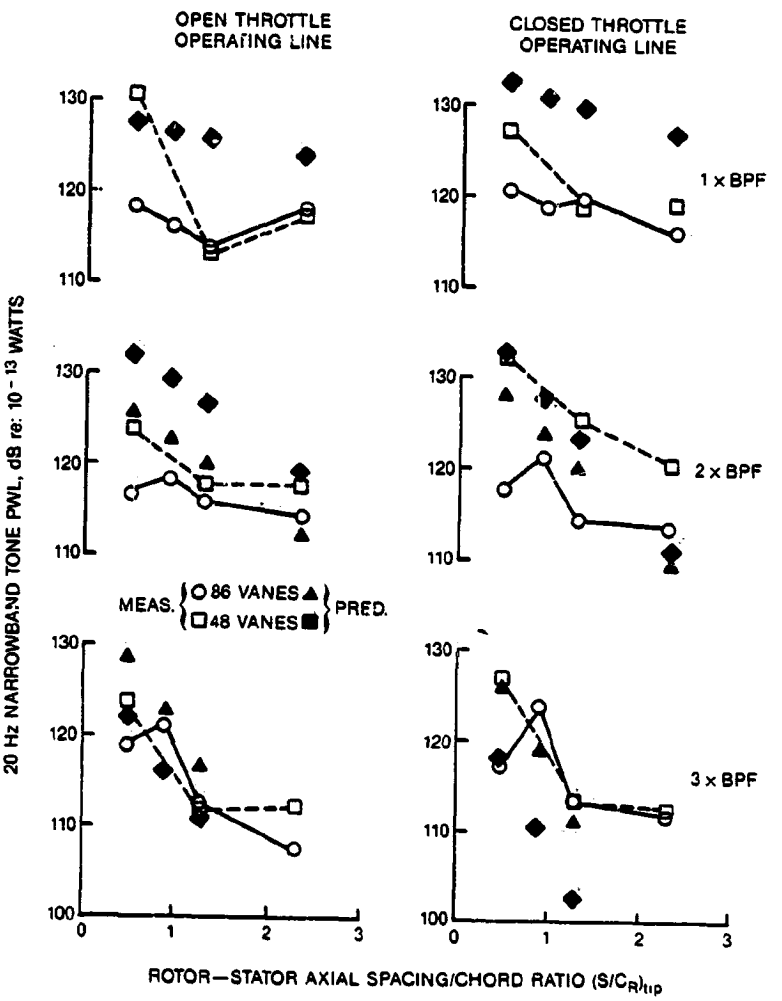

Figure 103. Predicted vs. Measured Tone PPWL vs. Spacing Trends at 69% N_F.

Similar aft duct tone level versus spacing trend comparisons are shown in Figures 107 and 108 for 69% and 80% speed, respectively. Again the predicted BPF tone levels are too high and had to be omitted for the 80% speed comparison on Figure 108. The agreement between prediction and measurement for 2X BPF levels is poor except for the eighty-six vane data at 69% speed where the agreement is good (Figure 107). The 3X BPF level versus spacing trends are predicted quite well except for the largest spacing ($s/c_R = 2.3$).

In reviewing all the prediction versus measurement comparisons shown in Figures 101 through 108, it is concluded that, generally, the prediction model does a reasonable job of predicting the inlet fan tone levels, considering the simplicity and approximate nature of the model, the assumptions and approximations that were made regarding aerodynamic input to the model. Unsatisfactory agreement was obtained for exhaust tone levels, partly because of uncertainty in the data levels resulting from measurement instrumentation, data reduction, and the data analysis methods employed.

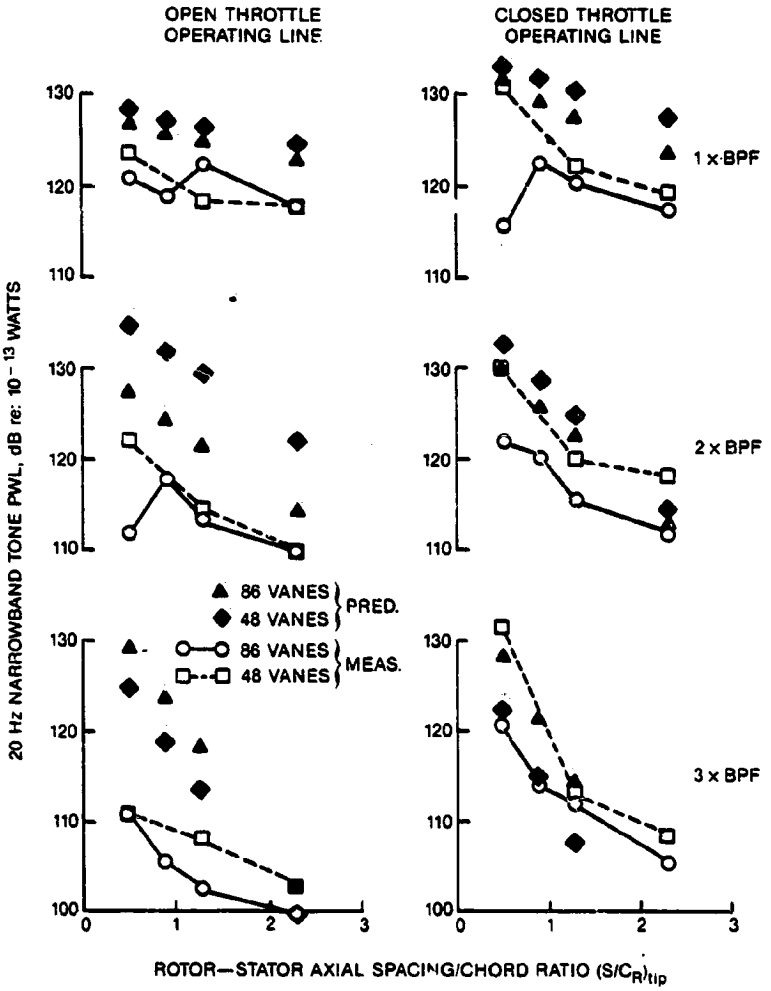

Figure 104. Predicted vs. Measured Tone PPWL vs. Spacing Trends at 75% N_F.

One consistent trend in the measurements not simulated by the prediction procedure, however, is the tendency for the tone level versus spacing characteristic to level out above a spacing (s/c_R) of about 1.5. The inability of the model to predict this trend can be due to at least three effects. First, the tone levels tend to approach the broadband noise flow level at large spacings so that any reduction in tone level below the broadband level cannot be observed. Second, the aerodynamic characteristics (vector diagrams, Mach number levels, etc.) may be significantly different from those estimated (based on the traverse data) for the largest spacings, since the traverse data was obtained for the closest spacing [6]. Referring to Figures 7 and 8, it is seen that the flow path geometry from $s/c_R = 0.5$ to $s/c_R = 2.3$ changes quite significantly and this may impact the radial distribution of flow properties at the stator leading edge. A third source of this discrepancy is postulated to be an inadequate modeling of the rotor wake behavior in large spacings. The Kemp-Sears model employed [8] does not take into account the merging of adjacent wakes at large spacings and the exponential (Gaussian profile) nature of the wake shape used forces rapid falloff of the wake gust harmonic coefficients (and hence noise level) at large axial spacings. As a final note, it is possible that another source of fan tones (inflow disturbances?) is creating a "floor" to the tone levels so that further increases in axial spacing would have little or no effect.

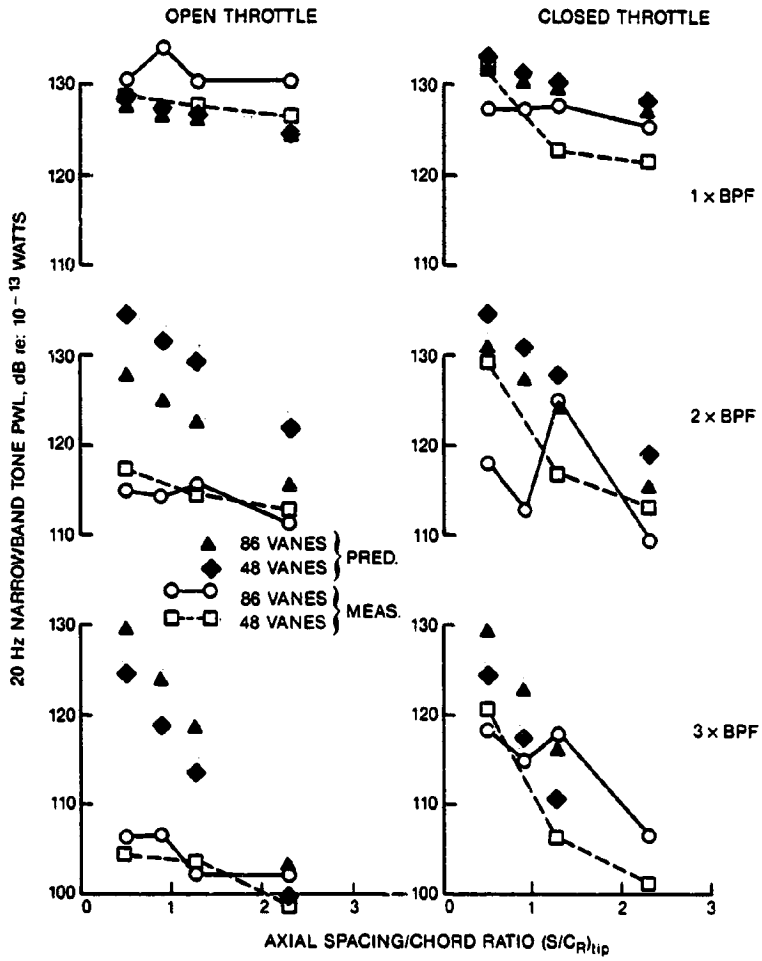

Figure 105. Predicted vs. Measured Tone PPWL vs. Spacing Trends at 80% N_F.

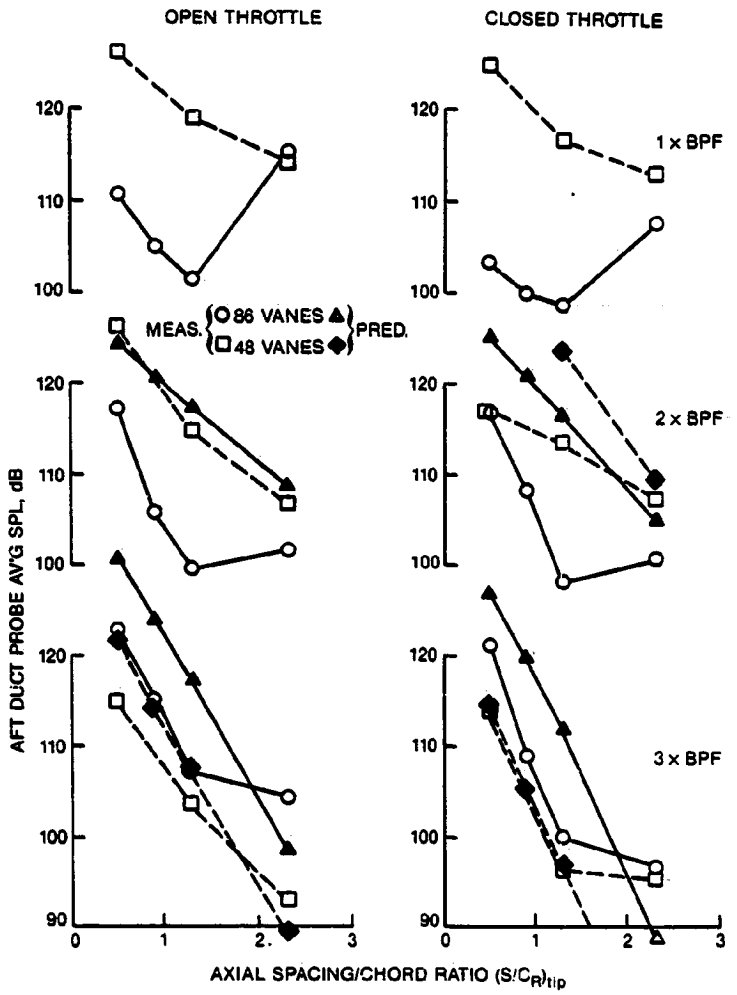

Figure 106. Aft Duct Probe Average SPL vs. Spacing Trends at 54% Speed.

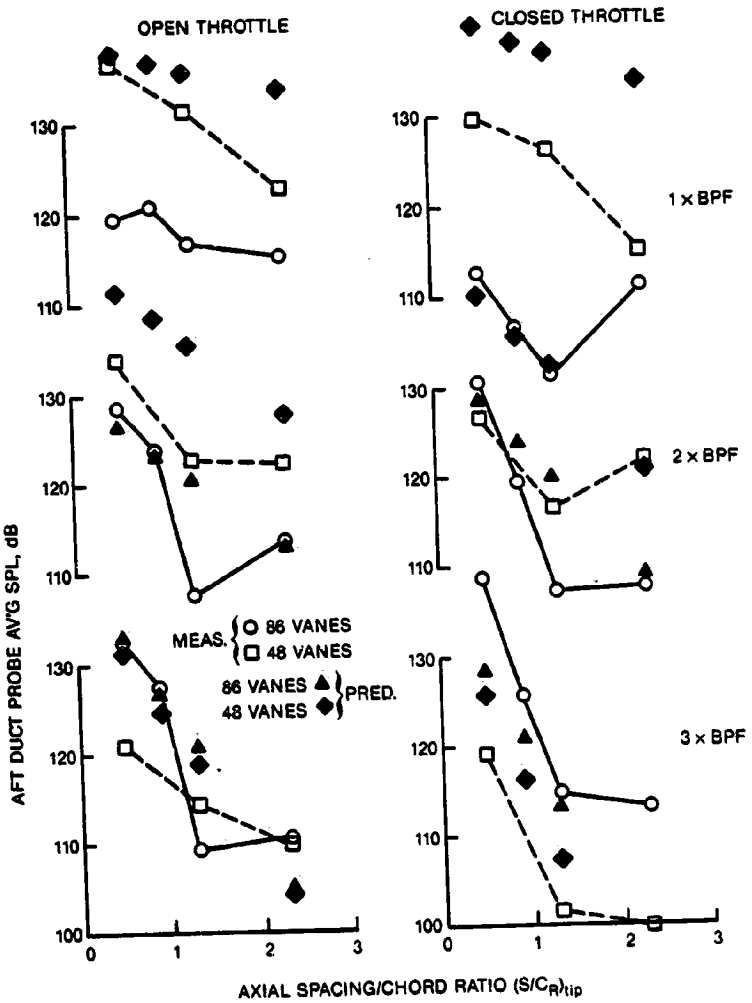

Figure 107. Aft Duct Probe Average SPL vs. Axial Spacing Trends at 69% Speed.

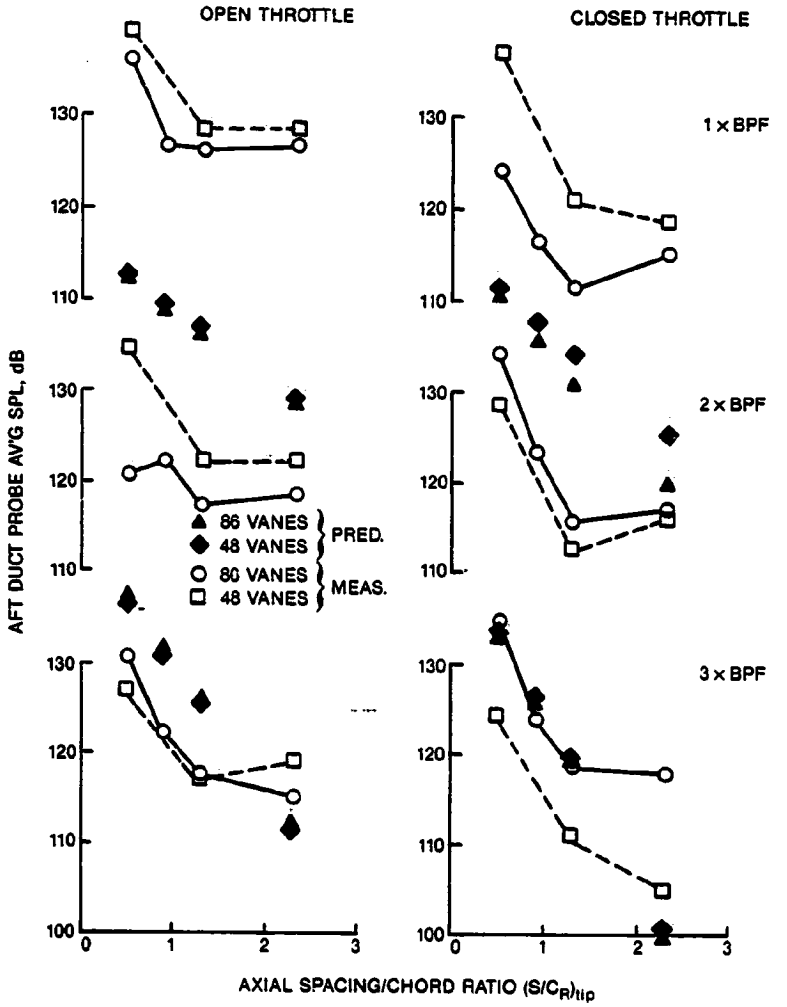

Figure 108. Aft Duct Probe Average SPL vs. Axial Spacing Trends at 80% Speed.

Section 10

CONCLUSIONS

Based on the results obtained from the combined experimental/analytical program documented in the preceding sections, several conclusions were drawn. First, for subsonic tip speeds, the inlet arc fan harmonic tone level spectrum shape depends on both vane number and spacing. For the high ($N_V/N_B \approx 2$) vane/blade ratio and close spacings, the third harmonic tone is higher in level than the second harmonic level. As spacing is increased, the higher harmonic tones drop more rapidly, shifting the spectrum peak to the second harmonic. For vane/blade ratios of about unity, the second harmonic tone dominates the spectrum at small spacings. Again as spacing is increased, the higher harmonics fall off more rapidly and the spectrum peak shifts to the first harmonic. These trends are qualitatively predicted by the theoretical model described herein, suggesting that the analytical model contains the correct physical mechanisms for predicting fan tone noise.

At supersonic tip speeds, the rotor-alone noise field generation dominates the forward radiated tone spectrum and spacing, and vane/blade ratio effects are minimal. In the aft duct, the effects of axial spacing and vane number are still evident, although not as strongly as for subsonic tip speeds. For a cut-off design (e.g., eighty-six vane configuration tested herein), the blade passing tone is not sensitive to axial spacing at speeds below the cut-off speed. Once the cut-off speed is exceeded, however, the BPF tone depends on spacing for the aft radiated noise. The forward radiated BPF tone does not, however, depend on spacing for the aft radiated noise because of the presence of a predominant rotor-alone field.

The blade passing tone for a cut-on fan design (e.g., the forty-eight vane configurations tested herein) is not nearly as sensitive to changes in spacing as the second and higher harmonics. Because of this, much larger spacings may be required to achieve noise levels equivalent to those of a cut-off design. This tradeoff is a function of the vane/blade ratios involved since the vane/blade ratio determines the number (and radiation efficiency) of spinning modes contributing to the tones and, therefore, their relative levels for a given spacing.

The effects of spacing and vane/blade ratio are not as dramatic on a one-third octave basis, since the higher harmonic tones become a small contributor to the one-third octave bands because of the wide band widths. The effect of spacing on tone level, i.e., falloff rate, becomes larger with increasing harmonic number. Since the tone contribution to the one-third octave band diminishes with increasing harmonic number, the net effect on the one-third octave spectrum is diminished.

The utilization of an inflow turbulence control screen (TCS) has permitted the measurement and detection of changes in the "internal" noise sources. Some residual inflow turbulence and/or distortion is still present and can produce residual BPF tones for a cut-off design as well as set a "floor" for the tone levels at large spacings. These conclusions are based on the observed insensitivity of forward radiated tone levels to spacing once the spacing exceeds approximately 1.5 chords and the evidence of low order (1 through 20 per rev) rotor excitation from the blade-mounted transducer measurements.

The directivity patterns of the fan tones, on a narrowband basis, are highly lobular, and the precise positions of the lobes are sensitive to speed. The measurement of tone directivities with discrete microphones every 10° is probably not sufficient to truly "capture" the tone directivity characteristics and the changes in these characteristics with speed, spacing, vane/blade ratio, etc. A traversing microphone would have provided better estimates of the actual characteristics.

The aft duct probe measurements reported herein have yielded encouraging results and the trends deduced from these measurements supported the trends observed from the forward arc for field measurements as well as having indicated some interesting differences between forward and aft radiated tone noise behavior. The two-immersion sampling method employed herein was, however, inadequate to provide more than qualitative trends. It may be possible, however, to obtain reasonably accurate quantitative trends if a continuous traverse of the aft duct probe were employed.

Section 11

RECOMMENDATIONS

From the results obtained in this program, and from the conclusions drawn from these results, several recommendations can be made regarding future activity in the present area of investigation. First, it would be useful to extend the present narrowband analysis of the far field microphone data to include the $\theta = 0°$, 10°, 20°, 70°, 80°, 100°, and 110° spectra at the higher speeds (above 54%) and both throttle settings. This would provide more accurate estimates of tone power levels for use in correlating with spacing, vane/blade ratio, and operating condition and would remove some of the uncertainty associated with the use of partial power level (30° – 60°) employed in the present study correlations. The uncertainties are largest for those tones that contain modes having small spinning lobe numbers such that the peak noise angle is less than 30°, and for modes having a large spinning mode number (near cut-off) such that the peak noise angle is greater than 60°.

A second recommendation worth considering is that detailed flow field measurements should be carried out on the configurations tested acoustically herein. These measurements should include radial rake (or traverse) measurements of total pressure, temperature, and flow angle at the rotor leading edge and trailing edge stations and arc rake measurements behind the stator at several radial immersions. An axisymmetric flow streamline analysis should then be carried out using the radial profile measurements as input, to construct the inlet and exit vector diagrams for each blade row at the speeds and throttle settings tested acoustically. This information would remove the uncertainty in the analytical model predictions associated with the input aerodynamic data since this input involved a considerable amount of interpolation, extrapolation, and "educated guessing" for the study reported herein.

A third recommendation to be made, which can be done in combination with the second, is that rotor-wake profile measurements should be made using hot wire probes. These measurements could provide information for correlating the acoustic results with the aerodynamics of the rotor wakes and also could provide necessary and scarce information for developing an improved model of rotor wake behavior. It is currently thought that much of the disagreement between model prediction and measurements observed in the present study is a result of an inadequate model of rotor wake behavior, especially at very small and very large distances from the rotor trailing edge.

A fourth recommendation to be made is that a more refined, analytical model of blade row potential field interactions should be developed. The current model employed for the present study is based on thin, small-camber airfoil approximations with the loading field concentrated at the point, usually the one-quarter chord point. It is known that hub sections of fan rotors have considerable camber and thickness; their loadings are distributed over most of the blade chord; thus they have a much greater potential field influence on a downstream stator than is currently predicted with the present technique. Similarly, the stator potential fields probably have a larger influence on the rotor than the present analysis predicts. This is suggested by the strong eighty-six per rev signal observed on the blade-mounted transducer at $s/c_R = 0.5$.

Finally, it is recommended that the acoustic tests be repeated with the fan turned around so that the aft radiated noise can be measured in the anechoic chamber with the far field microphones. This would provide aft radiated noise data to complement the forward radiated data base and would remove some of the uncertainty associated with proper interpretation of aft duct probe data. The aft duct probe measurements could be taken simultaneously, preferably as a continuous traverse from tip to hub, and these results could then be calibrated against the far field results. If such a calibration proves successful, future fan noise tests and experiments could employ (a verified) aft duct probe measurement for obtaining aft-radiated PWL spectra when only forward mode test operation is feasible.

Although some of the above recommendations are ambitious, the acoustic data bank established in the present program represents one of the few sets (if not the only set) of high tip speed design fan parametric noise data available, which is applicable to modern high bypass turbofan designs. These

recommendations are designed to "complete the picture" and to remove some of the uncertainties identified in the present study. These recommendations also aim at extending and verifying our present understanding of fan noise generation mechanisms through an intimate linkage with a logical prediction procedure — a procedure that shows much promise.

Section 12

REFERENCES

[1] Kantola, R.A. and Warren, R.E., "Basic Research in Fan Source Noise – Inlet Distortion and Turbulence Noise," NASA Contractor Report No. CR159451, December 1978.

[2] Shaw, L.M., Woodward, R.P., Glaser, F.W., and Dastoli, B.J., "Inlet Turbulence and Fan Noise Measured in an Anechoic Wind Tunnel and Statically with an Inlet Flow Control Device," AIAA Paper No. 77-1345, October 1977.

[3] Woodward, R.P., Wazyniak, J.A., Shaw, L.M., and MacKinnon, M.J., "Effectiveness of an Inlet Flow Turbulence Control Device to Simulate Flight Fan Noise in an Anechoic Chamber," NASA TM-73855, 1977.

[4] Morel, T., Discussion of "Control of Freestream Turbulence by Means of Honeycombs: A Balance Between Suppression and Generation," by R.I. Loehrke and H.M. Nagib, *Journal of Fluids Engineering*, Trans. ASME, September 1976.

[5] Stimpert, D. and Clemons, A., "Acoustic Analysis of Aft Noise Reduction Techniques Measured on a Subsonic Tip Speed 50.8 cm (20 in.) Diameter Fan," NASA Contract Report No. CR-134891, January 1977.

[6] Kovich, G., Moore, R.D., and Urasek, D.C., "Performance of Transonic Fan Stage with Weight Flow per Unit Annulus Area of 198 Kilograms per Second per Square Meter (40.6 (lb/sec)/ft^2)," NASA TM X-2905, November 1973.

[7] Kemp, N.H. and Sears, W.R., "Aerodynamic Interference Between Moving Blade Rows," *Journal of the Aeronautical Sciences*, Volume 20, No. 9, September 1953, pp. 585-597.

[8] Kemp, N.H. and Sears, W.R., "The Unsteady Forces Due to Viscous Wakes in Turbomachines," *Journal of the Aeronautical Sciences*, Volume 22, No. 7, July 1955, pp. 478-483.

[9] Osborne, C., "Compressible Unsteady Interactions Between Blade Rows," *AIAA Journal*, Volume 11, No. 3, March 1973, pp. 340-346.

[10] Mani, R., "Discrete Frequency Noise Generation from an Axial Flow Fan Blade Flow," *Journal of Basic Engineering*, Trans. ASME, Volume 92, Series D, No. 1, March 1970, pp. 37-43.

[11] Amiet, R.K., "High Frequency Thin-Airfoil Theory for Subsonic Flow," *AIAA Journal*, Volume 14, No. 8, August 1976, pp. 1076-1082.

[12] Kaji, S. and Okazaki, T., "Propagation of Sound Waves Through a Blade Row. I. Analysis Based on the Semi-Actuator Disk Theory," *Journal of Sound and Vibration*, Volume 11, No. 3, 1970, pp. 339-353.

[13] Mugridge, B.D. and Morfey, C.L., "Sources of Noise in Axial Flow Fans," *Journal of the Acoustical Society of America*, Volume 51, No. 5, Part 1, 1972, pp. 1411-1426.

[14] Woodward, R.P. and Glaser, F.W., "Effects of Blade-Vane Ratio and Rotor-Stator Spacing on Fan Noise with Forward Velocity," NASA TM-82690, August 1981.

[15] Shaw, L.M. and Glaser, F.W., "Mean Rotor-Wake Characteristics of an Aerodynamically Loaded 0.5 m dia. Fan," NASA TM-81657, 1981.

[16] Shaw, L.M., and Balombin, J.R., "Rotor-Wake Characteristics Relevant to Rotor-Stator Interaction, Noise Generation," AIAA Paper No. 81-2031, presented at AIAA 7th Aeroacoustics Conference, Palo Alto, CA, October 5-7, 1981.

[17] Homicz, G.F., Ludwig, G.R., and Lordi, J.A., "Theoretical and Experimental Studies of Discrete Tone Rotor-Stator Interaction Noise," AIAA 2nd Aeroacoustics Conference, Hampton, VA, March 24-26, 1975, Preprint No. 75-443.

[18] Kantola, R.A. and Gliebe, P.R., "Effects of Vane/Blade Ratio and Spacing on Fan Noise," AIAA 7th Aeroacoustics Conference, Palo Alto, CA, October 5-7, 1981, Preprint No. 81-2033.

Section 13

NOMENCLATURE

A - area

A_{ann} - annulus area

A_{sl} - annulus area associated with a given streamline

BPF - blade passage frequency

C_o - speed of sound

C_R - rotor chord

C_{DR} - rotor drag coefficient

F_m - unstead lift force on blade or vane associated with mode m

σ - frequency, Hz

$I_m^{\pm}$ - acoustic intensity generated at mode m radiated upstream (4) and downstream (−)

K2, K3, K4, K5, K6 - kulite sensor designations, see Figure 6

M_a - axial Mach number

M_e - effective Mach number $M_t/\sqrt{1-M_a^2}$

M_t - rotor blade transverse (wheel speed) Mach number

M_θ - rotor exit swirl Mach number, ΘM_t

m - circumferential (spinning) mode number

N_B - number of rotor blades

N_V - number of stator vanes

n - blade passage frequency harmonic number

P_R - fan stage total pressure ratio

PPWL - sound power level, re: 10^{-13} watts (summation of acoustic intensity from Θ = 30° to 60°)

S - axial spacing between rotor trailing edge and stator leading edge

V - velocity of flow relative to noise producing blade row

ω_{ch} - fan inlet corrected flow (corrected to standard day 59°F inlet temperature, 14.696 psia inlet pressure dry air), lb/sec

β - Mach number parameter $\sqrt{1-M^2}$

γ_R - rotor blade stagger angle, deg.

γ_S - stator vane stagger angle, deg.

$\eta\pm$ - fan duct modal radiation efficiency in the upstream (+) and downstream (-) directions

Θ - far field observer angle from fan inlet centerline, degrees; also used for fan rotor work coefficient. in Section 8

ν - source excitation radian frequency, rad/sec

ρ_a - ambient air density

Υ_R - rotor cascade solidity

Υ_S - stator cascade solidity

Ω - rotor radian frequency, 2Π (RPM)/60, rad/sec

Appendix A

DETAILS OF ROTOR-STATOR INTERACTION NOISE PREDICTION PROCEDURE

The acoustic intensity radiated upstream and downstream of a blade row element in the two-dimensional cascade approximation is given by

$$I_m^{\pm} = \frac{F_m^2}{2\rho_o C_o}\,\eta_m^{\pm} \tag{A-1}$$

where $I_m^{\pm}$ is the upstream-radiated intensity and I_m^{-} is the downstream-radiated intensity.

Also, ρ_o = ambient density in duct.

C_o = ambient speed of sound in duct.

F_m = unsteady blade force per unit annulus area for the m th circumferential mode.

$\eta_m^{\pm}$ = duct radiation efficiency (η_m^{+} for upstream, η_m^{-} for downstream) for the m th circumferential mode.

The expressions for $\eta_m^{\pm}$ as a function of n, B, V, M_t, M_a and M_y are given by Equations (22-28) of Reference [10]. They are as follows:

$$\eta_m^{+} = A_1^2 \left[\frac{-M_{a1} + k_1/\sqrt{m^2 + k_1^2}}{1 - (-k_1 M_{a1} + mM_{y1})/(nBM_t)} \right] \tag{A-2}$$

$$\eta_m^{-} = A_2^2 \left[\frac{M_{a2} + k_2/\sqrt{m^2 + k_2^2}}{1 - (k_2 M_{a2} + mM_{y2})/(nBM_t)} \right] \tag{A-3}$$

where M_{a1} = upstream axial Mach number

M_{a2} = downstream axial Mach number

M_{y1} = upstream absolute swirl Mach number

M_{y2} = downstream absolute swirl Mach number

M_t = blade speed (swirl) Mach number

B = number of rotor blades N_B

n = blade-passing frequency harmonic number

The coefficients A_1 and A_2 are the normalized acoustic pressure amplitude functions for upstream (A_1) and downstream (A_2) radiation, respectively. The term in brackets in Equations (A-2, A-3) above represents the conversion from acoustic pressure amplitude to acoustic intensity, accounting for flow convection effects. The coefficients A_1 and A_2 represent the conversion from unsteady lift energy to acoustic pressure amplitude. The grouping (nBM_t) in Equations (A-2, A-3) represents the non-dimensional acoustic frequency at which the sound is being radiated.

Expressions for A_1 and A_2 are given in Reference [10] as follows:

$$A_1 = \frac{1}{D}\left[k_1\Delta_2 \cos\xi + m\,(1 - M_{a2}^2)\,k_1 k_2 \sin\xi\right] \tag{A-4}$$

$$A_2 = \frac{1}{D}\left[-k_2\Delta_1 \cos\xi + m\,(1 - M_{a1}^2)\,k_1 k_2 \sin\xi\right]$$

$$D = (1 - M_{a2}^2)\,k_2\Delta_1 + (1 - M_{a1}^2)\,k_1\Delta_2 \tag{A-5}$$

where k_1, k_2, Δ_1 and Δ_2 are defined as follows:

$$\Delta_1 = \chi_1^2 - m^2 \tag{A-6}$$

$$\Delta_2 = \chi_2^2 - m^2 \tag{A-7}$$

$$k_1 = \frac{1}{\beta_1^2}\left[M_{a1}\chi_1 + (\chi_1^2 - \beta_1^2 m^2)^{1/2}\right] \tag{A-8}$$

$$k_2 = \frac{1}{\beta_2^2}\left[-M_{a2}\chi_2 + (\chi_2^2 - \beta_2^2 m^2)^{1/2}\right] \tag{A-9}$$

and

$$\chi_1 = (nBM_t) - mM_{y1} \tag{A-10}$$

$$\chi_2 = (nBM_t) - mM_{y2} \tag{A-11}$$

$$\beta_1 = \sqrt{1 - M_{a1}^2} \tag{A-12}$$

$$\beta_2 = \sqrt{1 - M_{a2}^2} \tag{A-13}$$

The mode number m is given by

$$m = nB - kV \tag{A-14}$$

where B and V are blade and vane number, respectively, and k is an integer. The angle ξ is the angle the unsteady lift vector makes with the upstream axial direction. The unsteady lift vector is assumed to be normal to the mean flow direction.

Equations (A-1) through (A-14) are used to compute the spanwise distribution of acoustic intensity of a given acoustic mode produced by a given spanwise distribution of unsteady blade force F_m. The parameters M_a, M_t, M_y, ξ are functions of spanwise position or radius. The parameters k_1 and k_2 given by Equations (A-8) and (A-9) are the upstream and downstream axial wave numbers, respectively. The determination of propagating modes m is governed by whether the term $(\chi_1^2 - \beta_1^2 m^2)^{1/2}$ in Equation (A-8) and/or $(\chi_2^2 - \beta_2^2 m^2)^{1/2}$ in Equation (A-9) have positive roots, such that k_1 and/or k_2 are always real.

The unsteady blade force per unit annulus area F_m is a function of the interaction mechanism producing it as well as the various operating parameters listed above. The unsteady force F_m is related to the unsteady vane lift force per unit span L'_v by

$$F_m = \frac{VL'_v}{2\pi r} \tag{A-15}$$

if the stator is the source; and to unsteady blade force L'_B by

$$F_m = \frac{BL'_B}{2\pi r} \tag{A-16}$$

if the rotor is the source (stator potential field-rotor interaction). The unsteady lift per unit span is evaluated using the unsteady gust models of Kemp and Sears [7,8], as modified for compressibility by Osborne [9]. The following paragraphs list the equations used to compute L'_B or L'_V for the various rotor-stator interaction sources.

1. STATOR POTENTIAL FIELD-ROTOR INTERACTION

For this interaction, the rotor is the source and Equation (A-16) applies. The unsteady lift on the rotor blade section, L'_B, is given by the general expression.

$$L'_B = \frac{L_R \Gamma_S}{\Gamma_R \beta_R} [1 - (1 - \beta_S)\, e^{-ix} \cos \chi]\, G_k\, K_L \qquad \text{(A-17)}$$

where L_R = rotor blade steady lift,

Γ_R = rotor blade steady circulation,

Γ_S = stator vane steady circulation,

β_R = rotor compressibility factor $\sqrt{1 - M_R^2}$

β_S = stator compressibility factor $\sqrt{1 - M_S^2}$

$\chi = \alpha_R + \alpha_S$

$M_R = V_R / C_o$, rotor average relative Mach No.

$M_S = V_S / C_o$, stator average absolute Mach No.

α_R = rotor average relative flow angle

α_S = stator average absolute flow angle

The parameter G_k defines the stator load-induced pressure field harmonic amplitude as seen by the rotor. The parameter K_L defines the unsteady lift response function of the rotor blade-section. These functions (G_k and K_L) are complex functions of Mach number M_R and M_S, and of blade and vane solidities and stagger angles. Expressions for these functions are given in Reference [9], and also in Appendix II of Reference [17].

2. ROTOR POTENTIAL FIELD-STATOR INTERACTION

For this interaction, the stator is the source, and Equation (A-15) applies. The stator vane unsteady lift is given by the general expression

$$L'_V = \frac{L_S \Gamma_R}{\Gamma_S \beta_S} [1 - (1 - \beta_R)\, e^{ix} \cos \chi]\, G_n\, K_L \qquad \text{(A-18)}$$

All terms in Equation (A-18) are as defined following Equation (A-17). The function G_n is now the rotor load-induced pressure field harmonic amplitude as seen by the stator. Also, K_L now defines the unsteady lift response function of the stator vane section. Expressions for these functions are given in Reference [9] and Appendix II of Reference [17].

3. ROTOR VORTEX-STATOR INTERACTION

For this interaction, the stator loading-induced pressure field excites the upstream rotor, producing an unsteady lift on the rotor. The unsteady rotor lift produces shed vorticity which convects downstream as a "gust." This "gust" excites unsteady lift on the stator vanes, and the stator is again the source. An expression for this unsteady stator vane lift was derived from the analysis of Reference [7], and is of the following form:

$$|L'_V| = L_S \sum_k \frac{\pi^2 \sigma_R \sigma_S}{\cos \alpha_R} \left\{ \frac{N_k}{D_k}\, C_k\, e^{-\pi k \epsilon_k} \right\} \qquad \text{(A-19)}$$

where

$$C_k = \frac{nV_R B}{kV_\infty V} \qquad \text{(A-20)}$$

$$N_k = |J(k\lambda_R)||S(k\omega_R)||S(n\omega_S)||H_k^S| \tag{A-21}$$

$$D_k = 1 + [(\cos\chi - C_k)/\sin\chi]^2 \tag{A-22}$$

$$\epsilon_k = \sigma_R\ (V/B)\ (2b/C_R) \tag{A-23}$$

The function H_k^S is a complex Bessel functions summation, given in Reference [7], involving the aerodynamic loading characteristics (i.e., stagger, camber, angle-of-attack) of the stator vane airfoil section. The functions $S(k\omega_r)$ and $S(n\omega_S)$ are convected-gust "Sears functions," Reference [8], and $J(k\lambda_R)$ is defined as

$$J\ (k\lambda_R) = J_0\ (k\lambda_R) - iJ_1\ (k\lambda_R) \tag{A-24}$$

where J_0 and J_1 are Bessel functions. The parameter λ_R is given by

$$\lambda_R = \pi n \sigma_R\ (V/B)\ \exp\ [-i\ (\pi/2 - \alpha_R)] \tag{A-25}$$

The parameters σ_R and σ_S are the rotor and stator cascade solidities (chord/spacing), respectively, b is the rotor-to-stator midchord-to-midchord axial spacing, and C_R is the rotor chord. Note that only the amplitude of L'_V is given by Equation (A-19); it is assumed that the individual sources act independent of each other, and the relative phasing between sources is neglected.

4. ROTOR-WAKE-STATOR INTERACTION

For this interaction, the rotor wake velocity profile is seen as a convected gust by the downstream stator cascade. The unsteady lift on the stator vane is calculated using the expressions given in References [8,9,17]. The calculation is of the following form:

$$L'_V = \frac{1}{2}\ \rho V_S^2\ C_S\ G_n\ T_n \tag{A-26}$$

where

C_S = stator vane chord

G_n = rotor wake gust amplitude

T_n = stator vane unsteady lift response

The wake gust amplitude is given in Reference [8] by the following:

$$G_n = \frac{2\sqrt{\pi}}{K}\ \frac{u_c \sin\chi}{V_S}\ \exp\ (-\pi^2 n^2/K^2) \tag{A-27}$$

where

$$K = \sqrt{\pi}\ \cos\alpha_R\ \frac{d_R}{Y} \tag{A-28}$$

and

$d_R = C_R/\sigma_R$ rotor blade spacing

Y = wake half-width

u_c = wake centerline velocity defect

The expressions for wake half-width Y and velocity defect u_c given in Reference [8] are as follows, in terms of distance X' downstream of the wake effective origin in the wake streamwise direction:

$$Y = (0.68/\sqrt{2})\ C_R\ (2C_{DR}\ X'/C_R)^{1/2} \tag{A-29}$$

$$u_c = 2.42\ V_R\ \sqrt{C_{DR}}/(2X'/C_R + 0.3) \tag{A-30}$$

where C_{DR} = rotor blade section profile drag coefficient. Alternative expressions for Y and u_c are given in Reference [13], and these were found to give better agreement with experiment in terms of predicting wake gust harmonic spectra. These expressions are as follows:

$$Y = \delta^*/(u_c/V_k) \tag{A-31}$$

$$u_c = 2V_R/\ \sqrt{(2X_t/C_R C_{DR}) + 4.0} \tag{A-32}$$

where

$$\delta^* = \frac{1}{2}\ C_R C_D\ [1 + 2.0 \exp\ (-0.16\ X_t/C_R C_{DR})] \tag{A-33}$$

Here, δ^* is the wake displacement thickness, and X_t is the streamwise distance downstream of the rotor blade trailing edge, $X_t = X' - 0.8\ C_R$. The wake effective origin for the Kemp and Sears model, Equations (A-27) and (A-28) is located at 30% of the rotor chord upstream of the trailing edge.

5. TRANSMISSION LOSS THROUGH THE ROTOR

For all the stator source mechanisms, the upstream-radiated acoustic modes must propagate through the upstream rotor before radiating from the inlet duct. An estimate of the pressure amplitude transmission loss is made for each computed spinning mode which propagates upstream. A two-dimensional (high-radius-ratio approximation) model based on actuator-disk theory is employed. The model accounts for rotor loading through the specification of swirl coefficient θ. Transmission loss is computed for each spinning mode which contributes to each tone separately, since the transmission loss is a function of mode number. At each spanwise location, the calculated upstream-radiated source levels are adjusted for transmission loss for each mode. The mode levels are then summed for each tone harmonic.

The actuator disk model employs conservation of mass and momentum across a blade row, as well as specifying a Kutta condition at the blade row trailing edge. For simplicity, a circumferentially constant rotor exit relative flow angle is assumed as the Kutta condition. This results in three equations to solve for three unknowns: (1) transmission coefficient T, (2) reflection coefficient R, and (3) vorticity wave amplitude V. For an upstream propagating incident wave, incident upon a rotor with downstream swirl Mach number My and no upstream swirl, the equations for calculating T are as follows:

$$a_i\ R + b_i\ T + c_i\ V = d_i \tag{A-34}$$

where

$$a_1 = M_a - \cos\ \theta_R$$

$$a_2 = 1 - M_{R2} \cos\ (\theta_R + \beta_2)$$

$$a_3 = \sin\ (\beta_2 + \theta_R)$$

$$b_1 = M_a - \cos\ \theta_T$$

$$b_2 = 1 - M_{R1} \cos\ (\theta_T - \beta_1)$$

$$b_3 = 0$$

$$c_1 = -1$$

$$c_2 = -[\cos \beta_2 - (k_x/k_y) \sin \beta_2] \; M_{R2}$$
$$c_3 = (k_x/k_y) \cos \beta_2 + \sin \beta_2$$
$$d_1 = M_a - \cos \theta_I$$
$$d_2 = 1 - M_{R2} \cos (\theta_I - \beta_2)$$
$$d_3 = -\sin (\theta_I - \beta_2)$$

The above equations are for equal axial Mach number, density and speed of sound upstream and downstream of the rotor. Equations (A-32) can be solved for R, T, and V by matrix inversion techniques or by direct substitution. The incident wave angle θ_I is related to spinning mode number m, frequency parameters ($\eta = nBM_t - mM_y$) and axial and swirl Mach numbers M_a and M_y by the following equation.

$$\sin \theta_I = m \left[\frac{-\eta - M_a \sqrt{\eta^2 - m^2 (1 - M_a^2)}}{\eta^2 + m^2 M_a^2} \right] \tag{A-35}$$

The reflected wave angle θ_R and transmitted wave angle θ_T are then calculated from the following equations:

$$\tan \theta_R = \frac{(1 - M_a^2) \sin \theta_I}{(1 + M_a^2) \cos \theta_I - 2M_a} \tag{A-36}$$

$$\tan \theta_T = \frac{G[M_a - \sqrt{1 - G^2 (1 - M_a^2)}]}{G^2 - 1} \tag{A-37}$$

where

$$G = \frac{\sin \theta_I}{1 - M_a \cos \theta_I - M_y \sin \theta_I} \tag{A-38}$$

The axial-to-tangential wave number ratio k_x/k_y is given by

$$k_x/k_y = -(1 - M_a \cos \theta_I)/(M_a \sin \theta_I) \tag{A-39}$$

A sketch of the relevant parameters and nomenclature is shown in Figure 109. Note that the transmitted acoustic pressure amplitude P_T and reflected pressure amplitude P_R are related to incident pressure amplitude P_I by the following:

$$P_T = TP_I \;, \quad P_R = RP_I$$

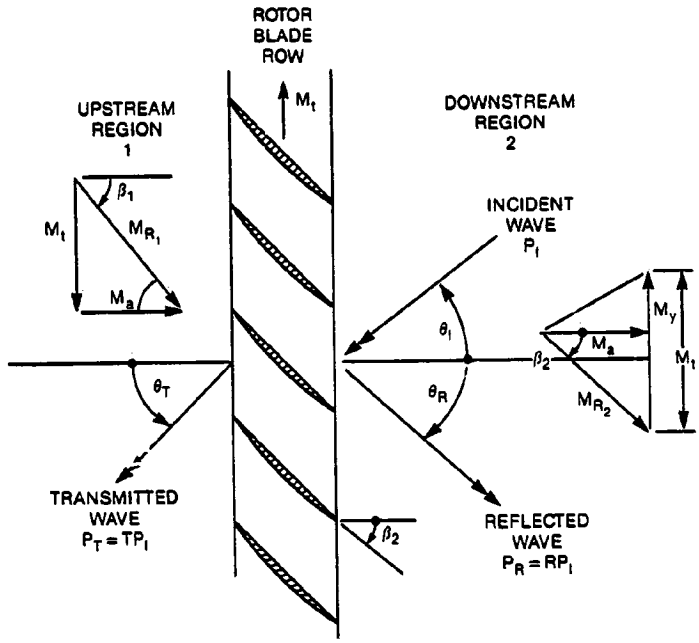

Figure 109. Parameters and Nomenclature for Rotor Transmission Loss Model Described in Appendix A.

Appendix B

TABULATION OF NARROWBAND TONE LEVELS

Table	Run No.	N_V	S/C_R
B1	9	86	0.5
B2	11	86	0.9
B3	6	86	1.27
B4	10	86	2.3
B5	12	48	0.5
B6	13	48	1.27
B7	15	48	2.3

Appendix C

TRACKING FILTER TONE ANALYSIS RESULTS

Fig.	Run	Rdg.	N_V	S/C_R	Run Type	Harm.
C1	9	67	86	0.5	Accel.	1
C2			86	0.5	Accel.	2
C3			86	0.5	Accel.	3
C4	9	68	86	0.5	Decel.	1
C5			86	0.5	Decel.	2
C6			86	0.5	Decel.	3
C7	11	55	86	0.9	Accel.	1
C8			86	0.9	Accel.	2
C9			86	0.9	Accel.	3
C10	11	54	86	0.9	Decel.	1
C11			86	0.9	Decel.	2
C12			86	0.9	Decel.	3
C13	8	22	86	1.27	Accel.	1
C14			86	1.27	Accel.	2
C15			86	1.27	Accel.	3
C16	8	21	86	1.27	Decel.	1
C17			86	1.27	Decel.	2
C18			86	1.27	Decel.	3
C19	10	69	86	2.3	Accel.	1
C20			86	2.3	Accel.	2
C21			86	2.3	Accel.	3
C22	10	68	86	2.3	Decel.	1
C23			86	2.3	Decel.	2
C24			86	2.3	Decel.	3
C25	12	32	48	0.5	Accel.	1
C26			48	0.5	Accel.	2
C27	13	32	48	1.27	Accel.	1
C28			48	1.27	Accel.	2
C29			48	1.27	Accel.	3
C30	15	33	48	2.3	Accel.	1
C31			48	2.3	Accel.	2
C32			48	2.3	Accel.	3

FIGURE C1

TRACKING FILTER TEST
(1500 Hz Bandwidth)
Far Field Microphone No. 7 (60° Angle)

Run	Reading	Run Type	Harmonic Tracked	Vanes	S/C	DV
9	67	Accel.	Fund	86	0.5	0.95

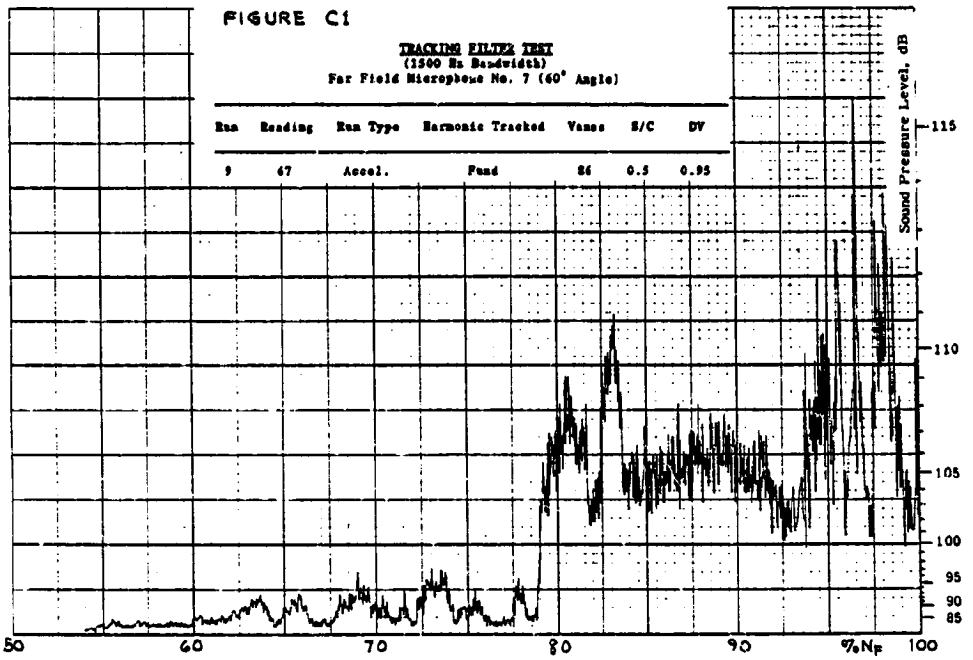

FIGURE C2

TRACKING FILTER TEST
(1500 Hz Bandwidth)
Far Field Microphone No. 7 (60° Angle)

Run	Reading	Run Type	Harmonic Tracked	Vanes	S/C	DV
9	67	Accel.	Second	86	0.5	0.95

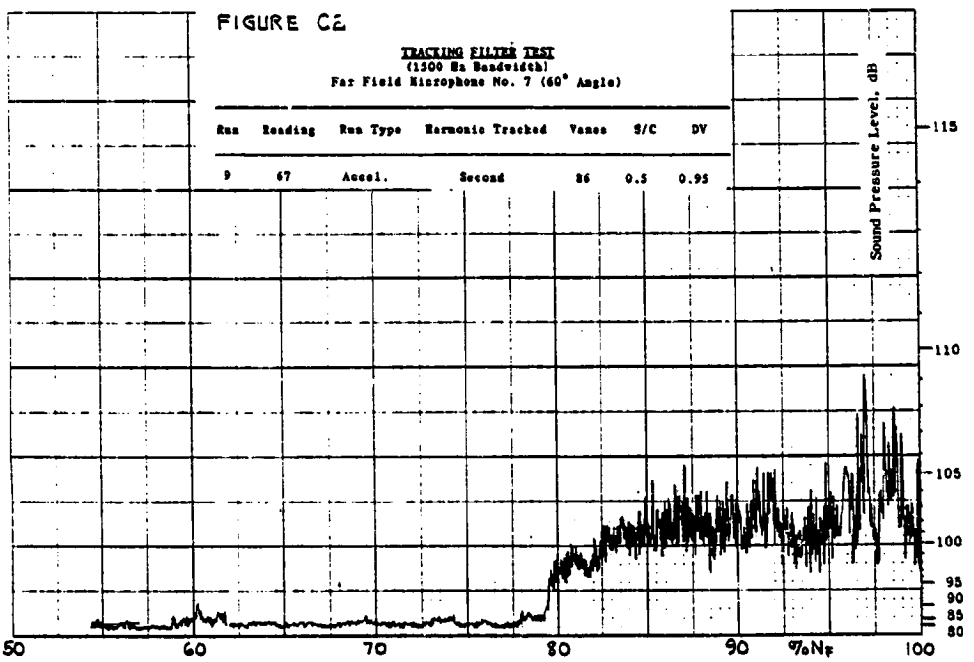

FIGURE C3

TRACKING FILTER TEST
(1500 Hz Bandwidth)
Far Field Microphone No. 7 (60° Angle)

Run	Reading	Run Type	Harmonic Tracked	Vanes	S/C	DV
9	67	Accel.	Third	86	0.5	0.95

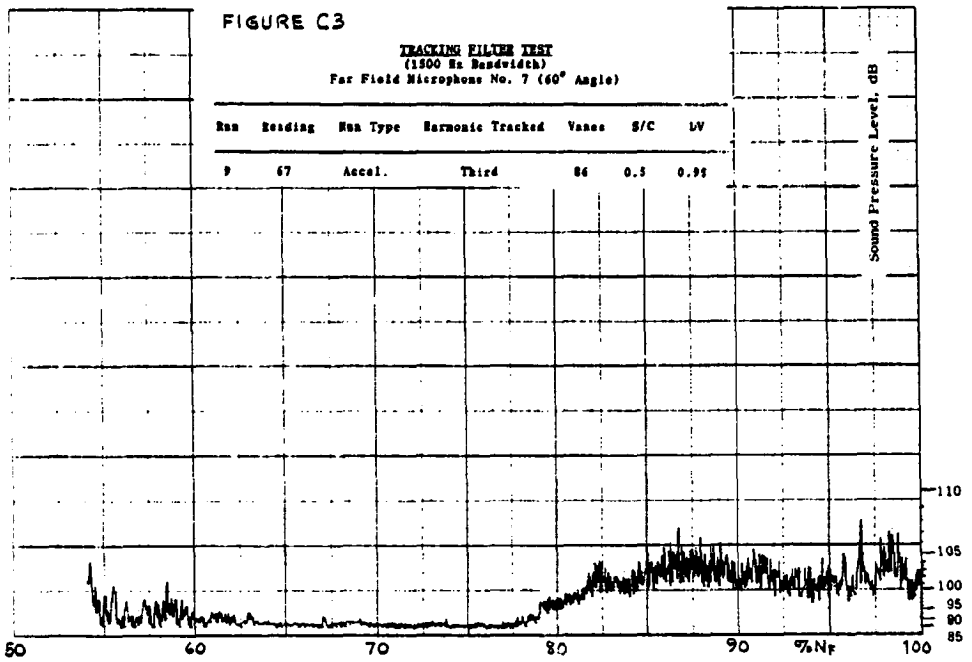

FIGURE C4

TRACKING FILTER TEST
(1500 Hz Bandwidth)
Far Field Microphone No. 7 (60° Angle)

Run	Reading	Run Type	Harmonic Tracked	Vanes	S/C	DV
9	68	Decel.	Fund	86	0.5	0.95

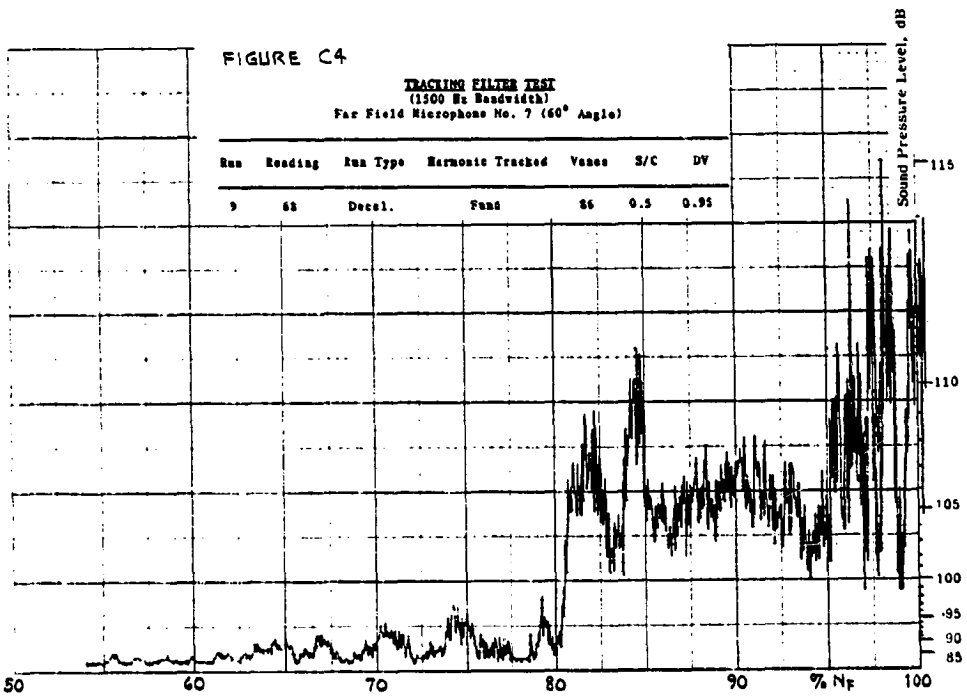

FIGURE C5

TRACKING FILTER TEST
(1500 Hz Bandwidth)
Far Field Microphone No. 7 (60° Angle)

Run	Reading	Run Type	Harmonic Tracked	Vanes	S/C	DV
9	68	Decel.	Second	86	0.5	0.95

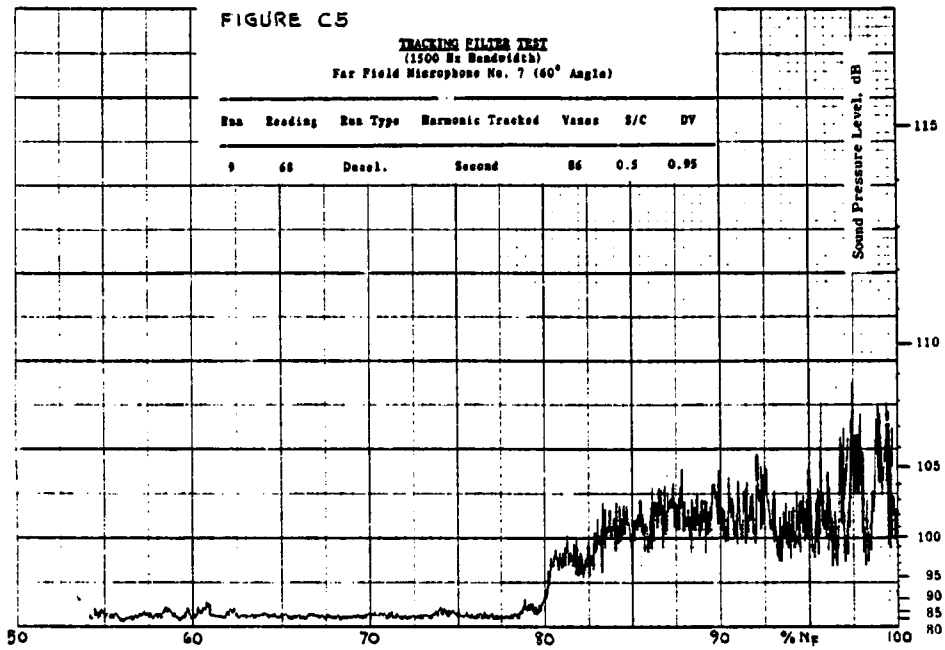

FIGURE C6

TRACKING FILTER TEST
(1500 Hz Bandwidth)
Far Field Microphone No. 7 (60° Angle)

Run	Reading	Run Type	Harmonic Tracked	Vanes	S/C	DV
9	68	Decel.	Third	86	0.5	0.95

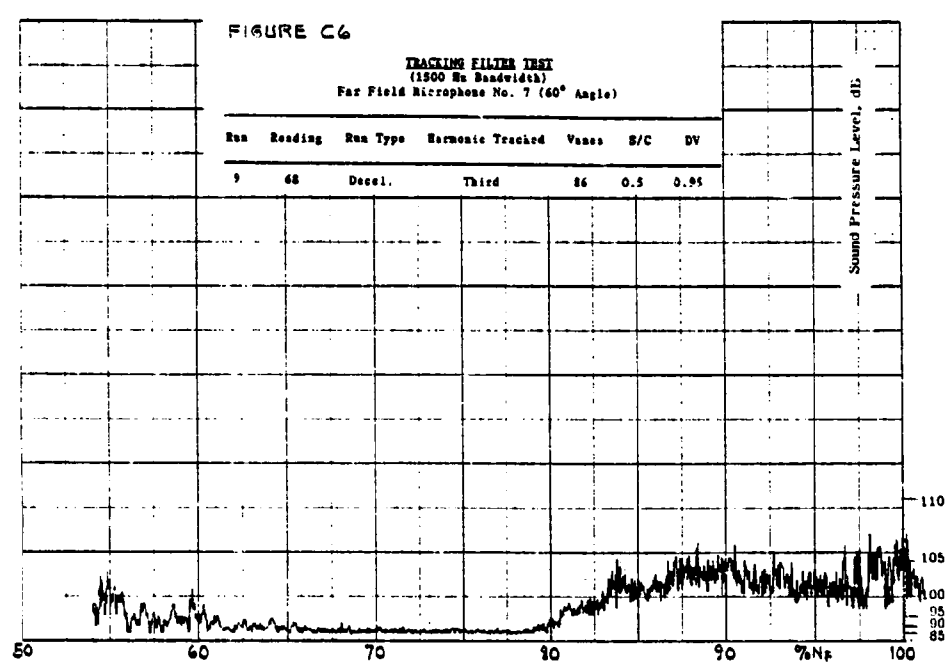

FIGURE C7

TRACKING FILTER TEST
(1500 Hz Bandwidth)
Far Field Microphone No. 7 (60° Angle)

Run	Reading	Run Type	Harmonic Tracked	Vanes	S/C	DV
11	55	Accel.	Fund	86	0.9	0.95

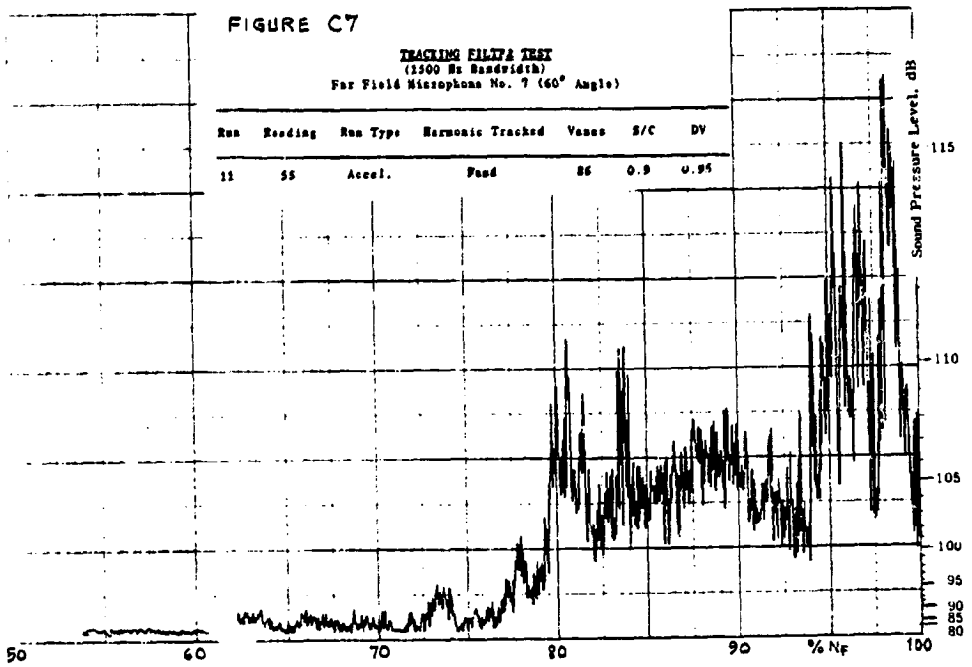

FIGURE C8

TRACKING FILTER TEST
(1500 Hz Bandwidth)
Far Field Microphone No. 7 (60° Angle)

Run	Reading	Run Type	Harmonic Tracked	Vanes	S/C	DV
11	35	Accel.	Second	86	0.9	0.95

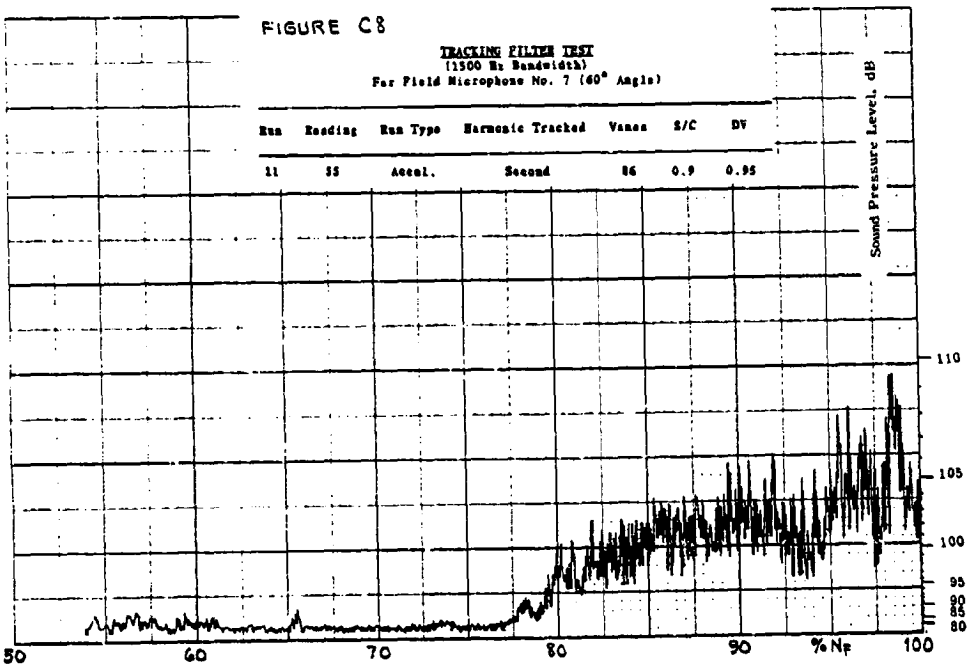

FIGURE C9

TRACKING FILTER TEST
(1500 Hz Bandwidth)
Far Field Microphone No. 7 (60° Angle)

Run	Reading	Run Type	Harmonic Tracked	Vanes	S/C	DV
11	55	Accel.	Third	86	0.9	0.95

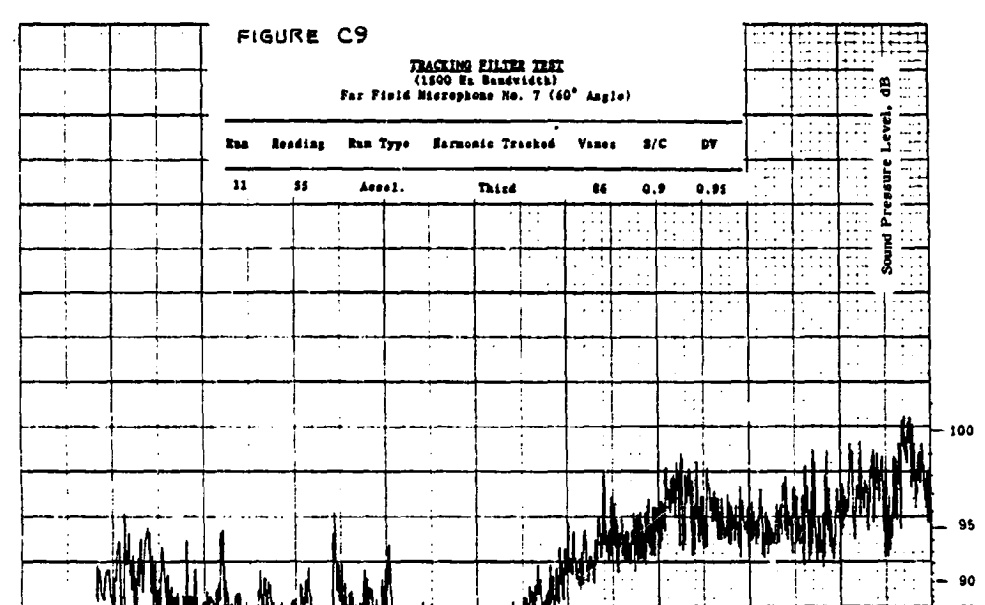

FIGURE C10

TRACKING FILTER TEST
(1500 Hz Bandwidth)
Far Field Microphone No. 7 (60° Angle)

Run	Reading	Run Type	Harmonic Tracked	Vanes	S/C	DV
11	54	Decel.	Fund	86	0.9	0.95

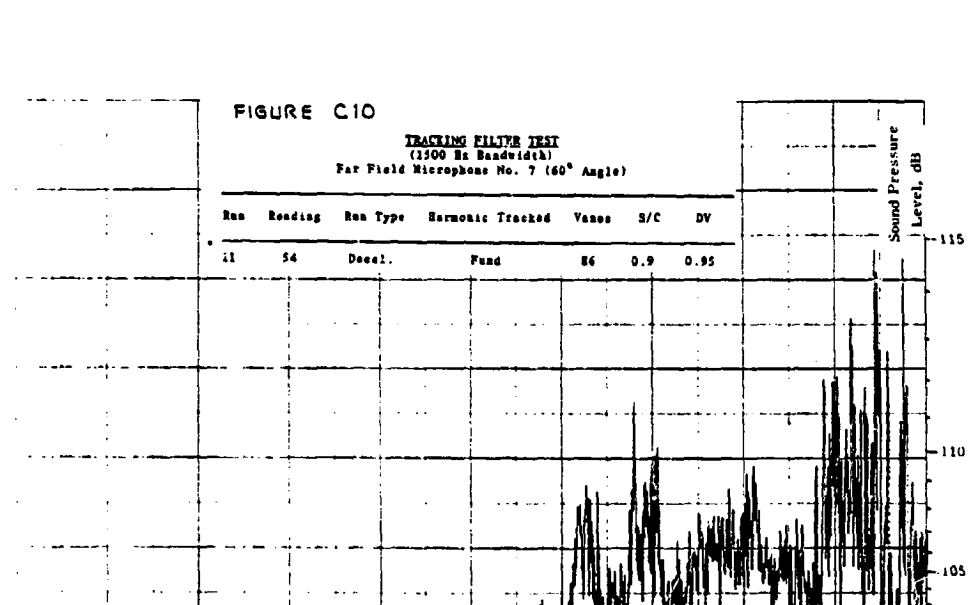

FIGURE C11

TRACKING FILTER TEST
(1500 Hz Bandwidth)
Far Field Microphone No. 7 (60° Angle)

Run	Reading	Run Type	Harmonic Tracked	Vanes	S/C	DV
11	54	Decel.	Second	86	0.9	0.95

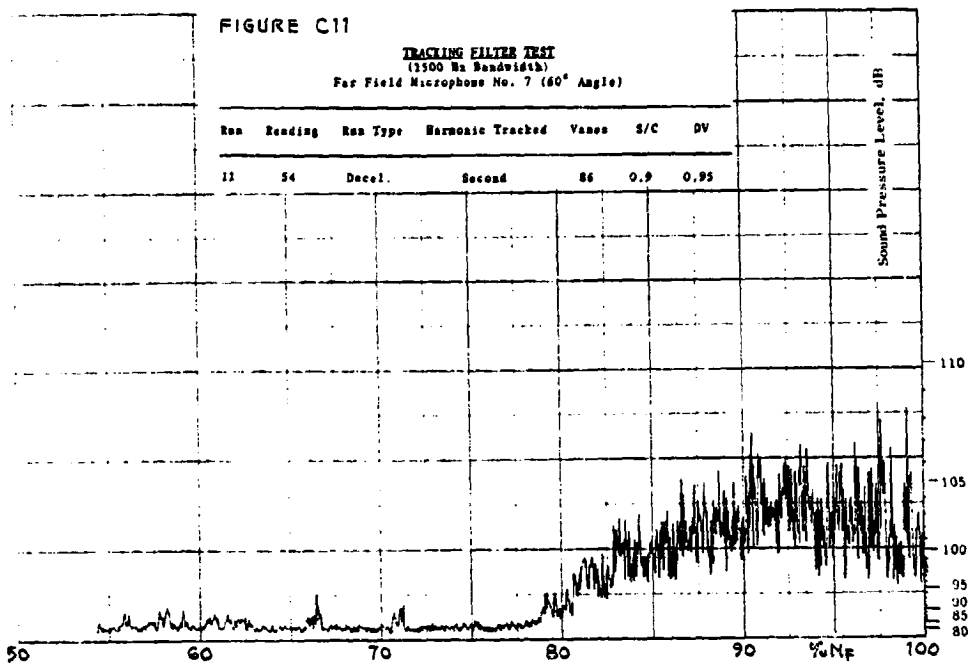

FIGURE C12

TRACKING FILTER TEST
(1500 Hz Bandwidth)
Far Field Microphone No. 7 (60° Angle)

Run	Reading	Run Type	Harmonic Tracked	Vanes	S/C	DV
11	54	Decel.	Third	86	0.9	0.95

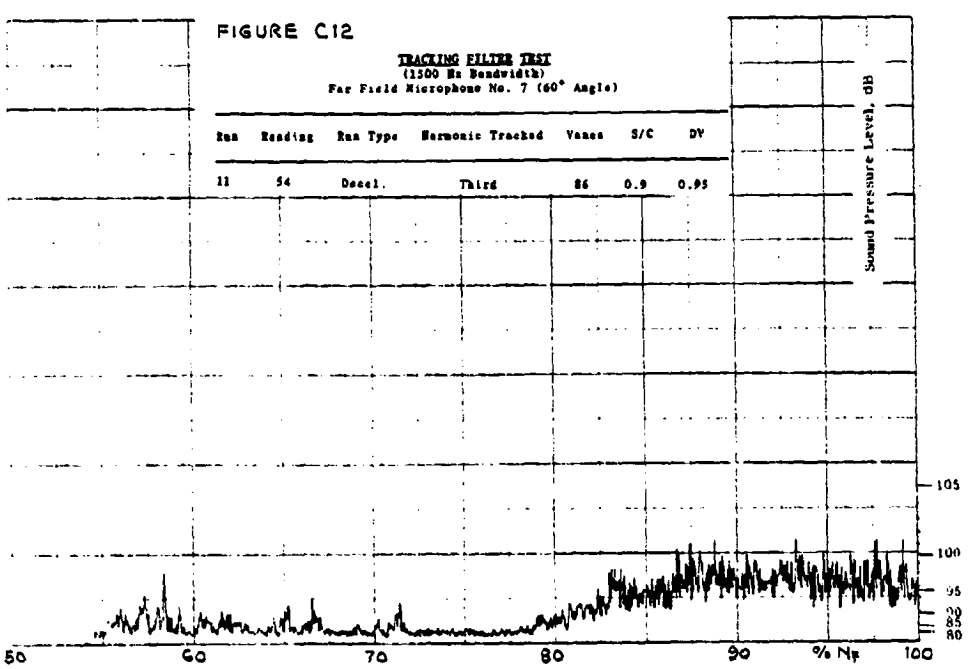

FIGURE C13

TRACKING FILTER TEST
(1500 Hz Bandwidth)
Far Field Microphone No. 7 (60° Angle)

Run	Reading	Run Type	Harmonic Tracked	Vanes	S/C	DV
8	22	Accel.	Fund	86	1.27	0.95

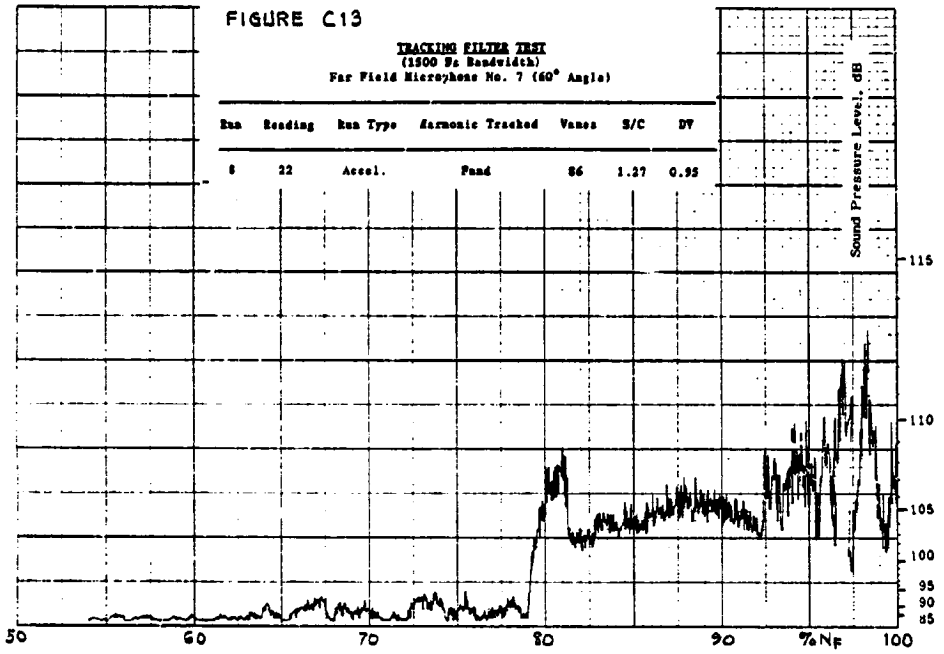

FIGURE C14

TRACKING FILTER TEST
(1500 Hz Bandwidth)
Far Field Microphone No. 7 (60° Angle)

Run	Reading	Run Type	Harmonic Tracked	Vanes	S/C	DV
8	22	Accel.	Second	86	1.27	0.95

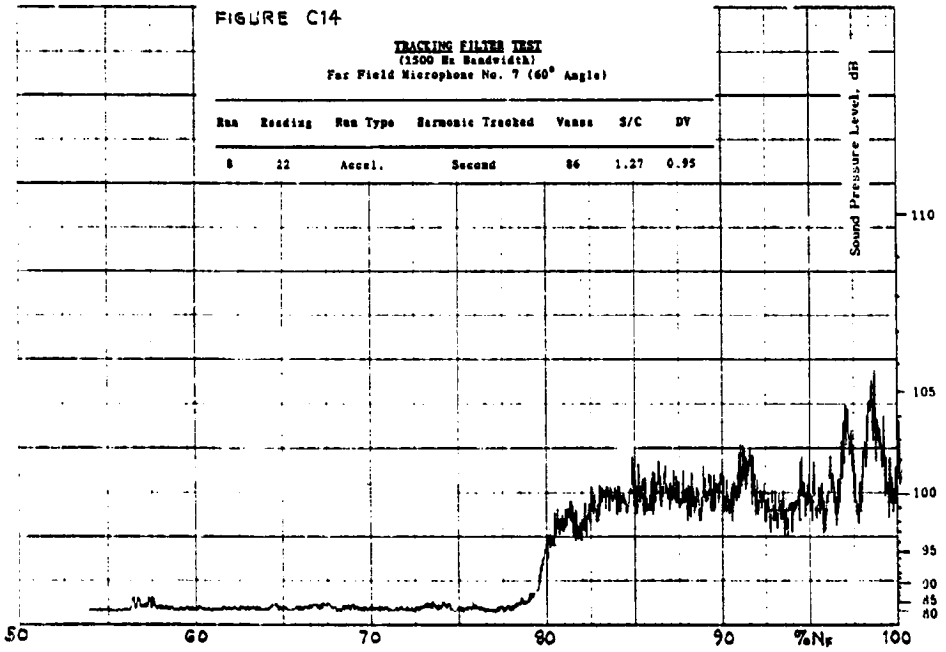

FIGURE C15

TRACKING FILTER TEST
(1500 Hz Bandwidth)
Far Field Microphone No. 7 (60° Angle)

Run	Reading	Run Type	Harmonic Tracked	Vanes	S/C	DV
8	22	Accel.	Third	86	1.27	0.95

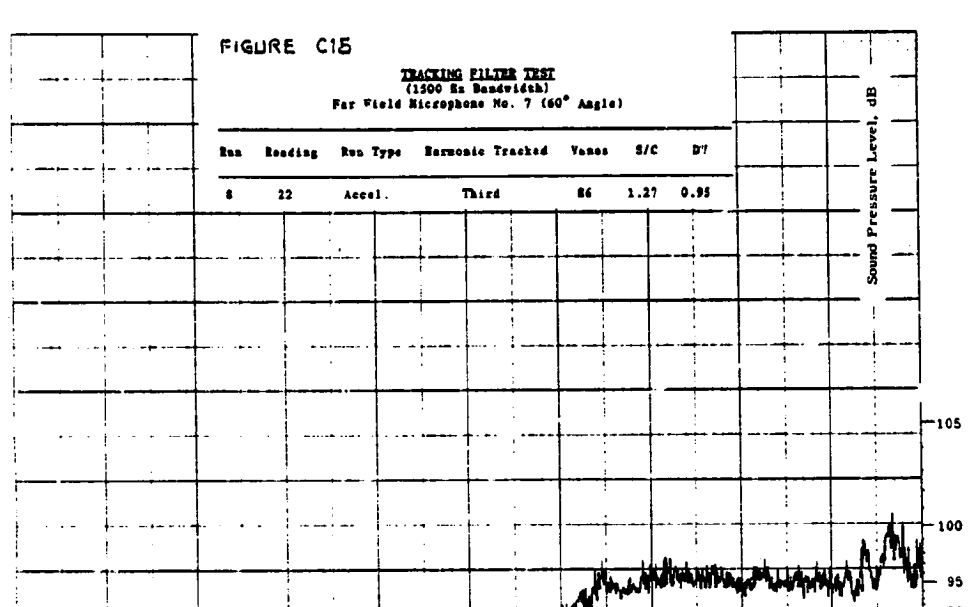

FIGURE C16

TRACKING FILTER TEST
(1500 Hz Bandwidth)
Far Field Microphone No. 7 (60° Angle)

Run	Reading	Run Type	Harmonic Tracked	Vanes	S/C	DV
8	21	Decel.	Fund	86	1.27	0.95

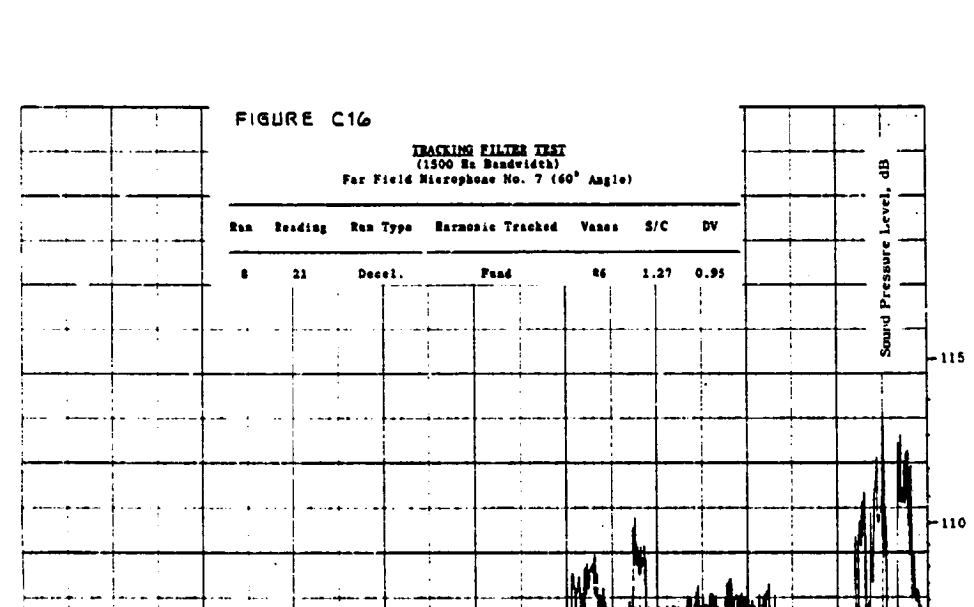

FIGURE C17

TRACKING FILTER TEST
(1500 Hz Bandwidth)
Far Field Microphone No. 7 (60° Angle)

Run	Reading	Run Type	Harmonic Tracked	Vanes	S/C	DV
8	21	Decel.	Second	86	1.27	0.95

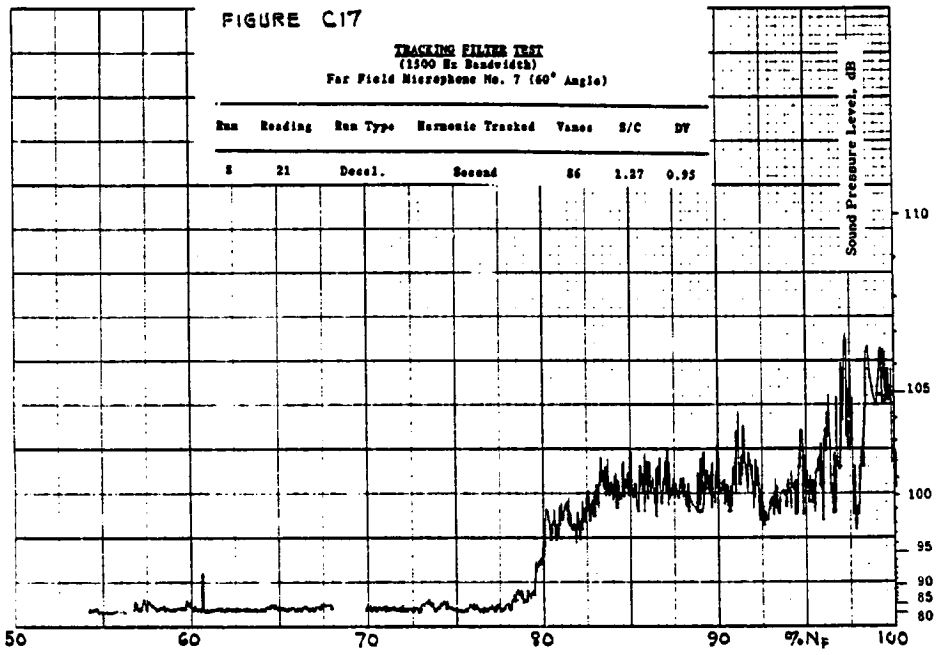

FIGURE C18

TRACKING FILTER TEST
(1500 Hz Bandwidth)
Far Field Microphone No. 7 (60° Angle)

Run	Reading	Run Type	Harmonic Tracked	Vanes	S/C	DV
8	21	Decel.	Third	86	1.27	0.95

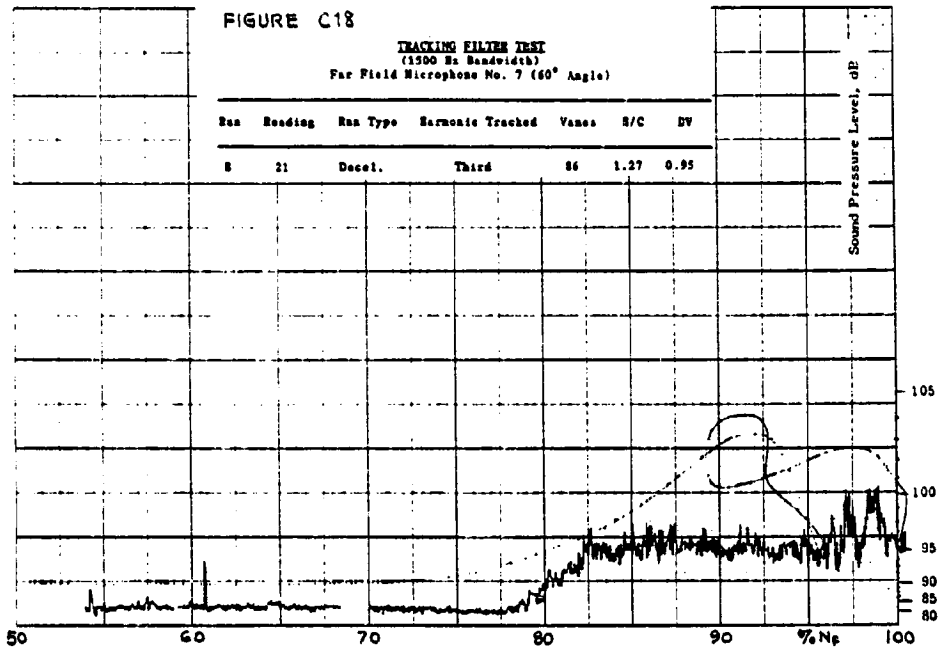

FIGURE C19

TRACKING FILTER TEST
(1500 Hz Bandwidth)
Far Field Microphone No. 7 (60° Angle)

Run	Reading	Run Type	Harmonic Tracked	Vanes	S/C	DV
10	69	Accel.	Fund	86	2.3	0.95

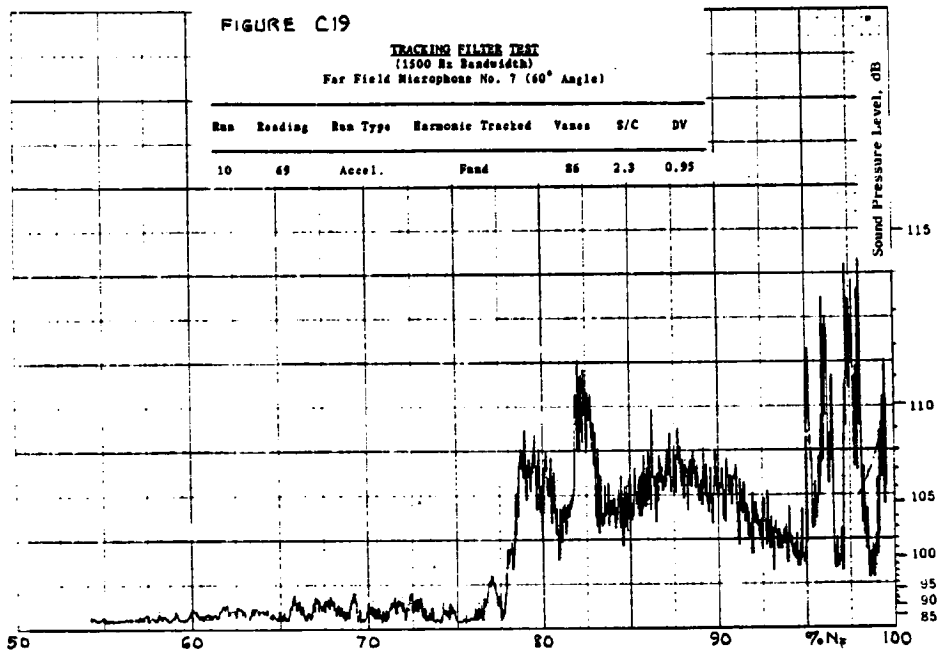

FIGURE C20

TRACKING FILTER TEST
(1500 Hz Bandwidth)
Far Field Microphone No. 7 (60° Angle)

Run	Reading	Run Type	Harmonic Tracked	Vanes	S/C	DV
10	69	Accel.	Second	86	2.3	0.95

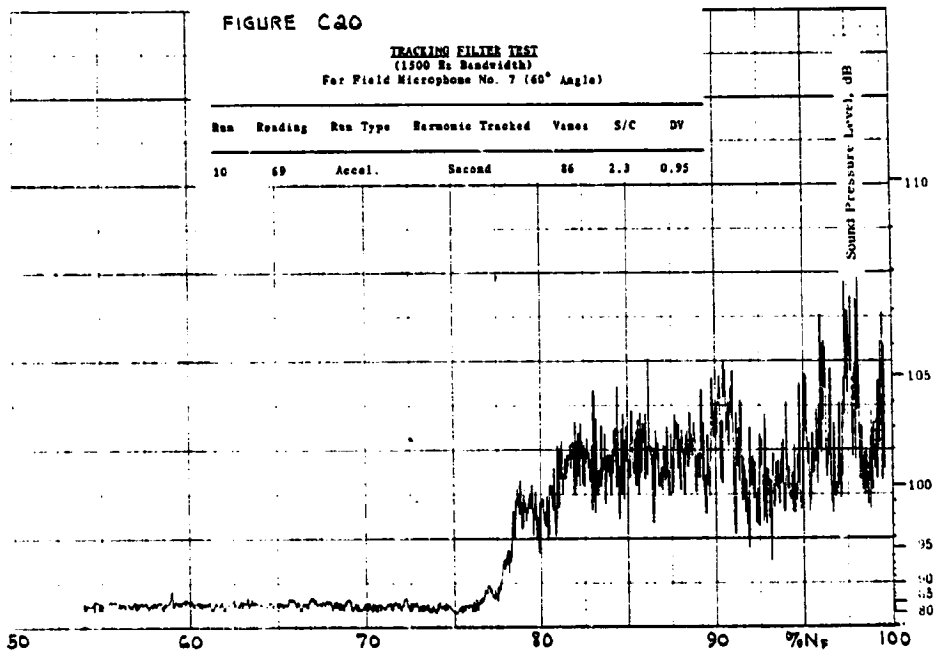

FIGURE C21

TRACKING FILTER TEST
(1500 Hz Bandwidth)
Far Field Microphone No. 7 (60° Angle)

Run	Reading	Run Type	Harmonic Tracked	Vanes	S/C	DV
10	69	Accel.	Third	86	2.3	0.95

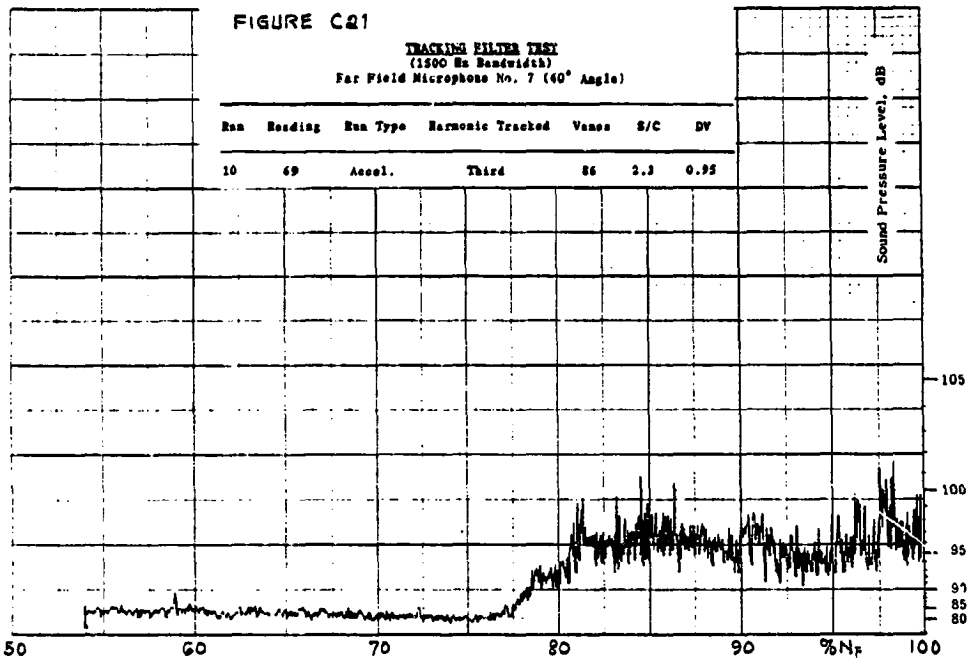

FIGURE C22

TRACKING FILTER TEST
(1500 Hz Bandwidth)
Far Field Microphone No. 7 (60° Angle)

Run	Reading	Run Type	Harmonic Tracked	Vanes	S/C	DV
10	68	Decel.	Fund	86	2.3	0.95

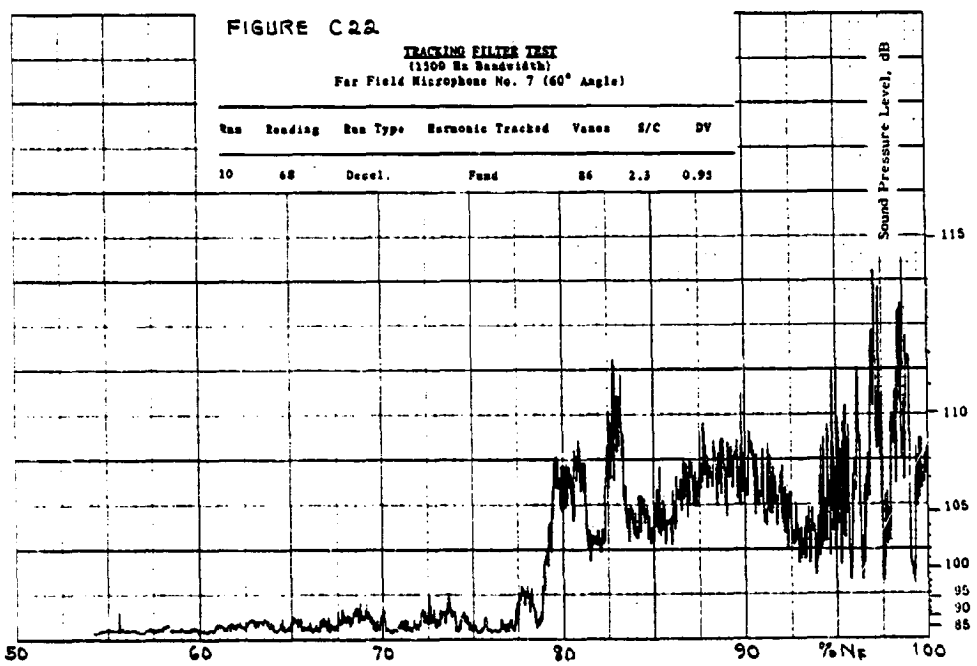

FIGURE C23

TRACKING FILTER TEST
(1500 Hz Bandwidth)
Far Field Microphone No. 7 (60° Angle)

Run	Reading	Run Type	Harmonic Tracked	Vanes	S/C	DV
10	68	Decel.	Second	86	2.3	0.95

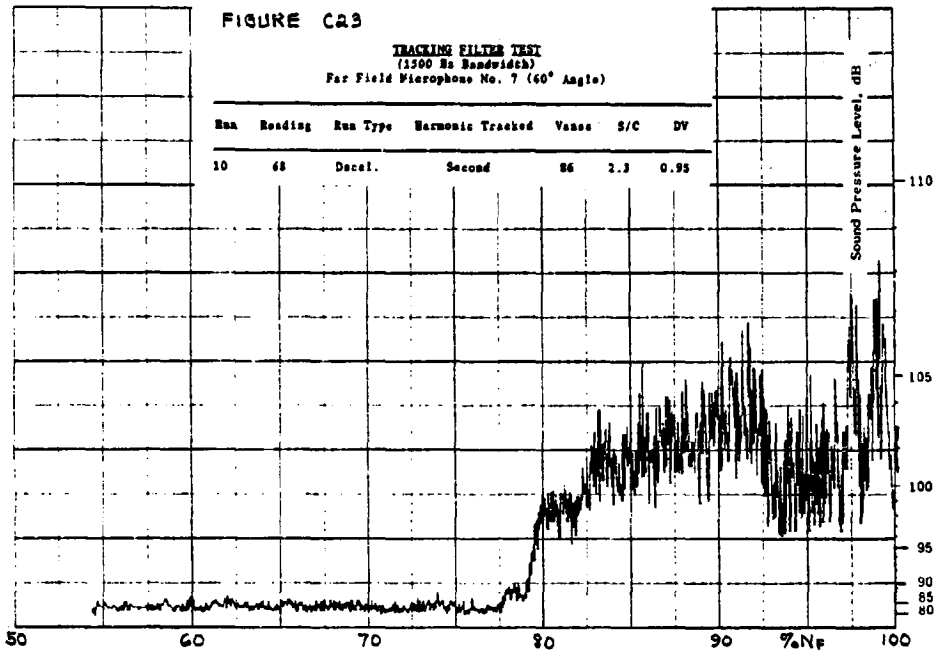

FIGURE C24

TRACKING FILTER TEST
(1500 Hz Bandwidth)
Far Field Microphone No. 7 (60° Angle)

Run	Reading	Run Type	Harmonic Tracked	Vanes	S/C	DV
10	68	Decel.	Third	86	2.3	0.95

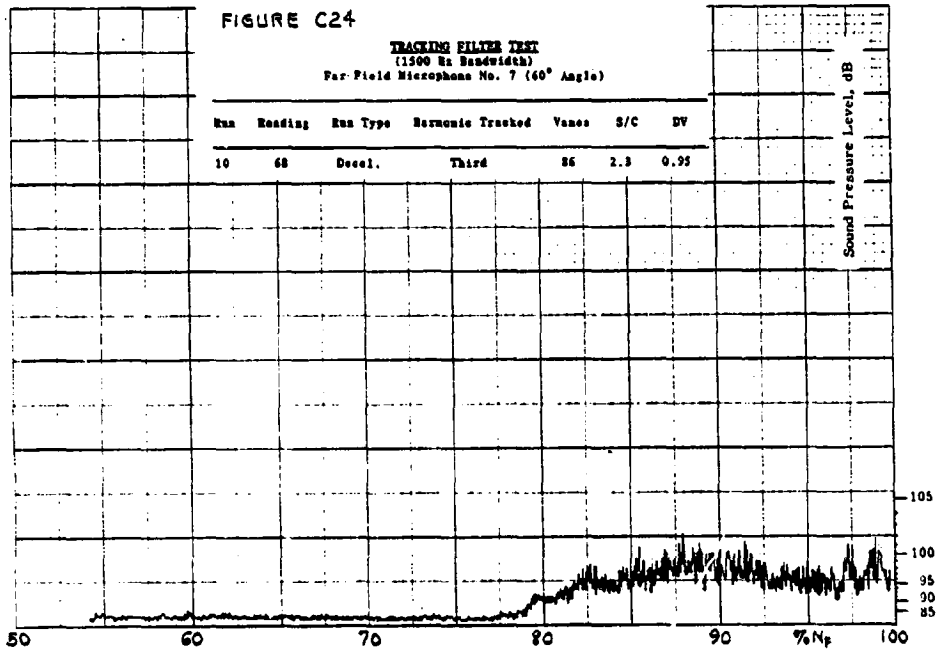

FIGURE C25

TRACKING FILTER TEST
(1500 Hz Bandwidth)
Far Field Microphone No. 7 (60° Angle)

Run	Reading	Run Type	Harmonic Tracked	Vanes	S/C	DV
12	32	Accel.	Fund	48	0.5	0.88

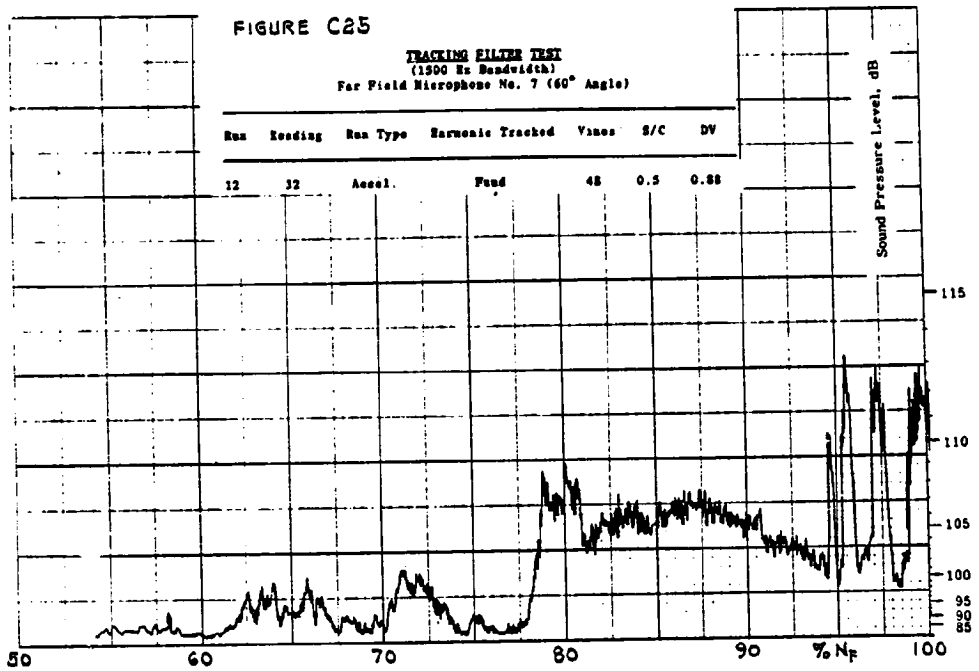

FIGURE C26

TRACKING FILTER TEST
(1500 Hz Bandwidth)
Far Field Microphone No. 7 (60° Angle)

Run	Reading	Run Type	Harmonic Tracked	Vanes	S/C	DV
12	32	Accel.	Second	48	0.5	0.88

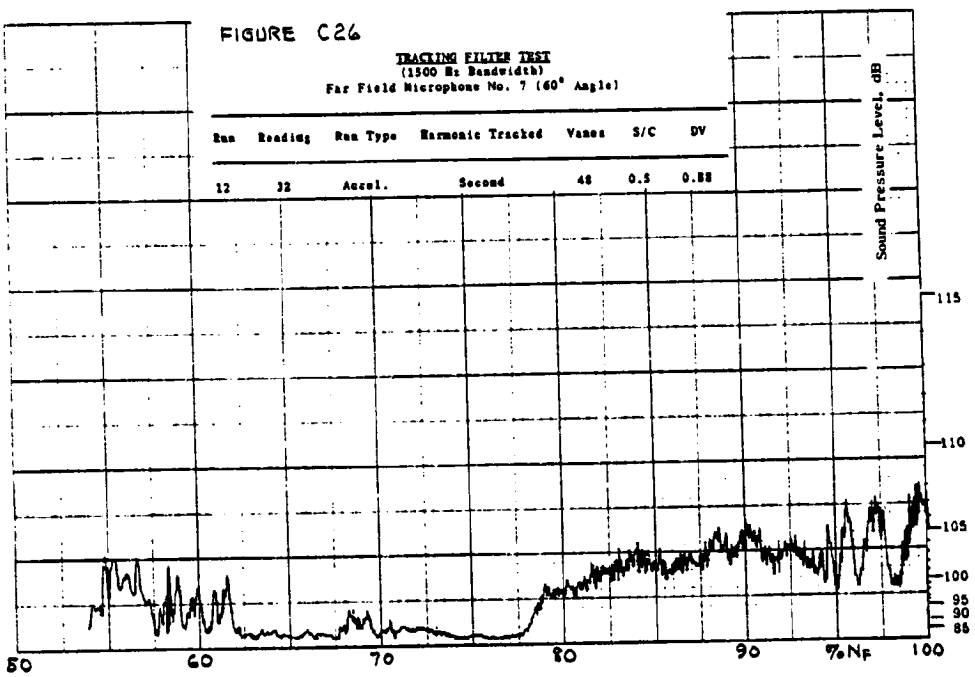

FIGURE C27

TRACKING FILTER TEST
(1500 Hz Bandwidth)
Far Field Microphone No. 7 (60° Angle)

Run	Reading	Run Type	Harmonic Tracked	Vanes	S/C	DV
13	32	Accel.	Fund	48	1.27	0.95

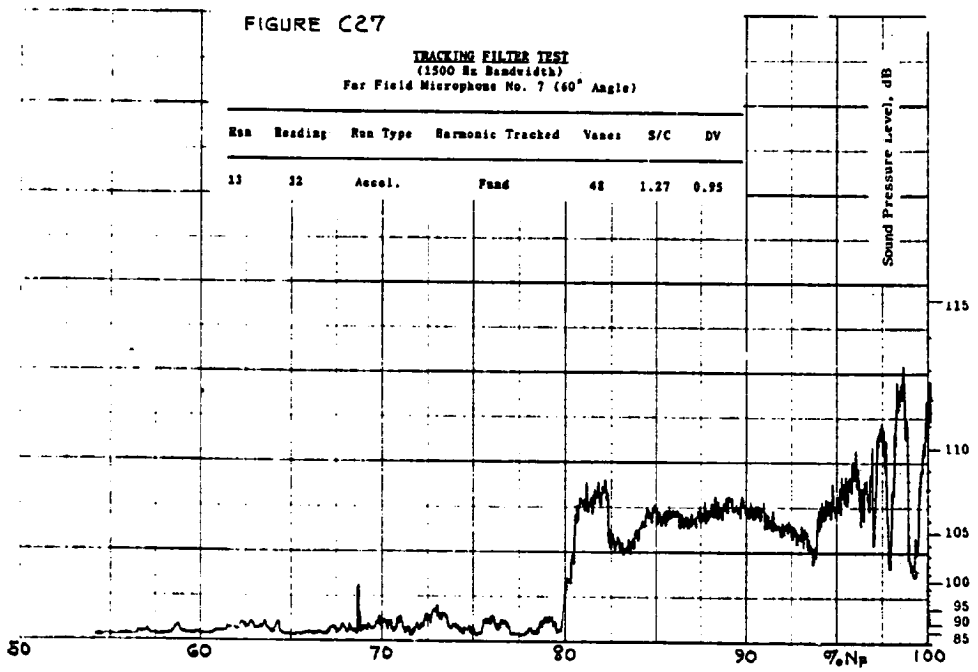

FIGURE C28

TRACKING FILTER TEST
(1500 Hz Bandwidth)
Far Field Microphone No. 7 (60° Angle)

Run	Reading	Run Type	Harmonic Tracked	Vanes	S/C	DV
13	32	Accel.	Second	48	1.27	0.95

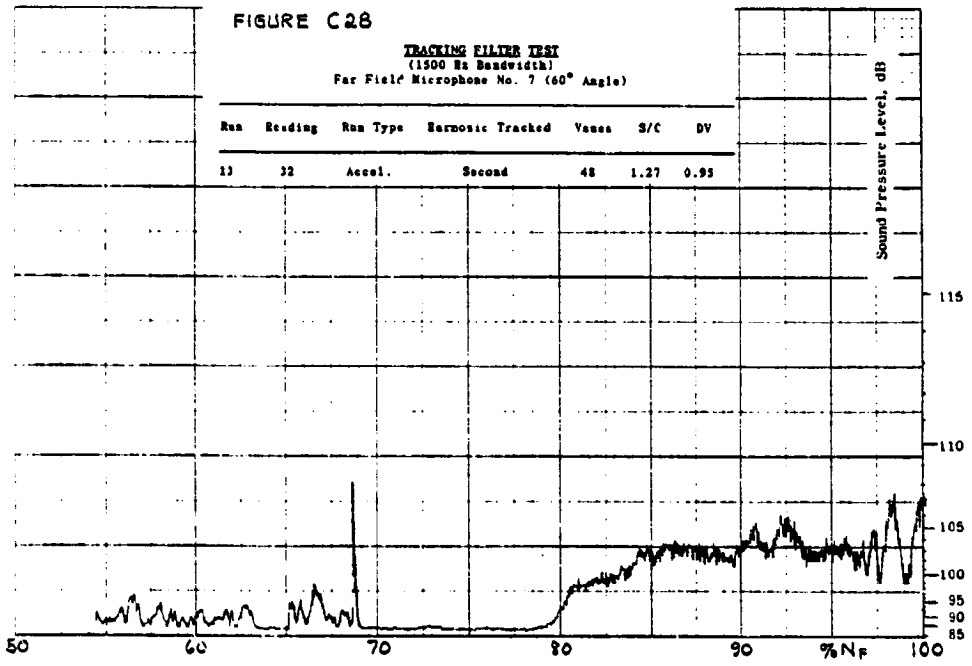

FIGURE C29

TRACKING FILTER TEST
(1500 Hz Bandwidth)
Far Field Microphone No. 7 (60° Angle)

Run	Reading	Run Type	Harmonic Tracked	Vanes	S/C	DV
13	32	Accel.	Third	48	1.27	0.95

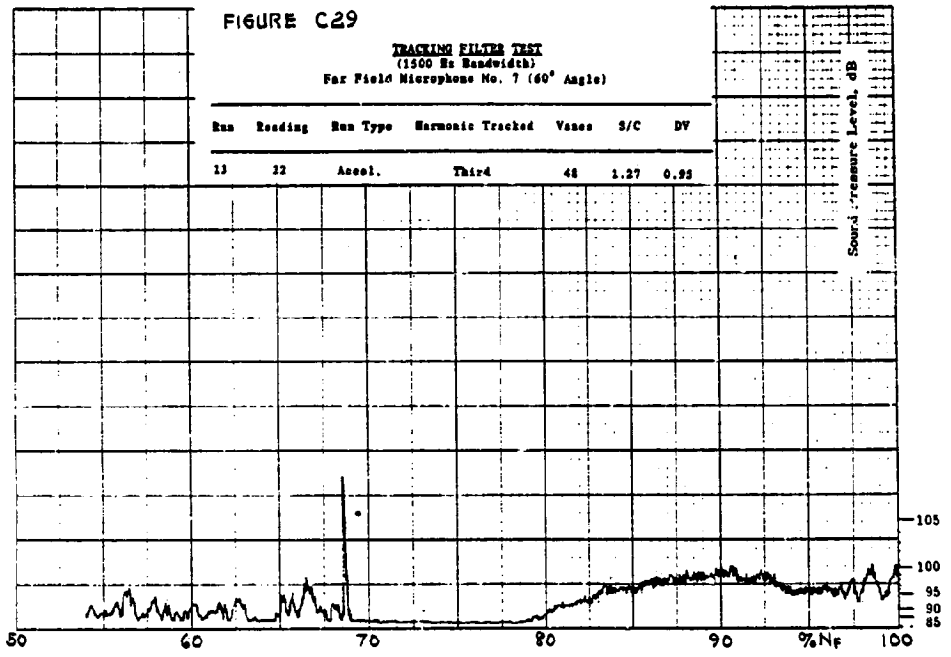

FIGURE C30

TRACKING FILTER TEST
(1500 Hz Bandwidth)
Far Field Microphone No. 7 (60° Angle)

Run	Reading	Run Type	Harmonic Tracked	Vanes	S/C	DV
15	33	Accel.	Fund	48	2.3	0.88

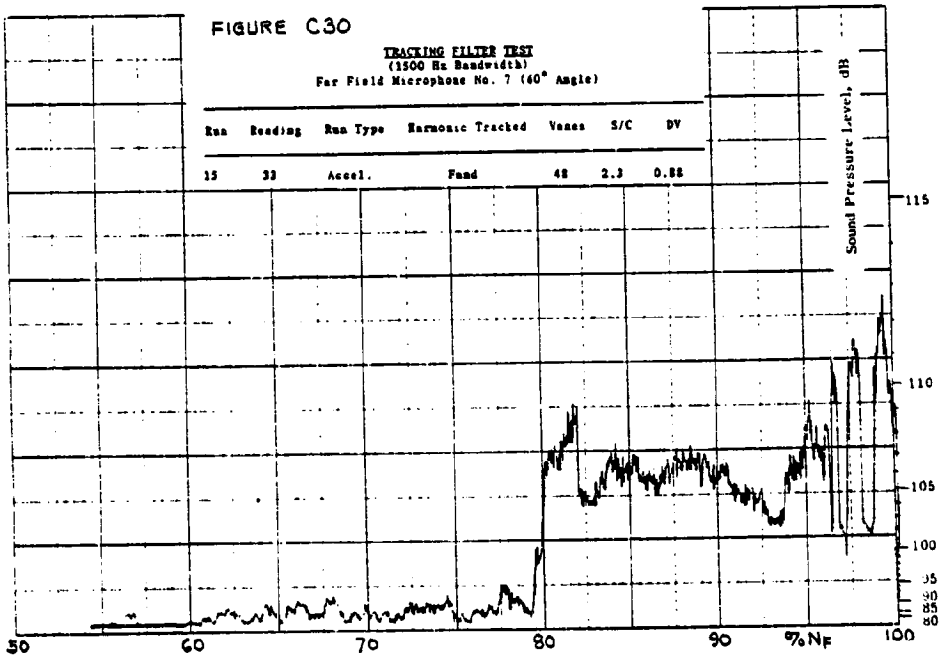

FIGURE C31

TRACKING FILTER TEST
(1500 Hz Bandwidth)
Far Field Microphone No. 7 (60° Angle)

Run	Reading	Run Type	Harmonic Tracked	Vanes	S/C	DV
15	33	Accel.	Second	48	2.3	0.88

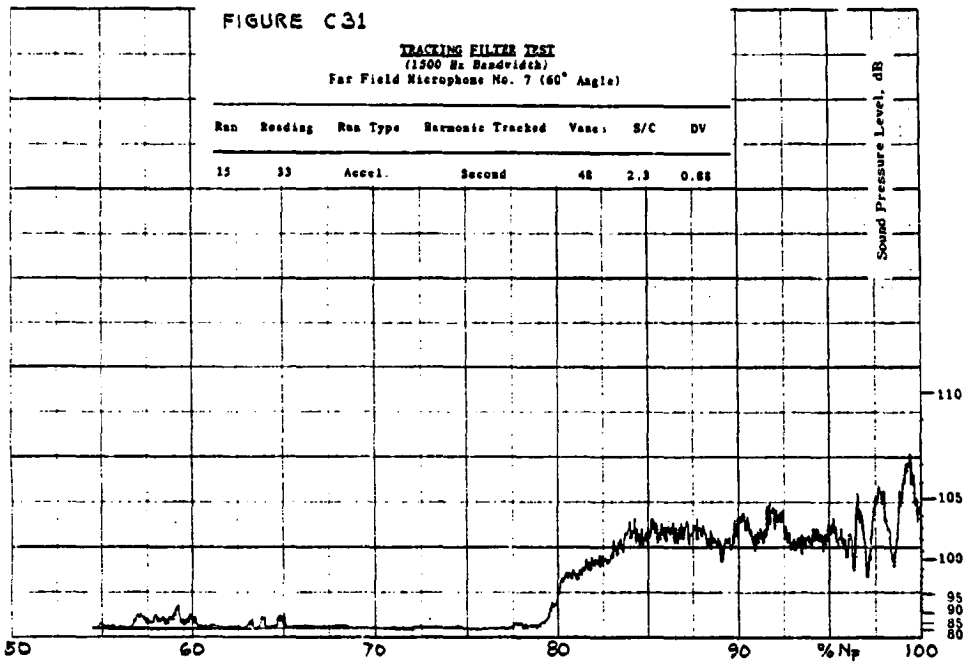

FIGURE C32

TRACKING FILTER TEST
(1500 Hz Bandwidth)
Far Field Microphone No. 7 (60° Angle)

Run	Reading	Run Type	Harmonic Tracked	Vanes	S/C	DV
15	33	Accel.	Third	48	2.3	0.88